J. Paulo Davim
Editor

Surface Integrity in Machining

Springer

Surface Integrity in Machining

J. Paulo Davim
Editor

Surface Integrity in Machining

Springer

Editor
J. Paulo Davim, PhD
Department of Mechanical Engineering
University of Aveiro
Campus Universitário de Santiago
3810-193 Aveiro
Portugal
pdavim@ua.pt

ISBN 978-1-84882-873-5 e-ISBN 978-1-84882-874-2
DOI 10.1007/978-1-84882-874-2
Springer London Dordrecht Heidelberg New York

British Library Cataloguing in Publication Data
A catalogue record for this book is available from the British Library

Library of Congress Control Number: 2009939258

TINALOX® is a registered trademark of CemeCon AG, Adenauerstraße 20 A4, 52146 Würselen, Germany. http://www.cemecon.de

Cover design: eStudioCalamar, Figueres/Berlin

Printed on acid-free paper

Springer is part of Springer Science+Business Media (www.springer.com)

Preface

A surface can be defined as a border between a machined workpiece and its environment. The term surface integrity describes the state and attributes of a machined surface and its relationship to functional performance. In general, surface integrity can be divided into two aspects: first the external topography of surfaces (surface finish) and second, the microstructure, mechanical properties and residual stresses of the internal subsurface layer. For example, surface integrity is commonly defined as "the topographical, mechanical, chemical and metallurgical state of a machined surface and its relationship to functional performance". Performance characteristics that are usually sensitive to surface integrity include, for example, fatigue strength, fracture strength, corrosion rate, tribological behavior (friction, wear and lubrication, dimensional accuracy, etc.

This book aims to provide the fundamentals and the recent advances in the study of integrity surface in machining processes.

Chapter 1 of the book provides the definition of surface integrity and its importance in functional performance. Chapter 2 is dedicated to surface texture characterization and evaluation. Chapter 3 describes residual stresses and microstructure modification, as well as the mechanical properties in the subsurface layer. Chapter 4 contains information on characterization methods of surface integrity. Chapter 5 is dedicated to surface integrity of machined surfaces by traditional and nontraditional machining. Finally, Chapter 6 is dedicated to surface integrity of micro/nano-finished surfaces.

The present book can be used as a textbook for a final undergraduate engineering course or as a topic on manufacturing at the postgraduate level. Also, this book can serve as a useful reference for academics, manufacturing researchers, manufacturing, materials and mechanical engineers, professionals in machining and related industries. The interest of scientific in this book is evident for many important centers of the research, laboratories and universities throughout the world. Therefore, it is hoped this book will inspire and enthuse other researches in this field of science and technology

The editor acknowledges Springer for this opportunity and for their enthusiastic and professional support. Finally, I would like to thank all the chapter authors for their availability for this work.

University of Aveiro
Portugal, June 2009

J. Paulo Davim

Contents

List of Contributors

Prof. Viktor P. Astakhov
(Chapter 1)
Department of Mechanical Engineering
Michigan State University
2453 Engineering Building
East Lansing
MI 48824-1226
USA
E-mail: astakhov@msu.edu

Prof. Georgios P. Petropoulos
(Chapter 2)
Department of Mechanical
and Industrial Engineering
University of Thessaly
Pedion Areos
38334 Volos
Greece
E-mail: gpetrop@mie.uth.gr

Dr. Constantinos N. Pandazaras
(Chapter 2)
Department of Mechanical
and Industrial Engineering
University of Thessaly
Pedion Areos
38334 Volos
Greece
E-mail: panda@mie.uth.gr

Prof. J. Paulo Davim
(Chapter 2)
Department of Mechanical Engineering
University of Aveiro
Campus Santiago
3810-193 Aveiro
Portugal
E-mail: pdavim@ua.pt

Prof. Janez Grum
(Chapter 3)
Faculty of Mechanical Engineering
Aškerčeva 6
1000 Ljubljana
Slovenia
E-mail: janez.grum@fs.uni-lj.si

Prof. Jianmei Zhang
(Chapter 4)
The University of Texas at El Paso
Department of Industrial Engineering
500 W University Ave
El Paso
TX 79968
USA
E-mail: jzhang2@utep.edu

Prof. Z. J. Pei
(Chapter 4)
Kansas State University
Department of Industrial
and Manufacturing Systems Engineering
2011 Durland Hall
Manhattan
KS 66506
USA
E-mail: zpei@ksu.edu

Prof. Wit Grzesik
(Chapter 5)
Faculty of Mechanical Engineering
Department of Manufacturing Engineering
and Production Automation
Opole University of Technology
P.O. Box 321
45-271 Opole
Poland
E-mail: w.grzesik@po.opole.pl

Prof. Bodgan Kruszynski
(Chapter 5)
Faculty of Mechanical Engineering
Department of Machine Tools
and Manufacturing Engineering
Technical University of Lodz
Stefanowskiego 1/15
90-924 Lodz
Poland
E-mail: kruszyn@p.lodz.pl

Prof. Adam Ruszaj
(Chapter 5)
Faculty of Mechanical Engineering
Institute of Manufacturing Engineering
and Production Automation
Cracow University of Technology
Al. Jana Pawla II
31-864 Cracow
Poland
E-mail: ruszaj@m6.mech.pk.edu.pl

Prof. M.J. Jackson
(Chapter 6)
Center for Advanced Manufacturing
Purdue University
401 North Grant Street
West Lafayette
Indiana
IN 47907
USA
E-mail: jacksomj@purdue.edu

1

Surface Integrity – Definition and Importance in Functional Performance

Viktor P. Astakhov

Department of Mechanical Engineering, Michigan State University,
2453 Engineering Building East Lansing, MI 48824-1226, USA
E-mail: astakhov@msu.edu

This chapter presents an overview of the nature of the surface that results from manufacturing processes, as this nature has long been recognized as having a significant impact on the product performance, longevity and reliability. Surface alterations may include mechanical, metallurgical, chemical and other changes. These changes, although confined to a small surface layer, may limit the component quality or may, in some cases, render the surface unacceptable. A basic understanding of the changes in the condition of the surface is very much required if improvement in product quality is to be attained. Surface integrity (SI) reveals the influence of surface properties and condition upon which materials are likely to perform. It has long been known that the method of surface finishing and the complex combination of surface roughness, residual stress, cold work, and even phase transformations strongly influence the service behavior of manufactured parts as fatigue and stress corrosion.

1.1 Introduction

All the varied modern technologies depend for the satisfactory functioning of their processes on special properties of some solids. Mainly, these properties are the bulk properties, but for an important group of phenomena these properties are the surface properties. This is especially true in wear-resistant components, as their surface must perform many engineering functions in a variety of complex environments. The behavior of material therefore greatly depends on the surface of the material, surface contact area and environment under which the material operates. To understand the surface properties and their influence on the performance of

various components, units and machines, a branch of science called surface science has been developed.

A *surface* can be described in simple terms to be the outermost layer of an entity. An *interface* can be defined to be the transition layer between two or more entities that differ either chemically or physically or in both aspects. Hudson [1] defines a surface or interface to exist in any system that has a sudden change of system properties like density, crystal structure and orientation, chemical composition, and ferro- or para-magnetic ordering. Surfaces and interfaces can be examined closely using the high-resolution microscopy, physical and chemical methods available. For their realization, a great number of simple and highly sophisticated testing machines have been developed and used [2, 3]. These tools have been built by humans to sate their innate curiosity of surface and interface interaction phenomena.

Surface science can be defined as a branch of science dealing with any type and any level of surface and interface interactions between two or more entities. These interactions could be physical, chemical, electrical, mechanical, thermal, biological, geological, astronomical and maybe even emotional [4].

1.1.1 Historical

The birth of surface science could perhaps be attributed to the first few moments of the Big Bang with all the complex surface interactions following the birth of the Universe. Although the earliest known documented record of interest in physical surface phenomena are the inscriptions of the Babylonian cuneiform dating back to the time of Hammurabi (1758B.C.) which talk about a certain practice called *Babylonian Lecanomancy* [5], surfaces have had a bad reputation for a long time: they are – inherently – superficial, even diabolical;[1] they were considered deceptive and, therefore, morally suspicious. The Greek philosopher Democritus of Abdera believed that the essence of a thing is hidden in its interior, while the (misleading) sensate qualities are caused by the surface. It was not until the middle of the 19th century that a cautious acknowledgement of surfaces began: in art, literature, and the sciences. The intellectual prerequisite was to ascribe *positive* qualities to surfaces – in the widest sense. After this idea had been established, the progress of surface science, led by pioneers such as J.W. Gibbs (surface thermodynamics) and I. Langmuir (adsorption and thin films), was rapid.

In 1877, J. William Gibbs laid down the mathematical foundations for statistical mechanics and thermodynamics. In this effort he completely described the thermodynamics of surface phases [6]. Then came Irving Langmuir (Nobel Laureate in Chemistry, 1932) who made major contributions in the knowledge of surface phenomena and whose stupendous efforts led to the recognition of surface science as a significant research field [7]. He developed the first quantitative theory of adsorption in 1915 and also did research on oil films, lipids, biofilms and molecular

[1] As Wolfgang Pauli (1900–1958), a traditionalist, expressed it: “God made solids, but surfaces were the work of the Devil.” This very popular quotation exists in a great variety of versions.

monolayers while working in the laboratories of General Electric at Schenectady, N.Y. He also carried out fundamental research on work functions of metals and came out with a detailed model on thermionic emission. A comprehensive collection of his multidisciplinary research pursuits is found in the classic historical reference [8].

Surface physics was in a nascent stage after the discovery of the electron and the atom, and it wasn't until the 1960s that surface physics actually progressed to be an independent field. This was made possible by the ultra high-vacuum technology, newly developed sophisticated surface analysis tools and digital age computers that allowed for comparisons of actual theoretical calculations with available reliable experimental data.

Earlier events that had a direct impact on surface physics development were the work on thermionic emission by Irving Langmuir, the explanation of the photoelectric effect by Albert Einstein (Nobel Laureate in Physics, 1921) and the confirmation of De Broglies' assertion of the wave nature of quantum-mechanical particles through electron diffraction by Clinton Davisson and Lester Germer [7]. Davisson shared the Nobel Prize for Physics in 1937 with G.P. Thompson. The next two decades produced intensive theoretical research in this field.

The invention of the transistor in 1947 marked a milestone in the lineage of surface physics. Work in solid-state physics and semiconductors picked up pace after the war and since then surface physics has been moving along at a steady pace with new theories being put forward and contributions from several rewarding researchers.

The term *surface science* came into common use in the early 1960s. Although there had been many previous studies of surfaces and surface phenomena, some of which led to the Nobel prize winning work of Langmuir for his studies of absorption and of Davisson and Germer on the demonstration of low-energy electron diffraction, these studies were generally classified under various other scientific subdisciplines, such as physical chemistry or electron physics [9].

Since its inception, the field of surface science has undergone an explosive expansion. This expansion has been driven by the combination of the ready availability of ultrahigh-vacuum environments, the development of techniques for the preparation of microscopic single-crystal surfaces, and the application of an increasingly complex array of surface analytical techniques, which have made possible characterization of the structure and reactivity of a wide range of surfaces [7]. A classification of some of the important areas in the different fields of surface science is shown as an illustration in Figure 1.1.

Surface engineering is almost as old as structural materials used by men. From the beginnings of time until the early 1970s, mankind has worked on the development of surface engineering, although not aware of the concept [10]. Surface engineering provides one of the most important means of engineering product differentiation in terms of quality, performance and life-cycle cost. The term surface engineering has been in use for over 15 years. It may be defined as: The design of surface and substrate together as a functionally graded system to give a cost-effective performance enhancement of which neither is capable on its own. This is by definition a highly interdisciplinary activity (Figure 1.2). The successful implementation of surface engineering requires an integrated approach at the design

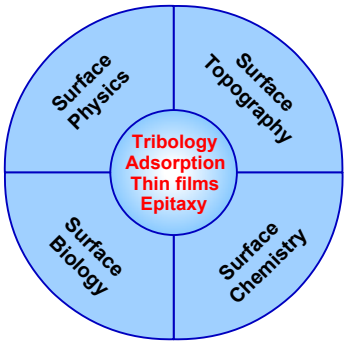

Figure 1.1. Important areas of surface science

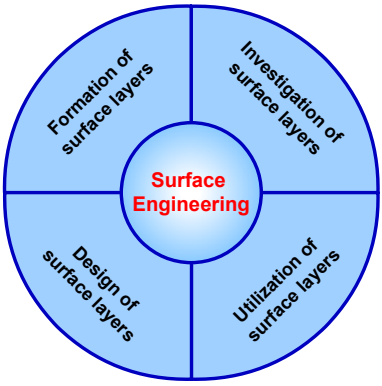

Figure 1.2. Important areas of surface engineering

stage, involving collaboration between design and surface engineers, as is increasingly being realized by managers in diverse industry sectors. In addition to being able to solve problems, surface engineering technologies have the ability to supply *added value* and thus add profit. The aim in surface engineering is to manipulate appropriate technologies to achieve optimal surface property designs for specific applications in the most cost-effective manner. Surface engineering thus has the ability to act as a bridge, transferring technology and expertise between end-user sectors that would not normally benefit from this cross-fertilization.

Surface engineering is a multidisciplinary activity intended to tailor the properties of the surface of engineering components so that their serviceability can be improved. The ASM Handbook defines surface engineering as "treatment of the surface and near-surface regions of a material to allow the surface to perform functions that are distinct from those functions demanded from the bulk of the material" [11]. Surface engineering aims to achieve desired properties or characteristics of surface-engineered components including:

- improved corrosion resistance through barrier or sacrificial protection;
- improved oxidation and/or sulfidation resistance;

- improved wear resistance;
- reduced friction energy losses;
- improved mechanical properties, for example, enhanced fatigue life, hardness or toughness;
- improved electronic or electrical properties;
- improved thermal insulation;
- improved biological properties;
- improved aesthetic appearance;
- and many others.

1.1.2 General Surface Considerations

An accurate description of the surface structures and especially surface composition of multicomponent systems is basic to the understanding of a variety of important surface phenomena. Such surface phenomena include heterogeneous catalysis, corrosion, adhesion, and lubrication. Also, electrical properties of interfaces can be greater influenced by compositions in the near-surface region.

A useful conceptual approach to the description of mixture surfaces is to model the energy of the system (e.g., an alloy) as if the components (e.g., atoms) of the system were connected by chemical bonds characteristic of the two species participating in the bond. This approach has been extremely successful in the development of solution thermodynamics of liquids and solids and has been called a quasichemical treatment [12] the term "quasichemical" leads to some confusion because it also has been applied to a specific type of non-random mixing model by Guggenheim (as presented by Graessley in [13]) as well as others. To avoid the ambiguity, the term "pairwise bond approach" is proposed to simplify a chemical description of interactions [12]. From this chemical description one can see why the mixture may experience the enrichment of at least one component in the surface region. The difference in bonding between like and unlike components in the mixture, and the absence of some bonds in the surface, result in a composition in the surface region different from the bulk composition.

Many surface-science-related publications discuss mainly the basic scientific properties of surfaces that are clean and in thermodynamic equilibrium, or nearly so. Many real surfaces that have been produced by machining are not smooth, and subjected to oxidation. All metals (except for gold and platinum metals) have stable oxides in air at room temperature. The surfaces of metal exposed to air are therefore oxidized, with the oxide layer growing at a rate determined by the diffusion of metal and oxygen atoms through the surface layer. When the surface is altered mechanically by machining, heavy plastic deformation of the surface layer occurs. During this deformation, oxide particles are forced under the surface and oxidized parts of the surface become covered with the displaced material. A mechanically produced surface therefore has a layer of a heavy disturbed mixture of metal and oxide on the outside, with a transition zone to the normal lattice below it.

Whereas the clean surfaces at high temperatures are (or approached) their equilibrium shape and are atomically smooth, the manufactured (machined) surface is still effectively immobile. A surface that is smooth in the technical sense will be

very rough on the atomic scale. The surface roughness in this case is determined by the forming operation that was used to produce the surface.

When two reasonable clean and smooth metal surfaces are in atomic contact then interatomic forces across the area of contact give very strong adhesion causing formation a metallic junction. When a tangential force is applied to cause such surfaces in contact to slide over each other then either the junction is broken or the metal fails in shear a small distance away from the junction if the junction is stronger than the shear strength of either metal brought in contact.

A manufactured surface is not perfectly flat (round). As a result, the real contact area of two manufacturing surfaces in contact is normally much smaller that the apparent contact area, as these surfaces are contacted by their asperities. This results in the constancy of the friction coefficient of a pair of manufactured surfaces over a wide range of normal pressures. Due to the elastic deformation of the asperities, the actual contact area (and thus the friction force) increases with the normal pressure keeping the same friction coefficient as the ratio of the frictional and normal forces (stresses). Chemisorbed and adsorbed layers on a manufactured surface serve as a boundary-layer lubricant that significantly reduces the bonding forces in the contact.

1.1.3 Real Surfaces of Solids

The physics and chemistry of solids deal with an idealized surface, and thus are rarely concerned with real-world surface imperfectness. A real surface may look clean and polished, however, the surface microlayers, as shown in Figure 1.3, have been formed due to external factors including manufacturing, temperature action and oxide formation. Depending on the manufacturing process involved in producing a material, a zone of work-hardened material will occupy the base of these additional layers. Above this worked layer is an amorphous or microcrystalline

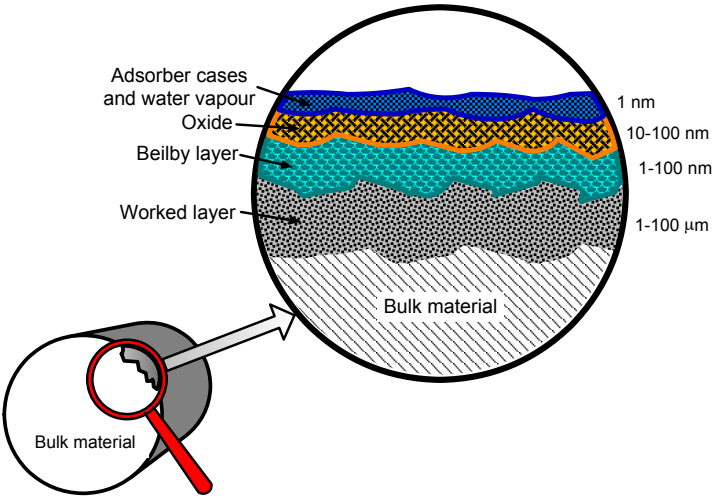

Figure 1.3. Schematic representation of a metal surface

structure, called the "Beilby" layer, which is a result of melting and surface flow during machining of the molecular layers [14]. An oxide layer sits on top of the Beilby layer, due to the oxygen available from the external environment, and surface oxidation mechanisms. A layer of adsorbents occupies the outer region and this is made up of water vapor or hydrocarbons from the environment that may have condensed and physically or chemically adsorbed onto the surface.

The surface structure may change in service. For example, microscopic investigation of surface layers on rails showed severe plastic deformation due to the normal pressure as well as shearing, together with a rapid change of temperature at service conditions lead to decomposition of the initial pearlite structure accompanied by surface oxidation, defect formation, carbon clustering, precipitation of nanosize carbide particles and austenitization of the material [15]. SEM study of fracture surfaces and fatigue crack initiation due to low-temperature irradiation showed that this radiation causes an increase in stress amplitude and a reduction in fatigue lifetime corresponding to radiation hardening and loss of ductility [16]. Neutron-irradiated samples showed a brittle fracture surface, and it was significant for large strain tests.

Other examples are: (a) environmental stress cracking of plastics by some chemical environments [17], (b) turbine vane and blade material surface deterioration caused by erosion [18], (c) surface corrosion [19], etc.

1.2 Surface Integrity: Known Notions

1.2.1 State-of-the-art

An excellent historical development of surface integrity (hereafter, SI) notion, as it is understood in manufacturing, was published by M'Saoubi *et al.* [20]. It is pointed out that the pioneering work of Field and his co-workers at Metcut (Cincinnati, OH, USA), through a series of publications, made a significant contribution to the subject setting the stage for future work [21–23]. They were indeed the first to introduce the concept of "SI" by means of defining the *inherent or enhanced condition of a surface produced in machining or other surface generation operation* [21]. Their subsequent comprehensive review of surface integrity issues that are encountered in machined components was among the first in the published literature [22], and this work emphasized the nature of metallurgical alterations occurring in the surface and subsurface layers of various alloys from conventional and non-conventional machining processes. Typical surface alterations were termed plastic deformation, microcracking, phase transformations, microhardness, tears and laps related to built-up edge formation, residual stress distribution, etc. They later provided a detailed description of measuring methods available for SI inspection [23], and presented an experimental procedure for assessing SI parameters. Their methodology specifies the use of three different levels of SI data sets to study and evaluate the characteristic features of machined surfaces (Table 1.1). Their ground-breaking achievements on the subject have contributed to a worldwide recognition and timeless value to this discipline leading to the subsequent establishment of an American National Standard on SI (ANSI B211.1, 1986).

Table 1.1. Different levels of surface integrity (SI) data set (source [23])

Minimum SI data set	**Standard SI data set**	**Extended SI data set**
Surface finish Microstructure (10× or less Microcracks Macrocrack indications Microstructure Microcracks Plastic deformation Phase transformation Intergranular attack Pits, tears, laps, protrusions Built-up edge Melted and re-deposited layers Selective etching Microhardness	Minimum SI data set Fatigue test (screening) Stress corrosion test Residual stress and distortion	Standard SI data set Fatigue test (extended to obtain design data) Additional mechanical tests Tensile Stress rapture Creep Other specific tests (e.g., bearing performance, sliding friction evaluation, sealing properties of surface)

SI concerns not only the topological (geometric) aspects of surfaces but rather the whole assemblage of their physical, mechanical, metallurgical, chemical and biological properties and characteristics. Its objective is to assure the required service properties of surfaces in part and product manufacturing because many manufacturing operations directly affect these properties. For example, Figure 1.4 shows

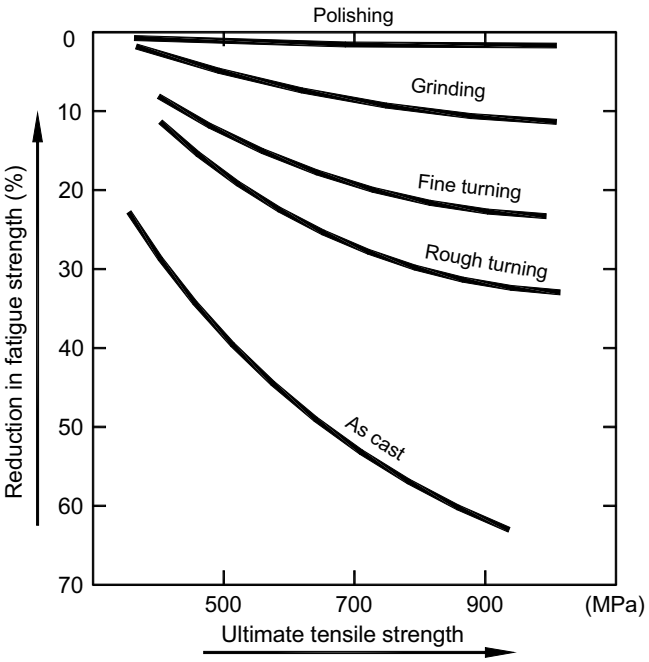

Figure 1.4. Reduction in fatigue strength of cast steel subjected to various surface-finishing operations

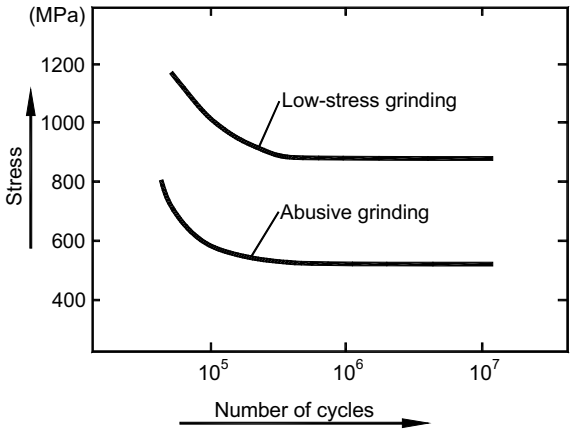

Figure 1.5. Showing that the location of the fatigue curve of ANSI 4340 steel quenched and tempered to HRC 51 depends on the mode of grinding

the influence of the surface-finishing operation on the fatigue strength of cast iron [24]. As seen, this strength depends on the particular machining operation chosen to finish the surface of a part as well as on the ultimate tensile strength of the work material. The rougher the surface, the greater the difference. The matter becomes more complicated when one realizes that SI depends not only on the chosen surface-finishing manufacturing operation but also to a great extent on the particular regime of this operation. To exemplify this point, Figure 1.5 shows the severe reduction in fatigue strength in grinding when an abusive regime is used [24]. Needless to say, SI depends on many system properties and characteristics of the entire machining system, which includes the tool and tool holder, spindle and prime drive, fixture and feed drives, coolant and method of coolant delivery, and many others that make the whole concept of SI in manufacturing rather complicated.

1.2.2 Some Typical Defects of the Machined Surface Affecting its SI

Various defects are caused by and produced during part manufacturing compromising SI. These defects can be classified as those of the original material and those imposed during manufacturing. Amongst many defects found in practice, the following are most common:

- Cracks are external or internal separations with sharp outlines. Cracks requiring a magnification of 10× or higher to be seen by a naked eye are called microcracks.
- Metallurgical transformation involves microstructural changes caused by temperature and high contact pressures. Included are phase transformations, re-crystallization, alloy depletion, decarburization, and molten and re-cast, re-solidified, or re-deposited material, as in electrical-discharge machining.
- Residual stresses caused by process forces, deformations and temperatures.
- Craters are shallow depressions.
- Inclusions are small, non-metallic elements or compounds in the metal.

- Intergranular attack is the weakening a grain boundary by liquid-metal embitterment or corrosion.
- Pits are shallow surface depressions, usually the result of chemical or physical attack.
- Plastic deformation is a severe surface deformation caused by high stresses due to friction or tool in manufacturing.

Visually distinguished microcracks are normally formed in the machining of brittle materials (Figure 1.6) or low-speed machining operations (Figure 1.7). This is because high temperature and pressure in machining of ductile materials causes healing of visible cracks. In service, however, such cracks may came to light as the strength of the healed bonds is smaller that that of the original material. Figure 1.8 shows a fatigue crack developed in the trunnion pin of an airplane. It originated in the root of the machining groove due to hidden pre-existed surface damage and was associated with shallow intergranular penetrations. Figure 1.9 shows a fretting crack developed from a grinding defect on a crankshaft shoulder.

Material-removal processes introduce structural changes to the surface of a workpiece. Severe plastic deformation of the machined surface occurs due to the action of the cutting forces and friction of the tool flank (Figure 1.10). This plastic deformation results in cold working of the surface layer. Hardness and tensile strength are increased with the degree of cold work, whilst ductility and impact values are lowered. The greater ductility of the work material, the deeper the cold-worked layer. Figure 1.11 shows a cold-worked layer formed in the turning of 304/304L stainless steel.

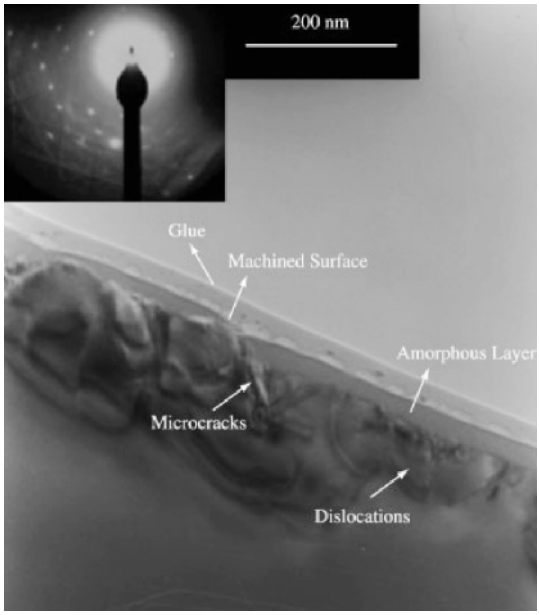

Figure 1.6. TEM cross-sectional image and diffraction pattern of a monocrystalline silicon sample turned with a single-point diamond tool

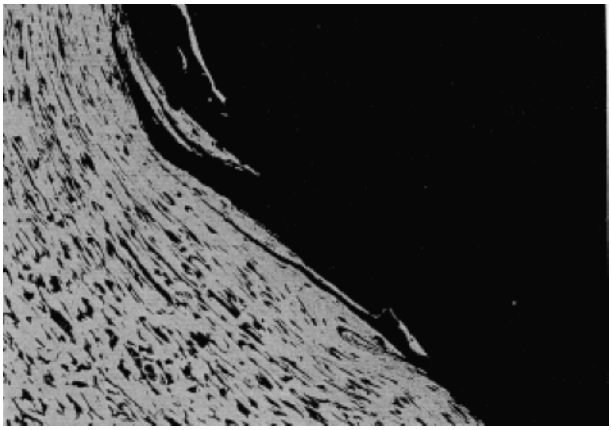

Figure 1.7. Micrograph of flaking found at the base of a thread in the fractured bolt (100×)

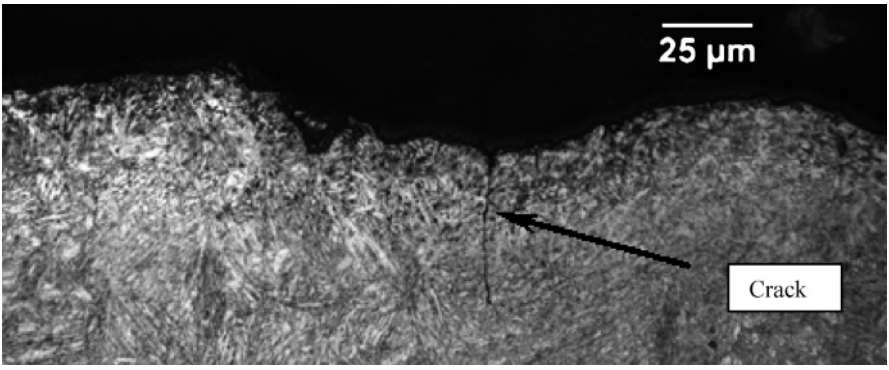

Figure 1.8. Fatigue crack indicated by arrow

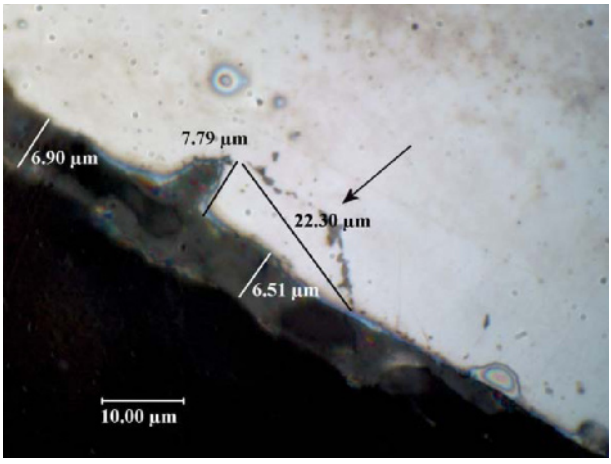

Figure 1.9. Fretting crack developed from a grinding defect on a crankshaft shoulder

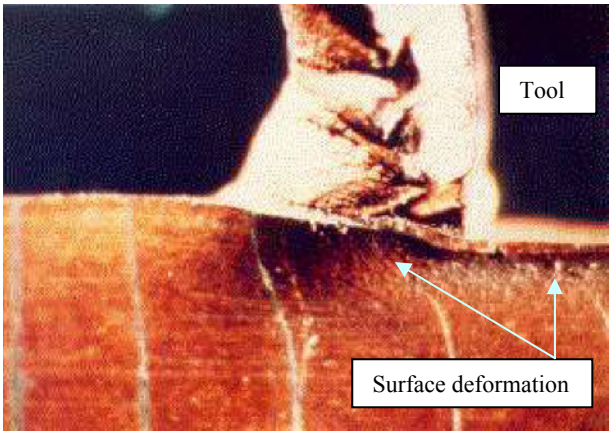

Figure 1.10. Surface plastic deformation in machining

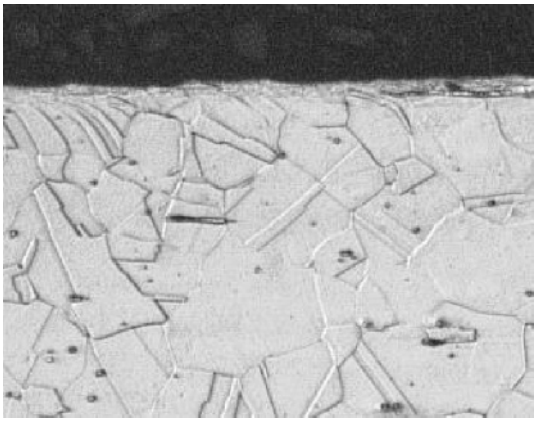

Figure 1.11. Microstructure showing deformation of grains at surface and otherwise normal microstructure of Type 304/304L stainless steel. (500×)

When hardened materials are machined, however, the surface modification may occur because of rapid thermal working, resulting in metallurgical transformation and possible chemical interactions. The worked surface can exhibit a vastly different structure compared to that of the bulk of the material. The white layers, metallurgical change and residual stresses are three basic facets of this layer [25].

The term “white layer” originated from the fact that these surfaces appear white under an optical microscope or featureless in a scanning electron microscope (SEM). Thus, in the literature, the term “white layer” is used as a generic phrase referring to very hard surface layers formed in ferrous materials under a variety of conditions, which appear white under the microscope [26]. Although the term “white layer” has become the customary way of referring to such layers, other terms such as white etching layer, non-etching layers, white phase, phase-transformed materials are also used [27].

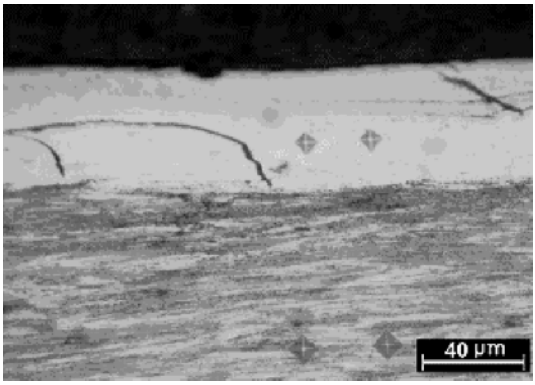

Figure 1.12. White layer formed in hard turning of ANSI 1065 steel

Perhaps the earliest mention of the presence of hard white layers on surfaces was in 1912 by Stead [28], who observed white etching layers on the surfaces of used steel wire ropes. He interpreted this as the formation of martensite as a result of frictional heating in service followed by quenching due to the colder sublayers. White layers in their different forms are as a result of factors attributed to the material removal process, such as thermal, mechanical or chemical unit events [27]. These can be directly related to factors such as strain, strain rate, heating rate, cooling rate and local environmental operating conditions. Figure 1.12 shows an example of the white layer.

Grinding requires a very large energy input per unit volume of material removed. The majority of this energy is converted to heat, which is concentrated in the surface layers of the material, within the grinding zone and as a result of this, a rapid rise in the localized temperature within the surface can occur. The actual rise in temperature depends on a range of factors, including the type of coolant, the method of coolant supply, the type of grinding wheel and the speed and depth of cut of the wheel. During grinding of hardened and tempered steel samples, the production rate, i.e., the stock removal rate, is limited by the increasing risk of thermal damage to the component. The severity of such damage, also known as grinding burns, depends on the temperature to which the workpiece surface was heated.

Figure 1.13 shows an extreme case of grinding burns on a high-speed steel hub rake face. Figure 1.14(a) shows an excessive wear of the hob rake face due to its low hardness (as seen in Figure 1.14(b)) caused by the grinding burns.

The problems caused by non-metallic inclusions and porosity are of major concern to cast iron and aluminum casting foundries and their customers in the automotive industry. The requirement to produce such castings economically, with reduced inclusions, is constantly growing. Micro inclusions can have a significant adverse effect on mechanical properties and may also impair machinability.

The yoke is a typical automotive part made of cast iron. Figure 1.15(a) and (b) show unmachined and machined yokes. Figure 1.15(b) shows a dark area on the machined surface on the cope side of the casting. The location was just below an exothermic riser. The initial thoughts were that the casting had not “cleaned-up”

and some of the oxidized "as-cast" surface remained. However, further examination of the microstructures of the white and dark areas (Figure 1.15(c) and (d)) revealed flake and vermicular graphite in the dark areas rather than nodules. Contaminated metal from the riser had apparently fed into the casting, causing the degraded microstructure. Changing the location of the risers solved the problem. Rather than placing an individual riser on top of each casting, a single riser was placed in the runner system between the ingates of two separate castings. This changed the feeding pattern so that no contaminated metal entered into the casting. This improved the SI of the machined surface.

While grinding is meant to improve the arithmetic average parameter of surface roughness (R_a) of the cast iron surface, it exposes ferrite caps or pulls them out, leaving tiny peaks or craters in the bearing surface. Caps also may be smeared over during grinding, effectively disguising them in the surface (Figure 1.16(a)). Subsequent operations such as microfinishing would then pull them out (Figure 1.16(b)), thus appearing to make the surface finish worse if only R_a is considered. Figure 1.17 shows that the root cause of this phenomenon is empty nests after particles of graphite are removed from the surface by the finishing operations.

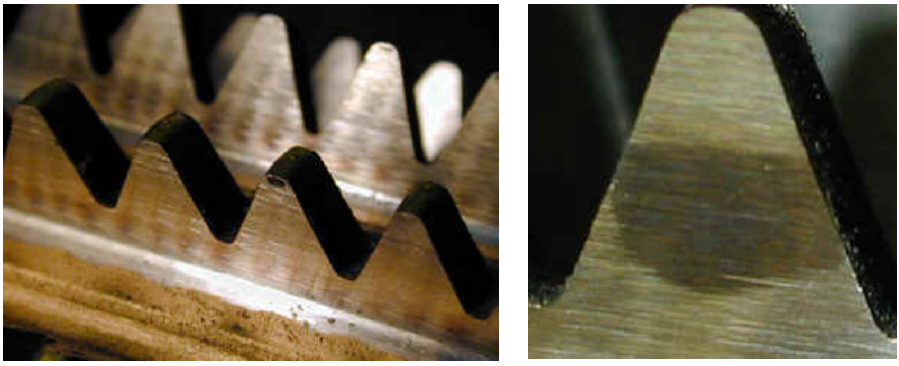

Figure 1.13. Grinding burns on the rake face of hob teeth

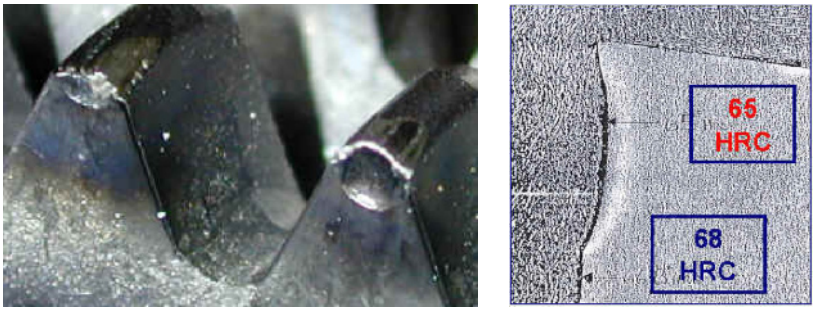

(a) (b)

Figure 1.14. Excessive wear of the hub rake face (a) due to loss of hardness on grinding (b)

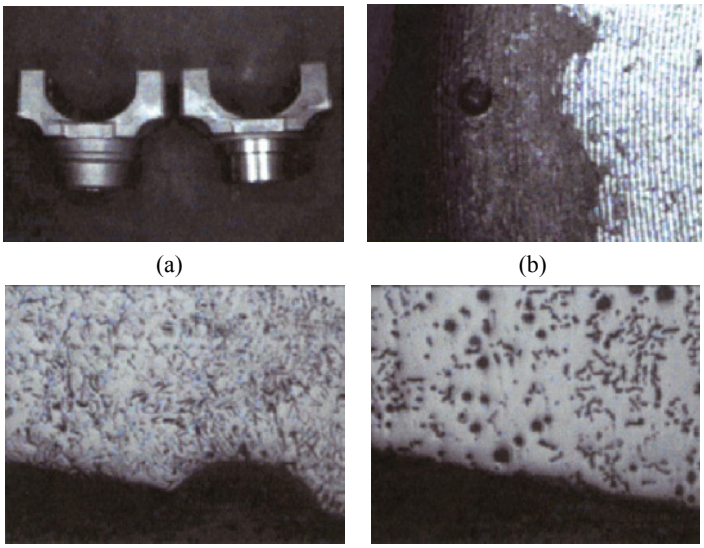

(a) (b)

(c) (d)

Figure 1.15. Graphite degradation that extended into the casting: (a) unmachined and machined castings, (b) dark area on machined surface, (c) microstructure in dark area, 100×, and (d) microstructure in white area, 100×

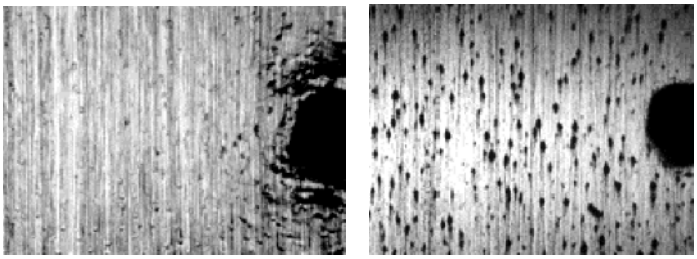

(a) (b)

Figure 1.16. Micrographs compare the surface of nodular iron crankshaft bearing journal before (50×) (a) and after (×100) (b) a three-stage microfinishing process

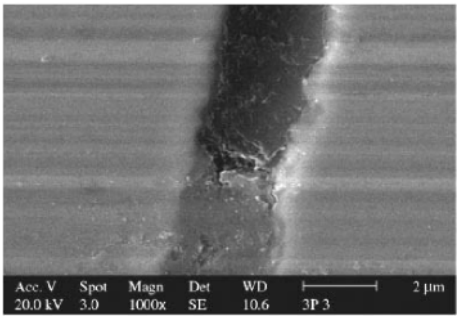

Figure 1.17. Partially empty nest after the phase of graphite removal. 1000× SEM image; SE mode

1.2.3 Obsolete Parameters in SI Data

Unfortunately, this is not acknowledged in Table 1.1 by the founders of the SI concept who represented SI as a manufacturing-related notion. As a result, the minimum, standard and extended SI data sets include only characteristics for a certain particular case. Moreover, these data sets include out-of-date components that, in the author's opinion, should not be there.

As an example, consider the built-up edge included as the component of the minimum SI set data. First, this parameter is not measurable so it cannot be included as a requirement in any technical documentation (drawing, process layout etc.). Second, the built-up edge should not normally occur in modern machining operations. Unfortunately, it is not well understood by many specialists and practitioners in the field. The available technical literature adds some confusion to the matter creating the impression that the built-up edge causes surface finish problems [29–31]. For example, the Machinery's Handbook reads "The principal cause of a poor surface finish is the built-up edge which forms along the edge of the cutting tool." (page 969 in [32]). A need is felt to clarify the issue.

To understand the discussed phenomena at the level of physical metallurgy, one should recognize that metal cutting is the purposeful fracture of the work material as defined by Astakhov [33]. The work spent in purposeful fracturing of the layer being removed, i.e., its fracture toughness, should be considered as the prime parameter in determining the cutting force and the energy spent in machining. Therefore, one should consider the mechanics of fracture [34] and the importance of the process temperature in this mechanics [35].

According to Atkins and Mai [34] and Komarovsky and Astakhov [36], there is a marked increase in the strain at fracture and also in the work of fracture, at about 0.18–0.25 of the melting point (T_m). It explains a number of "strange" results obtained by Zorev in his tests at low cutting speeds [37]. This phenomenon also explains the large size of the zone of plastic deformation observed at low cutting speeds and incorporated in the chip-formation model discussed by Astakhov [33]. The known built-up edge is the result of the discussed high plasticity region in front of the tool rake face within the contact length. Exceptions are certain *fcc* metals and alloys (Al, Cu, Ni, Pb) that do not normally cleave. As such, there is no transition in values, which gradually rises with temperature.

As discussed by Astakhov [35], if the cutting process takes place at the optimum cutting temperature, the built-up edge does not form at all, so it does not have any effect on surface finish. Figure 1.18 exemplifies this statement. As seen, the built-up edge affects the surface finish only when working with low cutting speeds when the cutting temperature is below the optimal cutting temperature (Figure 1.18(a)). When the cutting temperature is close or equal to the optimal cutting temperature, the built-up edge does not form at all so the surface roughness is practically equal to the so-called theoretical surface roughness determined by tool geometry and the cutting feed, Figure 1.18(b) [35].

Figure 1.19 shows the comparison of the surface finish calculated through the tool geometry and the cutting feed with that obtained experimentally at two different cutting speeds. As seen, when the cutting speed is selected so that the cutting temperature is close to the optimal cutting temperature (depending upon particular

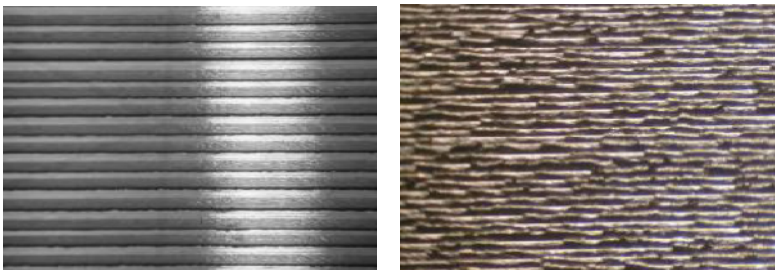

(a) (b)

Figure 1.18. Surface finish in logitudinal turning. Work material – ANSI 1045 steel, tool material – Carbide P10 (14%TiC,8%Co), rake angle $\gamma_n = 7^o$, flank angle $\alpha_n = 9^o$, tool cutting edge angle $\kappa_r = 93^o$, tool cutting minor cutting edge angle $\kappa_{r1} = 27^o$, tool nose radius r_n = 1 mm, depth of cut d_w = 0.3 mm at different cutting conditions: (a) cutting speed v = 12 m/min, feed f = 0.38 mm/rev, (b) v = 250 m/min, f = 0.45 mm/rev.

cutting feed as it also affects the cutting temperature), the actual and the calculated surface roughnesses are close to each other. When the combination of the cutting speed and feed results in the optimal cutting temperature, they are the same. In the example shown in Figure 1.18(b), it happened at a cutting speed of v=250 m/min and cutting feed f=0.24 mm/rev. Therefore, one can assess the optimality of any real cutting process by a comparison of the calculated and actual surface roughness. When all parameters of the machining system (machine tool, fixture, coolant, machining regime, etc.) are selected properly, the calculated and actual surface roughness should be the same.

1.3 Surface Integrity: A New Vision

1.3.1 Problems with the Existing Notions of SI

Although it is stated that the growing concern in the aerospace, automotive and biomedical industrial segments of the manufacturing industry is to build in absolute reliability with maximum safety and predictability of the performance of all machined components [20], in the author's opinion, no proper definition of this term is available to date. SI is an important consideration in manufacturing operations because it influences the properties of the product such as fatigue strength, resistance to corrosion, and service life. However, no one source seems to describe how to carry out this consideration practically.

In the author's opinion, the root cause of the problem lies in insufficient and non-systematic information about SI from the two most common viewpoints: the role of SI in the product and part design and the formation of a specific set of SI requirements in various manufacturing process.

There is a definite lack of systemic information at the level of handbooks and standards on the quantitative correlation between SI and part performance, although a number of research papers have been published attempting to establish

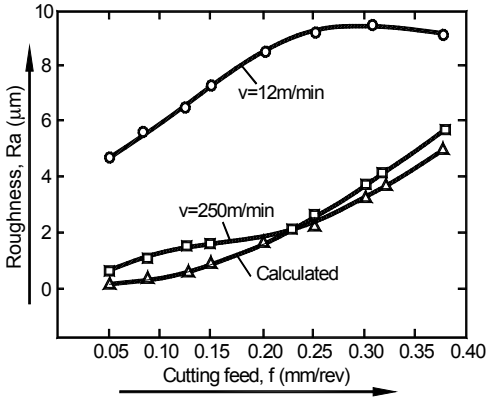

Figure 1.19. Calculated and actual surface roughness at two different cutting speeds (the cutting tool and work material are the same as those in the legend of Figure 1.18)

such correlations, for example, between surfaces finish and fatigue life [38–47], SI and corrosion behavior [48–50]. As a result, the vast majority of part drawings contain information only on surface finish, rarely surface texture and bulk material properties. Except for very few specific cases, no physical, mechanical, metallurgical and chemical properties of the surface layer such as the level and depth of cold-working, sign, depth and distribution of superficial and in-depth manufacturing (commonly, machining) residual stresses and so on are provided to manufacturing. As a result, the selection of manufacturing operations and their regimes is focused on achieving the dimensional, shape and surface finish requirements at minimum manufacturing costs. To the best of the author's knowledge, no one literature source, tool company catalog, machining/manufacturing handbook, shop manual, etc., considers the selection of the components and parameters of a manufacturing operation accounting on SI requirements.

Consider a practical example. The first issue the engineer must resolve in terms of surface finish is what type of surface will best fulfill the intended function of the part. There may be many factors that influence this decision, such as desired luster, adhesion, friction, and so on. A clear understanding of performance requirements will influence the selection of the manufacturing process and the specific measurement parameters that should be used, and could have a dramatic effect on cost reduction. Once the decision on the required surface finish is made, the next challenge is to select the proper machining operation to achieve the desired surface finish. A great variety of available cutting tool designs, tool materials, tool geometries, essential features and properties of machining systems, coolants, fixtures, etc., makes it difficult to assign SI requirements even in the simplest machining operations such as turning, milling and drilling. Figure 1.20 shows that the achievable surface finish (as one of the simplest yet practical parameters of SI) varies hundreds of per cent for the listed operations.

As is known [23, 24, 26], SI describes not only the topological (geometric) aspects of a surface and its physical and chemical properties, but also mechanical and metallurgical properties and characteristics, as indicated in Table 1.1. However,

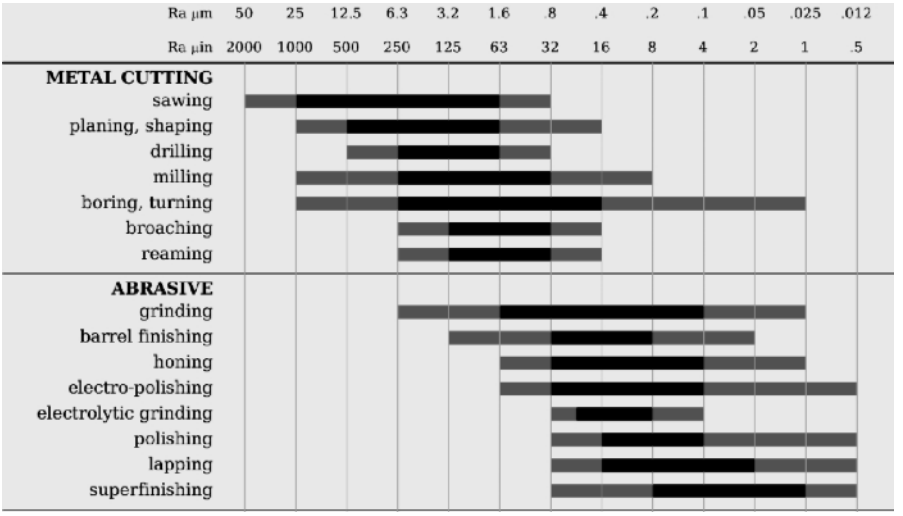

Figure 1.20. Typical surface finish for basic machining operations

when it comes to practical implementation of this seemingly useful concept, no recommendations are available to embed the requirements of SI in technical documentation. Even for parts with coatings, only the coating chemical composition and thickness are indicated, while the most important parameters affecting coating performance such as its adhesion to substrates, actual contact area, density limits and others are normally missed on part drawings. For case-hardened parts with carburized or carbonitrided and heat-treated surface layers to enhance the hardness and chemical composition of the contact areas, only the minimum case thickness and its hardness are specified, while other important properties are often left to the discretion of manufacturing.

In the author's opinion, there are two prime reasons for this:

- The available studies on SI are particular to the conditions of the tests. There is no one study that systematizes in a quantitative manner the available information on the influence of SI on part performance thus providing a part or machine designer clear guidelines for specification of the parameters of surface integrity on the drawing and in technological manuals.
- Design for manufacturing (known as DFM [51]) courses offered at Universities and in industry aim for consenting companies to consider the general engineering art of designing products in such a way that they are easy to manufacture. The basic idea exists in almost all engineering disciplines focusing on the methodology and analysis of the proper part and machine design to make manufacturing and inspection easy and thus to reduce the total cost of the product. Unfortunately, practical aspects of SI are commonly not considered in these courses.

Over the past decade, intense global competition forced many manufacturing companies to examine their business practices and to evaluate how to meet the challenges of economic globalization. Wide recognition of a need to improve product and process quality is obvious. Reduction of weight of machines, while

increasing their durability and dependability, support extended warranty and meet conditions of safety standards (for example, crashworthiness in the automotive and aerospace industries) forced many manufacturers to use better part materials and impose higher requirements to their manufacturing quality. Because it is accomplished through more precise modeling and calculation of component strength and structural integrity, greater understanding of the physics of strength and fracture control, SI and surface engineering are coming to the forefront of these activities as they are two major reserves and contributors in the pursuit of designing and manufacturing better parts and machines.

Fortunately, the increased requirements on SI come together with:

- New machine tools and assembly units capable of producing surfaces of high quality equipped with advanced controllers capable of producing parts and machine with repeatable quality.
- Wide availability of inexpensive measuring equipment to evaluate SI that are used on the shop floor. It is common nowadays that a powertrain plant in the automotive industry is equipped with an advanced materials lab having sophisticated equipment for inspecting part and surface metallurgy, physical and chemical surface properties.

Therefore, it seems that the scene is set for the implementation of the ideas of SI in continuous efforts to improve the quality of the product while reducing their manufacturing costs.

1.3.2 Definition

Surface integrity in the engineering sense can be defined as a set of various properties (both, superficial and in-depth) of an engineering surface that affect the performance of this surface in service. These properties primarily include surface finish, texture and profile; fatigue corrosion and wear resistance; adhesion and diffusion properties. When applicable, other service properties such as for example, optical properties, absorptivity, adsorption, bonding capability, emissivity, flatness, frictional resistance, score strength, stain resistance, surface temperature, surface tension, thermal emissivity, washability, wettability, biological and chemical properties, should also be considered.

The defined SI parameters are classified as:

- geometrical parameters (e.g., surface finish, texture, bearing curve parameters);
- physical parameters (e.g., microhardness, residual stresses, microstructure);
- chemical parameters (e.g., affinity oxidation, adsorption, chemisorption, surface electrical polarization, surface chemical reactions,);
- biological parameters (e.g., cell attachment, cell proliferation).

A simplified checklist for SI considerations is shown in Figure 1.21. For each and every responsible part, a set of unique SI requirements is defined depending upon:

- service (working) conditions of the surface: forces, temperatures, contact stresses, environment, etc.;
- comprehensive analyses of the mode and root cause of failure of similar parts.

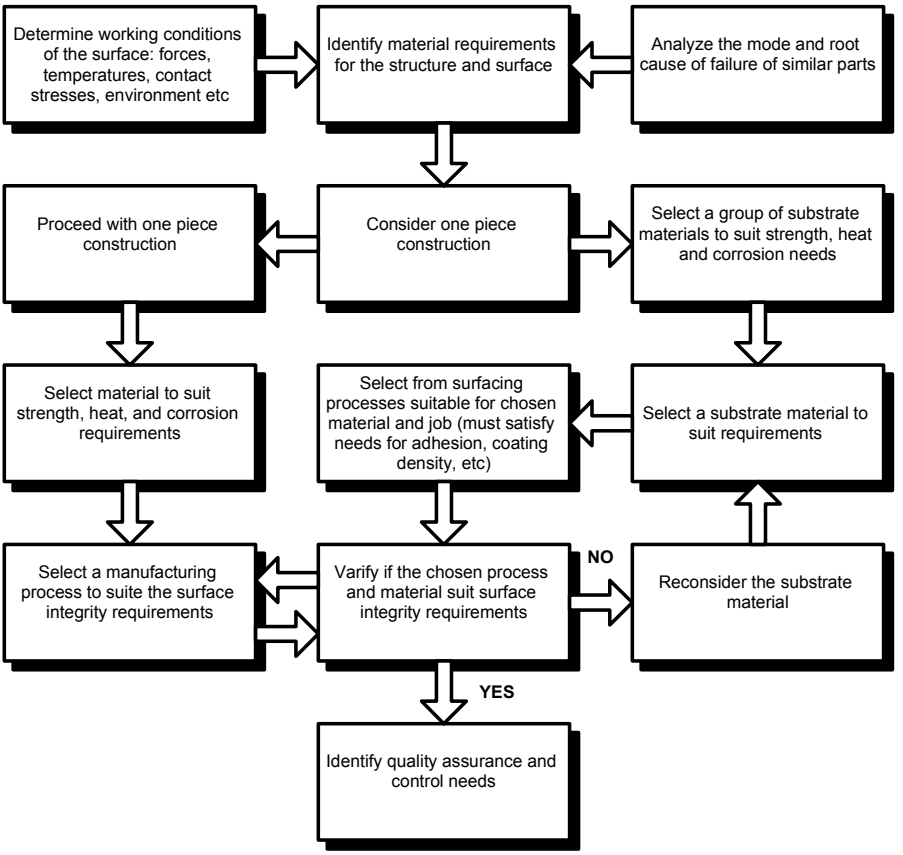

Figure 1.21. A simplified checklist for SI considerations

Almost any working condition can cause material degradation. Mechanical stresses and shocks, heat, light, short-wavelength, electromagnetic radiation, radioactive emission, interactions with bacteria, fungi or other life forms; all this can damage materials. Classification of materials degradation according to its basic cause is a first step in assigning of SI requirements for a specific part in a specific situation.

Unfortunately, the known notion and methodologies of SI do not pay sufficient attention to the formation of SI requirements. Rather, the fixed sets of requirements shown in Table 1.1 are offered. Moreover, the surface properties and defects listed above are related mainly to metals. For plastics and composite materials, a considerably different array of defects are considered such as, for example, density variation, resin cracks/crazing, cut and broken fibers, fuzzing and fraying, wrinkles, moisture, etc. [52]. The criticality of a defect for a particular composite component depends on its design requirements. The defect criticality level varies from one component design to another. Depending on design requirements, the presence of some defects below a certain threshold may not affect the performance of the part. Degradation in properties depends on the type, number, location, and

size of the defect. The criticality level of each and every defect has to be estimated for each component.

In general, voids do not degrade performance of pressure vessels (burst pressure). However, voids degrade most of the resin-dominated properties, i.e., shear, compression, transverse tension, bearing, and flexure. Fatigue, creep, and impact properties are also affected. Generally, each 1% increase in void content degrades the properties by 2–15%. The exact amount of degradation depends on the property and material system (fiber/resin), with degradation generally maximum for the first few percentages of void content.

1.3.3 Surface Integrity vs. Material Degradation

To appreciate the importance of SI in the formation of the quality of any product, one should understand the concept of material degradation in the sense introduced by Bachelor *et al.* [53]. From the point that any part/component leaves the final operation in its manufacturing, it is subjected to some form of degradation, although such degradation may not always be readily observed and measured. The rapid rusting of freshly machined steel surface is a common example of immediate material degradation, which could be considered as accumulating damage. Such damage continues throughout the part/component lifetime and material/surface degradation of some responsible component can be a limiting factor defining the lifetime of the unit/machine. Operational loads, shocks and stresses, temperatures and energy flow, the presence of aggressive media and fields (electromagnetic radiation, etc.) and many others have a shared feature of reducing the performance of engineering materials to cause their eventual failure. A simple definition of material degradation is that it is the consequence of a wide range of physical processes; it is almost universal in occurrence and is one of the major engineering problems.

Material degradation imposes a cost penalty on responsible parts and structures. For example, a mechanical structure has to be made with extra material on it to account for corrosion-induced loss, fatigue or strength reduction in service. If such losses and reductions are minimized due to proper selection of SI parameters, the extra material could be dispensed with and more load could be carried by the structure or a smaller loss of efficiency would occur during the lifetime of this structure (Figure 1.22). Progressive wear that occurs between pistons and cylinder liners inside an internal combustion engine causes leakage of combustion gases from inside the cylinders and the engine gradually becomes less efficient. It reduces the power of the engine and compromises its initial fuel economy and thus limits the lifetime of the whole engine.

According to Bachelor *et al.* [53], materials degradation is defined in terms of loss of performance of an engineering system. Lost of performance can relate to many service parameters, e.g., increased vibration of an engine due to wear of the crankshaft. For any component of equipment there is a critical minimum level of performance, e.g., whether a useful image is obtained from the optical system or where a gear tooth breaks due to fatigue. For the engine with worn cylinders, wear can increase the clearance between the piston and cylinder to such an extent that there is very low compression of combustion gases. It this case the engine can be

considered to have failed, as it will no longer be able to pull the car or truck up the hill. A mechanical degradation proceeds at a rate that varies with local conditions and failure occurs if the performance declines below the critical level. Loss of efficiency occurs if performance declines but remains above the critical level during the service lifetime. This view of mechanical degradation is illustrated schematically in Figure 1.22.

In the author's opinion, the future studies of SI should be directed at finding the SI parameters controlling the gradient of material degradation in service and the assurance of these requirement in machining operations. The true cost of material degradation should be evaluated and then balanced against the cost of SI necessary to achieve the cost-effective rate.

Moreover, machining operations should be compared in terms of surface degradation rate due to surface damage imposed by machining. As such, those operations that improve SI compared to the common should be properly evaluated and cataloged. It then should be made available to a broad pool of design/manufacturing/process engineers. For exemplification, two ready-to-use solutions for improving SI in two of the most common machining operations are considered here. The first one relates to carbide indexable inserts used in turning and drilling, while the second one relates to grinding.

There are two basic zones of wear in cutting tools: flank wear and crater wear [54]. The flank wear is most common in machining of abrasive and difficult-to machine materials in the automotive and aerospace industries. It ranges from moderate flank wear tolerated in finishing operations (Figure 1.23.(a)) to severe flank wear commonly found in roughing operations (Figure 1.23(b)). It is obvious that as tool flank wear increases, SI deteriorates proportionally. Therefore, the flank wear width selected as the tool-life criterion is assigned to be much smaller for the finishing operation than that for roughing. It is understood that this increases the direct tooling cost associated with finishing operations.

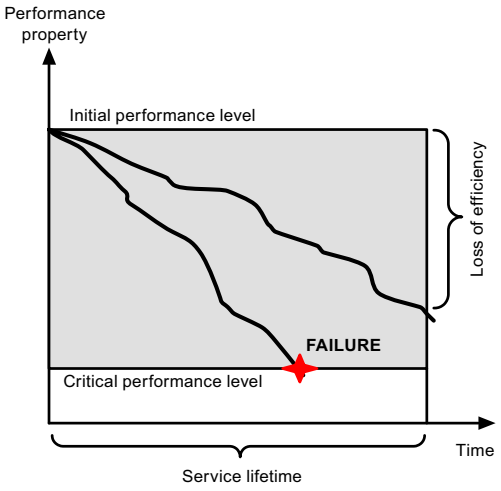

Figure 1.22. Graphical definition of materials degradation as loss of performance of an engineering system

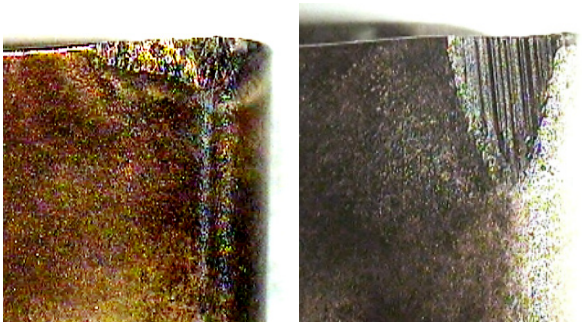

(a) (b)

Figure 1.23. Flank wear in (a) finishing, and (b) roughing

To reduce the harmful influence of flank wear on SI, an insert with restricted flank face can be used [55]. Figure 1.24(a) shows a standard square carbide indexable insert widely used in industry. Figure 1.24(b) shows an insert with the restricted flank face 1 that is a part of body 2 where a layer of copper 3 is located behind the restricted flank face. This layer serves as a heatsink for the thermal energy released at the tool flank – workpiece contact surface.

Figure 1.25 shows a FEA comparison between the temperatures fields between the standard and new inserts. Experimental results showed that up to a 100°C flank contact temperature reduction can be achieved. The higher the cutting speed, the greater the reduction.

Sintered Al_2O_3 ceramics are an attractive material for high-temperature applications because of their unique properties such as high strength, oxidation resistance, thermal shock and wear resistance. However, these excellent properties cause low machinability of such ceramics. The machining cost of ceramics reaches 80% or more of the total component cost.

Grinding using diamond abrasive wheels is widely used as an efficient and effective technique for a finishing process of ceramic materials. This machining operation, however, inevitably generates both brittle fractures and ductile flaws in ground surface layers of ceramic materials. Excessive forces during the grinding process generate defects such as chips, cracks, flaws, and/or fissures. The grinding

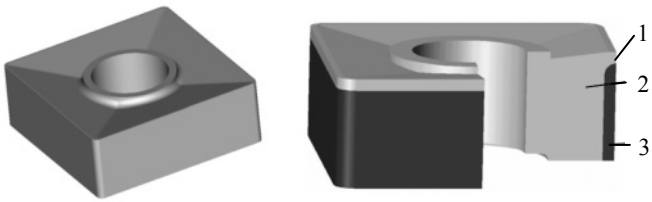

(a) (b)

Figure 1.24. Standard square carbide indexable insert (a) and a new inset with the built-in heatsink made of a layer of copper (b)

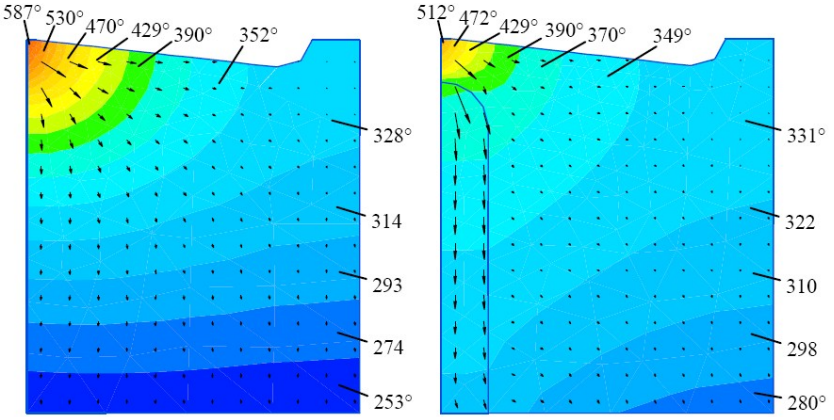

Figure 1.25. Temperature fields in machining INSI1045 steel with P20 uncoated carbide insert: cutting speed v=150 m/min. Feed f=0.1 mm/rev, depth of cut d_w=0.5 mm; (a) standard insert, and (b) new insert with heatsink.

defects decrease the strength of ceramics. The size of machining damage reached from several tens to several hundred micrometers. For removing damaged layers, additional manufacturing operations are normally required.

For a conventional grinding system, grinding depths and table-feeding speeds are the only factors controlled. Normally, the feeding speed is maintained at a constant value so such grinding is known as constant-feeding-speed (CSF) grinding. Excess forces on the grinding plane generate excess stresses, and defects in ground surface layers. The size of the damaged layer ranges from several tens to several hundred micrometers. Figure 1.26(a) shows schematically defects generated by excessive forces during conventional CSF grinding [56].

To reduce surface damage, a regulated force feeding (RFF) can be used. In this method, the table-feeding rate is altered depending on grinding conditions monitored by the grinding force. This force is used to maintain the constant grinding energy within the tool life of the grinding wheel. It shows that a much shallower damaged surface layer is achieved with this method of grinding. The comparison of the structure strength of the specimens ground using CSF and RFF grinding methods showed that the fracture strength of the machined specimen is not affected by RFF grinding, while it reduces after CFR grinding (Figure 1.27) [57]. The higher the grinding productivity, the greater the reduction.

1.3.4 Surface Integrity Requirements Depend on the Working Conditions

This section aims to show that considerable different SI considerations are used for various parts depending upon their service conditions.

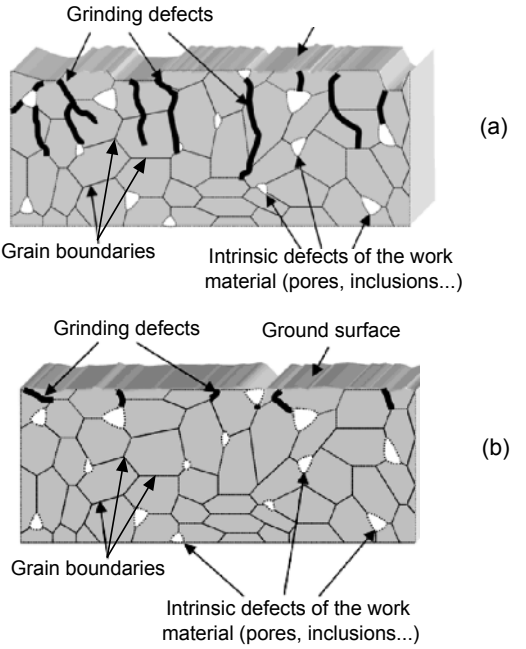

Figure 1.26. Schematic of surface damage during two grinding methods: (a) CSF, and (b) RFF

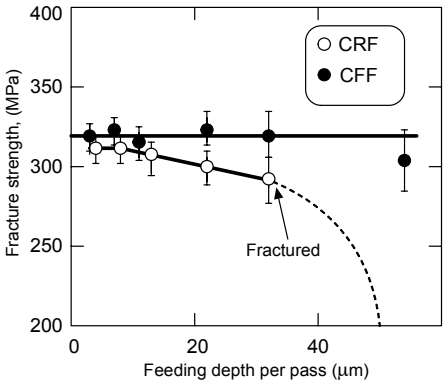

Figure 1.27. Fracture strength versus feeding depth for the specimens ground using the CSF and RFF grinding methods

1.3.4.1 SI in Cylinder Liners

Engine blocks for internal combustion engines have for a long time been made of cast iron for the resistance to cylinder wear caused by rapid sliding movement of the piston. The quality of this bore and its wear resistance determine the efficiency and life of the engine. The use of cast iron results in heavy engine blocks that runs counter to the modern trend of providing lighter weight vehicles for increased fuel

economy. Light alloy (aluminum and magnesium) cast engine blocks were introduced to achieve significant weight reduction.

To provide a compatible wear surface for the pistons operating in such engine blocks, cast iron cylindrical liners are commonly used (Figure 1.28). After been made by centrifugal casting, these liners are heat treated and semi-finished, then cooled down and placed into the block using the interference fit. The final boring and honing bring the engine cylinder to the desired level of quality. It is understood that the requirements to SI of such liners are exceptionally high as the surface quality of these liners defines to a great extent the overall quality of the engine.

Figure 1.29 shows a drawing of a semi-finished liner and Figure 1.30 shows the SI requirements. As the liner is a critical part, the SI requirements are rather tough and the compliance with these requirements adds a lot of additional cost because inspection and customer approval are required for every production lot of castings and semi-finishing. Proper inspection of SI requires sophisticated materials and metallurgical test equipment and trained personnel. Figure 1.31 shows a fragment of an inspection report.

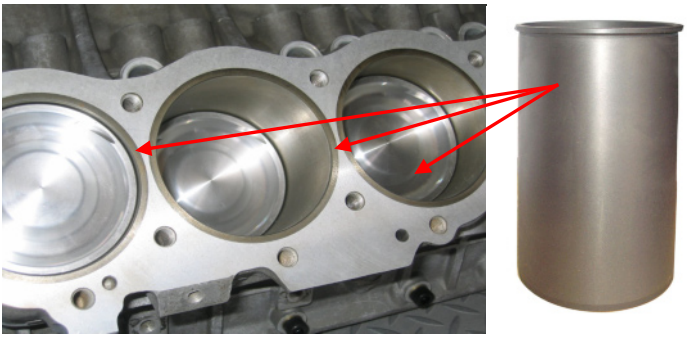

Figure 1.28. Engine block with liners and a cast iron liner

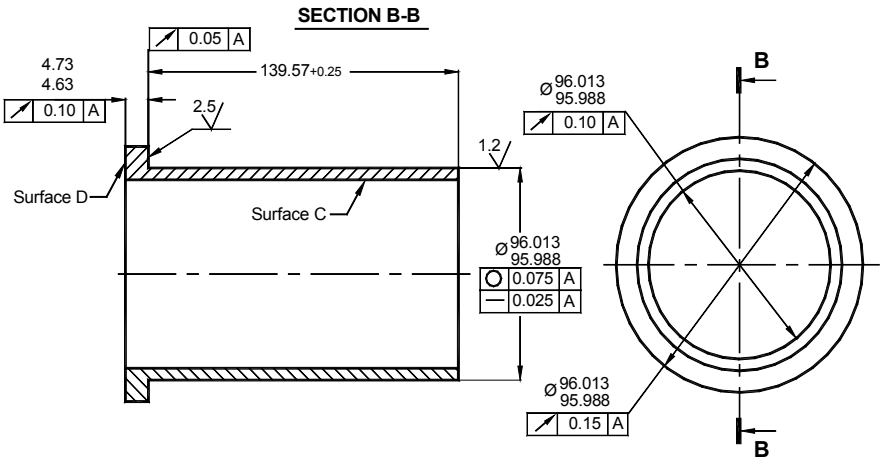

Figure 1.29. Fragment of a drawing of a semi-finished liner

ALLOWABLE VISIBLE CASTING DEFECTS ON CYLINDER BORE SURFACE:
1. MAXIMUM OF 4 PITS NOT EXCEEDED 0.5 MM IN DIAMETER AND DEPTH, SPACED OF MAXIMUM 6.0 MM APART.
2. MAXIMUM OF 2 CLUSTERS, FINE NON-INTERCONNECTED PITS OF 0.25 MM DIA MAX. EACH CLUSTER MUST BE CONTAINED WITHIN A 8.0 MM DIA CIRCLE.

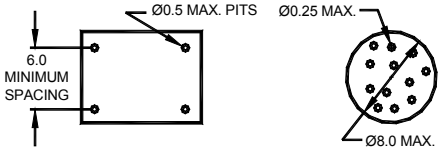

3. MATERIAL: W4-G250SP-L2 CENTRIFUGALLY CAST GRAY CAST IRON
MANDATORY CHEMISTRY (%)

CARBON	3.23-3.50
SILICON	2.25-2.80
SULFUR	0.04-0.07
CARBON EQUIVALENT	4.1-4.4 C.E.=C%+(Si%+P%)/3

4. MICROSTRUCTURE
GRAPHITE FLAKES TO BE PREDOMINANTLY TYPE A, SIZE 4-7 PER ISO945WITH TYPE B PERMISSIBLE AND MINIMAL AMOUNT OF TYPE D AND E WITH NO FLAKES LARGER (@100X) THAN 5.0MM LONG WHEN ITS WIDTH IS GREATER THAN 2.5MM.
5. MATRIX SHALL CONTAIN 95% MINIMUM LAMELLAR PERLITE, UP TO A COMBINED TOTAL OF 0.5% MAXIMUM FERRITE, CARBIDE AND STEADITE IS ALLOWED, SUCH CONSTITUENTS BEING FINELY DISPERSED AND NOT IN THE FORM OF MASSIVE PARTICLES OR A CONTINUOUS NETWORK.
6. HARDNESS TO BE 95-106RB. AVERAGE OF THREE READING TAKEN AT SURFACE D.
7. ALTERNATE BRINEL HARDNESS (TO BE USED ON SECTIONED RAW CASTING WHEN GEOMETRY REQUIREMENTS OF ISO 6506 CAN BE MET WITH EITHER 750 KG LOAD AND 5.0 BALL OR 187.5 KG AND 2.5 BALL. HARDNESS TO BE 207 TO 285 BHN.
8. MICROSTRUCTURE TO BE MEASURED AT WEARING SURFACE C AS DEFINED BY AN AREA 250-490 BELOW THE FLANGE TOP FACE C.
9. TENSILE STRENGTH 240 N/MM2 MINIMUM. TENSILE STRENGTH BASED ON TEST SPECIMEN FROM TOP HALF OF LINER.
10. PRODUCTION SAMPLE APPROVAL REQUIRED BY THE POWERTRAIN ENGINEERING PRIOR TO PRODUCT SHIPMENTS.
11. NO VISIBLE RUST OR CORROSION ALLOWED. ANY CORROSION INHIBITOR ON CYLINDER LINER MUST BE A DRY TYPE COATING APPROVED BY PRODUCT ENGINEERING. CYLINDER LINERS MUST BE CLEAN AND FREE OF ANY DIRT AND DEBRIS WHICH MAY BE HARMFUL TO CYLINDER LINER INSTALLATION EQUIPMENT AND INSTALLATION PROCEDURE.
12. GENERAL.
WELD REPAIR OR OTHER PLUGGING IS NOT PERMITTED.
NO VISIBLE POROSITY ALLOWED OB SURFACE “C” AND “D”
CASTINGS OTHERWISE MUST BE FREE OF CRACKS, BLOWS AND INCLUSIONS

Figure 1.30. SI requirements to a semi-finished liner

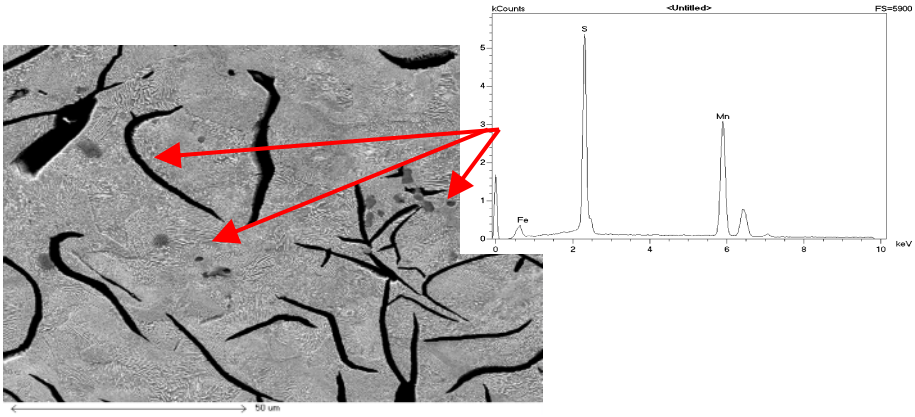

Figure 1.31. Analysis of the microstructure, flake size and MnS inclusions

As seen, SI requirements are mainly physical and metallurgical because they can be inspected when a liner is not yet inserted into an engine block. The surface topography requirements are assigned to the finished block.

1.3.4.2 SI in Transplants

Currently, most dental implant systems are made of commercially pure titanium (cpTi) because of its high *in-vitro* and *in-vivo* biocompatibility. This material allows direct bone-to-implant contact that has also been called "osseointegration" [58]. To improve the bone integration of Ti implants, surface treatments such as surface machining, acid etching, electropolishing, anodic oxidation, sand blasting or plasma spraying may be undertaken to induce chemical modifications associated with alterations of SI [59]. *In-vitro* studies have shown that surface roughness is an important parameter influencing basic biologic responses [60, 61]. Several studies have shown that cell response is improved by SI of Ti surfaces. Wennerberg *et al*. [62] evaluated implants with different SI obtained by blasting with particles of Al_2O_3, and reported that rough implants have greater bone contact compared with a turned surface and that the surface blasted with 75-µm particles showed more bone-to-implant contact than either a 25-µm or a 250-µm blasted surface. These results suggested that an intermediary average roughness (R_a) would optimize bone formation in close contact with the implant.

Evaluations of *in-vitro* biocompatibility of Ti using osteoblast cell cultures have also indicated that rough surfaces would favor the development of some cell activities. Cell attachment increases on rough surfaces [60]. Collagen synthesis, extracellular matrix, cytokines such as PGE2, growth factors and bone-like formation are also favored by rough surfaces [61, 63]. However, differences in the origin of the cells and the experimental methods make direct comparisons of results difficult or even questionable. Evaluations of biocompatibility through cell culture would have to be made using primary culture because the biomaterials will interact with these kinds of cells after *in-vivo* implantation [64]. Cells derived from osteosarcoma cannot present total differentiation *in-vitro*, while immortalized lineage can present different phenotypic expression of the cells from which they were originated [65]. The cell-culture system used in this study was human bone marrow directed *in-vitro* to form osteoblastic cells. This culture system contains mesenchymal stem cells (progenitor cells) that have the potential to differentiate into various cell types depending on the culture condition [66].

The effect of Ti surface roughness on the response of human bone marrow cell culture evaluating cell attachment, cell proliferation, total protein content, alkaline phosphatase (ALP) activity, and bone-like nodule formation [67] is presented here as an example of the influence of SI on the biological properties of a surface. The experimental titanium discs of 4 mm height used in the study were made using commercial bar stock of 12 mm diameter. All discs were polished with SiC papers in the sequence of grits 280–600–1200. Discs were subsequently subjected to the following treatments: Ti-smooth, polished with Al_2O_3 cloths to a final grain of 0.05 µm; Ti-25, blasted with 25-µm particles of Al_2O_3; Ti-75, blasted with 75-µm particles of Al_2O_3; Ti-250, blasted with 250-µm particles of Al_2O_3. All discs were cleaned in an ultrasonic bath and autoclaved before use in the cell-culture experiments. The Ti surfaces were evaluated by scanning electron microscopy (SEM) (Figure 1.32).

The results of the study are presented in Table 1.2. As seen, relatively poor correlation of the results with Ti surface roughness expressed only by R_a (the arithmetic average of the absolute values) indicates that this parameter of SI is insufficient for the considered case. The surface texture, topography, parameters of the cold-worked layer (microstructure, hardness, and residual stresses) should also be considered.

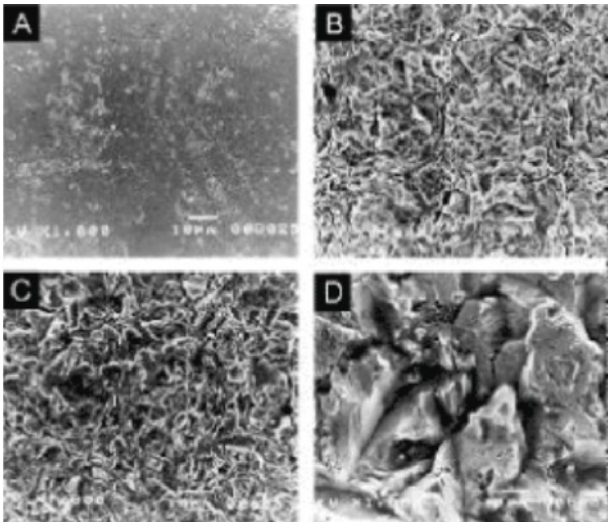

Figure 1.32. Scanning electron micrographs (1000×) of the surface of the discs. A: Ti-smooth; B: Ti-25, C: Ti-75, and D: Ti-250

Table 1.2. Cell attachment (% of the initial number of cells) after 4 h, cell proliferation expressed as doubling time (h) between 0 and 21 days, total protein content (μg protein/10^4cell) normalized by the number of cells counted after 21 days, ALP activity (μmol ρ-nitrophenol/h/μg protein/10^4cell) normalized by the total protein content and by the number of cells, after 21 days, and bone-like nodule formation (% of total disc area) after 21 days in culture on Ti discs. All data are reported as mean ± standard deviation (n=5) [67].

	T-smooth	**Ti-25**	**Ti-75**	**Ti-250**
Cell attachment	31.30 ± 9.72	32.50 ± 16.08	23.80 ± 6.92	25.30 ± 14.22
Cell proliferation	211.44 ± 10.67	238.95 ± 13.91	183 ± 14.70	174.35 ± 9.83
Total protein	7.67 ± 2.41	2.87 ± 2.50	5.62 ± 1.06	6.99 ± 0.95
ALP activity	0.20 ± 0.04	0.08 ± 0.03	0.34 ± 0.07	0.28 ± 0.09
Bone-like nodule formation	25.24 ± 8.40	32.63 ± 18.44	40.36 ± 18.60	29.60 ± 17.93

1.4 Concluding Remarks

Since its introduction, the notion of SI has attracted the attention of many researches and practitioners in manufacturing. However, not much progress was achieved in practical implementations of its basic concepts since then. Being recognized as important in improving the quality of machined parts, the concept of SI remains at its infant stage. In other words, everybody seems to like it, but not much has been done to advance the concept to the next stage of maturity.

Good ideas fail mostly because they are not allowed sufficient time to succeed. More time allows an idea to mature, and also enables it to benefit from favorable

marketplace changes. Additionally, the backers behind the idea get to learn from failure and are able to market the idea better.

The time needed for a new manufacturing concept to establish itself is mainly a function of the effort required of users to switch their mindset to the new concept and be productive. Some technologically simple ideas, e.g., tool coatings, can be instant successes, but more sophisticated multidisciplinary concepts as SI need many years to gain a foothold. The experience gained with the implementation of the main concepts of SI suggests that it may require more than a few decades to gain credibility.

The most difficult issue is the presentation of SI requirements in technical documentation: handbooks, manuals, manufacturing standards. There are a number of problems in this:

1. No one study published since the introduction of the SI notion contains a practical methodology and working example of the implementation of SI parameters shown in Table 1.1.
2. A great variety of work materials, machining operations, machining regimes, coolant brands, conditions and methods of supply, design and conditions of machine tools and many other factors that may affect SI make for a practically infinite number of possible combinations each constituting a particular case of machining. In the author's opinion, the only way to deal with this problem is to implement the similarity theory in metal machining [68]. It should help to generalize many results on SI obtained thus far, providing practical guidelines for implementation of these results in the process of selection of cutting tool, machining regime and other variables of a particular machining operation.
3. The catalogs of various tool manufacturing companies do not contain any information of SI that makes a practical engineer unable to select a cutting tool based on the ideas of SI.
4. Handbooks on machining, for example Machinery's Handbook [69], discuss only the roughness parameters definitions, measurement and designation on the drawing, while other parameters listed in Table 1.1 are not even mentioned.
5. Manufacturing is now confronted with needs to improve efficiency and cut direct manufacturing cost per unit. Aggressive machining regimes, high-speed machining, near-dry and dry machining, combining roughing and finishing operations in one are some common ways to achieve these goals. Unfortunately, SI gradually became of least concern in many machining cost-reduction considerations as it does not relate (at least, directly) to the process economy.

Machining process parameters that affect/improve SI should be assigned selectively for critical parts or even to critical machined surfaces to minimize an increase in cost of machining due to improved SI. Although SI guidelines should be primarily intended for finishing machining operation where the final components surfaces are produced for the use in service or for further surface-engineering applications (e.g., coatings), it is important, however, to know the type and depth of surface alternation on rough operations. This is because the subsequent finishing operation may be greatly affected by this alternation. Furthermore, imperfections concealed by rough machining are exceptionally deceptive and may easily lead to failures during subsequent finishing operations or in the service life of the product.

References

[1] Hudson, B. (1992) Surface Science – An Introduction, Boston: Butterworth-Heinemann.

[2] Riviere, J.C. (1990) Surface Analytical Techniques, Oxford: Oxford Science Publications.

[3] Walls, J.M., ed. Methods of Surface Analysis: Techniques and Applications. 1992, Cambridge University Press: New York.

[4] Asthana, P., Micro-and Nano-Scale Experimental Approach to Surface Engineering Metals, in Mechanical Engineering, in Mechanical Engineering. 2006, Texas A&M University: College Station, TX. p. 131.

[5] Williams, J.A., Tabor, D. (1977) The role of lubricants in machining. Wear 43: 275–292.

[6] Gibbs, J.W. (1928) The Collected Works of J. Willard Gibbs, New York: Longmans, Green and Co.

[7] Zangwill, A. (1988) Physics at Surfaces, Cambridge: Cambridge University Press.

[8] Langmuir, I. (1960) The collected works of Irving Langmuir;: With contributions in memoriam, including a complete bibliography of his works. TWELVE VOLUME SET, New York: Pergamon Press.

[9] Hudson, J.B. (1998) Surface Science: An Introduction, New York: John Wiley & Sons

[10] Reidenbach, F., ed. *ASM Handbook: Volume 5: Surface Engineering* 10th edn. 1994, ASM International: Materials Park, OH.

[11] Cotell, C.M., Sprague, J.A., *Preface, Surface Engineering*, in *ASM Handbook*. 1994, ASM International: Materials Park, OH.

[12] King, R.I., *Chapter 1: Historical Background*, in *Handbook of High-Speed Machining Technology*, R.I. King, ed. 1985, New York: Chapman and Hall.

[13] Graessley, W.W. (2003) Polymeric Liquids and Networks: Structure and Properties, New York: Taylor & Francis.

[14] Finch, G.I., Quarrell, A. G., Roebuck, J. S. (1934) The Beilby Layer. Proceedings of the Royal Society of London. Series A 145(855): 676–681.

[15] Jirásková, Y., Svobodaa, J., Schneeweissa, O., Davesb, W., Fischer, F.D. (2005) Microscopic investigation of surface layers on rails Applied Surface Science 239(2): 132–141.

[16] Hirose, T., Tanigawa, H., Ando, M., Kohyama, A., Katoh, Y., Narui, M. (2002) Radiation effects on low cycle fatigue properties of reduced activation ferritic/martensitic steels Journal of Nuclear Materials 307–311: 304–307.

[17] (2003) Characterization and Failure Analysis of Plastics, Materials Park, OH: ASM International. http://asmcommunity.asminternational.org/portal/site/www/AsmStore/ProductDetails/?vgnextoid=66b975dfae0f8110VgnVCM100000701e010aRCRD

[18] Sotnikov, A.A., Stepanov, V.N., Livshits, A.M., Bukchin, S.M. (1994) Improvement of turbine blade systems to reduce cavitation erosion Power Technology and Engineering 28(12): 746–750.

[19] Masakazu, O., Hiroshi, M., Kazuyuki, M., Tomoyoshi, O., Masayuki, U. (2005) Surface corrosion of various kinds of metals by atmospheric pollution. Bulletin of Hiroshima Kokusai Gakuin University 38: 69–83.

[20] M'Saoubi, R., Outeiro, J.C., Chandrasekaran, H., Dillon Jr., O.W. and Jawahir, I.S. (2008) A review of surface integrity in machining and its impact on functional performance and life of machined products. Int. J. Sustainable Manufacturing 1(1/2): 203–236.

[21] Field, M., Kahles, J.F. (1964) The surface integrity of machined and ground high strength steels. DMIC Report 210: 54–77.

[22] Field, M., Kahles, J.F. (1971) Review of surface integrity of machined components. Annals of the CIRP 20(2): 153–162.

[23] Field, M., Kahles, J.F., Cammett, J.T. (1972) Review of measuring methods for surface integrity. Annals of the CIRP 21: 219–238.

[24] Kalpakjian, S. and S.R. Schmid (2001) Manufacturing Engineering and Technology. 4th edition ed, New Jersey: Prentice-Hall.
[25] Chou, Y.K., Evans, C.J. (1999) White layers and thermal modelling of hard turned surfaces. International Journal of Machine Tools and Manufacture 39: 1863–1881.
[26] Griffiths, B.J. (1993) Modeling complex force system, Part 1: The cutting and pad forces in deep drilling. ASME Transactions, Journal of Engineering for Industry 115: 169-176.
[27] Bosheh, S.S., Mativenga, P.T. (2006) White layer formation in previous termhard turning of H13 tool steel at high cutting speeds using CBN tooling. International Journal of Machine Tools and Manufacture 46(2): 225–233
[28] Stead, J.W. (1912) Micro-metallography and its practical applications. Journal of Western Scottish Iron and Steel Institute 19: 169–204.
[29] Nakayama, K., Shaw, M.C., Brewer, R.C. (1966) Relationship between cutting forces, temperatures, built-up edge and surface finish Annals of CIRP 24: 211–223.
[30] Masounave, J., Youssef, Y.A., Beauchamp, Y., Thomas, M. (1997) An experimental design for surface roughness and built-up edge formation in lathe dry turning. International Journal of Quality Science 2(3): 167–180.
[31] Stenphenson, D.A., Agapiou, J.S. (1996) Metal Cutting Theory and Practice, New York: Marcel Dekker.
[32] Oberg, E., Jones, F.D., Horton, H.L., Ryffel, H.H. (2004) Machinery's Handbook. 27th edn, New York: Industrial Press.
[33] Astakhov, V.P. (1998/1999) Metal Cutting Mechanics, Boca Raton, USA: CRC Press.
[34] Atkins, A.G., Mai, Y.W. (1985) Elastic and Plastic Fracture: Metals, Polymers. Ceramics, Composites, Biological Materials, New York: John Wiley & Sons.
[35] Astakhov, V.P. (2006) Tribology of Metal Cutting. Tribology and Interface Engineering Series, No. 52, ed. B.J. Briscoe, London: Elsevier.
[36] Komarovsky, A.A., Astakhov, V.P. (2002) Physics of Strength and Fracture Control: Fundamentals of the Adaptation of Engineering Materials and Structures, Boca Raton: CRC Press.
[37] Zorev, N.N. (1966) *Metal Cutting Mechanics*. 1966, Pergamon Press: Oxford.
[38] Javidi, A., ieger, U., Eichlseder, W. (2008) The effect of machining on the surface integrity and fatigue life. International Journal of Fatigue 30(10-11): 2050–2055.
[39] Seemikeri, C.Y., Brahmankar, P.K., Mahagaonkar, S.B. (2008) Investigations on surface integrity of AISI 1045 using LPB tool. Tribology International 41(8): 724–734.
[40] Liu, J., Yue, Z.F., Liu, Y.S. (2007) Surface finish of open holes on fatigue life. Theoretical and Applied Fracture Mechanics 47(1): 35–45.
[41] Choi, Y., Liu, C.R. (2006) Rolling contact fatigue life of finish hard machined surfaces: Part 1. Model development. Wear 261(5–6): 485–491.
[42] Matsumoto, Y., F. Hashimoto, and G. Lahoti (1999) Surface Integrity Generated by Precision Hard Turning. Annals of the CIRP 48/1: 59–62.
[43] Lennon, A.B., McCormack, B.A.O., Prendergast, P. J. (2003) The relationship between cement fatigue damage and implant surface finish in proximal femoral prostheses. Medical Engineering & Physics 25(10): 833–841.
[44] Paulin, C., Ville, F., Sainsot, P., Coulon, S., Lubrecht, T. (2003) Effect of rough surfaces on rolling contact fatigue theoretical and experimental analysis. Tribology and Interface Engineering Series 43: 611–617.
[45] Hutson, A.L., Niinomi, M., Nicholas, T., Eylon, D. (2002) Effect of various surface conditions on fretting fatigue behavior of Ti–6Al–4 V. International Journal of Fatigue 24(12): 1223–1234.
[46] Chen, H.Y., Hickel, R., Setcos, J.C., Kunzelmann, K-H. (1999) Effects of surface finish and fatigue testing on the fracture strength of CAD-CAM and pressed-ceramic crowns. The Journal of Prosthetic Dentistry 82(4): 468–475.

[47] Bayoumi, M.R., Abdellatif, A.K. (1995) Effect of surface finish on fatigue strength. Engineering Fracture Mechanics 51(5): 861–870.
[48] Asquith, D.T., Yerokhin, A.L., Yates, J.R., Matthews, A. (2007) The effect of combined shot-peening and PEO treatment on the corrosion performance of 2024 Al alloy. Thin Solid Films 516(2–4): 417–421.
[49] Aballe, A., Bethencourt, M., Botana, F.J., Marcos, M., Sánchez-Amaya, J.M. (2004) Influence of the degree of polishing of alloy AA 5083 on its behaviour against localised alkaline corrosion. Corrosion Science 46(8): 1909–1920.
[50] Reddy, B.S.K., Ramamoorthy, B., Nair, P.K. (2005) Surface integrity aspects and their influence on corrosion behaviour of ground surfaces. IE(I)-Journal-PR 86: 35–38.
[51] Poli, C. (2001) Design for Manufacturing: A Structured Approach, Woburn, MA: Butterworth-Heinemann.
[52] Laroux, K. (1988) Troubleshooting Manufacturing Processes: Adapted from the Tool and Manufacturing Engineers Handbook: a Reference Book for Manufacturing Engineers, Managers, and Technicians, Dearborn, MI: SME.
[53] Batchelor, A.W., Lam, L.N., Chandrasekaran, M. (1999) Materials Degradation and its Control by Surface Engineering, London, UK: Imperial College Press.
[54] Astakhov, V.P., Davim, P.J., *Tools (geometry and material) and tool wear*, in *Machining: Fundamentals and Recent Advances*, P.J.Davim, Editor. 2008, Springer: London. p. 29–58.
[55] Nehoroshkov, S.V. (2006) Model of heat flows in cutting with inserts having heatsink (in Russian). Research in Russia 5(2): 1254–1256.
[56] Kim, H.J., Matsumaru, K., Takata, A, Ishizaki, K. (2003) Grinding behavior of silicon wafer and sintered Al_2O_3 by constant-force-feeding grinding systems. Advances in Technology of Materials and Materials Processing Journal (ATM) 5(2): 50–53.
[57] Kim, H.J., Matsumaru, K., Takata, A, Ishizaki, K. (2004) Reduction of ceramic machining defects by regulated force feeding grinding system. Advances in Technology of Materials and Materials Processing Journal (ATM) 6(2): 290–297.
[58] Castellani, R., de Ruijter, J.E., Renggli, H., Jansen, J.A. (1999) Response of rat bone marrow cells to differently roughened titanium discs. Clin Oral Impl Res 10: 369–378.
[59] Anselme, K., Linez, P., Bigerelle, M., Le Manger, D., Hardouin, P., Hildebrand, H.F., Lost, A., Leroy, J.M. (2000) The relative influence of the topography and chemistry of TiAl6V4 surfaces on osteoblastic cell behaviour. Biomaterials (21): 1567–1577.
[60] Bowers, K., Keller, J.C., Randolph, B., Wick, D., Michaels, C. (1992) Optimization of surface micromorphology for enhanced osteoblast responses in vitro. Int J Oral Maxillofac Impl 7: 302–310.
[61] Martin, J.Y., Schwartz, Z., Hummert, T.W., Schraub, D.M., Simpson, J., Lankford Jr, J., Dean, D.D., Cochran, D.L., Boyan, B.D. (1995) Effect of titanium surface roughness on proliferation, differentiation, and protein synthesis of human osteoblast-like cells (MG63). J Biomed Mater Res 29: 389–401.
[62] Wennerberg, A., Albrektsson, T., Johansson, C., Andersson, B. (1996) Experimental study of turned and grit-blasted screw-shaped implants with special emphasis on effects of blasting material and surface topography. Biomaterials 17: 15–22.
[63] Groessner-Schreiber, B., Tuan, R.S. (1992) Enhanced extracellular matrix production and mineralization by osteoblasts cultured on titanium surfaces in vitro. J Cell Sci 101: 209–217.
[64] Deligianni, D.D., Katsala, N.D., Koutsoukos, P.G., Missirllis, Y.F. (2001) Effect of surface roughness of hydoxyapatite on human bone marrow cell adhesion, proliferation, differentiation and detachment strength. Biomaterials 22: 87–96.

[65] Cooper, L.F., Masuda, T., Ylilheikkila, P.K., Felton, D.A. (1998) Generalizations regarding the process and phenomenon of osseointegration. Part II. In vitro studies. Int J Oral Maxillofac Implants 13: 163–174.
[66] Wilke, A., Orth, J., Lomb, M., Fuhrmann, R., Kienapfel, H., Griss, P., Franke, R.P. (1998) Biocompatibility analysis of different biomaterials in human bone marrow cell cultures. J Biomed Mater Res 40: 301–306.
[67] Rosa, A.L., Beloti, M.M. (2003) Effect of cpTi surface roughness on human bone marrow cell attachment, proliferation, and differentiation. Braz. Dent. J. 14(1): 16–21.
[68] Astakhov, V.P. (1998) Metal Cutting Mechanics, Boca Raton: CRC Press.
[69] Oberg, E., Jones, F.D., Horton, H.L., Ryffel, H.H. (2008) Machinery's Handbook 28th edn. Toolbox, New York: Industrial Press.

2

Surface Texture Characterization and Evaluation Related to Machining

Georgios P. Petropoulos[1], Constantinos N. Pandazaras[1], J. Paulo Davim[2]

[1] Department of Mechanical and Industrial Engineering, University of Thessaly, Pedion Areos, 38334 Volos, Greece,
E-mail: gpetrop@mie.uth.gr, E-mail: panda@mie.uth.gr

[2] Department of Mechanical Engineering, University of Aveiro, Campus Santiago, 3810-193 Aveiro, Portugal,
E-mail: pdavim@ua.pt

This chapter is aimed at providing current knowledge on the association of surface texture with machining, along with recent advances in surface characterization and evaluation. Various texture parameters, adopted by ISO standards or not, are described and their distinctive power is considered. Arithmetic parameters, statistical and random process functions serve as measures for rendering in-height and in-length surface characteristics and allow multiparameter analysis of the surface, something quite necessary under current high requirements for precision and operation. Theoretical models for roughness parameters and experimental trends with regard to machining conditions are discussed. Isotropy of machined surfaces is also considered and methods for surface typology are finally discussed.

2.1 General Concepts of Surface Topography

2.1.1 Introductory Remarks

The various manufacturing processes applied in industry produce the desired shapes in the components within the prescribed dimensional tolerances and surface quality requirements.

Surface topography and texture is a foremost characteristic among the surface integrity magnitudes and properties imparted by the tools used in the processes, machining mostly, and especially their finishing versions.

And it has to be considered from two standpoints, i.e., process control and tribological function, in the context that to achieve the proper functionally oriented surface the appropriate manufacturing method must be performed along with the inverse problem of controlling the forms of texture that various processes generate related also to the improvement of the latter and of the machine tools, accordingly.

Over the years the characterization and evaluation of engineering surface texture has constituted a challenging metrological problem that has remained open so far, especially when high-precision and/or functional performance requirements exist. This fact is attributed to the usually complicated form of surface textures and the need to obtain a satisfying description globally, as well as at various levels.

Traditionally, surface texture has been used more as an index of the variation in the process due to tool wear, machine tool vibration, damaged machine elements, etc., than as a measure of the performance of the component; a stable process combined with the specification of the arithmetic average, R_a, was considered to be enough in industrial practice.

Emerging technological advances put new limits in manufacturing tolerances and better understanding of tribological phenomena on the other hand, implied the need for functional surface characterization, which in turn caused a proliferation of parameters.

A vast amount of research works towards a concise and proper characterization of surface texture is met in the literature with an inevitable emphasis on the association of profile characteristics with the manufacturing process parameters.

Surface typology, the classification of textures according to their shape followed by an exhaustive investigation on the capability of various manufacturing processes of producing these classes would be the most ambitious research goal.

The problem of achieving the necessary surface quality, in general, embraces the following:

- correlation between surface quality and the desirable function of the surface;
- selection of the manufacturing process or processes, as well as the implementation of optimal process parameters; and
- measurement of suitable representative surface characteristics.

2.1.2 Essential Definitions

A *technological* or *engineering* surface means any surface generated by manufacturing methods, such as cutting and grinding (mostly), forming and non-conventional material-removal processes (electrodischarge machining, waterjet, laser machining, etc.). The engineering surface achieves, after the relevant process, new properties and characteristics compared to the initial one, that constitute what we call *surface integrity*. This term refers to:

1. the geometric characteristics (texture, topography); and
2. physical-chemical, crystallographic characteristics and mechanical properties of the surface, like microhardness, residual stresses, plastically deformed or fractured layers, corrosion resistance, absorption, surface energy and others.

Surface integrity, as defined, is associated with the manufacturing process, as well as the environment for free surface, and the interface and working conditions in tribological systems.

Next, we will focus on the characterization and analysis of surface texture and mainly of *surface roughness*. It is worth giving here some useful definitions:

- *Nominal surface*: The workpiece surface with form and dimensions prescribed in the drawing; no surface irregularities are considered.
- *Real profile*: The surface profile representation as rendered by mechanical or optical measuring instruments. It should be noted that profile measurements are undertaken in the direction of a characteristic orientation of surface asperities, which usually coincides with a direction normal to the axis of the process (normal to cutting speed in cutting operations). A cut surface exhibits minimum unevenness parallel to the axis, whereas maximum asperity heights are encountered in the normal direction.

In this regard, the geometric deviations from the nominal surface fall within the following categories:

1. *Macrogeometric deviations* (errors): They are the first- and second-order deviations called *form errors* and *waviness*, respectively.
2. *Microgeometric deviations*: Third- and higher-order deviations, which correspond to the surface microform (surface roughness).

The different deviations are listed in Table 2.1, together with their principal sources. The above surface features along with possible corresponding causes are limited to cutting processes but are representative, as most of the industrial finishing operations are as such and the majority of them are used in tribological applications.

Table 2.1. Geometric deviations of machined surfaces (DIN 4760)

Order	Deviations	Causes
1st	Form errors (flatness, roundness, straightness, cylindricity, etc.)	Errors of machine tool slides, elastic deformations, erroneous fixation of tool or workpiece, severe tool wear
2nd	Waviness	Eccentric rotation of workpiece or tool, vibrations in the manufacturing system (process-tool–workpiece–machine-tool environment), tool wear, inhomogeneity of processed material
3rd	Grooves	Tool edge form, process kinematics, chip morphology
4th	Cracks	Tool-nose wear, built-up-edge formation, mode of chip formation, galvanic procedures
5th	Crystalline structure	Crystallization mode, irregularities due to chemical reactions, corrosive damage
6th	Crystalline formation	Physical and chemical alterations in the material fine structure, deformations of lattice

It is evident that errors of form and waviness can be restricted in many cases. On the other hand, surface roughness is inevitable, as it is caused by the influence of the cutting tool during the chip-removal procedure. In this way, roughness is the dominant magnitude related to the machinability of the processed material, the tool form, the machining conditions, the tolerance requirements (form and dimensional), tribological phenomena (friction, wear) and, in general, to functioning of technological surfaces. Furthermore, special knowledge and analysis of roughness effectively assists problems in simulations, optimization, adaptive control, etc., mainly in applications of modern manufacturing systems (CNC, FMS, CAD/CAM, CIM).

The requirements of current mechanical systems concerning the roughness of mating surfaces can be summarized as:

- The desirable degree of surface roughness for a given application has to be clearly specified in order to compromise the effective function of the surface and the minimization of production time and cost.
- Knowledge of roughness that can be achieved by the various machining processes is necessary, as well as the effect of the practical range of machining conditions employed.
- Standardization of representative roughness magnitudes is a must for developing instrumentation for relevant characterization and evaluation.

Also, an attempt should be made to set a limit for the minimum degree of roughness, as a higher class of roughness than necessary is not advantageous, exerting a negative effect on the process time and cost, whereas in the opposite case, surfaces imparted with higher unevenness are not acceptable as they show functional discrepancies.

A simple scheme of the interdependence of surface characteristics, the machining process system and the function of the surface is presented in Figure 2.1. Obviously, any approach to the problem of achieving the desirable roughness must consider these outlines.

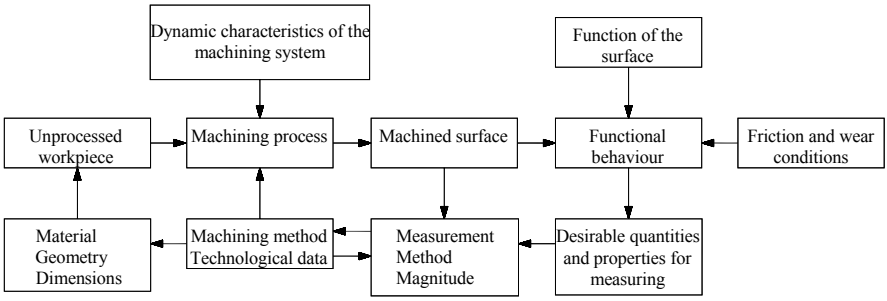

Figure 2.1. Scheme of interconnection among machined surface, process characteristics and surface function

2.2 Surface Texture Parameters

A plethora of surface parameters has been adopted by international standards and proposed in view of numerous research studies [1–4]. As aforementioned, this fact is ascribed to the usually complex form of surface profiles, and on the other hand to the need for the detailed description required in functional applications.

The parameters presented, with brief definitions and comments, in Sections 2.2.1 and 2.2.2 are mostly included in ISO 13565-2: 1997 standard, which is based on the "M" (mean line system).

2.2.1 Arithmetic Parameters

Amplitude Parameters

- R_a (CLA), arithmetic average roughness (center line average): the arithmetic average value of filtered roughness profile determined from deviations about the center line within the evaluation length; the most popular parameter for a machining process and product quality control. This parameter is easy to define, easy to measure even in the least sophisticated profilometers and gives a general description of surface amplitude. Though it lacks physical significance, it is established in almost every national standard for measuring roughness. On the other hand, it is insensitive to small variations in the profile and gives no information on the in-length characteristics, also no distinction is made between peaks and valleys.

  An indicative calculation of R_a is shown in Figure 2.2.

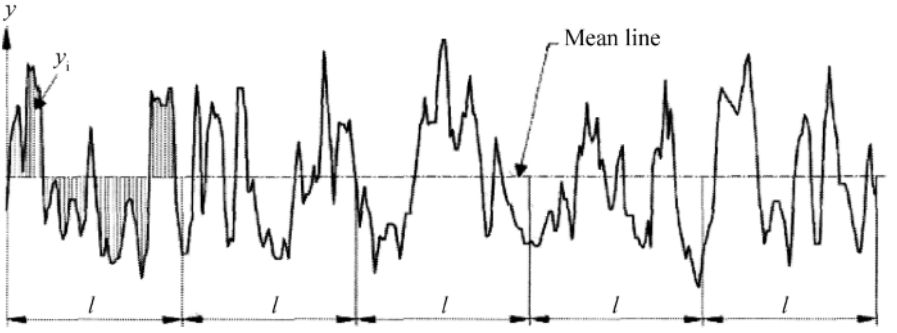

Figure 2.2. Mean line system and definition of R_a

- R_t, maximum peak to valley, the maximum peak to valley height of the filtered profile over the evaluation length; it is very sensitive to large deviations from the mean line and scratches. Very commonly used along with R_a as a general indicator.
- R_z, average peak to valley height; it smoothens large deviations that are not representative of the surface finish compared to R_t.

- R_q, root mean square or RMS roughness: the root mean square average of the roughness profile ordinates; it is more sensitive to peaks and valleys than R_a.
- R_p, the value of the highest single peak above the center line; it is sensitive to material removal from peaks.
- R_{pm}, the mean leveling depth; it gives proper characterization of bearing and sliding surfaces, and substrates to be coated.
- R_v, the deepest valley below the center line; it is an indicator of oil retention or the mechanical behavior of the surface under high stress.

In Figure 2.3 the representation of different characteristics by R_t, R_p and R_v is shown.

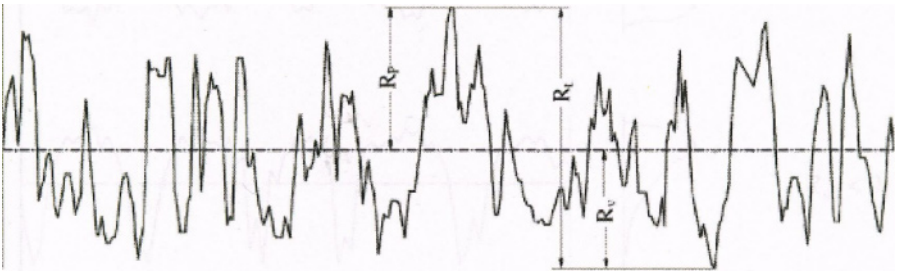

Figure 2.3. Definition of the R_t, R_p and R_v amplitude parameters

Spacing Parameters

- R_{sm}, the mean spacing of the asperities at the level of the central line; it provides approximation of the distance between successive peaks.
- λ_a, the average wavelength in the profile; the principal wavelength of the profile can be related to machining condition (feed, for instance).
- m, peak count: the number of profile peaks per unit length; it is useful in adhesive and coating applications.
- $n(0)$, number of intersections of the profile at the mean line; it gives rough information about the peak form.

Hybrid Parameters

- $R\Delta_a$, the average slope of the profile; it is closely associated with friction and hydrodynamic lubrication.
- $R\Delta_q$, the root mean square slope of the profile; it is more sensitive than $R\Delta_a$ to drastic changes in the profile due to wear.
- r_p, the average radius of asperities; a crucial parameter closely related to contact mechanics, wear and fatigue.
- R_{lo}, the developed length of the profile; it is a measure of the profile openness related directly to the profile slope and is a useful parameter for coating applications.

Surface Waviness

Surface roughness has attracted a lot of attention as an important machinability parameter. Surface waviness is usually considered more as a symptom of malfunctions in the machine tool system or poor machining, than a dependent machining variable.

Regarding its characteristics it is characterized by introduction of equivalent to roughness arithmetic and statistical function parameters in the corresponding standards.

- W_a, mean value of the waviness of the unfiltered profile.
- W_t, maximum value of the waviness of the unfiltered profile.

Both parameters should be considered in the case of severe vibration within the machine tool or from an external source, or eccentricity of the tool or the workpiece.

2.2.2 Statistical and Random Process Functions and Parameters

Surface texture analysis obtained by statistical and random process tools is more sophisticated and of scientific foundation than evaluation by arithmetic parameters.

Considering that a real profile $y(x)$ of a machined surface is one out of a statistical ensemble of possible profiles, it can be represented by a random process that can be sufficiently described by two functions; the height statistical distribution function $f(y)$ and the autocorrelation function $R(\lambda)$ or equivalently by the spectral density function or autospectrum $S(\omega)$, being the Fourier transform of $R(\lambda)$.

The height distribution $f(y)$ assigns a probability to some ordinate of the profile to lie at a given depth in regard to the central line. The most widespread distribution model is typically a Gaussian distribution that matches with reasonable approximation a significant number of engineering surfaces. $f(y)$ gives evidence and sometimes characterization of the profile shape and is directly associated with surface loading, wear, corrosion, etc. Interesting parameters are the central moments of first up to fourth order. The first-order central moment is the average height R_a and the second-order central moment stands for variance σ^2 (or $R_q = \sigma^2$). The third- and fourth-order central moments are skewness and kurtosis, accordingly; both provide more information on the real profile form.

Skewness ζ ($R_{sk} = \zeta$) evaluates the degree of asymmetry in cases of asymmetric distribution and is characterized as positive or negative, relevantly. Surfaces "empty" of material exhibit positive skewness, whereas negative skewness is presented by "full" surfaces. It is a significant parameter for tribological applications, such as bearing surface functionality, wear control and others. A Gaussian distribution presents $\zeta = 0$.

Kurtosis ξ ($R_{ku} = \xi$) describes the distribution sharpness and takes the value 3 for the normal distribution. For $\xi > 3$ the surface is dominated by sharp peaks (spiky), whereas if $\xi < 3$ the peaks are bumpy. In this regard, information is provided on the real area of contact and wear resistance, it is also possible to detect the periodicity of the profile ($\xi < 3$).

Another aspect of the profile height statistical distribution is given alternatively by the *cumulative probability function* $P(y>h)$, which reflects the cumulative probability of a profile height to be higher than a given level h, below the higher profile reference line. This function has a direct physical meaning, that of representing the real material cross section at each level h and it is also called the *bearing area curve* or *Abbott–Firestone curve*. Evidently, there is plenty of information provided by this curve about real contact and bearing capacity of surface.

The physical significance of R_{sk} and R_{ku} with regard to surface roughness is illustrated in Figures 2.4 and 2.5, respectively.

Every machining process, its mode and the conditions employed, imparts specific topographic features to technological surfaces. Thus, the cutting process will directly affect the bearing curve features. However, the literature on the connection of bearing ratio parameters to cutting conditions or to their interrelationship with other surface roughness parameters is quite rare.

As an indicator of the Abbott curve of the profile, the R_{tp} [%] bearing ratio parameter at 10% level below the upper reference line is usually used and is related to probable run-in behavior and wear resistance of surfaces.

Towards a surface roughness classification, *β (beta)* and *Fisher–Pearson* statistical systems have been proposed. Both possess the advantage of higher distinction of profile components, periodic and random, that are rendered to the machining method performed.

The determination of statistical distributions for the *inclination* and the *curvature* (radius) of profile peaks contributes useful information on the shape of the

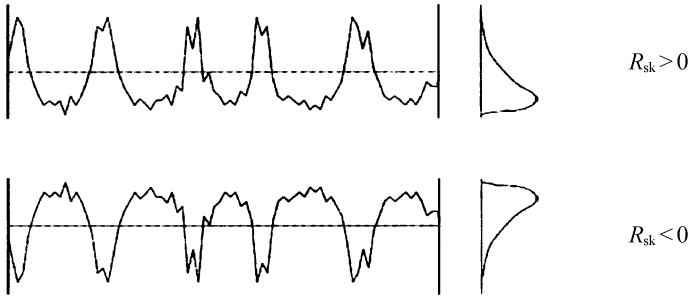

Figure 2.4. Oppositely signed values for skewness correspond to different surfaces

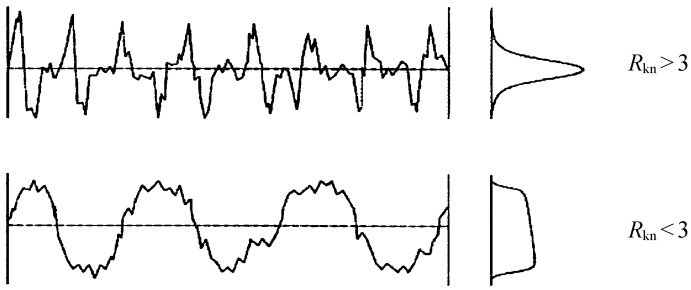

Figure 2.5. Different values of kurtosis reveal different surface features

asperities and further, about the machining process (for instance, the form of the tool nose during cutting), as well as the tribological behavior of the surface (elasto-hydrodynamic lubrication, thermal contacts, etc.).

The *autocorrelation function Ryy(λ)* or $R(\lambda)$ describes rigorously some surface features and its form reveals periodic and random characteristics of the profile. It is possible to analyze $R(\lambda)$ into a declining exponential term that corresponds to the random component and a trigonometric term that is relevant to a periodic component. The initial slope and the dropping rate are also indicators of randomness.

Different forms of autocorrelation along with the corresponding height distribution for different machining processes are shown in Figure 2.6.

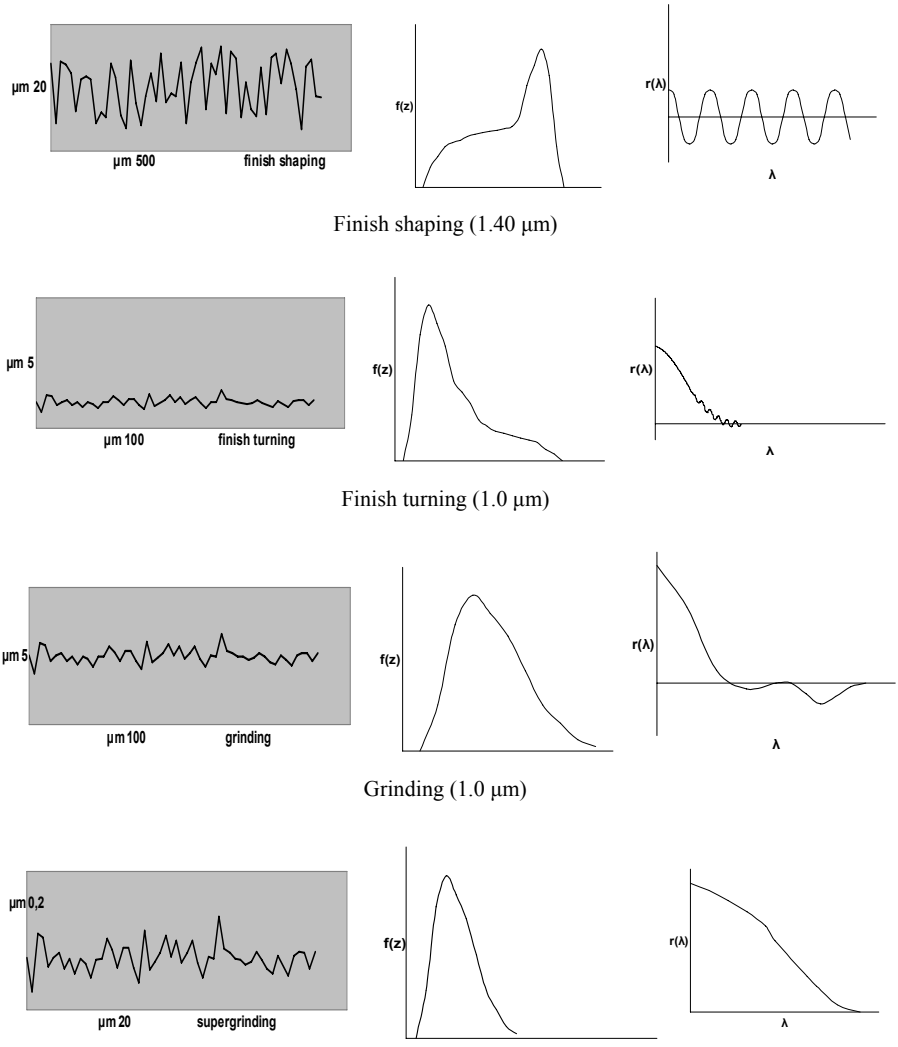

Figure 2.6. Shapes of height distribution and autocorrelation functions for given machining processes

Useful parameters of the autocorrelation function are:

- The *correlation length* λ^* is defined as the necessary length for reducing $R(\lambda)$ to 1/10 of its initial value $R(0)$, which is also its maximal value. The physical interpretation of λ^* is that it expresses the minimal distance between two profile points not interrelated; their generation is due to different causes during the machining operation or in the process of wear.
- The *mean correlation wavelength* λ_w indicates the mean wavelength of the profile asperities.
- In the case of three-dimensional illustration of the surface, the cross correlation function R_{xy} (λ) characterizes the orientation of the asperities in regard to the third dimension (z).

The spectral density function $Syy(\omega)$ constitutes an equivalent to the autocorrelation function, interconnected through a Fourier transform and expresses the spacing profile characteristics in the frequency domain. It offers direct evaluation of the periodic components of the profile under the form of discrete peaks.

The parameters for surface roughness analysis according to ISO 13565-2: 1997 standard are given in Table 2.2.

Table 2.2. The "conventional" ISO I13565-2: 1997 parameters

Parameter	Description
R_a	Profile average height
R_t	Maximum profile height
R_q	Standard deviation of the profile height distribution
R_p	Maximum profile peak height
R_v	Maximum profile valley depth
R_{DelA}	Average slope of the profile
R_{sk}	Skewness of the profile height distribution
R_{ku}	Kurtosis of the profile height distribution
R_{sm}	Mean spacing of the profile
R_{DelQ}	Root mean square slope of the profile
R_z	Average maximum height of the profile
R_{tp}	Bearing length ratio of the profile

2.2.3 Other Morphological Parameters

The surface motif combination is a method of analyzing surface texture alternatively to the "M" system and was introduced in the French automotive industry [5]. Now it is issued as an international standard, ISO 12085: 1996. It provides

a graphical evaluation of a surface profile without filtering waviness from roughness. A motif consists of the portion of a profile between two peaks and the final combination of these motifs eliminates "insignificant" peaks and retains "significant" ones. This method determines the upper points of the profile, which have functional importance by an envelope-based algorithm.

Another function-oriented system of surface analysis was developed in Germany (DIN 4776) and is now adopted in ISO 13565-2: 1996 to characterize stratified textures like the honed surfaces in internal combustion engine cylinders [6]. It is met many times in the technical literature as the "R_k" parameter group (R_k is the first out of five parameters used). The concept is to describe the shape of the relevant bearing (material ratio or Abbott) curves and to provide information on characteristics at different portions of the surface profiles.

In Tables 2.3 and 2.4 the parameters proposed by the two aforementioned standards are listed.

Table 2.3. The motif (R & W) parameters

Parameter	**Description**
R	Average depth of roughness motifs
R_x	Maximum depth of roughness motifs
A_r	Average spacing of roughness motifs
W	Average depth of waviness motifs
W_x	Maximum depth of waviness motifs
W_{te}	Maximum depth of the waviness profile
A_w	Average spacing of waviness motifs
K_r	Average slope of roughness motifs
K_w	Average slope of waviness motifs
P_t	Maximum depth of the raw profile

Table 2.4. The "R_k" family of parameters

Parameter	**Description**
R_k	Depth of the roughness core profile
R_{pk}	Top portion of the surface to be worn away
R_{vk}	Lowest part of the surface retaining the lubricant
MR1	Upper limit of the core roughness
MR2	Lowest limit of the core roughness

The representation of Abbott curves by the "R_k" parameters is given in Figure 2.7.

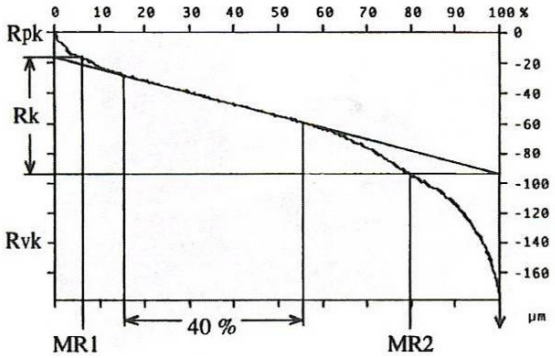

Figure 2.7. Definition of "R_k" parameters

2.2.4 Fractal Geometry Analysis

Fractal geometry is aimed at characterizing texture independently from the measuring instrument and the evaluation length and such an analysis has been introduced to render the microroughness of machined surfaces [7].

The main fractal parameters are fractal dimension D and topothesy L. To give a physical definition of these parameters, the fractal dimension D is an intrinsic property of the surface, which is scale independent and reflects the "complexity" of the profile structure. The topothesy L is a characteristic length representing the horizontal separation of profile heights corresponding to an average slope of one radian; it takes very small values.

Furthermore, the description provided by a fractal at the microroughness level may allow the control of the material properties and the type of the occurring chip formation, desirable or unwanted accordingly. But fractals, as expected, cannot provide a full-scale representation of a typical machined surface dominated by feed marks, it ignores the geometry of the cutting edge, while it is sensitive to cracks and microdefects.

2.2.5 ISO Standards on Surface Finish

- ISO 1302 – 2001 Indication of Surface Texture
- ISO 3274 – 1996 Nominal Characteristics of Contact (Stylus) Instruments
- ISO 4287 – 1997 Terms, Definition and Surface Texture Parameters
- ISO 4288 – 1996 Rules and Procedures for Assessment of Surface Texture
- ISO 5436-1 – 2000 Calibration, Measurement Standards
- ISO 5436-2 – 2000 Calibration, Soft Gages

- ISO 8785 – 1999 Surface Imperfections – Terms, Definitions and Parameters
- ISO 11562 – 1996 Metrological Characteristics of Phase Correct Filters
- ISO 12179 – 2000 Calibration of Contact (Stylus) Instruments
- ISO 12085 – 1996 Surface Roughness and Waviness – Motif Method
- ISO 13565-2 – 1996; Geometrical Product Specifications (GPS) − Surface texture: Profile method; Surfaces having stratified functional properties − Part 2: Height Characterization using the linear material ratio curve.

2.3 Shape Characterization of Surface Roughness Profiles

High functional requirements nowadays imply the control of profile shapes every manufacturing process imparts on the surface. Characteristics like periodicity or randomness, "emptiness" or "fullness" of the profile play an important role.

The following parameters, parameter ratios and functions are proposed and/or established to be sensitive in profile form [8]. They will be briefly discussed in view of their distinctive power and tribological significance.

Arithmetic Amplitude Parameters

These parameters cannot be considered alone, as they do not give information about the shape of the profile. Some combined ratios have been proposed though, as follows:

a) R_a/R_q: for the extreme theoretical cases of a sinusoidal and a random profile conforming to the Gaussian distribution this ratio takes the values 0.9003 and 0.7979, respectively; this ratio is simply indicative.
b) R_p/R_t: provides only general information on the "emptiness" or "fullness" of the surface, and is related to skewness of the profile height distribution
c) K: is called the solidity surface ratio, which is defined as $K = (R_t - R_p)/R_t$ and is associated with skewness.

Spacing parameters

a) R_{sm}: a characteristic magnitude in periodic profiles (e.g., turning, milling), where it corresponds to the feed rate value employed.
b) λ_a: gives relevant information with S_m. It can be used as a general measure of the mean distance of asperities on random profiles.
c) $n(0)$: detects existing periodicity of the profile without providing further information.
d) m: is correlated with $n(0)$ and directly to the machining process.

All three aforementioned parameters describe the number of microcontacts from the tribological standpoint.

Hybrid Parameters

a) $R_{\Delta a}$: is possible to characterize the machining process and is affected by the machining conditions, but does not determine the profile shape sufficiently.
b) r: is affected to a similar degree by the machining process, but does not describe particular profile features.
c) R_{lr}: the developed profile length to evaluation length ratio is connected to the profile openness and controls the corrosion resistance; by definition, it is proportional to $R_{\Delta a}$.

All these parameters, however, may describe indirectly the shape of the profile peaks.

Statistical Parameters

a) Profile height distribution
The form of this statistical function is very important as it is sensitive to the geometric features of the surface and to their variation. Multiparameter statistical systems like log-normal, beta, and Fisher–Pearson are used to model a variety of profile shapes and could contribute to any acceptable typology of machined surfaces. Apart from the shape of the distribution, the corresponding statistical moments are evaluated:

The standard deviation σ is equal to the R_q parameter. The third- and fourth-order moments – skewness and kurtosis – express geometric and physical features of the surface, respectively. The skewness controls the amount of existing material in the surface against voids. Kurtosis defines the sharpness of the peaks of the asperities. Low kurtosis values correspond to broad tips, whereas the opposite characterizes sharp "hills".

b) Bearing area or Abbott curve
This is equivalent to the cumulative probability of the profile heights and is directly related to the surface tribological behavior, and particularly, with the real contact area, asperities strength, and wear. The bearing area curve has been widely used in recent studies, and with the introduction of a relatively new standard, it can easily distinguish between random and periodic profiles and give functional descriptions by the "R_k" parameters (ISO 13565-2: 1997).

c) Autocorrelation function and autospectrum
- The profile autocorrelation function permits the qualitative discrimination of periodic and random components. The first attempt made towards surface typology.
- by Peklenik [19] defined five different autocorrelation forms, with the extreme cases corresponding to sinusoidal band white noise, respectively.
- The autocorrelation length β^* denotes the minimal distance between profile characteristics of different origin.
- The spectral density function, or autospectrum, enables the quantitative assessment of the various profile components, periodic and random, and is the Fourier transform of the autocorrelation function. Strongly periodic profiles, for instance, are characterized by the fundamental component (at the feed value), followed by a series of higher harmonics.

2.3.1 Functional Significance of Parameters

Based on the discussion in Section 2.3, surface parameters that can be correlated with various properties of a functional surface are presented in Table 2.5.

Table 2.5. Physical/functional significance of several surface texture parameters

Functional properties	R_a, R_q	R_p, R_{pm}	R_t, R_z	R_{sk}	R_{ku}	R_{sm}	R_{DelA}	W_a
Contact/Contact stiffness	*		**	*	*	**	*	*
Fatigue strength	*	*	**		*		**	
Thermal conductivity	*	**				**	*	*
Electrical conductivity	*					*	*	*
Reflexivity			**				**	
Friction and Wear	*		**	**	**	*	**	*
Lubrication	*	*	**	**	*		*	**
Mechanical sealing	*		**	**			**	**
Fatigue corrosion	*	*		*		*	*	
Assembly tolerances	*		**				*	**

Note: the two asterisks indicate a pronounced influence

2.4 Surface Texture Anisotropy

The wide variety of surface textures obtained in engineering manufacture can be further divided into isotropic or anisotropic. A texture is characterized as isotropic if its topographic properties are statistically independent of the measuring direction over the surface.

Most of the machined surfaces are topographically anisotropic; they possess a “lay” [9]. Machining processes with tools of defined geometry, namely turning, shaping and milling usually generate severe anisotropic patterns, whilst others like EDM create isotropic texture. The directional properties affect the tribological function of the surface (frictional behavior, wear, lubricant retention, etc.), also the state of anisotropy can change during function. Standardized lays are shown in Figure 2.8.

Considering the existence of isotropy or anisotropy on a surface, and their magnitudes, several criteria have been manifested in the literature. Most of them are based on an “anisotropy index”, a ratio combining topographic parameters, usually along two directions on the surface. Usually, values of these indices near unity characterize a surface as isotropic, whereas lower or higher values correspond to anisotropy.

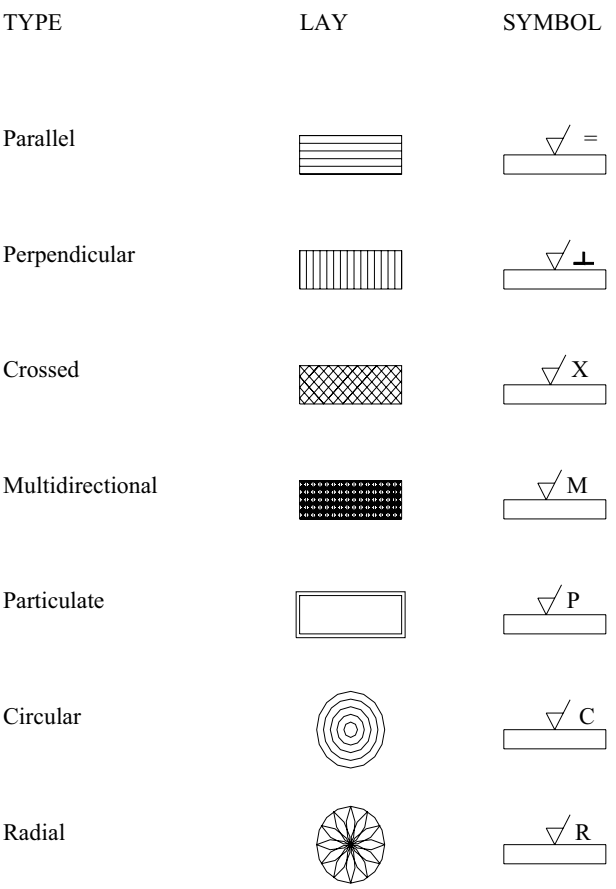

Figure 2.8. Different kinds of lay and associated symbols [9]

Some of the existing methods for evaluating surface texture anisotropy in view of the literature are:

a) The ratio γ of the autocorrelation lengths of two representative profiles along the principal axes of the surface, called the anisotropy index $\gamma = \frac{\lambda_{0.5yy}}{\lambda_{0.5xx}}$
b) The ratio of the unfiltered or raw profile of the minimum and maximum RMS slope values over the profile $\gamma = \frac{\Delta_{qyy}}{\Delta_{qxx}}$.
c) The long crestedness $\Lambda = \frac{2\sqrt{m_{20}m_{02} - m_{11}^{\ 2}}}{m_{20} + m_{02}}$ considers seven independent combinations of moments of the surface power spectral density function.
d) Fractal dimension and topothesy appear sensitive to the existence of anisotropy .
e) A parameter S_{tr} defined as the ratio between the axes of an ellipse fitted to a "rose plot" of Hurst coefficients can characterize anisotropy.

New suggestions for full-scale and morphological evaluation of surface anisotropy are, as follows:

The waviness component of the surface texture has to be considered in critical and high-precision applications, as well as in highly anisotropic textures, where the waviness shows the same directional variations with roughness (not necessarily with the same trend) and an integral texture anisotropy index could be proposed.

Abbott curves would offer a measure of anisotropy via corresponding parameters, standardized (ISO 13565-2: 1996) or not.

2.5 Association of Roughness Parameters with Machining Conditions

2.5.1 Theoretical Formulae

Theoretical or kinematic roughness: it is the lowest roughness possible that can be achieved for any machining process performed and given machining factors.

Theoretical roughness values can be determined analytically depending on the process kinematics and tool geometry [10].

Some well-known formulae for turning and milling are given below; see Figure 2.9.

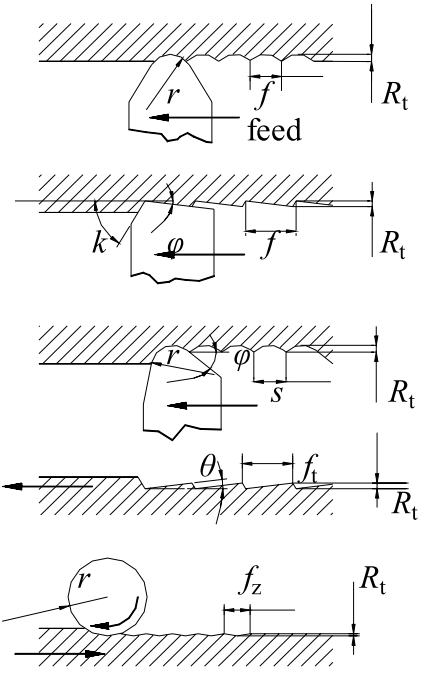

Figure 2.9. Theoretical forms of roughness in turning and milling

Turning

The maximum roughness value R_t is expressed as

a) $$R_t = \frac{1}{8}\frac{f^2}{r} \text{ [mm]}, \tag{2.1}$$

for a rounded tool tip with radius r in mm and feed f in mm/rev

b) $$R_t = \frac{f}{\cot\kappa + \cot\varphi} \text{ [mm]}, \tag{2.2}$$

for a perfectly sharp tool; κ and φ are edge angles with regard to feed

c) $$R_t \simeq f \cdot \tan\varphi + \frac{r}{2}\tan^2\varphi - \sqrt{2 \cdot f \cdot r \cdot \tan^3\varphi} \text{ [mm]}, \tag{2.3}$$

where $f \geq 2 \cdot r \cdot \tan\varphi$.

The average roughness height R_a for the (a) and (b) cases is given accordingly by

$$R_a = 0.0321 \cdot \frac{f^2}{r} \text{ [mm]} \tag{2.4}$$

$$R_a = \frac{f \cdot \tan\varphi}{4 \cdot (1 + \tan\varphi)} \text{ [mm]}. \tag{2.5}$$

Face milling

The maximum roughness height is approximated by

$$R_t \simeq f_z \tan\vartheta \text{ [mm]}, \tag{2.6}$$

where f_z is feed per tooth [mm/tooth] and θ is the tooth cut-off angle.

Peripheral (up) milling

The R_t and R_a parameters are calculated by

$$R_t \simeq \frac{1}{8}\frac{f_z^2}{r} \text{ [mm]} \tag{2.7}$$

$$R_a = 0.0321 \cdot \frac{f_z^2}{r} \text{ [mm]}, \tag{2.8}$$

where r is the cutter radius in mm.

2.5.2 Actual Surface Roughness

As established by experimental tests, the actual roughness values obtained are usually much higher than the theoretical ones. A decisive factor for the generation of the *actual* or *natural* roughness in cutting operations is the chip-formation mode (built-up-edge, discontinuous chip, thermal variations, shear zone expansion to workpiece subsurface, etc.) [11, 12]. Furthermore, other causes may be: chatter in the machine tool system, processed material defects, cutting-tool wear, irregularities in the feed mechanism, eccentric motion of rotating parts and others.

It is evident that actual roughness constitutes a complex problem in machining and it depends on the machining method, as well as the machining factors employed each time. The following factors have significant impact in cutting processes:

- cutting conditions (feed, cutting speed, depth of cut);
- process kinematics;
- cutting tool form and material;
- mechanical properties of the processed material;
- vibrations in the machine-tool system;
- precision-rigidity- working and service condition of the machine tool.

2.5.3 Experimental Trends of Roughness Against Machining Conditions

There is a plenty of data, in articles and project reports, in the literature on actual roughness for every machining process and a wide range of machining parameters.

In cases where it was possible, empirical predictive empirical models for the impact of various machining factors on roughness parameters were developed, exhibiting a varied degree of correlation. Also, data-mining techniques and artificial intelligence methods (genetic algorithms, artificial neural networks) were employed for this purpose [13].

A survey of such models is out of the scope of this section and in the following established experimental trends will be presented for typical conventional and non-conventional machining processes [14, 15]. The relevant diagrams describe qualitatively the association of R_a with machining conditions.

Turning

Feed exerts the major influence on roughness exhibiting an increasing trend; it is evident that the lowest feed values give an inferior finish because of the very small chip thickness leading to poor surface formation. At very low and low cutting speeds roughness is deteriorated due to discontinuous chip and built-up-edge formation, respectively. The depth of cut implies a slight increase in roughness and is not shown; this is true for stable (chatter-free) cutting.

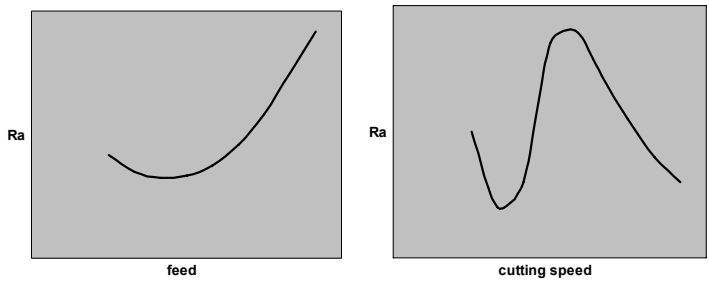

(a) (b)

Figure 2.10. Surface roughness R_a against cutting conditions in turning: (a) feed rate, and (b) cutting speed

Electrodischarge Machining (EDM)

Roughness in EDM increases, when both controlling parameters increase. As pulse current increases, discharges strike the surface more intensely, and the more pronounced erosion affect roughness. If pulse-on time increases, the amount of heat energy transferred increases and surface roughness is affected negatively by more material melting.

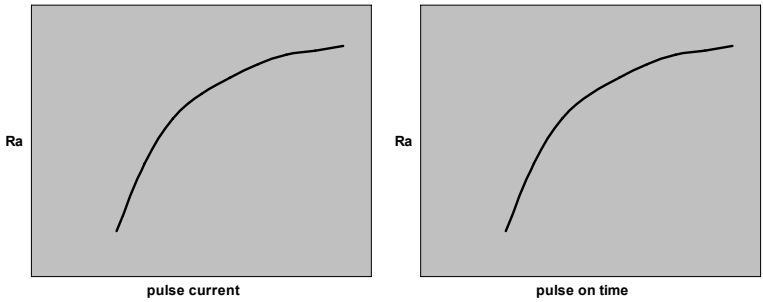

(a) (b)

Figure 2.11. Surface roughness R_a against cutting conditions in EDM: (a) pulse current, and (b) pulse on time

Abrasive Waterjet Machining (AWM)

An increase in stand-off distance implies an increase in surface roughness; this can be attributed to waterjet divergence with regard to stand-off distance, resulting in deteriorated roughness. Increased water pressure up to 300 MPa leads to better surface finish. Traverse speed causes a slight increase in roughness, as the cuts become wider and fewer abrasive particles act on the surface.

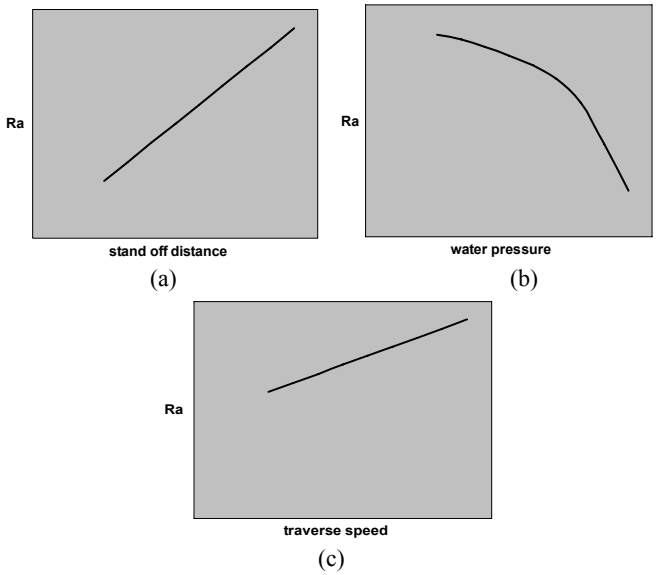

Figure 2.12. Surface roughness R_a against cutting conditions in AWM: (a) stand-off distance, (b) water pressure, and (c) traverse speed

2.5.3.1 Case Study (Influence of Cutting Conditions on the Surface Roughness Obtained by Turning) [16]

Surface finish is an important outcome in manufacturing engineering, as stressed many times in the foregoing. It is a characteristic that affects directly the performance of mechanical components and the production costs. Due to these facts, research developments have been carried out with the objective of optimizing the cutting conditions, to obtain a determined surface finish.

This study presents the influence of cutting conditions (cutting speed, feed and depth of cut – DOC) on the surface finish obtained by turning. It should be borne in mind that turning is regarded as a reference cutting process due to its relatively simple geometry and kinematics, and machinability data obtained in turning is of crucial importance.

In order to achieve the goal of this study, mainly the establishment of a correlation between cutting conditions and surface roughness, turning tests were effected with different cutting conditions, aiming at simulating them for finishing.

The material used in the tests of controlled turning was the free machining steel, 12L 13 (AISI). Cemented carbide inserts of TPUN 160308 P10 (ISO) type with a nose radius of 0.8 mm were used.

The measurements were undertaken over the turned surfaces using a profilometer and the surface optical examination was made by a scanning electron microscope (SEM).

Feed

In cylindrical turning, as in other cutting operations, the tool leaves a spiral profile (feed marks) on the machined surface. Figure 2.13 shows the influence of feed on surface roughness. If different feeds are compared possessing the same nose radius, the larger feed increases the separation between feed marks, leading to an increase in the value of the geometric theoretical surface roughness. The surface roughness increases with the feed according to the geometric theoretical model (Equation 2.1).

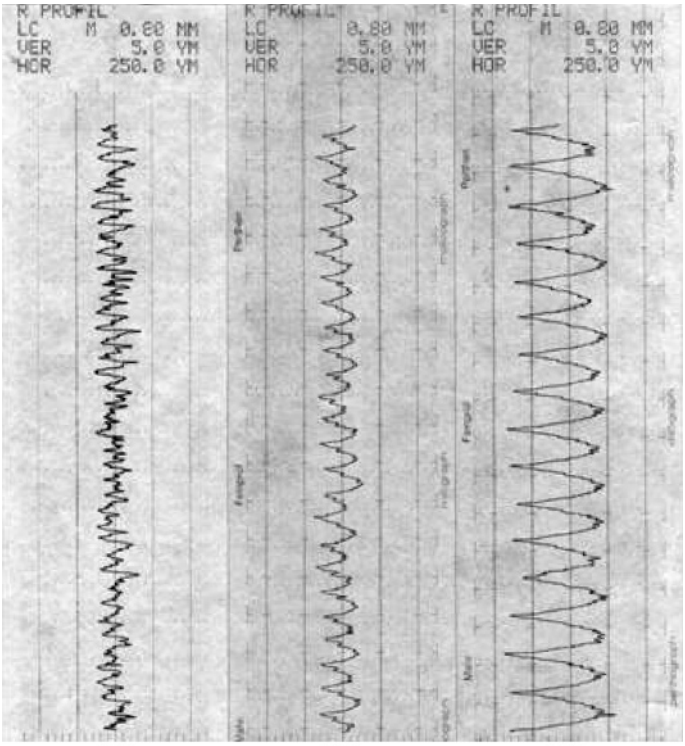

Figure 2.13. Surface roughness profiles for $V_c = 283$ m/min and DOC = 0.5 mm: (a) f = 0.10 mm/rev, (b) f = 0.16 mm/rev, and (c) f = 0.25 mm/rev

Cutting Speed

Figure 2.14 shows the influence of cutting speed on the surface roughness profile. The surface roughness increases with decrease of cutting speed. This fact can be attributed to a technological contribution inherent to the cutting process, which produces highly imperfect cutting surfaces, as may be confirmed in observations in SEM, changing the surface finish obtained by the geometrical model. It is still important to note that the geometric model does not consider the important influence of cutting speed on surface finish.

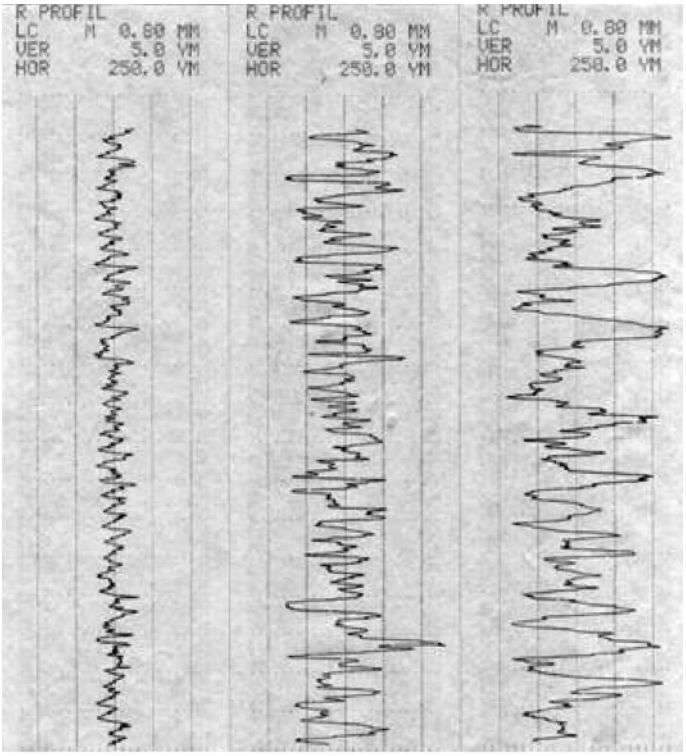

Figure 2.14. Surface roughness profiles for $f = 0.10$ mm/rev and DOC = 0.5 mm: (a) $V_c =$ 283 m/min; (b) $V_c = 141$ mm/min; and (c) $V_c = 71$ m/min

Depth of Cut

Figure 2.15 shows the effect of DOC on the surface roughness profile. In the range of finishing the increase of DOC has no significant influence on the surface roughness.

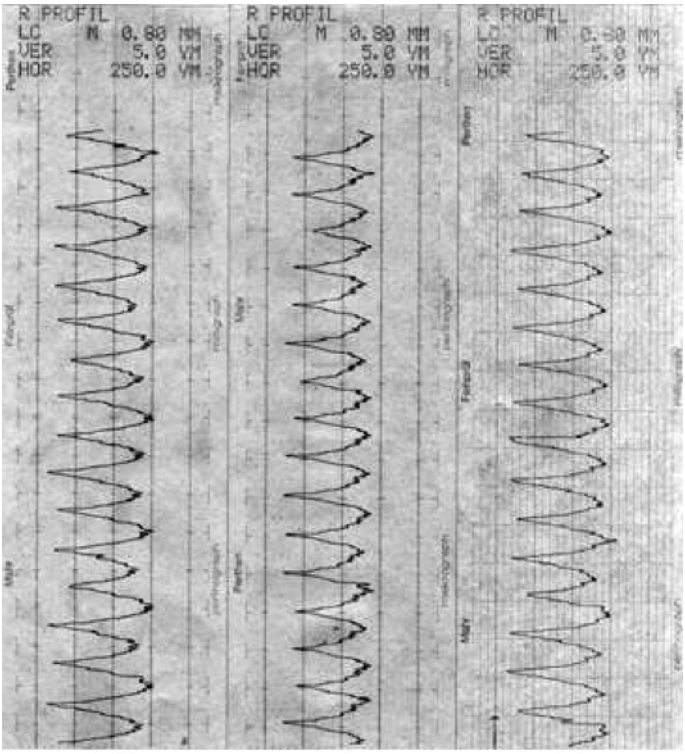

Figure 2.15. Surface roughness profiles for $V_c = 283$ m/min and DOC = 0.5 mm: (a) f = 0.10 mm/rev; (b) f=0.16 mm/rev; and (c) f=0.25 mm/rev

SEM Examination

Figures 2.16 and 2.17 present surfaces produced on steel by cutting with regard to feed, as observed with a SEM, for cutting speeds of 283 and 71 m/min, respectively. When cutting steel at low cutting speeds (Figure 2.17) an irregular type of roughness is frequently observed due to subsurface fracture and plastic deformation. Above a certain value of cutting speed these sources of roughness disappear. Factors influencing surface roughness at low cutting speeds are surface plastic deformation, tearing, cracking, etc., mainly due to built-up-edge formation.

The feed exerts the main influence on the surface finish obtained as rendered by the geometric theoretical model. The cutting speed is the cutting condition that has a great influence on the roughness right after the feed because of the technological contribution inherent to the cutting process; it becomes dominant in the presence of a built-up edge. Finally, the depth of cut has no significant influence on roughness in finishing operations.

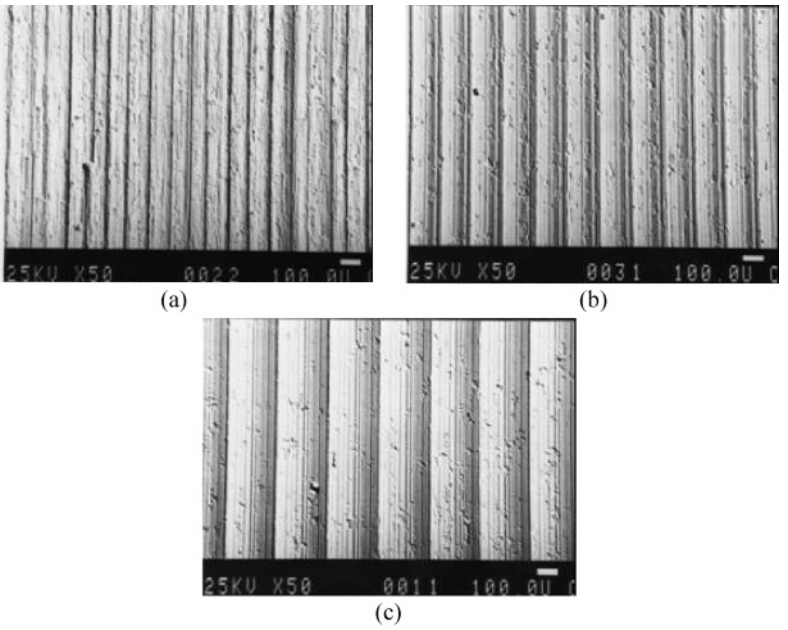

Figure 2.16. Surfaces produced on steel by turning, as observed with a SEM, $V_c = 283$ m/min and DOC = 0.50 mm: (a) $f = 0.10$ mm/rev; (b) $f = 0.16$ mm/rev; and (c) $f = 0.25$ mm/rev

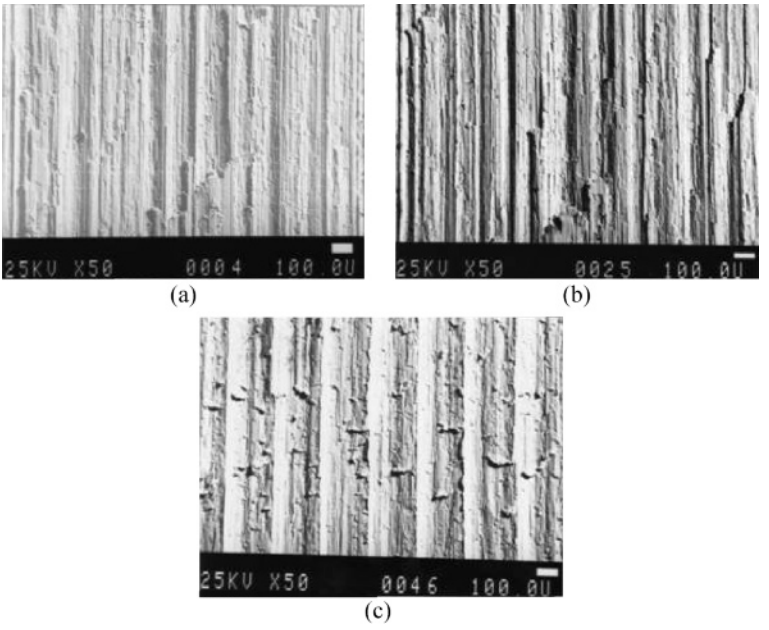

Figure 2.17. Surfaces produced on steel by turning, as observed with a SEM, $V_c = 71$ m/min and DOC = 0.50 mm: (a) $f = 0.10$ mm/rev; (b) $f = 0.16$ mm/rev; and (c) $f = 0.25$ mm/rev

2.5.3.2 Subsets of Roughness Parameters

Contemporary research studies are oriented towards reduction of roughness parameters in appropriate subsets, where every parameter introduced would correspond to different surface characteristics [17]. Such a goal will facilitate the exchange of scientific information on surface roughness prediction and quality control in research and industry.

Concerning turning operations, as turning is a reference cutting process, amplitude roughness parameters are associated with feed rate and cutting speed but other statistical or hybrid parameters do not correlate with cutting conditions over their whole practical range. Parameters that are uncorrelated to cutting conditions, as well as with other parameters, can make up a desirable subset because each single parameter is considered to quantify different characteristics of the surface.

Regarding the whole spectrum of the cutting conditions employed, a minimum concise set of parameters for basic research should be R_a, R_{sk}, R_{ku}, R_{DelQ} and R_{lo} [18].

2.5.4 Range of Roughness – Cutting Processes

Surface roughness obtained by different cutting processes varies due to different process kinematics, different chip-formation modes, different tool geometry, different tool-wear modes, cutting fluid. In this way, amplitude parameters like R_a take significantly higher or lower values, when cutting the same material by different methods. In Table 2.6 ranges of achieved R_a values according to the usual cutting methods are presented.

Table 2.6. R_a values obtained by different machining processes

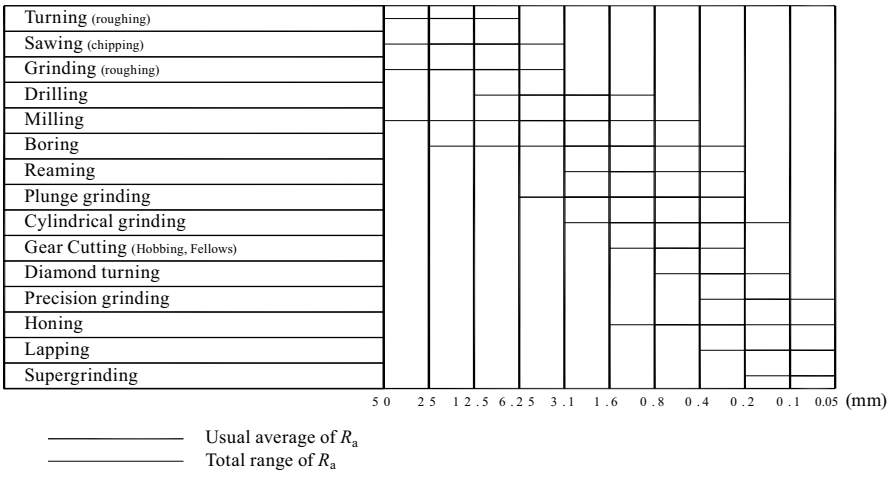

2.6 Correlation of Surface Roughness and Dimensional Tolerances

The existence of surface roughness produces an amount of uncertainty in the measurement of workpiece dimensions. In this regard, the variation of dimension induced due to roughness, should conform to the corresponding tolerance field [19].

Predictive mathematical models for relating roughness to tolerances have not been developed in view of the literature and the following data is obtained from standards to serve as a guide in practice.

Recommended relationships between the maximum roughness height R_t and the tolerance field of a nominal dimension T are, as follows:

- $R_t = 0.25\ T$ for rough surfaces;
- $R_t = 0.125\ T$ for finished surfaces.

In the Italian surface roughness standard UNI 3963 dimensional tolerances are related to roughness, as presented in Table 2.7.

ISO 286 implements 20 grades of accuracy to satisfy the requirements of different industries. (IT01, IT0, IT1, IT2, IT3, IT4, IT5, IT6). Production of gauges and instruments;. (IT5, IT6, IT7, IT8, I9, IT10, IT11, IT12). Precision and general Industry; (IT11, IT14, IT15, IT16) Semi-finished products; (IT16, IT17, IT18) Structural engineering.

Table 2.7. Maximum allowable R_a values in regard to nominal dimensions and their assigned tolerances according to ISO 286

Tolerance according to ISO	**Dimensional range**									
	≤3		**>3≤18**		**>8≤80**		**>80 ≤250**		**>250**	
	T (μm)	R_a (μm)	T (μm)	R_a (μm)	T (μm)	R_a (μm)	T (μm)	R_a (μm)	T (μm)	R_a (μm)
IT6	6	0.2	8–11	0.3	13–19	0.5	22–29	0.8	32–40	1.2
IT7	10	0.3	12–18	0.5	21–30	0.8	35–46	1.2	52–63	2
IT8	14	0.5	18–27	0.8	33–46	1.2	54–72	2	81–97	3
IT9	25	0.8	30–43	1.2	52–74	2	87–115	3	130–155	5
IT10	40	1.2	48–70	2	84–120	3	140–185	5	210–250	8
IT11	60	2	75–110	3	130–190	5	220–290	8	320–400	12
IT12	100	3	120–180	5	210–300	8	350–460	12	520–630	20
IT13	140	5	180–270	8	330–460	12	540–720	20	810–970	–
IT14	250	8	300–430	12	520–740	20	870–1150	-	1300–1550	–

2.7 Surface Typology

The main goal of the numerous roughness parameters should be a proper texture shape classification with the aid of statistical or random process analysis, which has been called the typology of surfaces. This had gained much attention in the late 1960s and the 1970s especially in the research works of Peklenik [20] and Whitehouse [21], proposing the autocorrelation function and the beta statistical model, respectively, as means for the desired typology and a big relevant project carried out by the CIRP [22], where a great number of machining operations and roughness parameters, was evaluated.

Unfortunately, no agreement has been reached and this subject remains a long standing problem unsolved if not too ambitious up to now. Probably, this happens due to the very high demands nowadays for the components functionality, which led to the proliferation of the parameters proposed and standardized in order to describe almost every aspect of texture.

However, contemporary evolutions like 3D profilometry and different mathematical approaches like fractal and Markov analysis give the opportunity of introducing new functionally oriented parameters that could be more successful for this task; but it is too early to appreciate their effectiveness.

In conjunction with these developments, an exhaustive investigation must be carried out into the particular surface texture characteristics every individual machining process creates, taking into account apart from the workpiece material, the different kinematic modes it possesses and covering a wide range of cutting factors employed in practice.

2.7.1 Typology Charts

An effort on expanding these approaches was made with more data, systematically obtained in view of correlating turned profiles of different shapes with the cutting conditions applied [8].

The corresponding results are interpreted in the form of charts compared with the relevant "classical" charts. In Figure 2.18 the kurtosis and skewness of the measured surfaces are shown. A cluster of points appears, as kurtosis and skewness are not interrelated but can fix the boundaries of surface textures in view of the shape for a wide range of cutting conditions employed. The area of high concentration of values located at the lower-right side of the diagram corresponds to regular chip formation.

A chart comprising the parameters of the beta statistical function is illustrated in Figure 2.19. The values are less scattered now and compared to the Whitehouse beta function typology (Figure 2.19(b)) the range is wider due to the fact explained before.

An approach through the Fisher–Pearson parameters is proposed and the corresponding chart is shown in Figure 2.20. It has a resemblance to the beta function, as expected, but it may distinguish more explicitly between different texture shapes [13]; so it could be considered as a satisfactory method towards the desired process identification.

The presented data is representative of a wide range of turned metal surfaces encountered in practice but is certainly not exhaustive. A chance of modifying the charts again could be given if worn tools are used and considered in different stages of wear and special turning versions are performed.

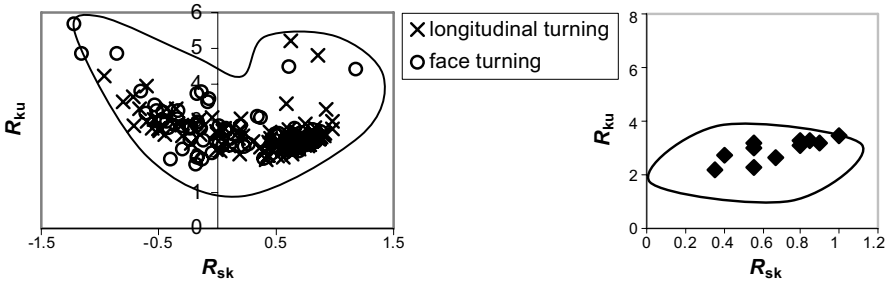

Figure 2.18. Kurtosis against skewness chart (a) and the relevant chart (b) [20]

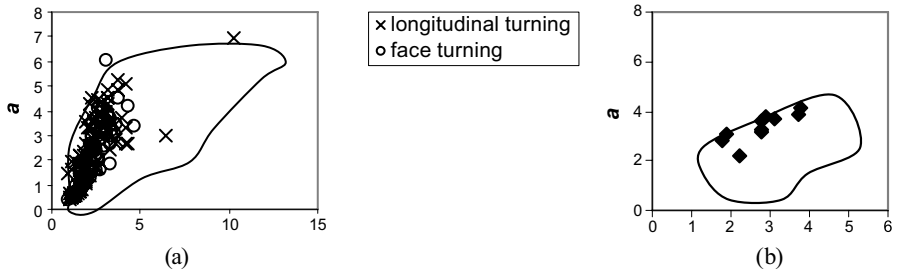

Figure 2.19. Beta function parameters chart (a) and the relevant chart (b) [20]

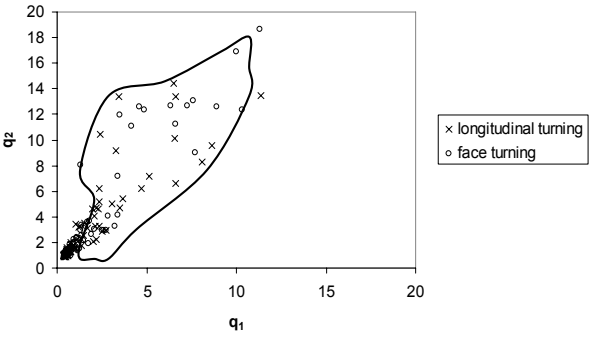

Figure 2.20. Pearson parameters chart [8]

References

[1] Dagnall H. (1996) Exploring Surface Texture, Taylor Hobson Publishing Ltd, Leicester

[2] Whitehouse D (1996) Handbook of Surface Metrology, Institute of Physics Publishing for Rank Taylor-Hobson Co., Bristol

[3] Humienny Z. (ed.) (2001) Geometrical Product Specifications, Chapter 16: "Roughness, Waviness and Primary Profile" by L. Blunt and X. Jiang, Warsaw University Printing House, Warsaw

[4] MacDonald B.C. and Co Basic Components & Elements of Surface Topography http://www.bcmac.com/PDF_files/Surface%20Finish%20101.pdf

[5] Dietzsch M., Papenfluss K, Hartmann, T. (1998) The MOTIF-method (ISO 12085) – A suitable description for functional, manufactural and metrological requirements, International Journal of Machine Tools and Manufacture, 38, No 5–6, 625–632

[6] King T G, Houghton N E (1995) Describing distribution shape: R_K and central moment approaches compared, International Journal of Machine Tools and Manufacture, 35/2, 247–252

[7] Hasegawa M, Liu, J, Okuda K, Nunobiki M (1996) Calculation of the fractal dimensions of machined surface profiles, Wear, 192, 40–45

[8] Petropoulos G P Pandazaras C N, Vaxevanidis N M, Antoniadis A (2006) Multi-parameter identification and control of turned surface textures, International Journal of Advanced Manufacturing Technology, 29, No. 1 & 2, 118–128

[9] Thomas T R, Rosen B-G, Amini N, (1999) Fractal characterization of the anisotropy of rough surfaces, Wear, 232, 41–50

[10] Boothroyd G (1975) Fundamentals of Metal Machining and Machine Tools, Scripta Book Company, Washington. DC

[11] Armarego E J A, Brown R H (1969) The Machining of Metals, Prentice-Hall, New Jersey

[12] Petropoulos P G (1973) The effect of feed rate and of tool nose radius on the roughness of oblique finish turned surfaces, Wear, 23**,** 299–310

[13] Benardos P G, Vosniakos G-C (2003) Predicting surface roughness in machining: a review, International Journal of Machine Tools & Manufacture, 43, 833–844

[14] Gosh A, Mallik A K (1995) Manufacturing Science, East West Press, New Delhi

[15] Kruszynski B, van Luttervelt K A (1989) The influence of manufacturing processes on surface properties, Advanced Manufacturing Engineering, 1, 187–202

[16] Davim J.P. (1991) Influência das condições de corte na microgeometria das superfícies obtidas por torneamento, MSc thesis, University of Porto, Porto (in portuguese)

[17] Nowicki B (1985) Multi-parameter representation of surface roughness, Wear, 102, 161–176

[18] Petropoulos G, Pandazaras C, Vaxevanidis N, Ntziantzias I, Korlos A, (2007) Selecting subsets of mutually uncorrelated surface roughness parameters in turning, International Journal of Computational Materials Science and Surface Engineering, 1, Nr. 1, 114–128

[19] S. Kalpakjian (2006) Manufacturing Engineering and Technology, 5th edn, Addison-Wesley Publishing Company**.**

[20] Peklenik J (1967) Investigation of the surface typology, Annals of the CIRP, Vol. 15

[21] Whitehouse D J (1978) Beta functions for surface typologie?, Annals of the CIRP, 27, No. 1, 539–553

[22] Peters J, Vanherck P, Sastrodinoto M. (1979) Assessment of surface typology analysis techniques, Annals of the CIRP, 28, No. 25, 39–553

3

Residual Stresses and Microstructural Modifications

Janez Grum

Faculty of Mechanical Engineering, Aškerčeva 6, 1000 Ljubljana, Slovenia
E-mail: janez.grum@fs.uni-lj.si

This chapter presents an "overview" of residual stresses and microstructural modifications in surface layers. Surface alterations may include mechanical, metallurgical, chemical and other changes in workpieces by machining. The applications of some of these concepts in turning, milling and grinding are discussed in this chapter.

3.1 Development of Surface Integrity

As to machine components in operation, one should be aware that there surfaces are subjected to the strongest loads as well as to environmental influences in a mutual contact. In addition to mechanical and thermal stresses, environmental influences and influences of other components, which are, during their operation, subjected to sliding or rolling contacts, should be taken into account. At the extreme right side of the scheme there are listed phenomena that can be found in machine components due to operating circumstances, including fatigue, creep of materials, wear and corrosion. In order to provide an adequate life of a machine component, a suitable material, an adequate construction and processing, particularly surface processing, should be selected. Presuming that the material and construction chosen are the right ones, correct material processing, particularly of a surface layer, should be provided to ensure an adequate life of a machine component.

Surfaces of machine components being most stressed, all attention should be paid to treatment processes, with which the size and variation of residual stresses can be influenced. If the influence of mechanical stresses on material wear or development of stress corrosion is to be reduced, then a suitable size and variation of residual stresses in a surface layer of a machine component shall be provided [1, 2].

Highly exacting machine components for the most exacting applications resulted, in the early 1960s in the development of a new scientific discipline, i.e. surface integrity [3–5]. Surface integrity takes into account the influences of manufacturing processes and machining conditions on the quality of a surface and a thin surface layer with particular regard to a microstructure, hardness variation, i.e., microhardness, and residual stresses as well as influences on material fatigue and corrosion.

The scientific discipline of surface integrity describes only surface properties after different mechanical and thermal treatment processes. Professionals started wondering what is to be done to ensure adequate quality of individual machine components and what is to be taken into account when assessing the quality of a surface or of a thin surface layer to fulfil operating requirements.

A most important role in manufacturing technology is played by machining processes during which the blank/material has to be machined to reach its final state, i.e., the product with prescribed requirements. The quality of a product, however, depends very much on the selection of material and on the consequences that the machining processes have on products. Besides this, the required high quality of products also demands a constant development of new materials. Due to the alloying elements by the addition of which we wish to improve some specific properties these new materials usually also have extremely good mechanical properties but worse technological abilities. Therefore, it is necessary that the development of new machining materials should be followed also by the development of machine tools and corresponding machining processes inclusively the search of new materials for cutting tools [5, 14–16].

Figure 3.1 shows the influences exerted by residual stresses and load stresses on the actual stress in the thin surface layer. In order to provide favorable total stresses in a material during loading of a machine component, experts on manufacturing technologies should be well acquainted with the influences of manufacturing conditions on microstructure changes and, in turn, variations of microhardness and residual stresses in the surface layer with individual machining processes. As to

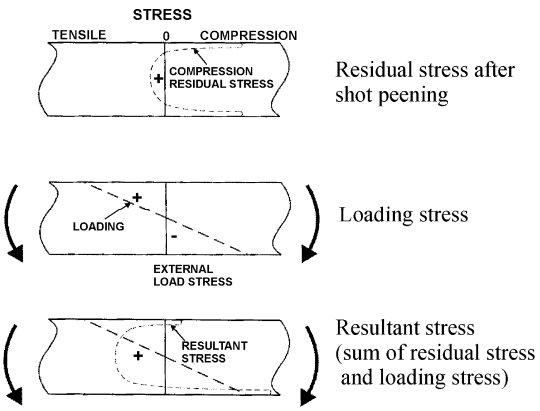

Figure 3.1. Importance of residual stresses in loaded machine component on actual stress variation

material fatigue from the viewpoint of residual stresses, suitable surface heat-treatment processes such as surface hardening, case hardening, nitriding, etc., can influence the occurrence of compressive residual stresses. In surface-hardening and case-hardening processes account should be taken that the quenching process may produce high internal stresses during heat treatment, which are due to temperature stresses occurring during cooling, i.e. quenching, which are, in a certain time interval, accompanied also by stresses due to phase transformations. High internal stresses during quenching may lead to high residual stresses that are related to volume changes and/or distortion of machine components. Since 1980 there has been a scientific discipline of surface engineering (1980) that has systematically studied various procedures for the improvement of surface properties.

Surface engineering involves the application of traditional and innovative surface technologies to engineering components and materials in order to produce a composite material with the properties of an unattainable base material with special surface treatments. Frequently, various surface technologies are applied to existing design engineering of components but, ideally, "surface engineering" involves component design and adequately applied surface technologies [6, 7].

The design of a surface and substrate together as a system offer cost- effectiveness of machine components including expertise about design and manufacturing.

One should be aware that every material treatment produces certain residual-stress variations and that every machining process will also change residual-stress variations. Control of volume changes and distortion of machine components and knowledge of residual stresses in them are becoming increasingly important in practical applications to high-tech products, particularly from the viewpoint of more adequate operating conditions and economical reasons. The start of organized treatment of distortion of machine components in steel quenching was a thematic conference in Chicago (1992) entitled "Quenching and Control of Distortion" under the auspices of the American Society for Metals and organized by Prof. G.E. Totten. He further organized three more thematic conferences on "Quenching and Control of Distortion", i.e., in Indianapolis (1996), Prague (1999), and Beijing (2003) [8–11]. With the aim of quality control of manufacturing of machine components, a Collaborative Research Center was founded at Bremen University in 2001, under a support of the "Deutsche Forschungsgemeinschaft" (DFG), including a new integral approach to product quality. A new scientific field within the project was called distortion engineering (2001). It has been directing research to a reduction of distortion and, consequently, cost-effective manufacture of components [12, 13].

3.2 Residual Stress Sources

Kloos and Kaiser [17] presented very important residual stresses induced by various ways of manufacturing. In almost all manufacturing processes, residual stresses are present in semi-finished products and machine components. This is the reason for numerous causes of residual stresses throughout all the different steps of production engineering processes. Residual stresses are effective static triaxial stresses that are in a state of equilibrium without the action of external forces and/or moments. They

always occur whenever a macroscopic cross-sectional area of a component or a microscopic area of a multiphase material is plastically deformed by external and internal forces. These forces may either be due to thermal loading, processes of diffusion or phase transformation in such a way that incompatibilities of strain may be caused. In the fulfillment of conditions of equilibrium volumetric changes take place during manufacturing of machine parts. Such conditions of residual stresses mostly cause shrinkage, processes formation of cracks and fractures as well as positive and negative influences on the mechanical properties of materials the behavior against stress corrosion and corrosion fatigue and on the wear behavior of various machine parts in contacts.

Compressive residual stresses of the first order in the surface layer of a component are highly important for the behavior of fatigue strength of the material under periodical or stochastic loading, since they cause a mean-stress displacement in the direction of compressive stresses, therefore preventing crack initialization and crack propagation. By the presence of compressive residual stresses there is longer service life of machine parts.

According to Figure 3.2, all the causes of residual stresses can be classified under the following three main groups: material, manufacturing, loading by service conditions [17].

In the production process of semi-finished products or machine components several production steps influence the present residual stress profiles. The resulting residual stresses at the end of the production processes and their distribution are of particular importance for the operational behavior of machine components.

The final step of production processes like shot peening are often applied with the aim of producing compressive residual stresses at the surface region. This

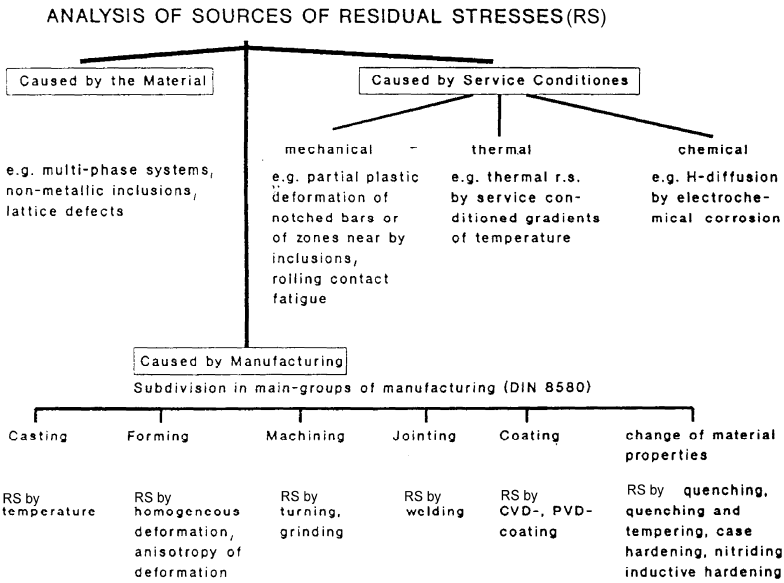

Figure 3.2. All the causes of residual stresses can be classified under the following three main groups: material, manufacturing, loading by service conditions [17]

process is becoming increasingly important, particularly in the case of welded joints, whereby it is applied for the reduction of tensile residual stresses. It is also possible to reduce tensile stresses in machine parts by the application of stress-relief annealing.

Stress relief annealing effect is related to should, however, be noted here that, there is a retainment of tensile residual stresses after this annealing, which can be as yield-point of the material according to the annealing temperature.

Different steps of the production engineering methods applied in the production of machine components would be presented, with emphasis on a final development of residual stresses after the machining process.

Figure 3.3 shows the application of the definition of residual stress of the first, second and third order in the workpiece.

Residual stresses of the 1st order related to coating are extended, according to the definition, over several single grains and are indicated in each case by a mean value. The thermal coefficient of expansion by comparison differs from that of the substrate material. The bigger the temperature difference between the temperature of deposition and the operational temperature of the coated component, the higher the resulting residual stress will be. Should the deposition take place at higher temperatures, so that the thermal coefficient of expansion of the surface layer is higher than that of the substrate material, there would be residual tensile stresses at the surface layer after the temperatures have equalized. If the change of solubility (dependent

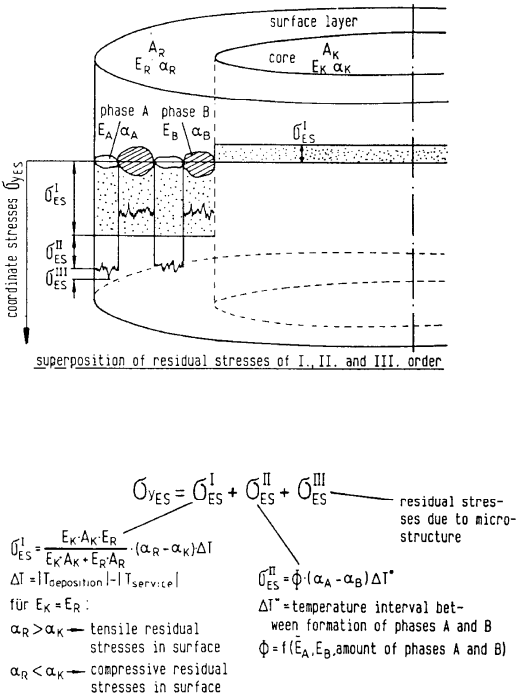

Figure 3.3. Analysis of residual stresses sources induced by material, manufacturing and operating conditions [17]

on temperature), causes the deposition of an alloy, and if this is quenched, resulting in a two- or multiphase form. The partial residual stress of each phase can be determined by X-ray diffraction under certain conditions. As in the case of every metallic material, the surface layer contains lattice defects of different types, whereby residual stresses of the third order occur.

During the coating processes, as well as in other manufacturing processes, superposition of residual stresses of the first, second and third order may occur so that, by measuring residual stresses of the 1st order alone does not give sufficient information on the damaging processes taking place in each phase. In this case, the X-ray diffraction is gaining increasing recognition by its application for the measurement of residual stresses of different phases.

Various manufacturing processes are described to show how the origins of residual stresses are attributed to: partial plastic deformation caused by mechanical loading, partial plastic deformation caused by inhomogeneous thermal loading, interaction between the mechanical and thermal state of the material, interaction between the thermal and metallurgical state of the material, interaction between the mechanical, thermal and metallurgical state of the material.

3.3 Residual Stress and Microstructure After Turning

3.3.1 Residual Stresses After Turning of Re-sulfurized Austenitic Steels

Saoubi *et al.* [18] carried out residual stress analysis in orthogonal machining of re-sulfurized AISI 316L steels. Residual stress profiles have been determined using the X-ray diffraction technique. The effects of cutting conditions on residual stresses are analyzed regarding thermal and mechanical events, during a cutting process. The tool temperature distribution has been determined by a specific CCD infrared camera.

Round bars of 150 mm diameter of two different 316L steel were selected for the study: one standard type (A) and another with improved machinability with sulfide inclusions (U) (Table 3.1). The two steels have an austenitic microstructure with grain size of 50 μm and a hardness value of 170 HV.

Orthogonal cutting tests were conducted with uncoated and coated tungsten carbide tools. The chemical vapor deposition (CVD) tool coating employed were triple-layer coatings of TiC-Al_2O_3-TiN having good wear-resistance properties. The orthogonal cutting conditions without cutting fluid and the tool geometry are given in Table 3.2.

Table 3.1. Chemical composition of AISI 316L steels [18]

Material	**Chemical composition (wt %)**											
	C	Si	Mn	Ni	Cr	Mo	S	P	N	Co	Cu	Fe
U	0.010	0.630	1.280	11.140	16.74	2.020	0.022	0.020	0.030	0.240	–	balance
A	0.012	0.60	1.71	11.58	17.09	2.20	<0.003	0.025	–	–	0.11	balance

Table 3.2. Cutting conditions and tool geometry [18]

Cutting tool reference	Rake angle γ (°)	Clearance angle α (°)	Cutting speed v_c (m/min)	Feed rate f (mm/rev)	Width of cut (mm)
K313 (WC/Co)	0 and 5	5	75–200	0.1–0.3	4
KC950 (WC/Co + TiC/Al_2O_3/TiN)	0	5	75–200	0.1–0.3	4
KC850 (WC/Co + TiC/TiCN/TiN)	0	5	75–400	0.1–0.3	4
H13 A (WC/Co)	0	11	75–280	0.1–0.3	6

Surfaces were electrolytically polished, step-by-step, in order to determine the evolution of the residual stresses profiles. The uncertainty on stress data is less than 50 MPa for depths of less than 200 μm, but reaches 150–200 MPa for greater depth values.

At given cutting conditions, tensile residual stresses were found on the surface in each case. The circumferential stresses were generally greater than axial stresses, with values reaching around 1000 MPa. Residual-stress profiles decreased continuously with depth down to a minimum compressive stress value and then increased to the corresponding value of the state before machining. There is only discussion about circumferential stresses. Figure 3.4 represents typical residual-stress profiles obtained when machining material U with a coated tool at given rake angle and cutting conditions. The Figure shows the in-depth evolution of the peak half width value for the same cutting conditions.

The different characteristic values associated with this profile are LCmax the maximal peak half-width value that gives information on the work-hardening state of the surface, the peak half-width value determined on the workpiece surface showing a significant surface work hardening, when compared to the undeformed core material value; and t_{LC}: the cutting-affected depth, which was taken as the value for which LC reached 1.2 times the nominal value of the undeformed mate-

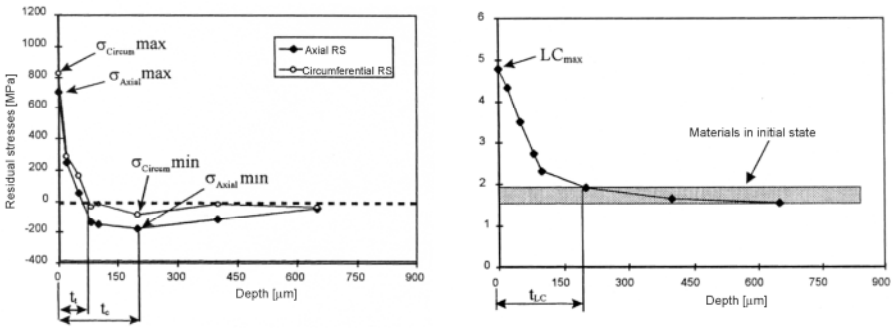

Figure 3.4. Typical residual stress profiles (a) and peak breadth profile (b) [18]

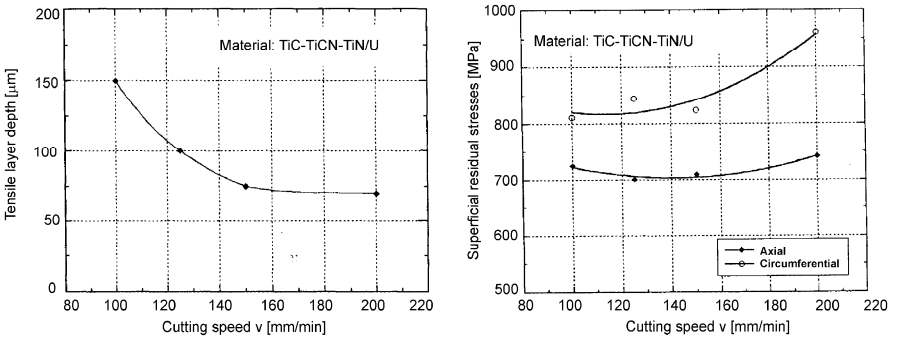

(a) (b)

Figure 3.5. Tensile layer depth (a) and as a function surface residual stresses (b) of cutting speed [18]

rial, this cutting-affected depth varying from 70 to 350 µm. Figure 3.5 shows the influence of machining parameters on residual stresses.

The influence of cutting speed was investigated for a given feed rate of 0.1 mm/rev and for the material/tool couple TiC-TiCN-TiN/U. Results show an increase of 140 MPa in the surface residual stress when the cutting speed increased from 100 to 200 m/min.

However, the thickness of the tensile layer decreased with the cutting speed. The subsurface stress values also tended to be less compressive with increase in the cutting speed and their minimal values were reached deeper into the workpiece surface. As for the peak half-width values, it can be seen from Table 3.3 that LC increases with increase in the cutting speed.

Residual-stress profiles were obtained for different values of feed rate. As an example, Figure 3.6 represents the stress gradient for a feed rate variation of 0.1–0.25 mm/rev. The cutting speed was fixed at 125 m/min, and the material/tool pairing was KC950 (tool 0°)/U. The minimum stress profiles were of compressive

Table 3.3. Influence of the cutting speed on the characteristic parameters of the stress analysis for material TiC-TiCN-TiN/U tool and $f = 0.1$ mm/rev [18]

v_c (m/min)	Residual stresses				Peak breadth LC (°)	Cutting-affected depth		
	$\sigma_{circum,max}$ (MPa)	$\sigma_{axial,max}$ (MPa)	$\sigma_{circum,min}$ (MPa)	$\sigma_{axial,min}$ (MPa)		t_t (µm)	T_c (µm)	T_{LC} (µm)
100	820	800	–90	–140	4.53	150	400	100
125	850	700	–70	–120	4.70	100	200	150
150	830	710	–80	–180	4.80	75	200	180
200	960	820	–40	–180	4.80	70	100	90

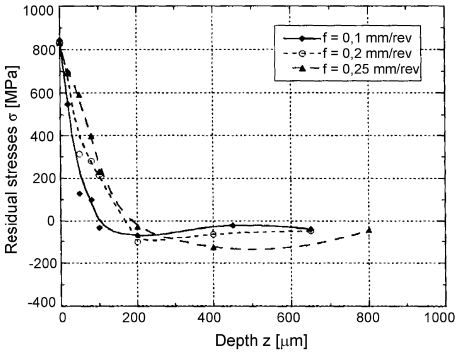

Figure 3.6. Residual tangential stress and peak breadth profiles as functions of feed rate (Material U; KC950 (0°) Tool; $V_C = 125$ m/min) [18]

nature and located deeper in the specimens. The minimal stress values were more compressive and were located deeper in the workpiece as the feed rate increased, although the surface residual stresses barely varied with feed rate.

3.3.2 Residual Stresses and Microstructure in the Surface After Turning Heat-treatable Steel

Ferlan [19] treated turning of frequently used heat-treatable 42CrMo steel, studying in particular the magnitude and variation of residual stresses in the formation of a white layer at a workpiece surface. Specimens for a microstructural analysis of a surface layer were prepared from ring sections used to measure residual stresses. Sections of numerous rings produced under different turning conditions were cut under mild conditions by a special cutter, then they were flattened with a fine grinder at a special device, and finally ground and polished. Specimens for the metallographic analysis were eventually polished with a diamond paste having an average grain size of 7.5 μm and an addition of Al_2O_3. The specimens were then etched with nital (3% HNO_3 + 97% alcohol).

Microstructure images were taken with an optical microscope with a magnification of 100 times and 500 times. Figure 3.7 shows a microstructure of a thin surface layer of the workpiece material that was turned with a cutting speed of $v_3 = 100$ m/min, at different tool rates.

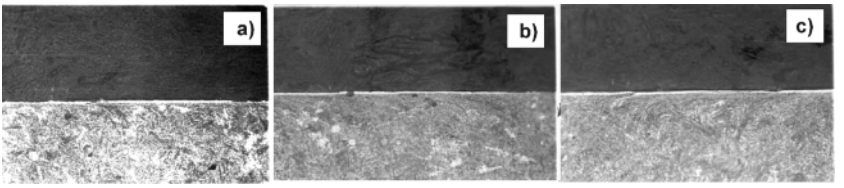

Figure 3.7. Microstructure of thin surface layer with white layer after turning with cutting speed of $v_4 = 200$ m/min, with worn tool, VB = 0.30 mm, and with different shifts: (a) $f_1 = 0.04$ mm/rev, (b) $f_2 = 0.132$ mm/rev, and (c) $f_3 = 0.314$ mm/rev [19]

After turning with the worn tool, VB>0.3 mm, numerous damages at the workpiece surface were detected. Turning with a worn tool, namely, generates more heat at a tool and at a workpiece; therefore, a thin austenitic-martensitic layer, known as a white layer, will occur at the workpiece surface.

The layer thickness was considerably below 10 μm and was easily detected in the metallographic examination of the specimens. Additionally, the layer depth with explicitly plastic deformation of the material after turning could be evaluated. The greatest surface-layer depth showing distinctly plastic deformation amounted to 70 μm and it was found in a specimen after turning with a cutting speed v_4 of 200 m/min and with the worn tool with VB_2>0.30 mm. The greatest portion of surface damages at the workpiece, e.g., galling and pulling-off, were found with low cutting speeds (v_1 = 20 mm/min, v_2 = 50 mm/min).

Residual stresses were measured in the specimens ground under different turning conditions. Rings with an external diameter of 76 mm, an internal diameter of 71 mm, and a width of 10.5 mm were prepared.

Residual stresses were measured with our own relaxation method, i.e., with electrochemical dissolution, using an adapted mode of deformation measurement at a ring half. The residual stresses measured after turning of the specimens made of heat-treatment 42CrMo4 steel provided very important information on the quality of a cutting process and on the condition of the surface layer in dependence of the processing conditions. Under normal turning conditions with a sharp tool residual tensile stresses occurred at the specimen surfaces. Increasing of a tool feed rate resulted in a reduction of the residual tensile stresses present and their transition, in a greater depth, to lower compressive stresses. On the contrary, compressive residual stresses occurred in the thin surface layer only in turning with a low feed rate (f_1 = 0.04 mm/rev) and with the strongly worn tool (VB>0.3 mm). Under such processing conditions, it may happen that the tool will get repulsed from the workpiece and the material at the workpiece surface compressed; consequently, compressive residual stresses will occur at the surface and in the thin surface layer.

To have a better view of the influences of the cutting conditions on the magnitude and variation of the residual stresses the latter are presented in a form of gradient with a depth, which illustrates through-depth variation of the residual stresses with arrows. Figures 3.8 and 3.9 show approximated variations of the residual

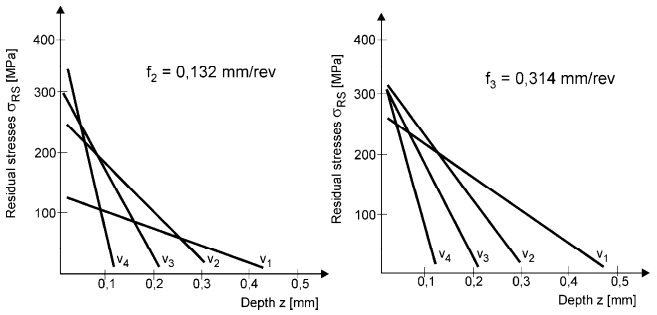

Figure 3.8. Influence of turning speed on magnitude and variation of residual stresses with feed rates (a) f_2 = 0.132 mm/rev; and (b) f_3 = 0.314 mm/rev [19]

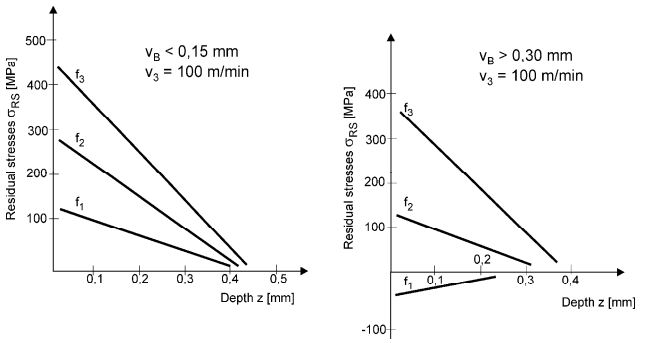

Figure 3.9. Influence of feed rate (f_1, f_2, f_3) on residual stresses after turning with cutting speed v_3 = 100 m/min, either with (a) sharp or (b) worn tool [19]

stresses with arrows as a function of the respective processing conditions, i.e. with different grinding speeds and the same feed rate and cutting depth, and with a specified turning speed and different feed rates.

Conclusions considering varying of residual stresses are as follows:
With lower feed rates, a grinding speed exerts a decisive influence on the magnitude and variation of the residual stresses in the thin surface layer. With higher feed rates, however, residual tensile stresses are almost the same at the surface, but with an increasing cutting speed the layer depth with residual tensile stresses gets reduced (Figure 3.9). Increasing of the cutting speed results in a reduced depth of material deformation, which is confirmed by the variations of residual stresses.

A turning speed exerts the strongest influence on the depth of the hardened surface layer, whereas the feed rate exerts a major influence on the magnitude of the residual stresses at the surface. It is also true that increasing of the feed velocity results in increased tensile residual stresses in the surface. Such a relation holds regardless of the turning speed chosen, but it is more distinct with lower speeds, and with both the sharp tool, VB<0.15 mm (a) and with the worn one, VB>0.30 mm (b).

A comparison of the variation and magnitude of the residual stresses at the specimens with the same cutting speed (v_3 = 100 m/min) and grinding depth (a = 1.0 mm), using the sharp tool (VB<0.15 mm) and the worn one (VB>0.30) shows a reduction of tensile residual stresses with feed rate (Figure 3.10). Thus, with the lowest feed rate, f_1 = 0.04 mm/rev, even compressive stresses occur, which confirms a more distinct effect of workpiece material compression in the surface layer.

Figure 3.10, left, shows the influence of a different degree of tool wear with a cutting speed v_3 of 100 m/min and with the lowest feed rate, f_1 = 0.04 mm/rev. The results obtained confirm that with a less worn tool the turning process is still satisfactory, whereas with a more strongly worn tool (VB>0.30 mm) workpiece material compression in the surface layer predominates, which results in the generation of compressive residual stresses in the surface. The diagram in Figure 3.10b shows that in grinding with a cutting speed v_3 of 100 m/min and higher feed rates f_2 and f_3, and with the sharp or worn tool very similar residual-stress variations are obtained, the residual-stress variations being somewhat lower and the hardened

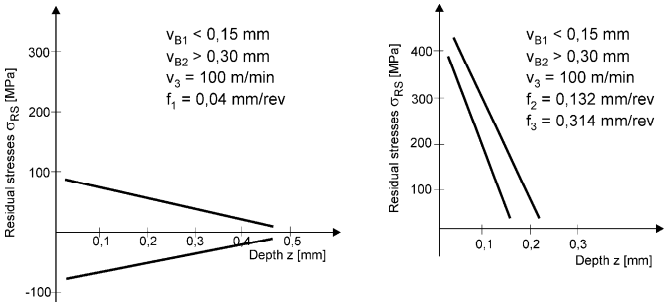

Figure 3.10. Influence of degree of tool wear VB on (a) magnitude and (b) variation of residual stresses after turning [19]

layer being a little thicker with the sharp tool. In general, it can be found that the influence of tool wear on the magnitude and variation of the residual stresses is not particularly distinct.

From the residual-stress variation and magnitude under different turning conditions and in turning with the sharp tool and the worn tool, it can be inferred that the stresses at the surface are rather high. With the most efficient turning, i.e., with cutting speeds $v_3 = 100$ m/min and $v_4 = 200$ m/min, and with higher feed rates f_2 and f_3, the tensile residual stresses at the workpiece surface exceed 400 N/mm^2. This value of the residual stress present attains almost 60% of the yield stress in a static test of 42CrMo4 steel. Consequently, it is assessed that the latter are not critical under static loading of components. On the contrary, with dynamically loaded components an amplitude stress can exceed the tensile residual stress at the surface, which may produce cracking and propagation of existing cracks.

Arunachalam *et al*. [20] researched residual stresses in age-hardened Inconel 718 machining with CBN and ceramic cutting tools. Increased productivity in machining of heat-resistant superalloys can be achieved by using advanced cutting tools such as ceramics and cubic boron nitride (CBN). The effects of these tools on the surface integrity, especially the residual stresses on high-speed machining of Inconel 718 has not been discussed. The residual stress after machining with CBN cutting tools has been investigated as a function of speed, depth of cut, coolant, tool geometry and tool coating. The results show that mixed ceramic cutting tools induce residual tensile stresses with a much higher magnitude than CBN cutting tools. The residual stresses and the surface roughness generated by CBN cutting tools are more sensitive to cutting speeds than depth of cut. The use of coolant results in either compressive residual stresses or lowers the magnitude of the residual tensile stresses, whereas dry cutting always resulted in residual tensile stresses. From this investigation, it is suggested that round CBN cutting tools should produce minimal residual tensile stresses and good surface finish.

Inconel 718 bars of diameter 100 mm and thickness 15 mm in solution treated and age-hardened condition having a hardness of 36 HRC were used as specimens in machining tests, a thin layer of 0.5 mm was machined with a new cutting tool from each specimen in order to remove the uneven surfaces due to the previous operation. The face machining operations were carried out with a constant speed.

All machining was performed with coolant except for that used to study the influence of dry cutting on the residual stresses. The two tool materials used in the study are pure CBN and mixed ceramic (Al_2O_3 and TiC). For each set of cutting conditions tested, two specimens were prepared.

The residual stress measurements were carried out on a Rigaku X-ray microarea residual stress analyzer. The $\sin^2\psi$ technique involving 10 tilt angles was selected because of its accuracy.

Figure 3.11 shows the influence of cutting tool type on the maximum value of residual stress at the surface with optimum cutting conditions. Ceramic tools cause the formation of residual tensile stresses much higher in value as compared to CBN tools. Due to the poor thermal conductivity of a mixed alumina ceramic tool, use of coolant is prohibited and so in general will lead to higher values of residual stresses due to the dominance of thermal effects. In the case of CBN cutting tools, the thermal conductivity is quite high and so use of coolant reduces the thermal effects and residual stresses are expected. Residual tensile stresses are caused by plastic deformation and thermal effects.

The effect of cutting speed on the residual stresses generated by the CBN (C1) cutting tool is shown in Figure 3.12. With the increase in the cutting speed, the residual stress at the surface changed from compressive to residual tensile stresses. As cutting speed increases, machining becomes more adiabatic, the heat generated in the shear zone cannot be conducted away during the very short time and so the temperature rise softens the metal and thus reduces the cutting forces.

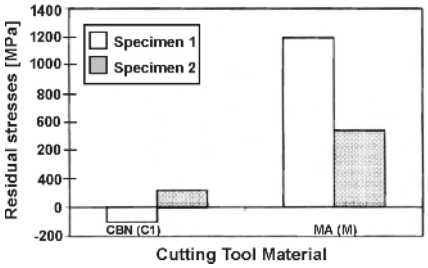

Figure 3.11. Influence of cutting tool material on the residual stresses under optimum cutting conditions [20]

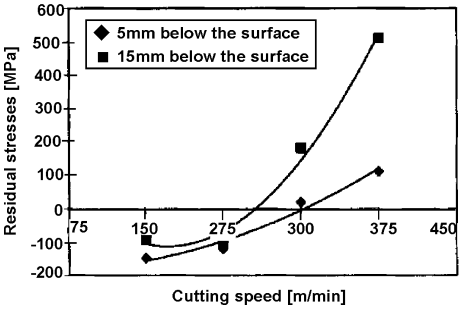

Figure 3.12. Effect of cutting speed on the residual stresses for CBN cutting tool (C1 type; $f = 0.15$ mm/rev, $a = 0.5$ mm) at 5 and 15 mm from the periphery [20]

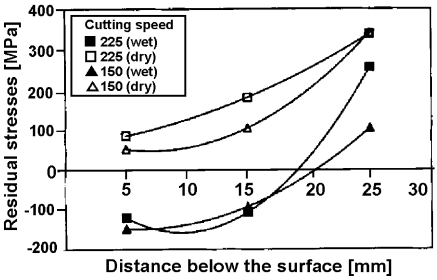

Figure 3.13. Effect of coolant on the residual stresses below the surface for CBN (C1 type) cutting tool at two different cutting conditions two speeds $v = 150$ and $v = 225$ m/min feed rate 0.05 mm/rev and cutting depth $f = 0.5$ mm [20]

Figure 3.13 shows the effect of coolant on the residual stresses. Dry cutting results in residual tensile stresses for the different cutting speeds tested. The use of coolant during machining results in compressive stresses 15 mm from the surface residual tensile stresses. The use of coolant lowers friction and increases the heat removal from the surface, thus results in the dominance of mechanical effects, obtaining compressive stress. Even with the use of coolant, the progress of cutting results in residual compressive stresses becoming tensile. This trend was observed in all the specimens tested in this study, confirming that residual stresses are very sensitive to machining parameters. This means that careful attention should be paid to finishing operations to obtain residual compressive stresses.

3.3.3 Influence of Tool Material Microstructures

Bouzakis *et al.* [21] studied wear phenomena in turning of PVD-coated inserts. The cemented carbide (HM) cutting inserts of K35 (ISO quality) and the TINALOX® variation of the $(T_{1-x}Al_x)N$ coating were selected as tool components. The SEM micrograph inserted in Figure 3.14 indicates the typical structure of the base material and the coating. The HIS deposition procedure of the TINALOX® coating is responsible for the attractive combination of very high bulk hardness, i.e., consequent increased wear resistance, and of the relatively low Young's modulus.

The tool operation in turning is characterized through the continuous chip formation and therefore by the approximately steady stress state that occurs at the tip of the cutting edge. The minimum applied cutting speed was 100 m/min, in order to avoid built-up-edge formation phenomena. The cutting edge status was systematically inspected for the early cutting time and the coated tip illustrated an indestructible texture up to an overall cutting length (OCL) less than 0.2 km, as can be observed in the SEM micrograph.

Figure 3.15 shows SEM micrographs to illustrate the wear condition of the cutting wedge after the removal of certain amounts of the overall chip length up to 15 km. Local failures appear at the transient region of the filleted cutting tip after this length.

The energy-dispersive X-ray (EDX) analyses inserted in the bottom part of the same figure, exhibit the type and extent of film fracture. The failed regions are the brighter colored ones, where the EDX microanalyses (regions B) indicate the expo-

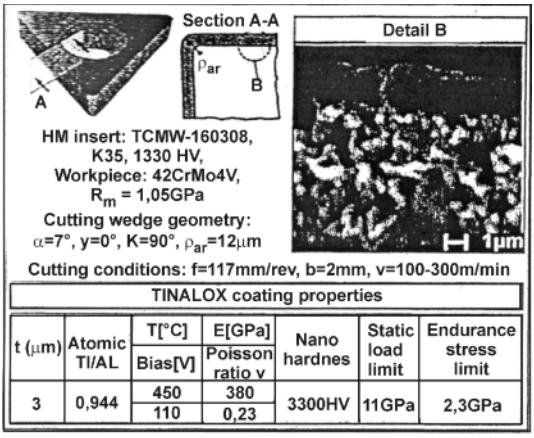

TINALOX coating properties						
t (μm)	Atomic Ti/AL	T[°C] / Bias[V]	E[GPa] / Poisson ratio ν	Nano hardnes	Static load limit	Endurance stress limit
3	0,944	450 / 110	380 / 0,23	3300HV	11GPa	2,3GPa

Figure 3.14. Material microstructure and properties of the coated inserts, used in the experiments [21]

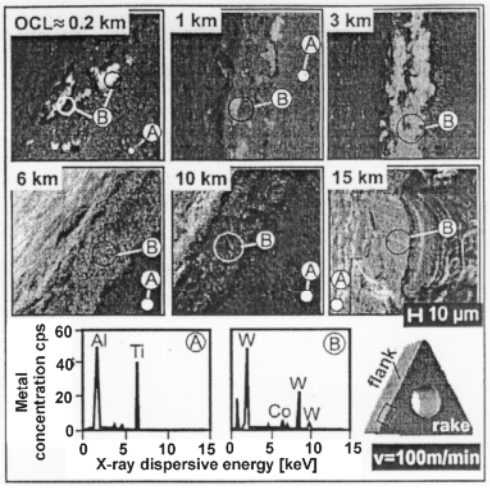

Figure 3.15. SEM and EDX results indicating the progress of the coating failure at $v = 100$ m/min [21]

sure of substrate components, i.e., tungsten and cobalt. The failed zones are growing slowly through the increasing of the cutting length, as can be observed in the related micrographs after 1, 3, 6, 10 and 15 km overall cutting length, whereas the flank wear also increases.

3.3.4 Influence of Flank Wear on Residual Stress Formation

Chen *et al.* [22] presented modeling of flank wear land and chip formation on residual stresses below the machined surface of titanium alloy Ti-6A-4 V. The workpiece was annealed at 700°C for 4 h and air cooled to provide a hardness of 35

±2HRC. The cutting tests were performed with an uncoated carbide tool with cutting speed 320 m min^{-1} and width of cut 1.0 mm. The tool's rake and clearance angles were +5 deg and +8 deg. It dry cutting environment was used in the tests. At tool wear 0.03 mm and 0.20 mm samples for the residual stress measurements of the machined surfaces were obtained. Depth residual-stress profiles were obtained by the X-ray diffraction technique and removal of thin layers by electrolytic etching. The X-ray diffraction apparatus has a beam size of 4 mm × 4 mm; the radiation source employed was CuKα.

The residual-stress profile is dependent on the cutting speed and flank wear length at a cutting speed 320 m min^{-1}. When the tool flank wear was 0.20 mm, residual tensile stresses were found near the surface, with the maximum value measured at the surface. Within less than 5 μm, from the newly machined surface, the tensile residual stresses drop to zero. When the tool flank wear was 0.03 mm, the residual-stress profile was different when compared with the larger flank wear length. The residual stresses on the surface were compressive and the maximum residual compressive stresses were found −10 μm from the surface. With the smaller flank wear length, no tensile residual stresses were observed. In general, thermal loading usually induces residual tensile stress and mechanical loading causes residual compressive stresses. When the tool is worn, a higher temperature is generated along the tool workpiece interface when compared to a sharp tool.

Figure 3.16 shows the temperature distribution below the surface on modeling. Higher temperature and penetration depths were observed with continuous chip when compared to a segmented type. For continuous chip, the proportion of heat energy flowing into the workpiece was 17%, whereas for segmental chip it decreased from 10% to 13% due to the steeper shear angle. In general, heat energy flows into the workpiece increased for lower shear angle. Therefore, the shear angle is lower for a continuous chip than for a segmented chip. When the tool is worn the temperature generated in the workpiece was higher when compared to a sharp tool.

Figure 3.17 shows the influence tool wear and chip formation on residual-stress distribution below the surface. When modeling without the crack module, continuous chips will be formed and residual stress on the surface will be tensile and followed by a more compressive residual stress. The more tensile residual stress was due to higher temperature field found in the workpiece material with continuous chip. The higher compressive residual stress was due to higher forces generated with continuous chip. Therefore with segmental chips, the surface residual stress was less tensile and the compressive stresses magnitude and depth were lowered. The modeled residual stress with segmental chips agrees better with experimental results during the cutting tests.

At flank wear ranging from 0.03 mm to 0.20 mm, the surface residual stress tends to the tensile region. This was due to the higher temperature generated along the tool workpiece interface, as shown in Figure 3.16. Similarly, the compressive stress penetrates deeper with the worn tool.

The finite-element models presented in this paper can predict the effects of tool wear and chip formation on temperature field, and residual stress distribution. The modeled residual stress agrees well with their experimental results.

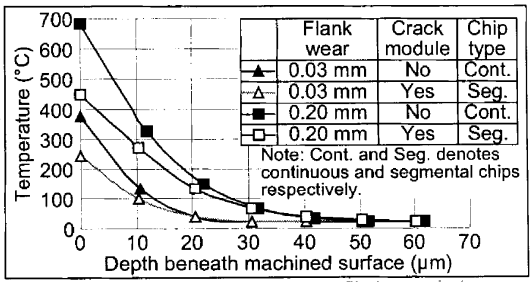

Figure 3.16. Temperature profile below the surface [22]

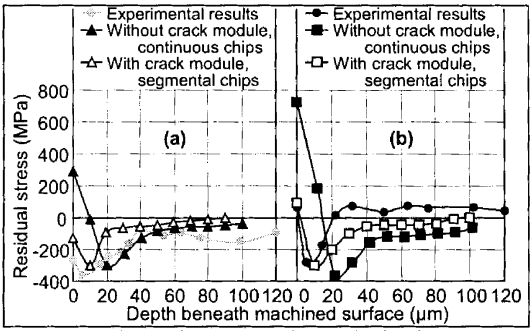

Figure 3.17. Effects of chip formation and (a) 0.03 mm and (b) 0.20 mm flank wear length on residual-stress profile [22]

3.3.5 Residual Stresses After Dry Turning

Outeiro *et al.* [23] discussed critical issues in difficult cutting materials that are often associated with short tool life and poor surface integrity, where the resulting tensile residual stresses on the machined surface fatigue life. Their study presents the influence of cutting parameters on surface integrity after dry turning of Inconel 718 and austenitic stainless steel with PVD-coated (TiAlN) and uncoated carbide tools.

Figure 3.18 shows residual-stress profiles in the surface layer induced by cutting with coated and uncoated cutting tools in the direction of primary motion. The figure shows residual-stress profiles in the surface layer in the direction of feed motion. Residual stresses are tensile at the surface and gradually shift to compressive values beneath the surface at the level corresponding to that in the work material before cutting. For the range of cutting conditions investigated, the residual stresses were tensile over 1000 MPa at the surface. The figure also shows that cutting with uncoated tools, when compared with the coated tools results in:

- higher surface residual stresses;
- lower thickens of tensile layer; and
- lower residual stresses in the surface layer with the maximum being shifted closer to the surface in cutting with uncoated tools.

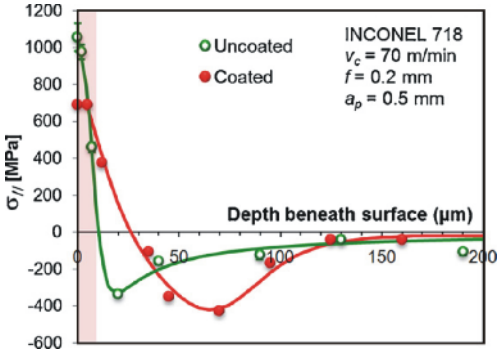

Figure 3.18. Residual-stress profiles in the direction of primary motion turning Inconel 718 [23]

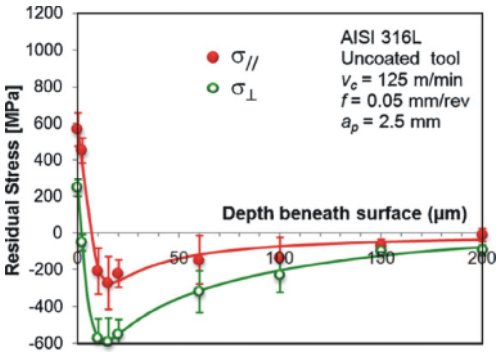

Figure 3.19. Residual-stress profiles after turning stainless steel AISI 316L [23]

Regarding cutting conditions investigated, residual-stress profiles generated by turning AISI 316L are also high tensile value at the surface, although not as high as those obtained by Inconel 718. As shown in Figure 3.19 both residual stresses are similar to those profiles observed in cutting profiles of Inconel 718.

3.3.6 Residual Stresses and Microstructures After Hard Turning

Byrne *et al.* [24] studied the functional behavior of machined parts that is strongly influenced by the fine finishing processes. High flexibility and the ability to manufacture demanding shapes of workpieces represent the main advantages of hard turning over grinding. The residual-stress values at the surface of the workpiece are mainly influenced by the friction between the workpiece and the tool. Figure 3.20 shows residual-stress profiles at hard turning with different state of tool VB = 0 µm and VB = 200 µm.

With an increasing flank wear the thermal load to the workpiece surface rises. A new cutting tool induces compressive residual stresses below the workpiece surface, whereas a worn tool causes tensile residual stresses and the appearance of a white layer with a very fine microstructure.

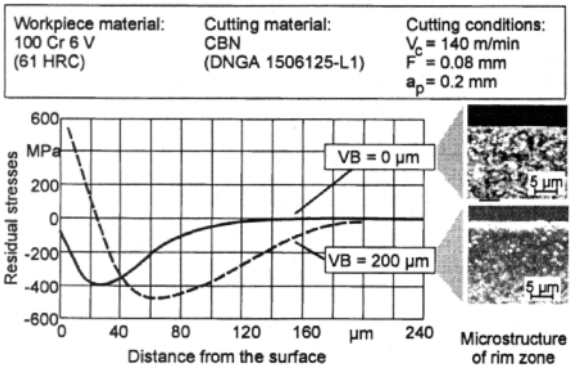

Figure 3.20. Residual stress and surface layer effects after hard turning [24]

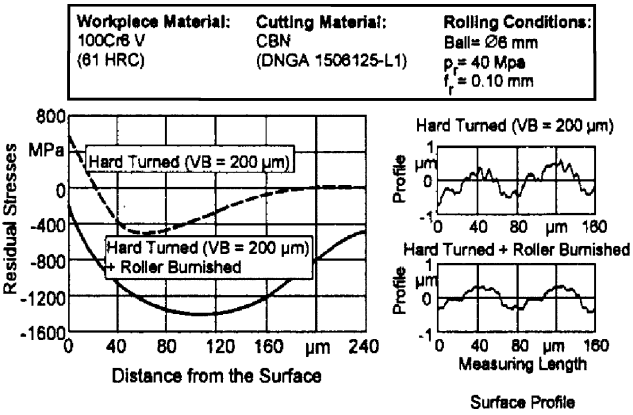

Figure 3.21. Surface layer effects due to roller burnishing [24]

Figure 3.21 shows residual-stress profiles at hard turning at tool wear VB = 200 µm and hard turning and roller burnishing at the surface.

For decades, low levels of lead have been added to free cutting and engineering steels to improve their machinability. In recent years the use of lead has become undesirable for environmental reasons. There has been great interest in the development of materials with alternative machinability enhancers as well as demands on the new additives that will not diminish the machining performance.

Dahlman et al. [25] researched the influence of rake angle and cutting parameters on residual stresses in hard turning. Hard turning is replacing grinding as a method in the production of precision steel products. Many researchers studied the effects on the residual stress and the improvement of the fatigue life of hard turned products. Face turning with constant cutting speed and changing of feed rate and cutting depth in AISI 52100 steel was used. The residual stresses were measured using the X-ray diffraction method in both speed and feed direction. The material was etched down to a depth of 100 µm in order to monitor residual stresses in the whole of the affected depth.

Figure 3.22 shows residual-stress profiles below the surface for cutting speed directions. The residual stresses were tensile at the surface for different rake angles. However, at a depth of about 5–10 μm, only compressive stresses could be observed. With an effective rake angle of –6°, the maximum compressive stresses were affected by the machining operation was about 30 μm at which point the stresses left from the heat-treatment operation leveled out at –100 MPa. The material used in this study was hardened steel, AISI 52100 with the hardness 62 HRC. Rings with an outer diameter of 340 mm and an inner diameter of 180 mm were turned on the face.

Figure 3.23 shows residual-stress profiles below the surface for cutting speed and feed directions on cutting with a tool rake angle of –21°.

When the effective rake angle was decreased to –21°, two phenomena occurred. Firstly, the level of compressive stresses increased to 500 MPa in the feed direction and 600 MPa in the speed direction, the position of the maximum compressive stress was still at 15 μm. Secondly, the affected depth increased to 40 μm.

Figure 3.24 shows residual-stress profiles at turning with a tool at rake angle –41°. The depth that the residual stress level was much greater, at almost 90 μm. The position of the maximum residual stresses moved deeper to a depth of 25 μm.

Figure 3.25 shows the effects of a rake angle of –61 on residual-stress profiles below the surface. In the feed direction, the maximum compressive stress was as high as 1050 MPa 30 μm below the surface. At a measuring depth of 100 μm below the surface the residual stress was approximately –550 MPa in both directions.

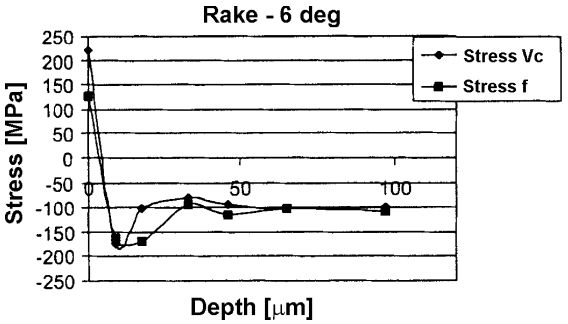

Figure 3.22. Residual stresses at a rake angle of –6° [25]

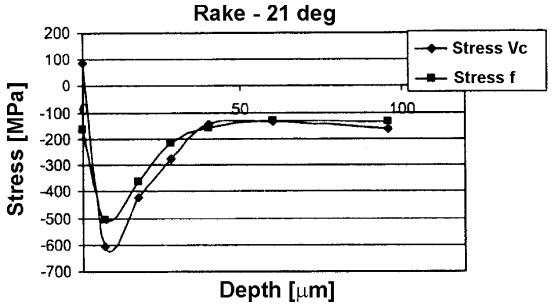

Figure 3.23. Residual stresses at a rake angle of –21° [25]

Rech and Moisan [26] presented surface integrity in finish hard turning of case-hardened steels. They investigated gear canebrakes in a hard turning process in mass production. Gear canebrakes are made of case-hardened 27 MnCr5 steel. The cementation process provides an 850 HV03 hardness on the surface and affects about 0.6 mm in depth, as shown in Figure 3.26.

The carbon composition of the case-hardened layer is nearly constant to the 0.3 mm regular depth. The carbon content in the layer is modified to 1% carbon.

The case hardening also modifies the residual stress profile, inducing compressive residual stresses. The removed depth of cut is 0.15 mm with turning operation before heat treatment. As one can observe the surface discovered by the hard turning operation should still have a 850 HV0.3 hardness and a tangential external residual stress of –400 MPa if the cutting process did not affect the machined surface.

Residual stresses profiles are presented in Figures 3.27 and 3.28.

Residual stresses are the results of three effects: mechanical, thermal, and metallurgical. In hard turning, these three effects are governed by properties of tool material and coatings, and their geometry including wear at various machining parameters. The changes in the physical properties of the workpiece surface due to hard turning have to be attributed to the cutting force and to the cutting temperature. In order to compare the changes caused by hard turning, it is essential to analyze the corresponding chip-formation mechanism. In the area around the tip of the cutting edge, the compressive stress levels must be very high. The high level of mechanical stress being exerted on the surface of the workpiece tends to induce compressive residual stresses.

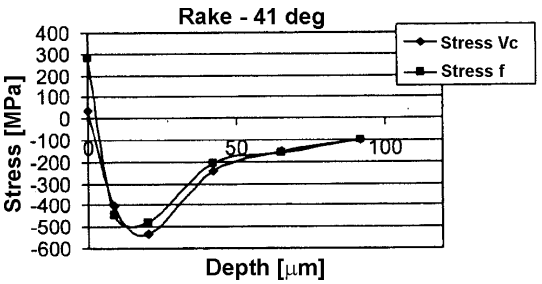

Figure 3.24. Residual stresses at a rake angle of –41° [25]

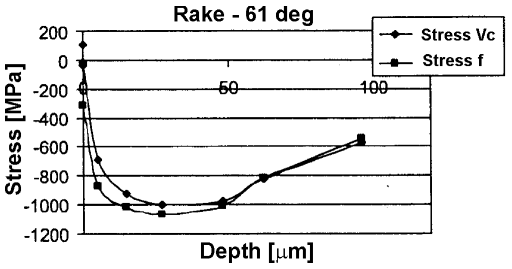

Figure 3.25. Residual stresses at a rake angle of –61° [25]

Thermal stresses result mainly from the friction between the wear land VB and the workpiece. The high direct stress levels cause high tangential stress that, in conjunction with the relative motion between cutting edge and workpiece, results in high levels of friction energy.

A typical residual stress profile in the tangential direction is shown in Figure 3.27(a). For a new insert and a cutting speed of 100 m/min, the surface residual

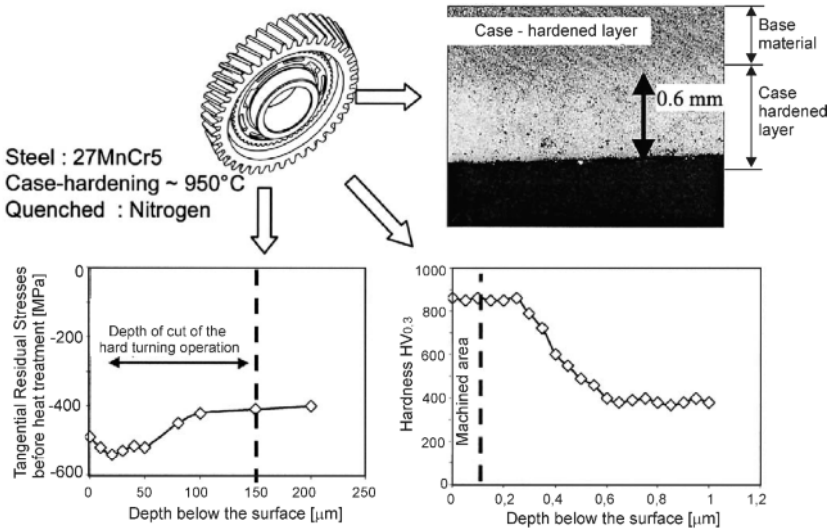

Figure 3.26. Properties of the machined surface after case hardening [26]

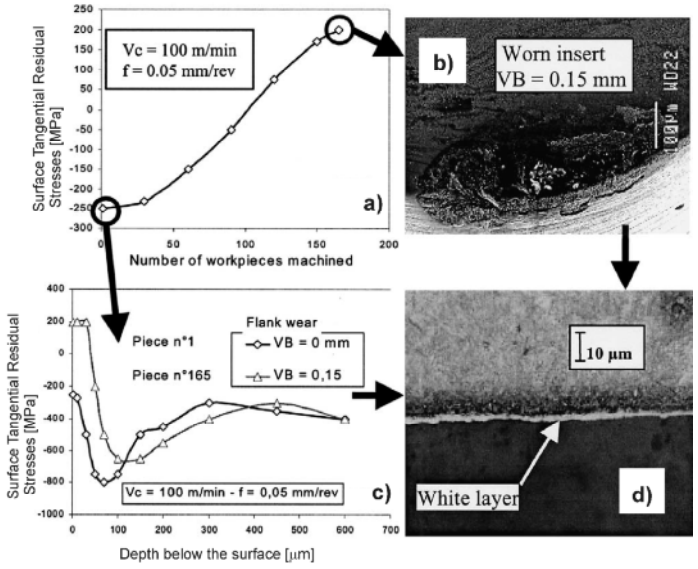

Figure 3.27. Influence of flank wear on the profile of residual stresses after hard turning [26]

stress is about −250 MPa. Beneath the surface the profile decreases to −800 MPa at 70 μm mm below the surface and then increases to the level of the bulk material (−400 MPa).

Figure 3.27(c) shows the influence of flank wear on the residual-stress profile. One can observe that the surface residual stress increases with flank wear and the maximum compressive residual stress shifts further below the surface.

Flank wear increases the level of friction energy and thus cutting temperatures. This indicates that a new cutting tool generates a compressive residual stress at the surface, whereas a worn tool tends to generate a tensile residual stress at the surface.

Figure 3.28(a) also shows the effect of feed rate on the residual stresses in the tangential direction. In the range of 0.05 to 0.1 mm/rev, the residual stresses near the surface shifted towards compression as feed rate was increased. On the other hand, in the range of 0.1 to 0.2 mm/rev, the residual stresses near the surface reduced the comparison stress with increasing feed rate towards tension. Figure 3.28(b) shows the evolution of the surface tangential residual stress as a function of the cutting speed for an uncoated CBN insert and for a TiN-coated CBN insert. TiN coating tends to decrease the surface residual stress between 150 and 350 MPa. The benefit of a coating is more important regarding the residual stress level for high cutting speeds. This improvement may be attributed to the good tribological behavior of TiN coating, which decreases the cutting friction energy and the mean cutting temperature at the tool chip interface.

Figure 3.29 shows the evolution of the surface tangential residual stress as a function of the cutting speed for different feed rates. One can observe that cutting speed tends to increase the surface residual stress, irrespective of the feed rate in the range of 50 to 150 m/min. On the other hand, the evolution of the curves changes above 200 m/min. It has to be noticed that the values of the residual stresses produced with cutting speeds of 200 and 250 m/min are not suitable for mass production.

Schwach *et al.* [27] presented surface integrity at hard turning on rolling contact fatigue. Hard turning normally produces favorable surface integrity that would improve component life in rolling contact.

Effects of the process-induced residual stress profile and the white layer on rolling contact fatigue (RCF) are poorly understood.

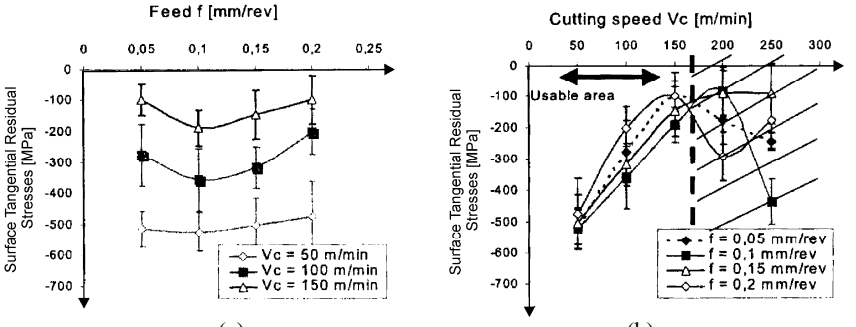

Figure 3.28. Influence of the cutting conditions on the residual stresses after hard turning at various cutting speeds (a) and feed rates (b) [26]

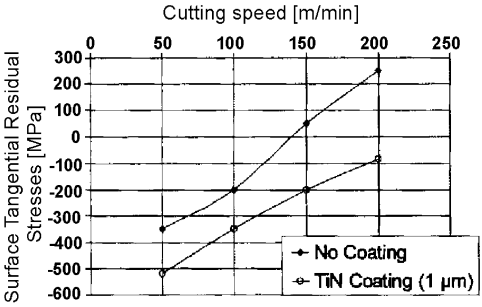

Figure 3.29. Influence of the TiN coating on surface residual stress after hard turning [26]

This study explains how residual stress and the white layer affect RCF. Based on the developed real-time RCF testing system, a series of RCF tests were conducted on hard-turned AISI 52100 steel specimens. A white layer induced by hard turning is very detrimental to RCF and reduce component life by six times. Residual-stress profiles are significant factors for RCF, while the depth of maximum compressive residual stress in the subsurface is not critical.

The flat-disc work specimens of AISI 52100 were heat treated to 61−62 HRc. Specimens were turned in a facing operation to maintain a constant cutting velocity as the cutting tool approached the center of the specimens. Four different machining conditions were used to produce distinct surface integrities; the same cutting tool (GE Super-abrasives BZN 8100 compact insert with a 0.015/15° chamfer and a radius of 6.35 mm) was used in all four machining conditions.

A novel design of a RCF testing system design was utilized in this experimental study. The test specimen is secured in a plate that rests upon a load cell and is positioned by four rods secured to the work table. Acoustic emission (AE) was used for fatigue monitoring and detection.

Figure 3.30 shows surface microstructure of the machined specimens. The specimens without white layers specimens (FS-1 and FS-2) show a uniform microstruc-

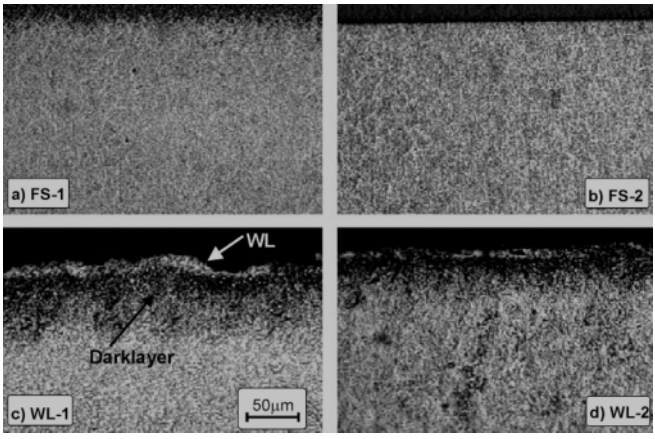

Figure 3.30. Surface microstructure of the machined specimens [27]

ture (Figures 3.30(a), (b)). While the white layer specimens (WL-1 and WL-2) in Figures 3.30(c) and (d), show a white surface layer with different thickness values (7.5 μm and 4.5 μm), followed by a dark layer and then the bulk material.

Figure 3.31 shows that the decrease in the feed will allow the surface residual stress to shift towards compression −21 μm. The first shows that the feed decrease from 0.5 mm/rev to 0.1 mm/rev causes the surface residual stress to go from approximately 230 MPa to −80 MPa. Similar trends can be found for the case of the feed shift from 0.08 mm/rev to 0.02 mm/rev. This means that the decrease in feed for this experiment may have significantly reduced the surface residual stress towards or into compression, giving a large difference in fatigue life.

Klocke and Liermann [28] presented axial and tangential residual-stress profiles after roller burnishing of hard turned surfaces. In a hard roller burnishing operation, a hydrostatically borne ceramic ball rolls over the specimen surface under high pressures. When combined with hard turning, this process provides a manufacturing alternative to grinding and honing operations.

The studies determined optimum working parameter ranges. Microstructure analyses and residual stress measurements were used to examine the effects of the process on the specimen surface. Hard roller burnishing transforms tensile residual stresses present in the surface layer after hard turning into compressive residual stresses. Hard roller burnishing has no effect on the formation of white layers in the surface.

Apart from its influence on surface microstructure, the effects of hard roller burnishing on the properties of the specimen surface layer are of interest. The effects of hard roller burnishing were examined for various original states of the material, using specimens that had been hard turned using cutting edges with various degrees of wear. The rolling pressure was also varied in the studies. The remaining rolling parameters were kept constant.

The mechanical stresses exerted on the specimen surface layer during hard roller burnishing lead to sustained modification of the residual stress profiles. Figure 3.32 shows tangential and axial residual stresses before and after hard roller burnishing for a new tool VB = 0 and worn out tool VB = 120 μm.

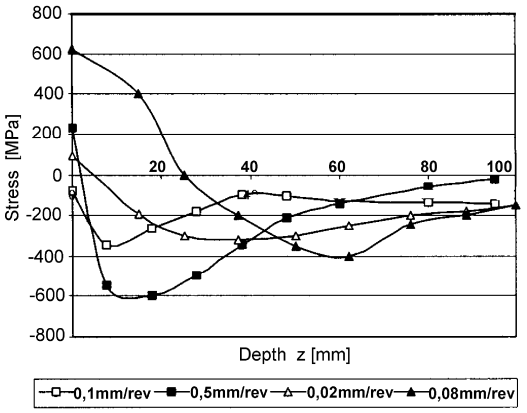

Figure 3.31. Effect of feed on residual stress [27]

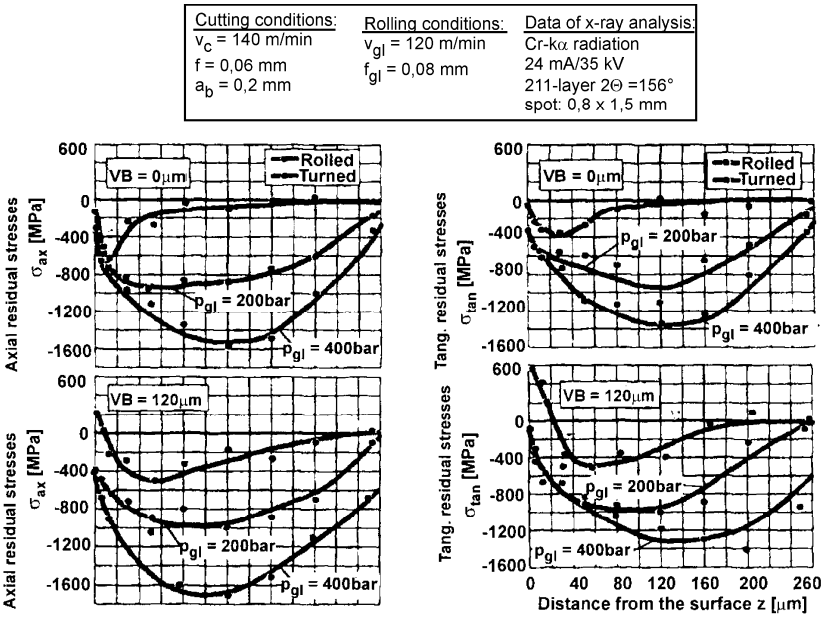

Figure 3.32. Residual stress profiles for a new tool and worn tool [28]

Residual-stress profiles after hard turning exhibit the familiar depth curves, dependent on the wear degree of the cutting edge. After hard roller burnishing, compressive residual stresses occur in the surface layer. Their curves are dependent on the rolling pressure and hence on the Hertzian stress during the roller burnishing operation. Residual stresses as high as −1600 MPa are measured at a depth 100 μm with a rolling pressure of 400 bar.

On the specimen surface influence of the preceding hard-turning operation a flank wear VB = 120 μm is used. The influence of rolling pressure on the residual stress profile is visible only from a depth of about 10 μm onwards, in accordance with the position of the comparative stress maximum due to Hertzian stress. The same residual stresses at the workpiece surface are found for both rolling pressures.

Grzesik *et al.* [29] presented the surface integrity of hardened steel parts in hybrid machining operations. The focus of their research was surface integrity generated in hard turning and subsequent finish abrasive machining. Insufficient magnitude of compressive residual stresses after hard turning determines the fatigue resistance of highly loaded transmission parts.

CBN turning was carried out on an ultraprecision facing lathe. The cutting edges of each tip were prepared to produce a chamfer with 0.1 mm width, −20° inclination angle, and the honing radius of 0.05 mm. Cutting parameters used were: cutting speed $v_c = 100$ m/min, feed rate $f = 0.1$ mm/rev, and depth of cut $a_p = 0.3$ mm. For comparison, hard turning operations (HT2) with mixed ceramic (Sandvik's CC650 grade) tools were carried out on a precision conventional lathe. In this case, cutting speed $v_c = 115$ m/min, feed rate $f = 0.1$ mm/rev, and depth of cut $a_p = 0.3$ mm.

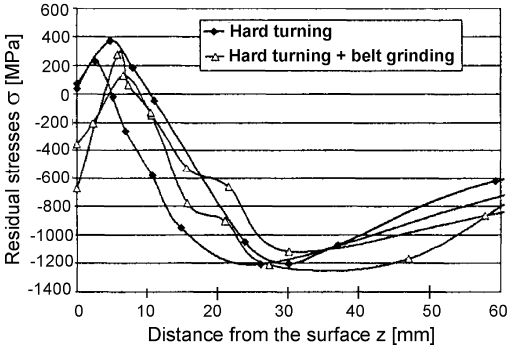

Figure 3.33. Residual-stress profiles below the surface obtained after CBN hard turning and hard turning followed by belt grinding operations [29]

Figure 3.33 presents tangential residual-stress profiles σ_{11} generated by CBN hard turning and hard turning followed by belt grinding operations. Hard turning followed by belt grinding gives higher compressive residual stresses at the surface, approximately 400–700 MPa.

Guo and Sahni [30] presented a comparative study of hard turned and cylindrically ground samples regarding white layer occurrence. Hard turning applications are not preferred, due to the existence of the process-induced white layer on the workpiece surface, which is often assumed to be detrimental to operation life.

The experiment was carried out on AISI 52100 in cold finished, spheroidized and annealed with Brinell hardness 183, cut into two groups 10 turning and 10 grinding specimens. Before heat treatment to the required hardness, the grinding specimens were gently ground to make the specimens thickness uniform. This step is essential to ensure generation of a uniform white layer in ground specimens.

Figure 3.34 shows the surface structure of the hard turned specimen under hard turning conditions; A 14.1-μm thick white layer, then a 34.4-μm dark layer, followed by the bulk material appears in the cross-section.

The transition zones between the white/dark layers and the dark layer/bulk material are also noticeable.

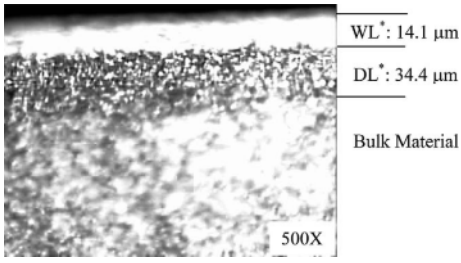

Figure 3.34. Surface structure of the hard turned specimens ($v = 2.82$ m/s, $f = 1.66$ mm/s, $a = 0.2$ mm, VB: 0.6 mm, WL: white layer, DL: dark layer) [30]

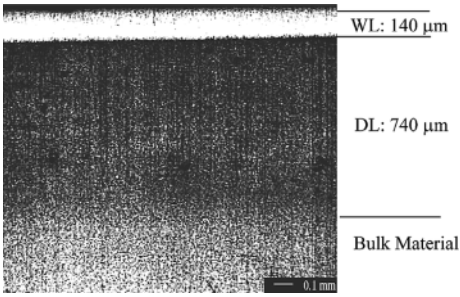

Figure 3.35. Surface structure of the ground samples ($v = 28.26$ m/s, $f = 8.33$ mm/s, $a = 0.13$ mm, worn grinding wheel) [30]

Table 3.4. Volume fractions for retained austenite in white and dark layers, bulk material, and untempered martensite [30]

Category	**Hard turning (%)**	**Grinding (%)**
White layer	10.64	2.88
Dark layer	11.68	0
Bulk material	3.44	–
Untempered martensite	4.0	–

A similar surface structure of the ground specimens samples, i.e., white layer, dark layer, followed by bulk material, also appears in Figure 3.35. It was found that the white layer thickness in grinding condition A is 21% larger than that in condition B.

Hashimoto *et al.* [31] studied the surface integrity of hard turned and ground surfaces and their impact on fatigue life. The test specimens were machined heat treated on AISI 52100 steel. Heat treatment consisted of austenitizing at a temperature of 815°C for 2 h, followed by quenching in an oil bath at 65°C for 15 min. Finally, tempering was conducted at 176°C for 2 h, which produced a final hardness of 61–62 HRC.

The basic mechanism for the more hardened ground surface layer is most likely due to the size effect induced by the severe strain gradient in grinding. The smaller down feed in grinding induces a severe strain gradient in the near surface, while the relatively larger depth of cut in turning may substantially reduce the size effect.

To evaluate the variation of fatigue life, three specimens of each surface type were tested. The average rolling contact fatigue (RCF) life tests and deviations are shown in Figure 3.36. It shows that the turned and polished surfaces have an average life 315.8 (±21.3) million cycles. It demonstrates that a superfinished turned surface may have more than 100% fatigue life than a ground one with an equivalent surface finish. The fundamental mechanisms that contribute to the fatigue difference between hard turning and grinding are the distinct surface microstructure and the material properties.

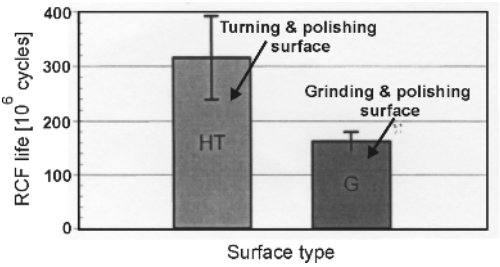

Figure 3.36. Life comparison of turned vs. ground specimens [31]

Abrão *et al.* [32] studied the surface integrity of turned and ground hardened bearing steel. They discussed several aspects of finish turning against grinding of hardened bearing steel, more specifically surface texture, microstructural alterations, changes in microhardness, residual stresses distribution and fatigue life. They found that for the operating parameters tested the microstructural alterations observed were confined to an untempered martensitic layer often followed by an overtempered martensitic layer. Compressive residual stresses were induced when turning using PCBN cutting tools followed by turning using mixed alumina tools and finally grinding with the best fatigue resistance.

Cylindrical grinding was performed on a universal grinding machine using the following parameters: wheel speed of 23 m s^{-1}, work speed of 8 m min^{-1}, infeed of 0.25 mm $pass^{-1}$ and transverse of 0.13 mm rev^{-1} using a Consort alumina wheel grade DA 60-LV1 and water-soluble oil coolant.

Figure 3.37 shows residual-stress profiles measured after turning with new and worn cutting tool average flank wear $VB_{13} = 0.27$ mm after grinding. The results indicate that compressive residual stresses were induced in each specimen. When turning with new cutting tools the intensity and depth of the compressive stress was much shallower (20–40 μm) than when using worn tools. With the turned specimens the highest stress value was obtained at approximately 5–20 μm below the machined surface. In contrast, the highest stress value given by the ground specimen was measured on the workpiece surface.

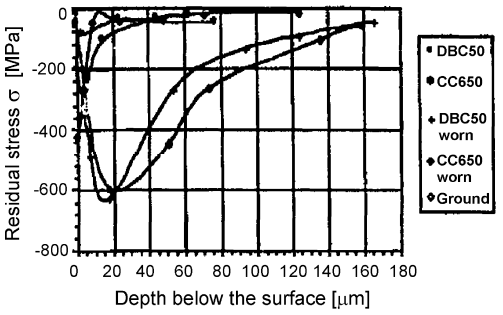

Figure 3.37. Residual-stress distribution after finish turning and grinding hardened bearing steel [32]

Figure 3.38 shows the fatigue life in the S–N curves. For the same applied load, a longer fatigue life was obtained on specimens turned with PCBN tools, although for a stress range of approximately 900 MPa, a run-out was obtained for both cutting tool materials. The shadowed area details the bounds of the results for the ground specimens that were not as consistent, however, the fatigue life was similar to that obtained with the specimens turned with CC650.

García Navas *et al.* [33] presented electrodischarge machining (EDM) versus hard turning and grinding with emphasis on comparison of residual stresses and surface integrity in AISI 01 tool steel. Electrodischarge machining (EDM) appears as an alternative to grinding and hard turning for the machining of tool steels because EDM allows the machining of any type of conducting material, regardless of its hardness.

Nevertheless, other factors must be taken into account in the selection of machining processes, especially in the case of crucial parts. These factors are related with surface integrity: residual stresses, hardness and structural changes generated by the machining processes. Production grinding generates compressive stresses at the surface, and a slight tensile peak, accompanied by a decrease in hardness beneath it. No microstructural changes are noticeable. Hard turning generates slight tensile stresses in the surface, accompanied by an increase in hardness and in the amount of retained austenite. Below the surface, residual stresses in compression are obtained as well as a decrease in hardness and in the volume fraction of retained austenite. Wire electrodischarge machining (WEDM) generates tensile residual stresses at the surface layer accompanied by the formation of a superficial "white layer" where there is a noticeable increase of the volume fraction of retained austenite and of the hardness. Consequently, among the three machining processes studied, WEDM is the most detrimental to surface integrity and, consequently, to the service life of the machined parts, because it promotes crack formation and propagation.

Figure 3.39 shows residual-stress profiles generated by each machining process. The depth profiles of the non-null components of the stress tensor (the two normal components (σ_{11} and σ_{22}) and the shear components σ_{12}) are represented in each graph.

Both WEDM processes generate tensile residual stresses at the surface that increase up to a maximum tensile peak at 20 to 30 μm below the surface, before tend-

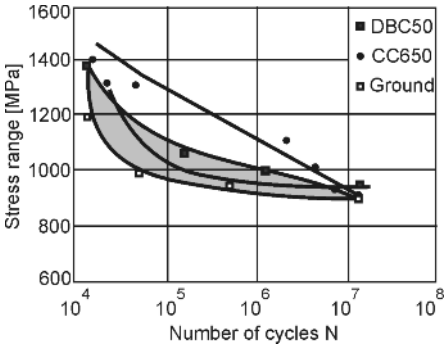

Figure 3.38. Fatigue life of finish turned and ground hardened bearing steel [32]

ing to a null value in the bulk material. The stress distribution on Figures 3.39(a) and (b) is not favorable, because tensile stresses are detrimental to the service life of the machined part as they promote crack formation and propagation by fatigue or other corrosion cracking. Comparing Figures 3.39(a) and (b), it is clear that WED-roughing the tensile stress state extends to about 80 μm, whereas after WED-finishing it extends to about 50–60 μm. Nevertheless, even the stress state generated by this finishing WED machining is more detrimental to the service life of the machined part than those generated by hard turning or grinding.

Production grinding (Figure 3.39(c)) generates compressive stresses at the surface but leads to a slight tensile peak just beneath it. This implies that the predominant factor is deformation, which leads to compressive stresses, but thermal effects also take part and lead to the formation of a tensile peak in the subsurface.

On the contrary, hard turning (Figure 3.39(d)) generates tensile stresses at the surface that tend to a minimum compressive peak beneath the surface, prior to tending to a null state in the bulk material. At hard turning the tool-part pressure is an important factor because it generates compressive stresses, but the friction between tool and piece generates high temperatures that lead to tensile stresses in the surface of the machined part. The least detrimental stress state in the surface is that obtained after production grinding, whereas below the surface it is preferable to the stress state generated by hard tuning. The featureless layer that is observed in the surface of the WEDM is often named a "white layer". This layer is due to the melting and rapid re-solidification of the metal during the EDM process. Oxidation is not excluded. In hard turning processes, a surface "white layer" can also be observed, particularly with worn tools. The hardness and volume fraction of retained

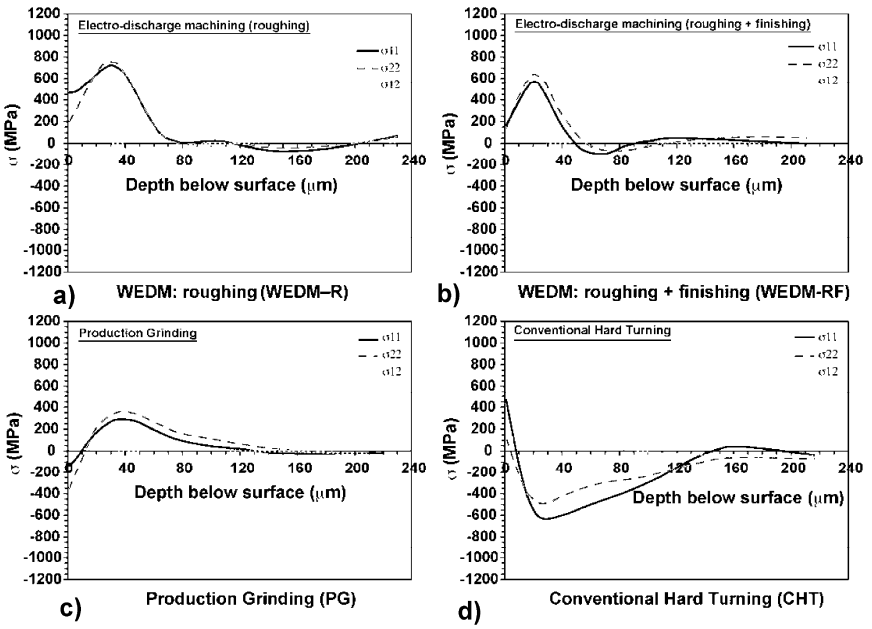

Figure 3.39. Residual-stress profiles for various machining processes [33]

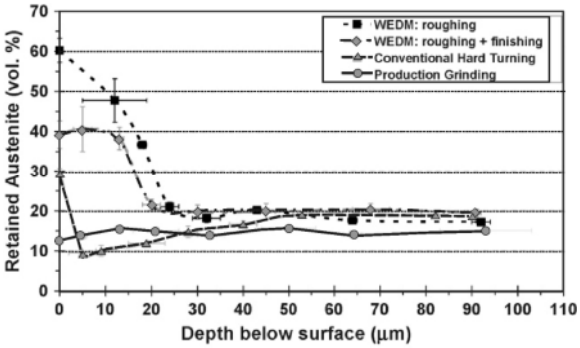

Figure 3.40. Retained austenite vs. depth below the surface [33]

austenite increases in the "white layers". Volume fractions of retained austenite were measured in specimens similar to those used for residual stress measurements. Figure 3.40 shows retained austenite depth profiles, obtained after removing layers of material by electrolytic polishing. The results obtained show that after grinding the volume fraction of retained austenite near the surface remains practically the same as the bulk non-machined specimen.

On the contrary, in the surface of the hard turned sample there is a significant increment in the volume fraction of retained austenite, which reaches a minimum just below the surface and afterwards tends to a stationary value in the bulk material.

3.4 Modeling of Turning and Hard Turning of Workpiece Materials

Chou and Evans [34] discussed white layers and thermal modeling of hard turned surfaces. White layers in hard turned surface are characterized as a function of tool flank wear at a chosen cutting speed. The white layer depth progressively increases with flank wear. It also increases with speed, but approaches an asymptote. A thermal model based on a moving heat source is applied to simulate the temperature field in machined surface and to estimate white layer depth. The analysis shows good agreement with the trend in experimental results. White layer formation seems to be dominantly a thermal process involving phase transformation of the steel and possibly plastic strain activated at machining material.

Flank wear and cutting speed effects on white layer depth are summarized in Figure 3.41. Error bars represent maximum and minimum values of three tests measurements of white layer depth. In general, white layer depth increases with increasing tool wear. White layer depth also increases with cutting speed, but the slope decreases with speed. This trend agrees with the theoretical analysis. In the largest flank wear case (VB = 300 μm), white layer depth decreases as speed increases from 3 to 4.5 m/s.

To further confirm the effect of cutting speed on white layer formation in a wide speed range with a large flank wear VB 300 μm), a workpice was machined ac-

cording to heat-treatment details (Set 2) with the same cutting conditions as the first set of experiments. Cutting speed ranged from 0.75 m/s to 7.5 m/s and three test measurements were carried out. The result shown in Figure 3.42 clearly indicates that white layer depth increases with cutting speed then approaches in the same trend as in the theoretical analysis. Variations between two sets of test measurements are due to different sources of workpieces.

Nasr *et al.* [35] presented modeling of the effect of tool-edge radius on residual stresses when orthogonal cutting AISI 316L. Tool-edge geometry has significant effects on turning process and surface integrity, especially on residual stresses and deformation zone. An arbitrary Lagrangian–Eulerian (ALE) finite-element model is presented to simulate the influence of four tool radii on residual stresses at orthogonal dry cutting austenitic stainless steel AISI 316L. Residual-stress profiles started with surface tensile stresses then turned, to be compressive

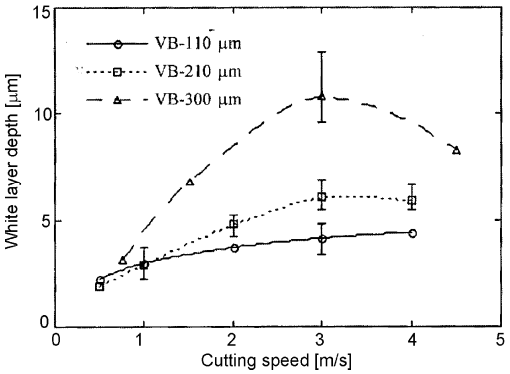

Figure 3.41. Measured white layer depth as a function of cutting speed for various flank wear values [34]

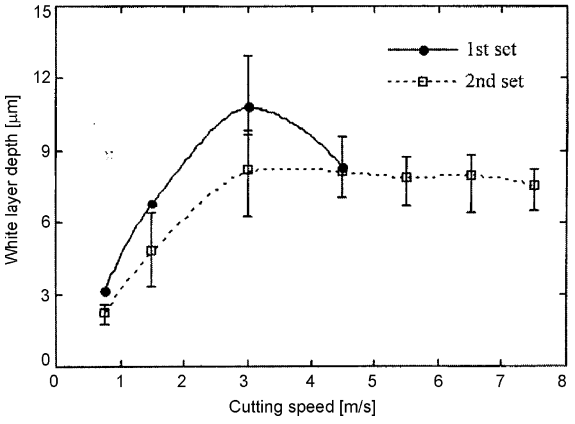

Figure 3.42. Cutting speed effect on white layer depth for different heat treatment of workpice (Set 1 and Set 2) [34]

with cementation aid the same trend was found experimentally. Large edge radius induced higher residual stress profiles, while it had almost no effect on the depth of tensile layer and pushed the maximum compressive stresses deeper into the workpiece.

Figure 3.43 shows the residual-stress profiles parallel to the cutting direction (RS11) for the simulated sharp tool (R20) and the corresponding experimental profile obtained by M'Saoubi *et al.* [36]. The figure presents a measured residual-stress profile using the X-ray diffraction method for the experimental profile and residual stresses calculated from the residual stress model.

Although both curves do not match exactly, which was expected *a priori*, the FE model correctly estimated the in-depth residual stress profile showing the same trend and starting with almost the same surface value as the experimental one. An exact match between FE and experimental results could not be expected because of the different sources of errors in each of them. The main sources of errors encountered in FE modeling could be summarized as: material modeling, numerical integration and interpolation, assumed friction condition, and re-meshing errors. Furthermore, simulations were run with the same tool, radius, while practically the tool edge may wear out or break down during cutting. The main sources of errors in experimental results are those encountered in residual-stress measurements, especially the etched depth. The workpiece material is not totally homogeneous, therefore it was considered to be a pure homogeneous material in the FE model. The predicted residual-stress profile had higher tensile and compressive magnitudes than the experimental profile. It is important to note that both profiles (FE and experimental) show a state of equilibrium between tensile and compressive residual stress

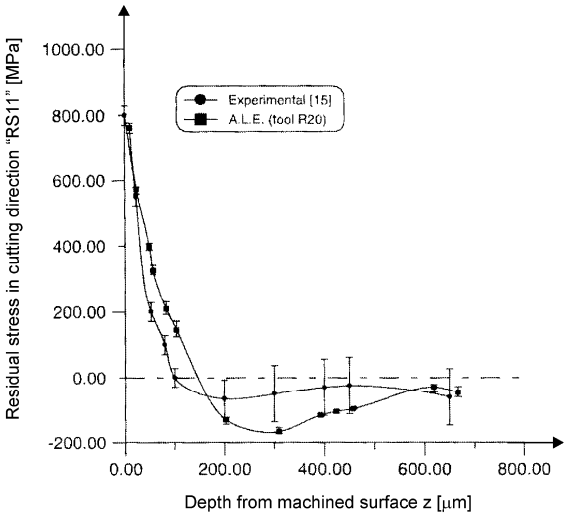

Figure 3.43. FE and experimental RS11 profiles for sharp tool [35]

Rech *et al.* [37] worked on characterization and modeling of the residual stresses induced by belt finishing on a AISI52100. A new technological process consisting of hard turning (HT) followed by abrasive machining, in place of the widely used method in industry, e.g., hard turning versus grinding has lately been launched in the automotive industry. Many transmission parts, such as synchronizing gears, crankshafts and camshafts require superior surface finish along with appropriate fatigue performance. A comprehensive characterization of part residual stresses produced in dry turning of a hardened AISI52100 bearing steel using PCBN tools, and also its modification after a special abrasive finishing operation such as belt finishing. The residual stresses generated in hard turning or in hard turning + belt finishing are investigated by two complementary means: an experimental X-ray diffraction characterization after each step of the process, and a finite-element model of the belt-finishing operation in order to understand better experimental results. The belt-finishing process improves significantly the surface integrity by the induction of strong compressive residual stresses in the external layer and by a great improvement of the surface roughness. In this study the biaxial residual stress with tangential (σ11) and axial (σ22) components was measured using the X-ray diffraction method, consisting in the determination of the variations in peak positions due to distortions of the crystalline lattice.

Figure 3.44 shows profiles of the tangential and axial stress components measured by X-ray diffractometry after hard turning and after hard turning + belt finishing. For each direction, two pieces have been produced with the same cutting conditions. It is necessary to keep in mind that the precision of the measurements has been quantified: ±60 MPa.

The two curves corresponding to the two pieces produced with the same conditions reveal that the deviation of residual-stress state is rather high. The shapes of the curves are similar for both pieces and both directions of measurements. Hard turning induces tensile stresses in the external layer and as a consequence, there is a peak of compression in the sublayer.

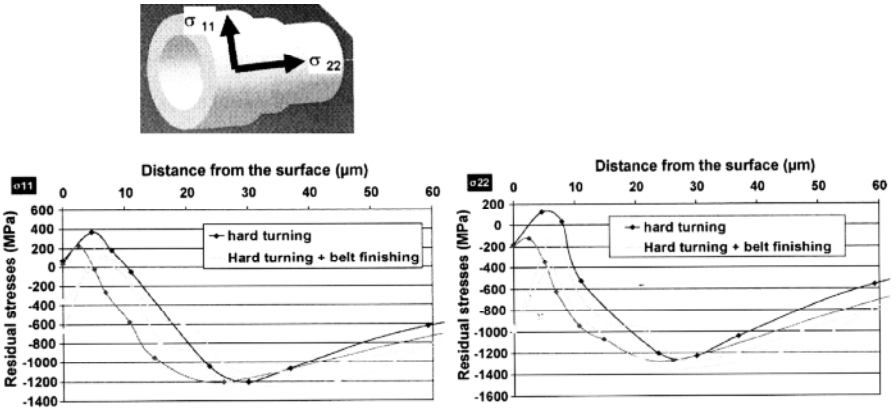

Figure 3.44. Residual stress profiles below the surface obtained after c-BN hard turning and belt-finishing operations [37]

3.5 Residual Stresses After Milling

Segawa *et al.* [38] worked on development of a new tool to generate compressive residual stress within a machined surface with the milling process. The diameter of the tool is 6 mm, and the tool body is made of high-speed steel. The cutting edges of the tool remove extra material and the projection pin compresses the machined surface to make plastic deformation simultaneously with the milling process. Figure 3.45 shows the schematic view of the machining process using the compressive residual-stress-generating cutter CCRSG.

They used a plate of rolled aluminum alloy 7075-T651, which had been heat treated. The size of the specimen was 6 mm × 90 mm × 150 mm. In this finishing process preparing for the test, a face mill of 85 mm diameter with four carbide inserts was used. The milling conditions were: spindle speed of 2200 min^{-1}, feed speed of 298 mm/min, and axial depth of cut of 0.1–0.2 mm. In the final process the axial depth of cut was decreased to 0.02–0.03 mm. Due to the care taken in the preparation of the test workpiece, the effects of this premachining process were considered negligible.

The residual stress on the specimen surface was measured using the X-ray diffraction method. The measured value range was −8 to 100 MPa.

Figure 3.46 shows residual-stress profiles below the depth of the machining surface with the CRSG cutter. On the machined surface, the residual stresses in dry and in all cutting fluid conditions were −100 and −200 MPa. It can be seen that the compressive residual stress below the surface is higher than on the surface. Clearly, the compressive residual stress of the machined surface in these conditions is higher than that in oil cutting conditions.

The peak of the compressive residual stress is observed at a depth of 0.05 mm from the surface. The peak value was observed at −400 and −350 MPa. In dry and in oil conditions, respectively. At a depth of 0.05 mm below a depth of 0.5 mm from the surface. Compressive residual stress improves the fatigue strength and resistance to stress-corrosion cracking. The highest value of compressive residual stress was generated below the surface. The fatigue life of the machined compo-

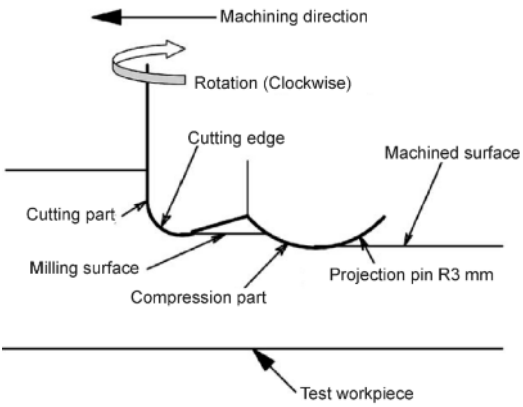

Figure 3.45. Schematic view of the machining state using the CCRSG cutter [38]

nent with this tool would be extended regarding residual stress fields.

Li *et al.* [39] carried out an FEM study on residual stresses induced by high-speed end milling of hardened steel SKD11. Milling of hardened steel SKD11 is usually a finishing process, therefore a stable cutting process must be guaranteed first. Residual stresses were studied in this paper with a finite-element method (FEM) for its significant influence on the quality of machined part. A two-dimension (2D) fully thermomechanical coupled finite-element (FE) model was employed to evaluate residual stress in a machined component. The same cutting tools were employed to model continuous feed milling process. Residual-stress profiles were obtained after end-milling and stress-relaxation stages. The predicted residual-stress profiles corresponded to experimental results.

Hardened steel SKD11 has wide applications in the mold and die industry. It is also a difficult-to-cut material due to its high strength and hardness that varies from 60 to 62 HRC. With the development of cutting tools, hard milling is becoming a feasible approach to traditional grinding and electron discharge machining (EDM) for its high machining efficiency. However, hard milling is often used as a finishing process, a stable cutting process should be guaranteed to obtain satisfied machining precision. Residual stresses existing in a machined product have a major influence on the quality of the machined part, in particular, its fatigue life and corrosion resistance. Predicting the distribution of residual stress induced by cutting process is very important.

As evidence of the ability of the simulation procedure to model residual stress, a comparison was carried out between FEM predictions and experimental measurements. Predicted residual-stress profiles were obtained until the workpiece was unloaded and left to cool down to room temperature. Figure 3.47 shows the comparison of the two residual stress between FEM and experiment. Although both of the curves do not match exactly, the FE model correctly estimates the in-depth RS profiles showing the same trend and starting with almost the same surface value as the experimental one.

In general, an exact match between FEM and experimental results could not be expected because of the different sources of errors in each of them. The main source of errors encountered in FEM modeling could be summarized as follows

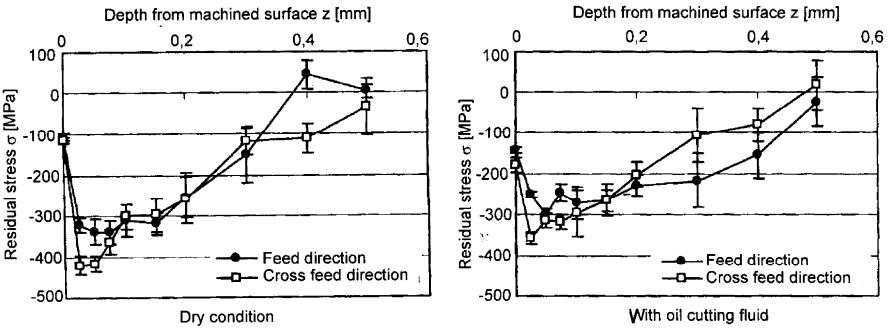

Figure 3.46. Residual stress profiles measured from the machined surface: (a) dry condition; and (b) with oil cutting fluid [38]

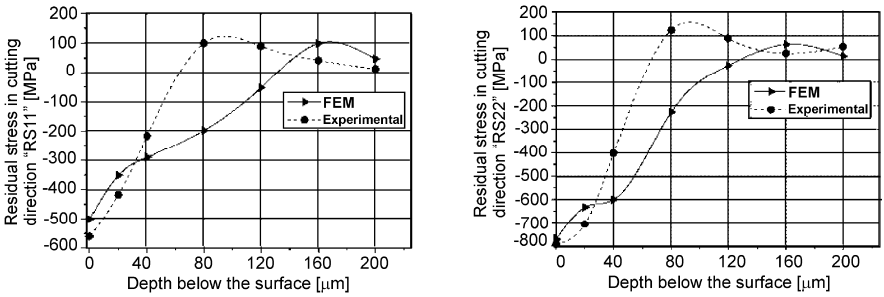

(a) (b)

Figure 3.47. Comparison of residual stress profile between FEM and experimental: (a) RS11, and (b) RS22 [39]

material modeling, numerical integration and interpolation, assumed friction condition. Furthermore, simulation runs with a constant tool edge radius, while practically the tool edge may wear out or break down during cutting. On the other hand, the main sources of errors in experimental results are those encountered in residual-stress measurement, especially in measuring the etched depth. Besides, the actual workpiece material is not homogeneous, while it is considered to be a pure homogenous material in the FEM simulation. However, it is important to notice that both FEM and experiments of the profiles show a state of equilibrium between tensile and compressive residual stress, as it should be.

3.6 Residual Stresses and Microstructures at the Surface After Grinding

Brinksmeier [40] presented the influence of process parameters quantities in grinding on residual stresses. The properties of the surface layer after different machining processes and conditions are a result of physical and chemical actions and do also belong to the properties of the workpiece. Figure 3.48 represents classification of a surface in surface layer properties after machining.

Residual machining stresses follow from the mechanical and thermal actions in the contact zone between tool and workpiece. The sources for these actions are in general the same for metal cutting and grinding (Figure 3.49).

Figure 3.50 shows the dependence between the residual stresses below the surface and the specific grinding power in surface grinding with an alumina grinding wheel. An increase of power will shift the residual stresses towards tension because a higher amount of heat has been produced in the contact zone. This results in an increase of thermal workpiece loading and thus in higher tensile stresses. It is remarkable that the results for different grinding conditions are fitting into one transfer function. This leads to the conclusion that the conditions for heat dissipation were independent of the grinding conditions.

A change in heat dissipation will happen if the process and the specification of the grinding wheel and coolant are changed.

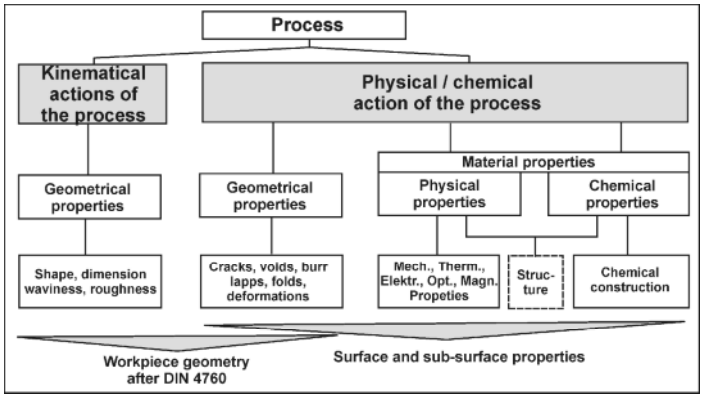

Figure 3.48 Classification of surface and surface layer properties [40]

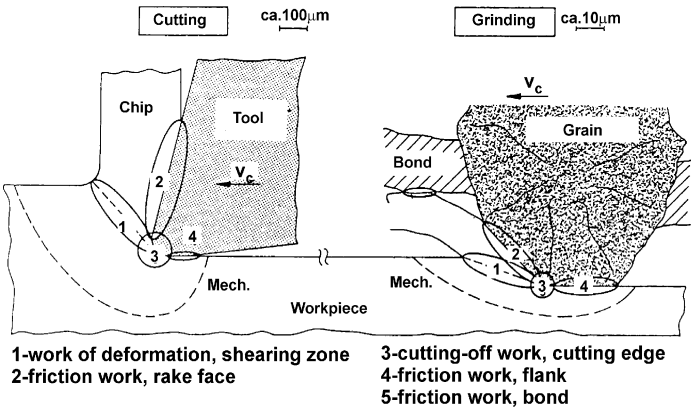

Figure 3.49. Sources of mechanical and thermal actions in turning and grinding [40]

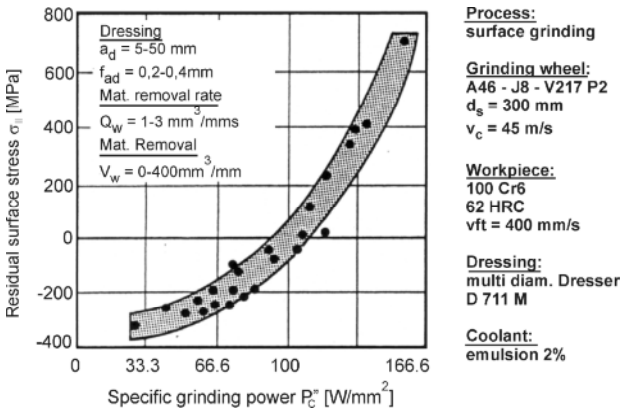

Figure 3.50. Residual stresses and specific grinding power [40]

It is interesting to see that these thermal-transfer functions are similar in their shape although the quantitative correlations may be different. In addition, it is obvious that grinding wheels with cubic boron nitride (CBN) abrasives lead to a more favorable state of residual stress, even at high amounts of grinding power. This is due to the higher heat conductivity of the CBN abrasive, compared to Al_2O_3. Thus, this physical property improves the conditions for heat dissipation in CBN grinding.

For flat grinding Brinksmeier [40] introduced a model for determining the direction and size of residual stresses after grinding due to the interaction between the mechanical and thermal state of the material. Figure 3.51 indicates the creation of residual stress in the case of a ground surface, with prevailing mechanical causes, as shown on the left side of the figure and prevailing thermal causes on the right side. The depth effect of each source of the residual stress depends widely upon the cutting conditions and frictional conditions between grinding wheel and workpiece material. The temperature distribution at various depths reveals that the maximum temperature on the surface ceases just before the end of the contact length.

Figure 3.52 shows the results of measurements made on the influence of the specific metal removal rate on the normal and tangential grinding forces during

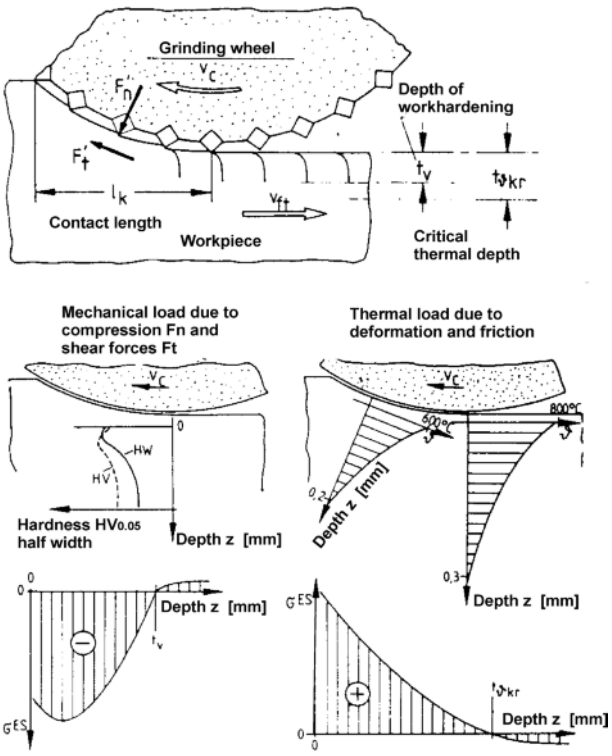

Figure 3.51. Residual-stress development during grinding due to mechanical and thermal loading in the surface layer [40]

grinding with corundum and cubic boron nitride (CBN) and the then created surface residual stresses, which were measured by X-rays. With roughly the same surface properties, the tangential forces for both types of grinding wheels are almost double in the case of the corundum as compared with those of the CBN.

On the other hand, surfaces of workpieces ground with Al_2O_3 only produced compressive residual stresses at lower specific rate of metal removal and then changed over to tensile residual stresses, whilst those surfaces ground with CBN produced only compressive residual stresses.

The different forms of residual stress are partly caused by the thermal energy introduced by the tangential forces and partly by the escaping of a greater part of the thermal energy through the grinding wheel due to the high thermal conductivity of the CBN grinding material.

Interactions between the mechanical, thermal and metallurgical state of the material. The increasing application of high-speed machining processes requires close investigation into mutual mechanical, thermal and metallurgical interactions in order to prevent crack initiation by grinding or the negative influence of tensile residual stresses on the fatigue strength of components. During grinding with extremely high speeds, the thermal portion of the frictional energy can become so high that a martensite transformation may take place, either through self-quenching or through coolants.

Figure 3.53 shows the distribution of the tangential residual-stress profile of a hardened rolling bearing from the material 100 CrMn6 after a grinding. Due to the high grinding temperatures, tensile residual stresses were released below the depth of 50 µm, which were almost completely reduced from the outer surface region as a result of a re-hardening zone.

Sosa *et al.* [41] also studied residual stresses. As opposed to the clear tendencies observed for distortion surface stresses do not show well-defined tendencies in relation to nodule counts and depth grinding conditions as shown in Figures 3.54(a) and (b).

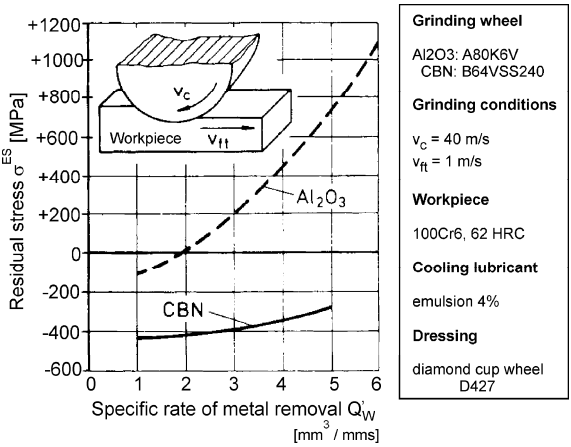

Figure 3.52. Effect of the grinding wheel material on grinding forces and residual stresses in the workpiece [40]

Figure 3.55 shows the profiles of in-depth residual stresses for all nodule counts at different grinding conditions. Tensile stresses are maximum in the surface, decrease in the subsurface layers, and become compressive at greater depths at 0,12–0,16 mm. The arithmetic mean stress δ_m in the tensile zone, calculated for each stress profile, for the highest nodule counts being coherent with the greatest distortion observed. This is in agreement with the verified correspondence between residual stresses and distortion, caused by materials machining. Therefore, in this study, it is consistent to adopt the mean stress δ_m as a correlation parameter between residual stresses and distortion. The influence of nodule count on stress δ_m can be analyzed taking into consideration the well-known thermal and mechanical phenomena that generate residual stresses during grinding.

On the one hand, it could be supposed that tensile residual stresses resulting from thermal effects during grinding are similar to all nodule counts.

Plastic deformation and the resulting compressive residual stresses produced by grinding change with nodule count and modifies the mechanical properties.

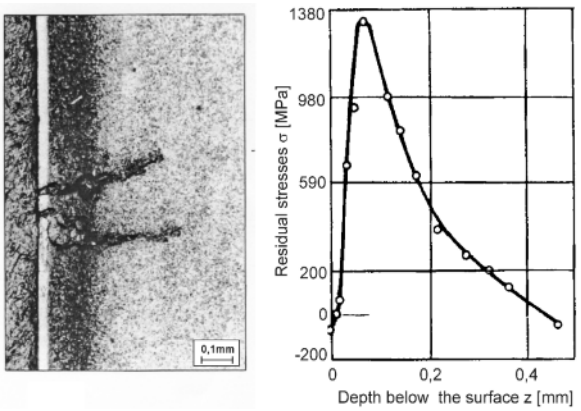

Figure 3.53. Re-hardened zone and residual-stress distribution in the hardened and ground bearing ring (material 100 CrMn 6) [40]

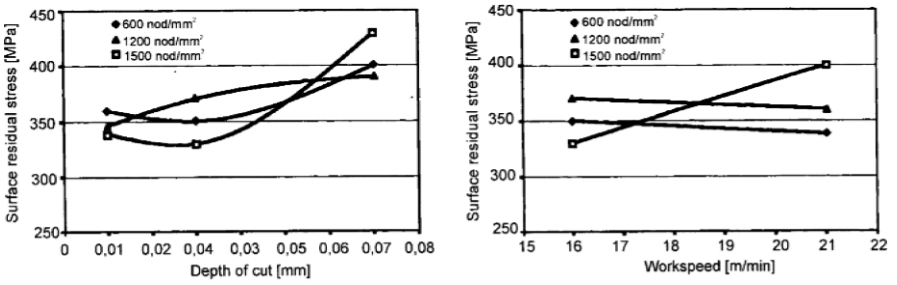

(a) (b)

Figure 3.54. Surface residual stress for different nodule counts as a function of: (a) depth of cut (v_w = 16 m/min) and (b) (a_p = 0.03 mm; constant v_s = 20 m/s) [41]

The fact that residual grinding stresses were tensile for all nodule counts, emphasizes the prevalence of thermal over mechanical effects. The greater mean stress of the highest nodule count specimens can be attributed to a lower plastic deformation during grinding, due to its greater hardness.

Grum and Ferlan [42] presented analysis of residual stresses in 42CrMo4 heat-treatable steel after induction surface hardening. The residual stresses on the main crankshaft bearings were measured on the bearing location in the middle (A), on the extreme left side (C) and on the extreme right side (G) (Figure 3.56).

Crankshafts were taken from production after induction hardening with the heat-treatment and machining conditions as specified in the technology sheet. For the bearing locations A and C two specimens were taken, i.e., one on the left side of the bearing location (A1, A2) and one on the right side (C1, C2). The bearing location G was tested by only one specimen having a double width.

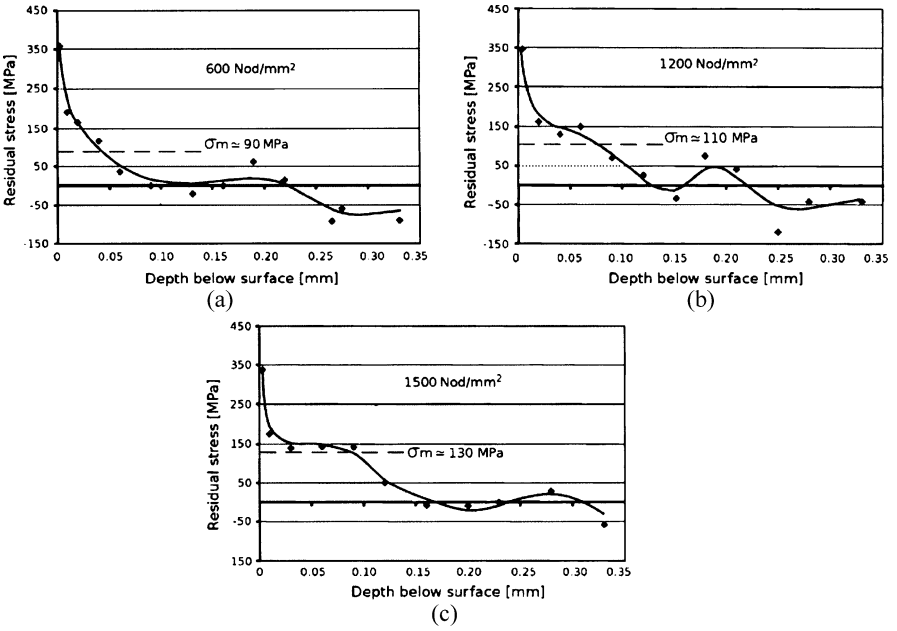

Figure 3.55. Residual-stress depth profile for each nodule count [41]

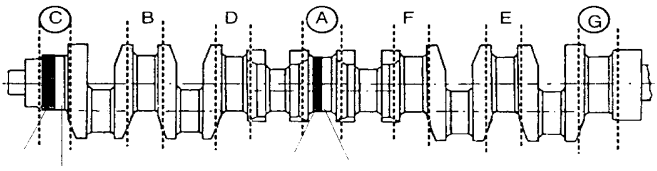

Figure 3.56. Analysis of the main crankshaft bearing after induction hardening [42]

Figure 3.57 shows the residual-stress distribution after induction hardening in the central bearing location (A). For this location residual stresses were measured on two specimens. The distribution of residual stresses on this place is, as expected, very similar on both specimens, the highest compressive stress ranging between 1020 to 1060 N/mm^2 in the depth around 250 μm and then slowly dropping to a depth of 3.5 mm having the size of around 800 N/mm^2, then experiencing a sharp fall to a depth around 5.5 mm.

The last phase in the manufacturing of crankshafts is fine grinding where in order to achieve the desirable condition of the surface and the surface layer [43–45], i.e., we have to ensure:

- suitable dimensions of the particular bearing locations with respect to the allowable deviations ($L \pm \Delta L$);
- suitable surface roughness R_a;
- that the grinding stresses are compressive or lowest tensile so that the favorable stress profile obtained by induction hardening of the surface layer is maintained;
- smallest changes possible in the microstructure and thus also smallest changes in the hardness and microhardness profiles in the heat-affected zone after grinding.

How is it possible to assure a desirable surface and surface layer quality after induction hardening and fine grinding? Finding an answer to this question requires a very good knowledge of the process of grinding on the microlevel as well as all mechanical and heat effects acting on the layer of the workpiece including the type and condition of the grinding wheel. An all-inclusive consideration of the numerous influences of the kind and condition of the tool on the changes on the surface and in the surface layer of the workpiece in the given machining conditions can be based on the descriptions of "surface integrity".

Figure 3.58 shows the conditions in the contact zone between the grinding wheel surface and the workpiece surface during the process. Thus, we can define the theoretical contact surface by the relative relation between the tool and the workpiece. The contact surface defined in this way is then considered in the calculations of forces, amounts of removed material per unit of time, etc.

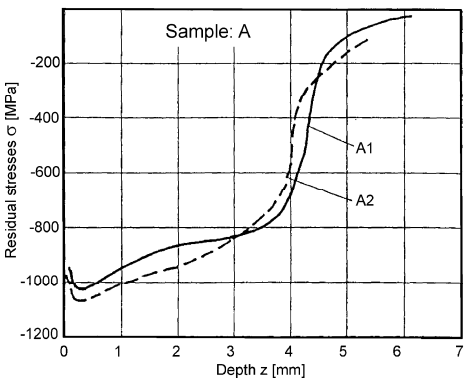

Figure 3.57. Residual-stress profile after induction hardening on the left (A1) and on the right specimen (A2) of the main bearing location A in the centre of the crankshaft [42]

Thus, Lindsay and Hahn [46] found by measurements on the grinding wheel surface that in fine grinding only 1–3% of grinding grains enter into real contact with the workpiece material. The contact surface between the grinding grains and the workpiece surface represents into the grinding tool and usually a larger part into the workpiece material. Inadequate selection of the machining conditions with respect to the given workpiece material and tool material may lead to too a strong heat flow, resulting in more or less distinct changes or damage of both materials in the pair.

In the analysis of microstructural changes in a thin surface layer of the material, it is possible to evaluate the size of the heat-affected zone. In Figure 3.59 we can see the time variation of the maximum temperature on the surface at the particular depths with respect to the workpiece speed v_w.

Knowing the temperature of melting and the temperature of the austenitization of the discussed steel, we can define the depth of the re-melted layer and the depth of the heat-affected zone.

Figures 3.60 and 3.61 show the effects of microstructural changes in the heat-affected zone due to the maximum temperatures on the surface and in the surface layer. The changes in the microstructure, microhardness and residual stresses extend to the depth of austenitization.

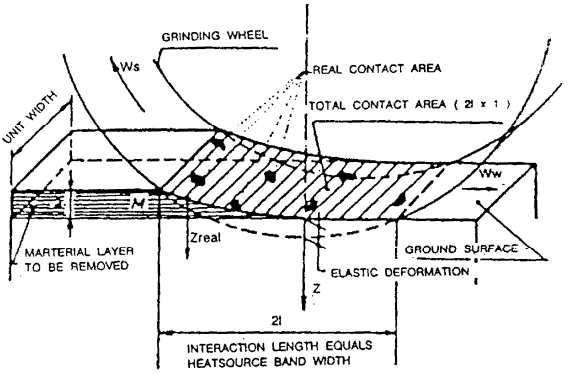

Figure 3.58. Geometry of theoretical contact and real contact area in grinding. The elastic flattening of the wheel causes an increase of interaction length [46]

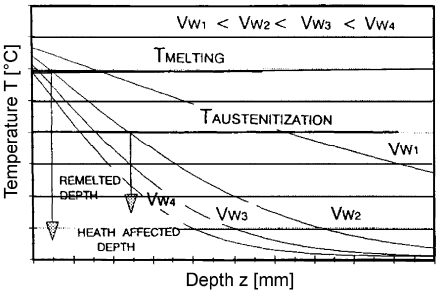

Figure 3.59. Maximum temperature drop as a function of depth in base material at various work speeds v_w [42]

For the grinding process the following conditions have been selected:

- different kinds of grinding wheels;
- different grinding conditions (fine, medium fine and rough).

Under different machining conditions of grinding, different temperature cycles were obtained on the surface and in the depth of the heat-affected zone that has effected microstructural changes and changes in the microhardness and residual stresses. Thus, on the surface a maximum temperature higher than the melting temperature of the workpiece material was obtained. The depth of the re-melted layer is only a few micrometers and makes a very fine ledeburite microstructure containing fine cementite spread in residual austenite. The newly formed micro-

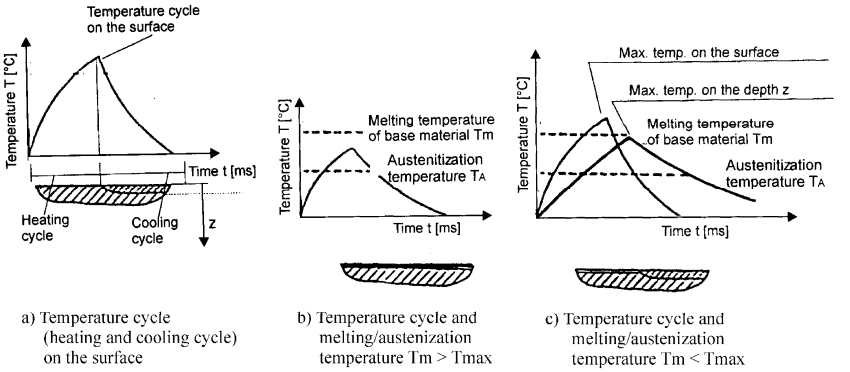

Figure 3.60. Grinding temperature cycles on the surface with respect of melting and austenitization temperature of the material [42]

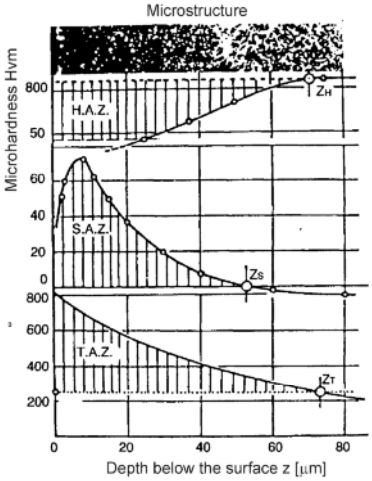

Figure 3.61. Surface damage of a ground surface in terms of microstructure change, microhardness variation and residual stress variation [42, 46]

structure has a slightly lower hardness than martensite. The residual stresses in the thin surface layer will be tensile due to plastic deformation of the surface layer in grinding caused by tensile forces in the contact zone of the workpiece material and to this should be added also the tensile stresses induced by the occurrence of residual austenite. In medium–fine grinding conditions, on bearing location A relative grinding tensile stresses amount to $+425\,N/mm^2$ and then change the sign in the depth around $175\,\mu m$ (Figure 3.62(a)). the relative grinding stress is obtained by measuring the residual stress after induction surface hardening and then by measuring on the same spot after induction surface hardening and grinding and then calculating their difference In Figure 3.62(b) we can see the measured absolute residual stress profile after induction hardening and grinding, and the measured residual stress profile after induction hardening. The results confirm as predominant the residual stresses, stresses induced by the plastic deformation of the material and a lesser influence of tensile stresses caused by the formation of residual austenite. On the basis of the measurements of residual internal stresses after induction hardening and/or induction hardening and grinding, we can conclude that:

For residual stresses after hardening and grinding, the conditions of rough-grinding are a more favorable choice. They lower to a lesser extent the desirable compressive residual stresses after induction hardening.

Grinding conditions can be chosen also so that the melting temperature of the workpiece material (fine-grinding conditions) is not exceeded. Then, the favorable compressive stresses after induction hardening are lowered only due to plastic deformation of the workpiece material during the process and thus relatively low tensile residual stresses are obtained. However, we should take into account that this will significantly lower the productivity.

Special attention should be paid to the selection of the kind of grinding wheel in terms of grinding wheel material, binding agent, hardness and pore density, since by a right selection we can contribute to higher cutting efficiency concerning the plastic deformation of the workpiece material. In this way we can keep the grinding tensile stresses as low as possible and make the compressive residual stresses induced by induction hardening the prevailing kind.

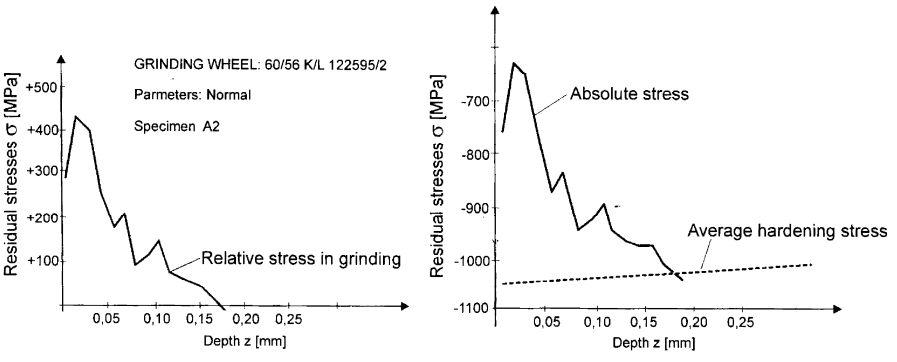

Figure 3.62. Residual-stress profile after induction-hardening and absolute grinding stress (a) and the profile of relative grinding stress (b) on bearing location A [43]

Induction hardening of surfaces creates a very desirable residual stress state. Residual internal stresses are always of compressive nature and are usually present to the depth of the induction-hardened layer [45].

A major difficulty in induction hardening is, however, to ensure a very slight/slow variation in hardness and the existence of compressive residual stresses in transition areas to the hardness of the core material. By gently varying the hardness and existence of compressive stresses in the transition area it is possible to diminish the notch effect induced by stress concentration. Additional grinding of an induction-hardened surface deteriorates the stress state in the surface layer, since grinding has always induced tensile stresses. By a correct selection of machining conditions and grinding wheel, taking into account its properties, the engineer will contribute to lower tensile residual stresses and will avoid deteriorating the favorable internal stress state after induction hardening.

Xu [49] studied the effect of grinding temperature on the surface integrity of a nickel-based superalloy. Excellent properties of superalloys together with their poor thermal diffusivity make them extremely difficult to machine and may lead to elevated temperatures at the grinding zone and possible thermal damage to the workpiece during grinding with abrasive wheels. K417 is a relatively new kind of turbine vane materials, which is a cast nickel-based superalloy and features good comprehensive properties such as high-temperature strength, high corrosion resistance, and good fatigue resistance.

Figure 3.64 shows residual-stress profiles in ground surfaces having different colors in which only the stresses in the direction perpendicular to the grinding direction are given. It can be seen that compressive stresses were generated on the ground workpiece surface layer.

Away from the ground workpiece surface, the compressive stresses increase to a maximum value and then decreases to that of the base material. The maximum stress on the puce surface is slightly smaller than for the other two cases and the location of the maximum stress is deeper from the ground surface.

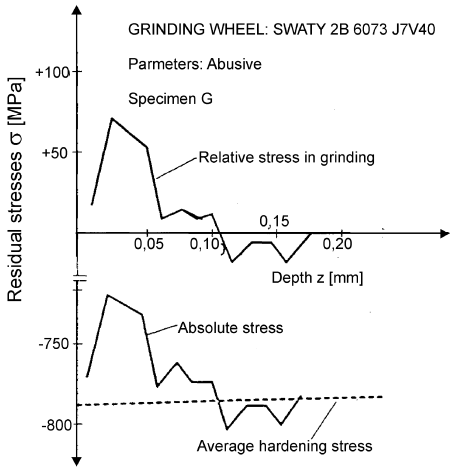

Figure 3.63. Residual-stress profile after induction hardening and grinding (absolute stress) and the profile of relative grinding stress on bearing location G [43]

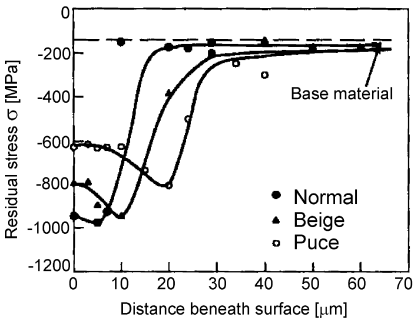

Figure 3.64. Residual-stress profiles at different grinding conditions showing various colors on the surface [49]

3.7 Modeling of Thermally Induced Damage in Grinding

Snoeys *et al.* [50] studied thermal models yielding a reliable evaluation of grinding processes. The relationship of grinding temperatures in the contact zone depending on kinetic parameters can be determined. The depth of the heat-affected zone in the workpiece can be calculated, workpiece burn predicted and the cause of residual stresses distribution can be calculated.

Their results show that grinders may lead to differences in heat balance and heat-flux distribution regarding reduced thermal damage. Maris and Snoeys [47] developed a reliable thermal model for thermal distribution prediction in workpiece during conventional grinding process at band heat source, depending on workpiece velocity v_w.

Figure 3.65 shows a schematic presentation of the various aspects of thermal damage in grinding as proposed by König [51]. Thermal damage is understood as a modification of the physical chemical properties of the workpiece surface layer. It can be manifested as the depth of heat-affected zone with untempered martensitic layer, oxidized layer, burned surface area, residual stress profile, surface cracks increased sensitivity for stress corrosion, reduced fatigue resistance, etc. The knowledge of the grinding temperature distribution is therefore essential for predicting or eliminating thermal damage [48].

A two-dimensional model can be used, provided that the grinding width is large with respect to the contact length (Figure 3.66).

The model itself is characterized by three physical quantities:

- the heat input into the workpiece and its distribution over the contact area;
- the real contact length (l_c); and
- the thermal characteristics of the workpiece material.

a) Actual heat input

The fraction of the heat source flowing directly into the workpiece is of special importance for its thermal load. Roughly 60–95% of the total generated energy flows into the workpiece, yielding a fast local increase of the temperature field.

b) Contact length

Another essential parameter is the real contact length l_c, which is a function of the wheel dimensions, compositions and characteristics.

The dimensions of the length of wheel–work contact (l_c) depends on the speeds and feed parameter because they govern the normal grinding force component in the contact area.

c) Thermal characteristics

Yet other physical quantities are the thermal characteristics of the workpiece and the grain material. Thermal characteristics are temperature dependent, using an adequately chosen average value may give a fairly good approximation of the temperature distribution. This assumption, of course, allows for an important simplification of temperature calculations.

Information related to the thermal and mechanical characteristics may be found in databanks.

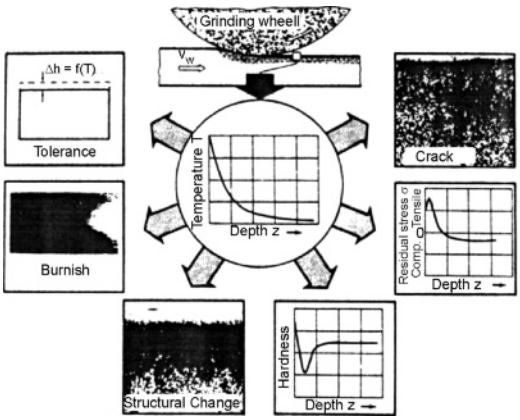

Figure 3.65. Thermal influence upon ground workpiece surface [51]

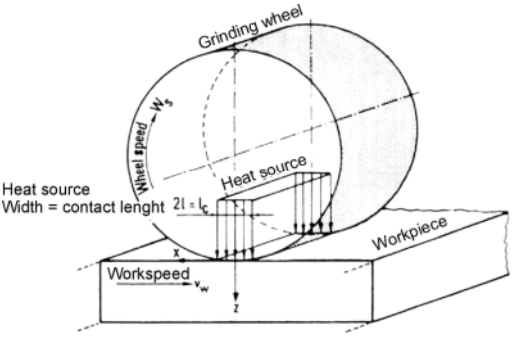

Figure 3.66. Two-dimensional thermal model representing grinding action [50]

It shows a theoretical evaluation of the depth of these influenced zones (Figure 3.67). The three critical temperatures are:

- tempering at 150°C;
- martensitic at 250°C;
- austenitic transformation at 800°C, for this particular steel (100Cr6), define three depths of affected zones;
- the heat affected zone z_T to be compared with the hardness affected zone z_H;
- the stress-affected zone z_{MS} associated with the depth at which the residual stresses are zero z_s;
- the untempered martensite layer z_{UM} corresponding with the trans-formation zone z_{ac1}.

It has been found that the depth of the tensile residual stress zone for hardened and tempered 100Cr6 ball-bearing steel can be calculated using the martensitic transformation temperature as a crucial temperature.

Mechanism of inducing residual stresses. The origin of thermally induced tensile stresses during grinding processes is schematically illustrated in Figure 3.68. The thermal cycle (0−Δ*T*) imposed upon the uppermost layer would result in a large thermal expansion ($\alpha\,\Delta T$); due to the deformation constraints created by the much stiffer and not thermally affected of the workpiece material large compressive stresses are built up during the heat-up period.

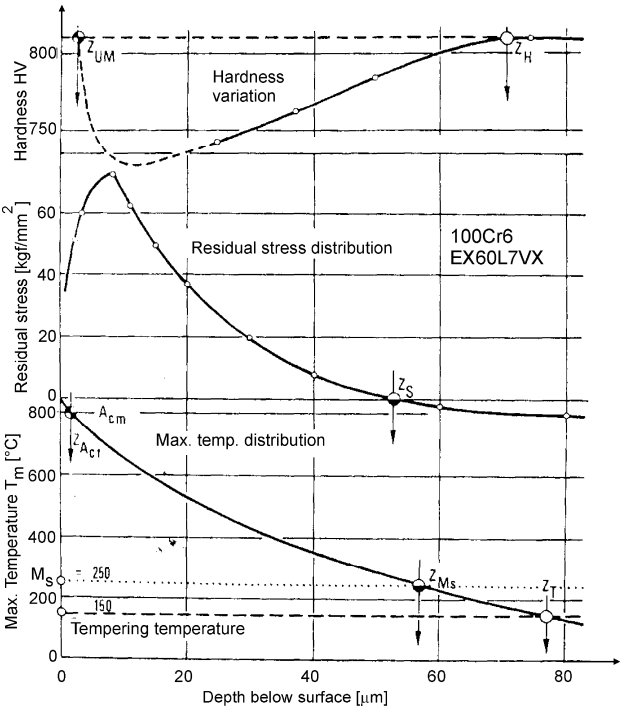

Figure 3.67. Thickness of thermal damaged layer: the three critical temperatures 150°C, 250°C and 800°C define three depths of affected zones [50]

The compressive stresses may easily surpass the yield stress at elevated temperatures. During the cooling-down period the stresses in the upper layers change elastically the stress–strain diagram. At the end of this thermal cycle tensile residual stresses are created that often are close to the yield of the abrasive material.

The stress–strain cycles of the upper layer, taking into account changes of material characteristics (yield, Young's modulus) due to temperature effects and strain hardening are represented in Figure 3.69.

Figure 3.70 indicates typical residual-stress profiles below the surface. As indicated on this figure the kinematical parameters on residual stresses turn out to be quite similar as their effect upon the temperature, magnitude in the contact zone.

Contrary to thermally induced stresses, mechanical-induced stresses are mainly yielding compressive stresses because of the Hertzian type of the stress field in the vicinity of the contact points with the grain tips.

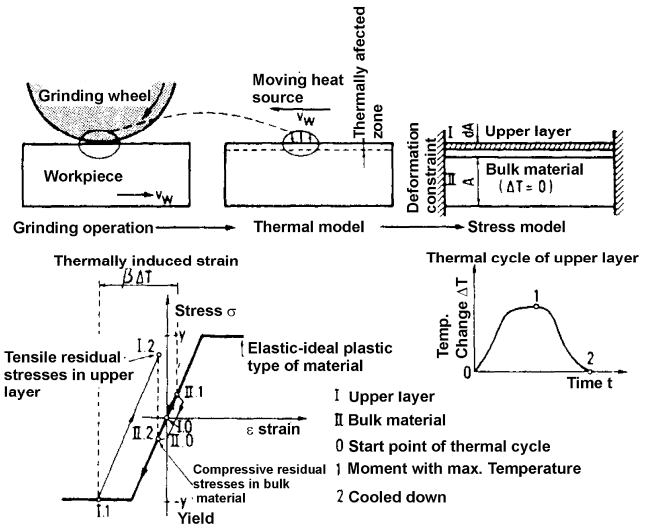

Figure 3.68. Mechanism of thermally induced tensile stresses in grinding [50]

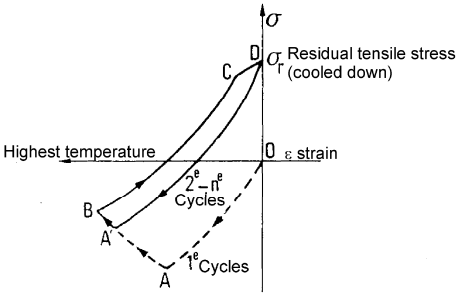

Figure 3.69. Stress–strain cycle of upper layer taking into account changes of material characteristics due to temperature effects [48]

As the mechanical effects of the grinding wheel are limited to depths of the order of 5 to 10 µm and considering the induced stresses, it means that the temperature history is the main cause of the residual stresses in grinding.

This effect is most important at the surface of abusively ground workpieces of easy-to-quench steels.

Compressive stresses occur due to the formation of untempered martensite and also to a second plastification of this layer.

In order to induce compressive stresses by "gentle" grinding operations on condition that the generated amount of heat is low enough and at sufficient workspeed to ensure that the temperature is always below the transformation. In such cases, thermal yielding can be avoided and mechanically induced stresses may become dominating. All the factors yielding low workpiece temperatures reduce tensile residual stresses.

Figure 3.71 shows the relationship between observed tensile residual stresses and calculated maximum temperature.

This relationship is given for alloyed high carbon steels and low carbon steels indicates the dominating role of temperature effects upon the residual stresses.

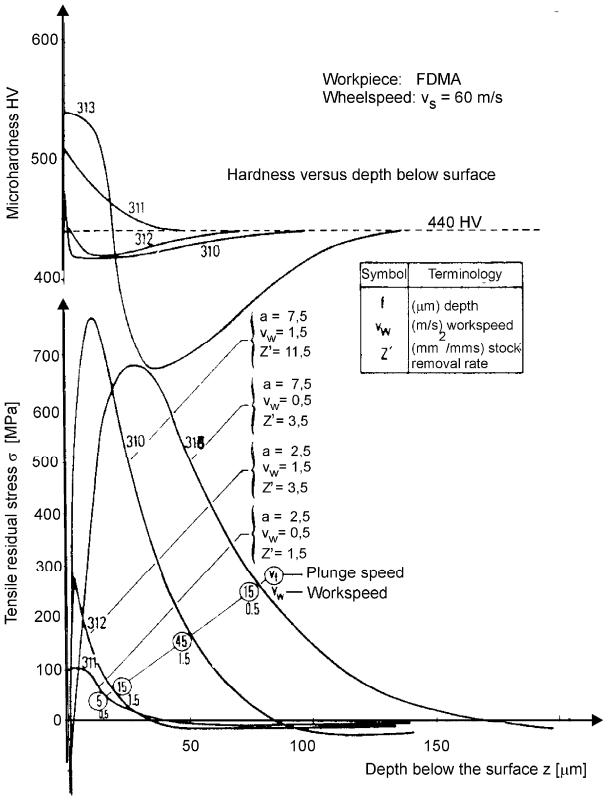

Figure 3.70. Residual stresses after plunge grinding of 0.3% carbon steel (hardened) [50]

In conclusion, the thermal damage of the workpiece can be predicted according to appropriate thermal model at the critical temperature yielding overtempering and austenitization. Experiments show a good correlation between predicted and measured depths of heat affected zones.

The residual stresses are a direct consequence of the high temperature generated. The resulting tensile stresses are due to plastic deformation caused by thermal expansion when grinding hardened steels with high martensite content.

The fatigue strength of ground workpieces is reduced by surface microcrack generation and tensile residual stresses. An adequate choice of grinding parameters during finishing, especially large workspeeds, may reduce this danger significantly.

Moulik *et al.* [52] presented simulation of thermal stresses on grinding.

An efficient finite-element procedure has been developed to calculate the temperatures and stresses arising due to a moving source of heat. The procedure is applied to calculate the thermal stresses produced in hardened steels during grinding. The thermal load during grinding is modeled as a uniformly or triangularly distributed, 2D heat source moving across the surface of a half-space, which is insulated or subjected to convective cooling. Figures 3.72(a) and (b) show the calculated temperature distributions across the surface of the specimen assumed to be an elastic solid when the heat source has moved.

The results of Figure 3.72(a) correspond to a uniformly distributed heat source, while those of Figure 3.72(b) are for the case of a triangularly distributed heat source having the same amount of total heat generation. Maximum surface temperatures produced by both types of heat sources are about the same at approximately 580°C but their locations are different. The peak surface temperature is shifted much more towards the trailing edge of the source for the triangular heat source than for the uniformly distributed one.

In order to calculate the residual stresses produced by the moving heat source, it is necessary for the specimen to be cooled down to room temperature. This occurs in grinding due to heat losses through the free surfaces of the specimen. The finite-element procedure was used to calculate the residual-stress profiles in the elastic-

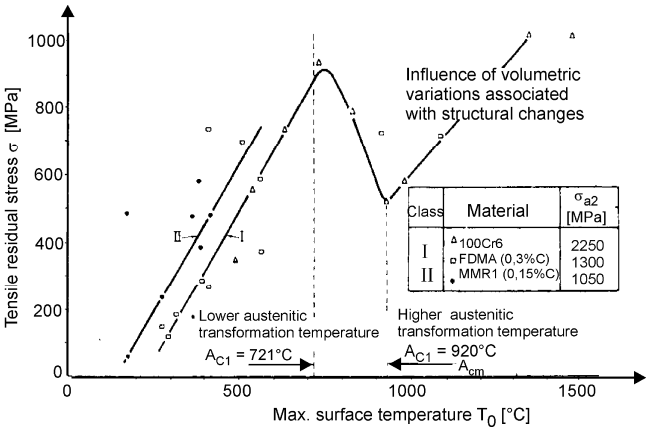

Figure 3.71. Relationship of temperature effects (thermal expansion and microstructural changes) and residual tensile stresses [50]

plastic half-space by assuming convection heat losses at the surface of the specimen. Two cases were investigated – dry grinding where the heat loss was assumed to take place by convection into air and wet grinding where the heat loss was assumed to take place into water.

A constant convection coefficient was assumed in both cases and the residual-stress profiles were calculated as the specimen cooled down to room temperature after being subjected to heating by the moving heat source.

Figures 3.73 and 3.74 show the finite element calculated residual-stress profiles (σ_x) in the surface layer for air and water cooling. The nature of the stress profiles

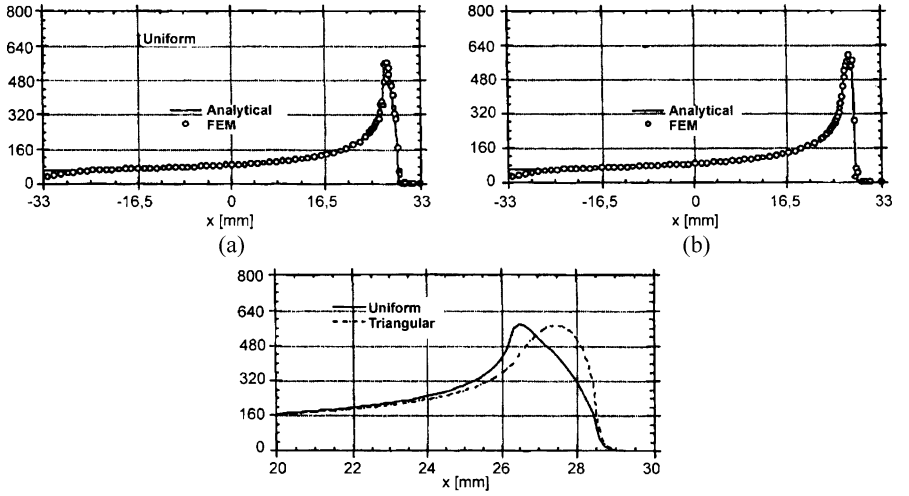

Figure 3.72. Temperature distribution on the surface of an elastic half-space for (a) uniformly distributed, (b) triangularly distributed source, and (c) superposition of temperature distributions in (a) and (b). v_w = 100 mm/s [52]

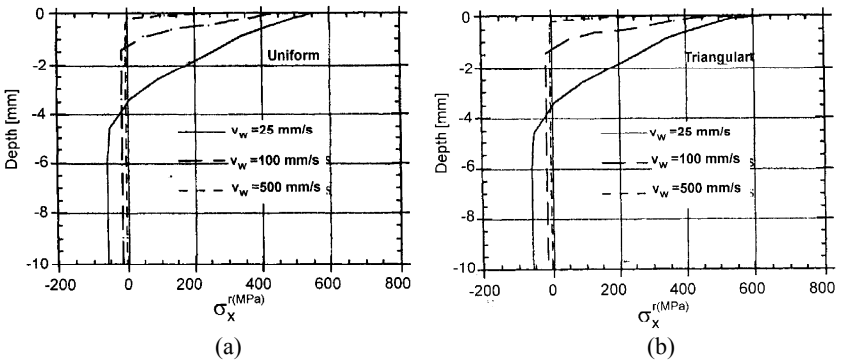

Figure 3.73. Residual tangential stress profiles (σ_x^r) below the surface (air cooled) for various heat source velocities for a (a) uniformly distributed source, and (b) triangularly distributed source [52]

(σ_x) and the magnitude of the surface stresses are similar in both cases. The velocity of the heat source influences the residual-stress profiles. The surface residual stress (σ_x) has its highest tensile value for the smallest heat source grinding velocity ($v_w = 25$ mm/s). The gradient of this stress at the surface is greatest for the heat source moving with the highest grinding velocity of $v_w = 500$ mm/s. Residual-stress profiles produced by the heat source at the surface are tensile in nature. This is consistent with observations from measurements of grinding residual stresses when heat generation and flow of heat into the workpiece is high and surface residual stresses are tensile.

They found that the magnitude of the tensile residual stress (σ_x) at the surface increases with increasing amount of heat generation. The highest value of the tensile residual stress was induced by the heat flux of strength $1.5q_0$; this value being ~550 MPa when the heat flux was uniformly distributed and ~700 MPa when triangularly distributed. Increasing tensile residual stresses at the surface being induced by bigger heat fluxes are consistent with experimental observations from grinding and welding processes.

Hamdi *et al.* [53] carried out residual stresses computation in a grinding process. Grinding induces residual stresses, which play an important role in the fatigue and wear resistance of the component. Conventional grinding leads to tensile residual stresses, while compressive stresses are obtained with high-speed grinding. A finite-element thermomechanical model for the calculation of residual stresses induced by a surface grinding process on a steel workpiece (AISI 52100) is presented. A model giving the energy conducted as heat in the workpiece as a function of the grinding wheel speed, the workpiece speed and the cutting depth, is proposed. This model is available for conventional grinding for wheel speeds less than 120 m s^{-1}. For these grinding conditions, the simulation leads to tensile residual stresses. The computation shows that the temperature in the grinding area increases when the peripheral wheel speed increases too. For wheel speeds corresponding to high-speed grinding, the surface temperature can reach values leading to an austenitic transformation and therefore, during cooling, the workpiece can be subjected to a superficial quenching, leading to compressive residual stresses.

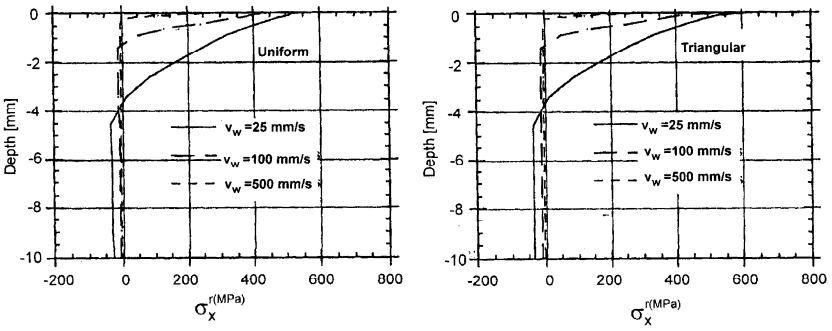

Figure 3.74. Residual tangential stress (σ_x^r) profiles below the surface (water-cooled) for various heat source velocities for a (a) uniformly distributed source and (b) triangularly distributed source [52]

The residual stresses computation is carried out in two stages. First, the temperature and distribution of stresses and strains distributions during the grinding process are calculated using a steady-state assumption. Then, starting from the results of the steady-state calculation, the final cooling is simulated in order to get the residual stresses. For each stage, the thermomechanical calculation is carried out in two steps. First, a thermal analysis is performed giving the temperature distribution in the workpiece. Then, a mechanical analysis uses the temperatures previously computed to calculate stresses and strains.

It is supposed that the steady-state conditions are fulfilled and the problem solved in a frame associated with the grinding wheel. This assumption avoids the need for a complete transient step by step analysis including the movement of the workpiece, which would need very much longer computation times. For this, a special procedure developed in the finite-element code SYSWELD+ for welding or surface treatment applications is used. From the thermal point of view, due to the movement of the workpiece a convention diffusion problem has to be solved.

The simulation presented in this paper does not give the expected results compared to the observations given by the high-speed grinding manufacturers concerning the compressive residual stresses. For the highest grinding wheel speed previously simulated, one can note that the temperature reaches about 750°C, which is very close to the temperature corresponding to the beginning of austenitic transformation. This can be pointed out qualitatively by reasoning on a simple constrained bar subjected to a thermal cycle inducing phase transformations as shown in Figure 3.75. It is rather usual that surface heat treatments lead to compressive stresses in the upper layers.

For higher grinding wheel speeds, higher temperatures must be reached leading to a heat-affected zone (HAZ) similar to those encountered with surface heat-treatment processes. Cooling conditions are such that martensitic transformation would take place in the HAZ during the final cooling. Volume changes accompanying phase transformations strongly modify the residual-stress state.

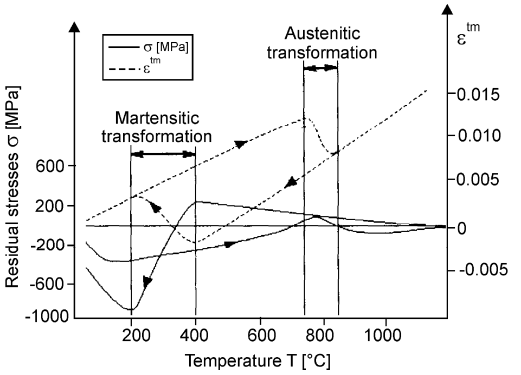

Figure 3.75. Influence of the phase transformations on the residual stresses [53]

References

[1] Bach FW., Laarmann A., Wenz T.: Modern Surface Technology, Wiley-VCH Verlag, Weinheim, 2004.

[2] Schulze V.: Modern Mechanical Surface Treatment, States, Stability, Effects, Wiley-VCH Verlag, Weinheim, 2006.

[3] Field M., Kahles J.F.: Review of surface integrity of machined component, Ann. CIRP, Vol. 20, No. 1, 1970, 107–108.

[4] Field M., Kahles J.F., Cammet J.T.: Review of measuring methods for surface integrity, Ann. CIRP, Vol. 21, No. 2, 1971, 219–237.

[5] Leskovar P., Grum J.: The metallurgical aspects of machining, Ann. CIRP Vol. 35, no. 2, 1986, 550.

[6] Bell T., Bloye A., Langan J.: Surface engineering of light metals, Heat Treatment and Surface Engineering: New Technology and Practical Applications, Proc. Of the 6th Int. Conf. On Heat Treatment of Metals,: Krauss G. (ed), Chicago, Illinois, ASM Int., 1988, 1–7.

[7] Betteridge D.F.: Surface engineering in the aero-engine industry; Past, Present and Future, Surface Engineering & Heat Treatment, Ed.: Morton P.H., The Institute of Metals, London, 1991, 43–79.

[8] Totten G.E.: Quenching and distortion control, Proc. of the First Int. Conf. on Quenching and Control of Distortion, Chicago, Illinois, ASM Int., 1992.

[9] Totten G.E., Howes M.A.H., Sjöstrom S., Funatani K.: Quenching and the control of distortion, Proceedings of the 2nd Int. Conf. on Quenching and the Control of Distortion, ASM Int., 1996.

[10] Totten G.E., Liščić B., Tensi H.M., The 3rd Int. Conf. on Quenching and Control of distortion, Prague, Czech Republic, ASM Int. 1999.

[11] Proceedings of the 4th Int. Conf. on Quenching and the Control of Distortion, Beijing, ASTM Int. 2003.

[12] Zoch H.W., Lübben T.H.: Proc. 1st Int. Conf. on Distortion Engineering 2005, Bremen, 2005.

[13] Grosch J., Kleff J., Lübben T.: 5th Int. Conf. on Quenching and Control of Distortion, Berlin, 2007.

[14] Trent F.M.: Metal Cutting, 2nd edn., Butterworths, London 1984.

[15] Leskovar P., Grum J.: Characteristics of the wear process in the cutting of free cutting steels, Int. J. Prod. Res., vol. 21, no. 5, 1983, 691–712.

[16] Leskovar, P., Grum J.: Wearing action at cutting plates of cemented carbides, Strojniški vestnik (Mechanical Engineering Journal), vol. 25, no. 3, 1979, 1–8.

[17] Kloos K.H., Kaiser B.: Residual stresses induced by manufacturing, residual stresses measurement, calculation, evaluation, Deutsche Gesellschaft für Wärmebehandlung und Werkstofftechnik, Deutsche Gesellschaft für Materialkunde, 1991, 205–226.

[18] M'Saoubi R., Outeiro J.C., Changeux B., Lebrun J.L., Morao Dias A.: Residual stress analysis in orthogonal machining of standard and resulfurized AISI 316L steels, Journal of Materials Processing Technology 96, 1999, 225–233.

[19] Ferlan, D.: Influence of conventional technological processes on surface integrity at various cutting conditions, MSc thesis, Faculty of Mechanical Engineering, University of Ljubljana, Ljubljana 1983.

[20] Arunachalam R.M., Mannan M.A., Spewage A.C.: Residual stress and surface roughness when facing age hardened Inconel 718 with cbn and ceramic cutting tools, Machine Tools & Manufacture, Elsevier, 2004, 879–887.

[21] Bouzakis K.D., Michailidis N., Vidakis N., Eftathiou K., Kompogiannis S., Erkens G.: Interpretation of PVD coated inserts wear phenomena in turning, Annals of the CIRP vol. 49, no. 1, 2000, 65–68.

[22] Chen L., El Wardany T.I., Harris W.C.: Modelling the Effects of Flank Wear Land and Chip Formation on Residual Stresses, CIRP Annals, vol. 53, no. 1, 2004, 95–98.
[23] Outerio J.C., Pina J.C., M'Saoubi R., Pusavec F., Jawahir I.S.: Analysis of residual stresses induced by dry turning of difficult-to-machine materials, CIRP Annals, vol. 57, no. 1, 2008, 77–80.
[24] Byrne G., Dornfeld D., Denkena B.: Advancing cutting technology, CIRP Annals 2003, Manufacturing Technology, vol. 52, no. 2, 2003, 483–507.
[25] Dahlman P., Gunnberg F., Jacobson M.: The influence of rake angle, cutting feed and cutting depth on residual stresses in hard turning, Journal of Materials Processing Technology 147, 2004, 181–184.
[26] Rech J., Moisan A.: Surface integrity in finish hard turning of case-hardened steels, Int. Journal of Machine Tools & Manufacture vol. 43, 2003, 543–550.
[27] Schwach D.W., Guo Y.B.: A fundamental study on the impact of surface integrity by hard turning on rolling contact fatigue, Int. Journal of Fatigue vol. 28, 2006, 1838–1844.
[28] Klocke F., Liermann J.: Roller burnishing of hard turned surfaces, Int. Journal Machine Tools Manufacturing, Vol. 38, no. 5–6, 1998, 419–423.
[29] Grzesik W., Rech J., Wanat T.: Surface integrity of hardened steel parts in hybrid machining operations, Journal of Achievements in Materials and Manufacturing Engineering, vol. 18, no. 1–2, 2006, 367–370.
[30] Guo Y.B and Sahni J.: A comparative study of hard turned and cylindrically ground regarding white layers, Int. Journal of Machine Tools & Manufacture vol. 44, 2004, 135–145.
[31] Hashimoto *et al.*: Surface integrity difference between hard turned and ground surfaces and its impact on fatigue life, Annals of the CIRP vol. 55, no. 1, 2006, 81–84.
[32] Abrao A.M., Adpinwall D.K.: The surface integrity of turned and ground hardened bearing steel, Wear vol. 196, 1996, 279–284.
[33] Navas G.V., Ferreres I., Maranon J.A., Garcia-Rosales C., Sevillano J.G.: Electrodischarge machining (EDM) versus hard turning and grinding with emphasis on comparison of residual stresses and surface integrity in AISI 01 tool steel, Journal of Materials Processing Technology 195, 2008, 186–194.
[34] Chou S.K., and Evans C.J.: White layers and thermal modeling of hard turning surfaces, Int. Journal of Machine Tools & Manufacture vol. 39, 1999, 1863–1881.
[35] Nasr M.N.A., Ng E.G., Elbestawi M.A.: Modelling the effects of tool-edge radius on residual stresses when orthogonal cutting AISI 316L, Int. Journal of Machine Tools & Manufacture 47, 2007, 401–411.
[36] M'Saoubi R., Outeiro J.C., Changeux B., Lebrun J.L., Dias A.M.: Residual stress analysis in orthogonal machining of standard and resulfurized AISI 316L steels, Journal of Materials Processing Technology 96, 1999, 225–233.
[37] Rech J., Kermouche G., Grzesik W., Garcia-Rosales C.: Characterization and modelling of the residual stresses induced by belt finishing on a AISI52100 hardened steel, Journal of Materias Processing Technology vol. 208, 2008, 187–195.
[38] Segawa T., Sasahara H., Tsutsumi M.: Development of a new tool to generate compressive residual stress within a machined surface, Journal of Machine Tools & Manufacture, 2004, 1215–1221.
[39] Li J.L., Jing L.L., Chen M.: An FEM study on residual stresses induced by high-speed end-milling of hardened steel SKD11, Journal of Materials Processing Technology 209, Elsevier, 2009, 4515–4520.
[40] Brinksmeier F.: The Influence of process quantities in grinding on residual workpiece stresses, Conf. on residual stresses, Darmstadt, 1990.
[41] Sosa, A.D., Echeverria M.D., Moncada O.J., Sikora J.A.: Residual stresses, distortion and surface roughness produced by grinding thin wall ductile iron plates, Int. Journal of Machine Tools & Manufacture vol. 47, 2007, 229–235.

[42] Grum J., Ferlan D.: Residual internal stresses after induction hardening and grinding, The 17th Heat Treating Society Conference & Exposition and the 1st Int. Induction Heat Treating Symp., Indiana, Materials Park, Ohio, USA, ASM Int., 1997, 629–639.
[43] Grum J.: Overview of residual stress after quenching part II: factors affecting quench residual stresses. Int. J. Mater. Prod. Technol., vol. 24, no. 1/2/3/4, 2005, 53–97.
[44] Grum J.: Analysis of residual stresses in main crankshaft bearings after induction surface hardening and finish grinding. Proc. of the Institution of Mechanical Engineers. Part D, Journal of automobile engineering, vol. 217, no. D3, 2003, 173–182.
[45] Grum J.: A review of the influence of grinding conditions on resulting residual stresses after induction surface hardening and grinding. J. Mater. Process. Technol., vol. 114, no. 3, 2001, 212–226.
[46] Lindsay R.P., Hahn R.S.: On the basic relationships between grinding parameters, Annals of the CIRP, vol. 19, 1971, 657–666.
[47] Moris M., Snoeys R.: Heat affected zone in grinding operations, 14th MTDR Conf. Manhester, 1973, 569–669.
[48] Hahn R.S., Linsay R.P.: The production of fine surface finishes while maintaining good surface integrity at high production rates by grinding, Proc. of the Fourteenth Int. Machine Tool Design and Research Conf., eds. Koenigsberger F., Tobias S.A., Manchester 1973, 645–652.
[49] Xu X.P., Yu Y.Q., Xu H.J.: Effect of grinding temperatures on the surface integrity of a nickel-based superalloy, Journal of Mater. Process. Technol., 129, 2002, 359–363.
[50] Snoeys R., Leuven K.U., Maris M., Peters K.U.: Thermally induced damage in grinding, Annals of the CIRP vol. 27/2, 1978, 571–581.
[51] König W., Hönscheid W., Lowin R.: Untersuchung der beim Schleifprozess entstehenden Temperaturen und ihre Auswirkungen auf das Arbeitsergebnis, Forschungsb. des Landes Nordrh. nr. 2648, Westdeutscher Verlag, 1977.
[52] Moulik P.N., Yang H.T.Y., Chandrasekar S.: Simulation of thermal stresses due to grinding, Int. Journal of Mechanical Sciences vol. 43, 2001, 831–851.
[53] Hamdi H., Zahouani H., Bergheau J.M.: Residual stress computation in a grinding process, Journal of Materials Processing Technology vol. 147, 2004, 277–285.

4

Characterization Methods for Surface Integrity

Jianmei Zhang[1] and Z.J. Pei[2]

[1] The University of Texas at El Paso, Department of Industrial Engineering, 500 W University Ave, El Paso, TX 79968, USA,
E-mail: jzhang2@utep.edu

[2] Kansas State University, Department of Industrial and Manufacturing Systems Engineering, 2011 Durland Hall, Manhattan, KS 66506, USA,
E-mail: zpei@ksu.edu

Since machined surface quality is a very important feature for numerous machine elements, many techniques have been developed to characterize and evaluate the surface integrity. This chapter reports a few general technologies used to characterize different aspects of the surface. In Section 4.1, some surface roughness measurement techniques will be introduced; in Section 4.2, X-ray diffraction and electron diffraction will be presented for crystalline structure; in Section 4.3, an X-ray energy-dispersive analyzer, Auger electron spectroscopy, and X-ray fluorescence are included for elemental analysis; Section 4.4 presents X-ray photoelectron spectroscopy and secondary ion mass spectrometry for chemical composition analysis; Section 4.5 reports the microcrystalline structure and dislocation density technology: transmission electron microscopy.

4.1 Surface Roughness Measurement Technologies

In general, there are four categories of measurement methods to evaluate the surface texture and the surface geometry: electronic-type measurement, optical-type measurement, visual- or tactile-type measurement, and scanning probe microscopy methods. The visual- or tactile-type measurement is the simplest and most straightforward method of surface measurement, also the least accurate. It is not presented in this chapter.

4.1.1 Electronic-type Measurement

There are two types of electronic instruments to measure the surface texture: averaging (or velocity) type and profiling (or displacement) type. In general, an averaging type employs a stylus that can be drawn across the surface to be measured. The vertical motion of the tracer is amplified electrically and is impressed on a recorder to draw the profile of the surface or is fed into an averaging meter to give a number representing the roughness value of the surface. This type of method requires interruption of the machine process, and the sharp diamond stylus may make microscratches on the tested surfaces.

As illustrated in Figure 4.1, in skidded gages, the sensitive, diamond-tipped stylus is contained within a probe, which has a skid that rests on the workpiece. Skidded gages (Figure 4.1(a)) can measure roughness only. Skidless gages (Figure 4.1(b)) use an internal precision surface as a reference, which enables skidless gages to be used for measurements of waviness and form, in addition to surface roughness [1].

Currently, several profilometers (stylus instruments) are commercially available to measure surface roughness. As an example, the profilometer is shown in Figure 4.2.

In this electronic instrument a pick-up with a diamond tip stylus 2 μm/90º is traversed across the test surface at a constant slow speed. When the stylus head moves horizontally, it also moves vertically to follow the surfaces deviations. The vertical movement is converted into a signal that represents the surface roughness profile. An example of surface roughness profile is shown in Figure 4.3.

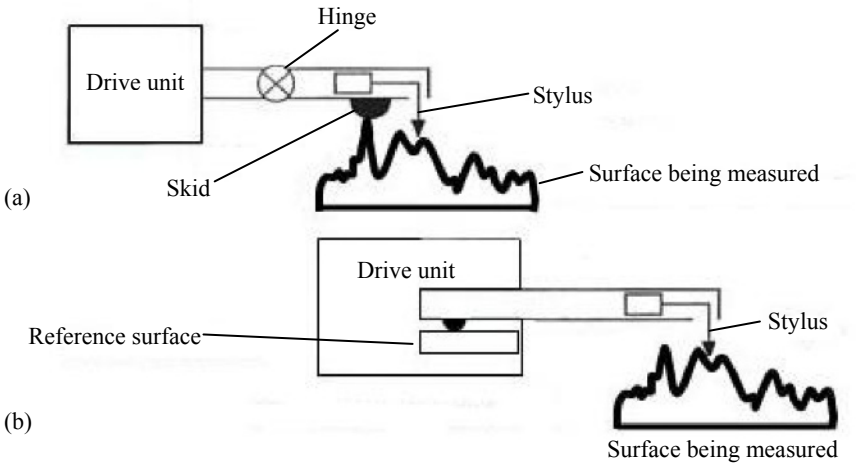

Figure 4.1. Illustration of (a) skidded gage and (b) skidless gage (after [1])

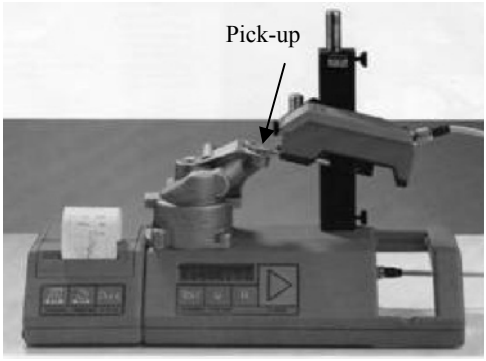

Figure 4.2. Profilometer for measuring surface roughness (courtesy of Hommelwerke)

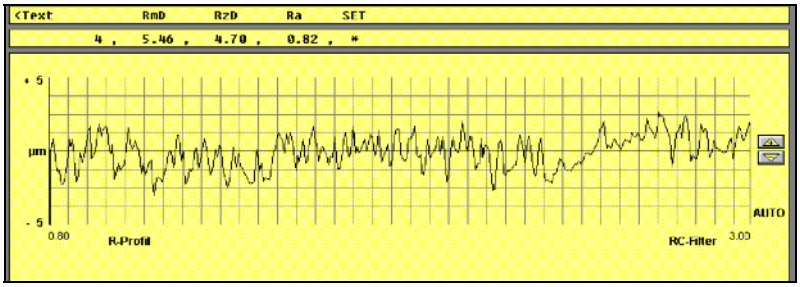

Figure 4.3. Example of a surface roughness profile

4.1.2 Optical-type Measurement

Surface topography can also be measured non-destructively by a variety of optical methods, from simpler equipment such as simple microscopes or three-dimensional microtopography, to highly sophisticated and refined techniques such as 3D interferometry. In this section, three optical measurement technologies are presented.

The first approach is total integrated scatter (TIS), originally developed by Davies [2]. As shown in Figure 4.4, the total intensity of the diffusely scattered light is measured by the detector.

TIS is the ratio of this quantity to the total intensity of reflected radiation (specular plus diffuse). TIS is shown to be related to the surface roughness parameter R_q. However, this method is practical only for very smooth surfaces with $R_q << \lambda$ (wavelength of the light) [2–4].

Another optical technique to measure surface roughness is the bidirectional scatter distribution function (BSDF). BSDF is defined as "the surface radiance divided by the incident surface irradiance" [4]. The surface radiance is the light intensity scattered through the scatter angle per unit illuminated surface area. The incident

surface radiance is the light intensity incident on the surface per unit illuminated surface area. As shown in Figure 4.5, BSDF is calculated by Equation 4.1:

$$\mathrm{BSDF} = \frac{P_\mathrm{s}/\Omega_\mathrm{s}}{P_\mathrm{i}\cos\theta_\mathrm{s}}\ , \tag{4.1}$$

where P_i is the incident light, P_s the scattered light, P_r the specularly reflected light, Ω_s the illuminated surface area, θ_i the incident angle, θ_s the scatter angle, and ϕ_s the angle between the scatter direction and X-axis (the scatter direction is determined by

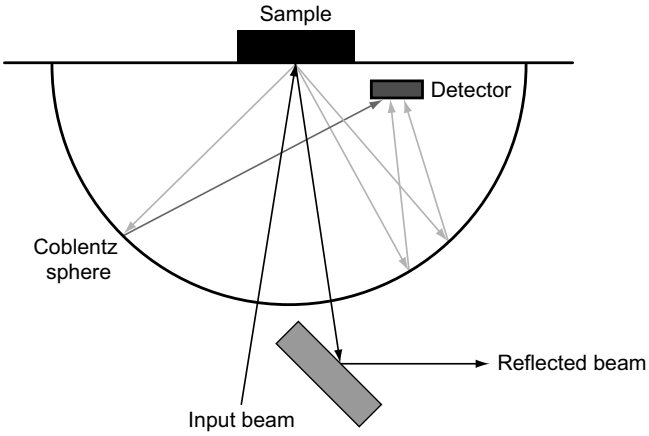

Figure 4.4. Illustration of TIS (after [2])

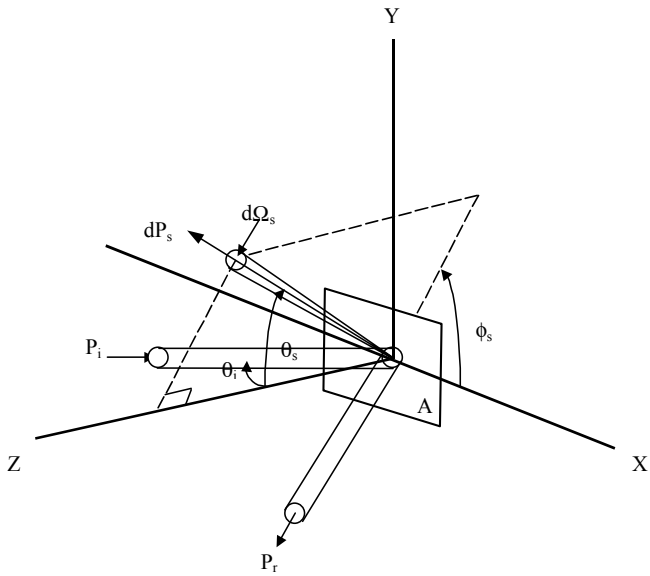

Figure 4.5. Geometry for definition of BSDF (after [4])

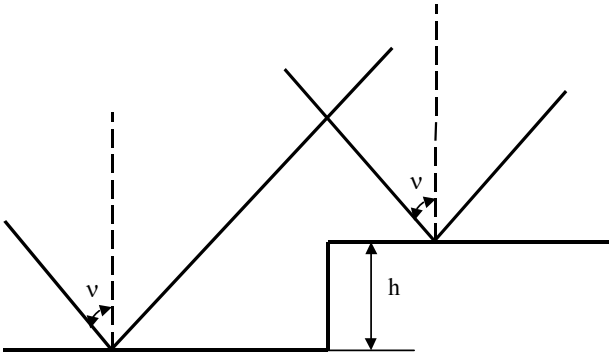

Figure 4.6. Difference caused by surface roughness (after [7])

P_s and Z-axis). A uniformly illuminated non-transparent isotropic surface is assumed for this technique, so BSDF is not applicable for the anisotropic surface [4, 5].

The third technique commonly used for surface analysis is the speckle contrast measurement. When coherent light illuminates the rough surface, the reflected beam accounts for part of the random patterns of bright and dark regions known as "speckle". The speckle pattern is created by the interference of wavelets scattered from points of different heights within the illuminated area (as shown in Figure 4.6, where v is the angle of illumination and h the height of the roughness) [6]. In the speckle contrast measurement, the average contrast, defined as the normalized standard deviation of intensity variations at the observed surface, has a strong, linear correlation with the surface roughness parameter R_a [7, 8].

4.1.3 Scanning Probe Microscopy Technologies

In scanning probe microscopy technologies, the surface can be measured and imaged to a very fine scale, down to the molecular level. Scanning tunneling microscopy (STM) and atomic force microscopy (AFM) are the major two types of scanning probe microscopy methods.

Figure 4.7 illustrates the working mechanism of STM. The basic idea is to bring a fine metallic tip close (a few Å) to a conductive sample. By applying a voltage between the tip and the sample, a small electric current (0.01–50 nA) can flow from the sample to the tip or reverse, which is called electronic tunneling. The exponential relationship between the tunneling current and the distance from the tip to the sample results in high vertical resolution.

By scanning the tip across the surface and detecting the current, the surface topography can be generated with very fine resolution. The lateral resolution is about 1 Å, whereas a vertical resolution up to 0.01 Å can be achieved. The STM can be used in ultrahigh-vacuum, air or other environments.

The STM is widely used for surface analysis. It can be used to study metals and semiconductor surface, especially semiconductors used in microelectronics fabrication. It can also be used to study microtopography and nanotopography of the surface on high-precision components. The major limitation of STM is that STM can

only be used for conductive or semiconductive surfaces. The resolution of mechanical components will depend on the ability to move the tip precisely and measure its position accurately [9–11].

In AFM, almost any type of surfaces, including polymers, ceramics, composites, glass, and biological samples can be characterized. A fine ceramic or semiconductor tip scans the sample surface, the tip is positioned at the end of the cantilever beam and as the tip is attracted or repelled, the deflection is captured by a laser reflecting at an oblique angle from the tip of the cantilever and the plot of laser deflection versus tip position on the sample provides the topography of surface, as shown in Figure 4.8.

A sharp probe is positioned close enough to the surface so that it can interact with the force fields associated with the surface. Then the probe is scanned across the surface in such a way that the forces between the probe and surface remain

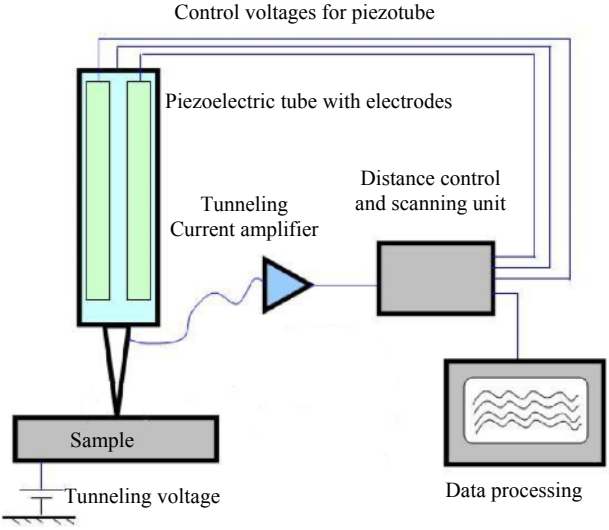

Figure 4.7. Illustration of STM (after [9])

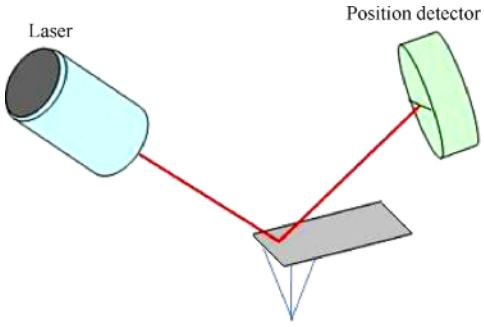

Figure 4.8. Illustration of beam deflection system by using a laser and photo detector to measure the beam position in AFM (after [12])

constant. By monitoring the precise motion of the probe when it is scanned over the surface, the topography of the surface can be constructed. The force on the probe is controlled by the feedback from the deflection of the laser beam on to the position detector. Magnifications of the AFM may be from 100 times to 100,000,000 times in the horizontal (x−y) and vertical axis [12].

4.2 Microstructure Characterization Technologies

4.2.1 X-ray Diffraction

X-ray diffraction is widely used as a non-destructive method to determine crystalline structure and residual stress from the lattice deformation of a crystal. A crystal lattice is a regular three-dimensional distribution (cubic, rhombic, etc.) of atoms in space. When X-rays come in at a particular angle, they are reflected specularly (mirror-like) from the different planes of crystal atoms. However, for a particular set of planes, the reflected waves interfere with each other. A reflected X-ray signal is only observed if Bragg's condition is met for constructive interference.

Figure 4.9 illustrates how X-ray diffraction works. Figure 4.9(a) shows X-rays incident upon a simple crystal structure, Bragg's condition is met for both ray A and ray B. Figure 4.9(b) shows the diffraction geometry.

The extra distance travelled by ray B must be an exact multiple of the wavelength of the radiation. This means that the peaks of both waves are aligned with each other. Bragg's condition can be described by Bragg's Law: $2d\sin\theta = m\lambda$, where d is the distance between planes, θ is the angle between the plane and the incident (and reflected) X-rays, m is an integer called the order of diffraction and λ is the wavelength [13, 14].

Figure 4.10(a) shows a standard X-ray diffraction pattern with aligned sharp peaks for a perfect crystal structure. During machining processes, residual stress may be resulted from non-uniform, permanent three-dimensional changes in the material. These changes usually occur as plastic deformation and may also be

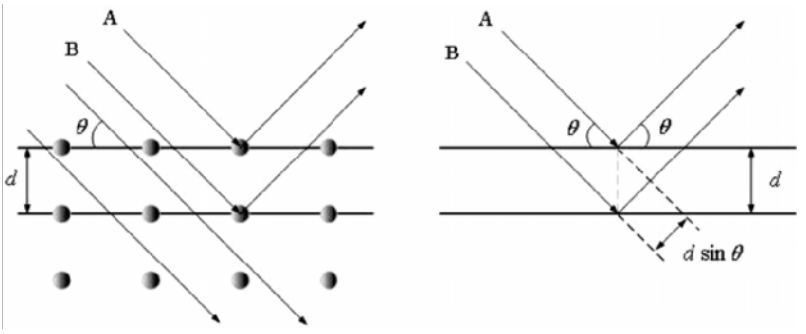

(a) (b)

Figure 4.9. Illustration of X-ray diffraction: (a) X-rays A and B incident upon a crystal, and (b) diffraction geometry (after [14])

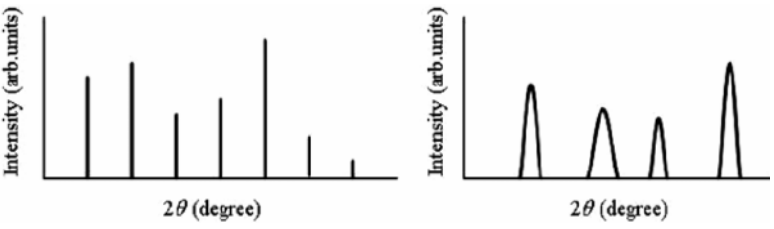

Figure 4.10. Illustration of X-ray diffraction patterns: (a) for a perfect crystal; and (b) for an imperfect crystal (after [14])

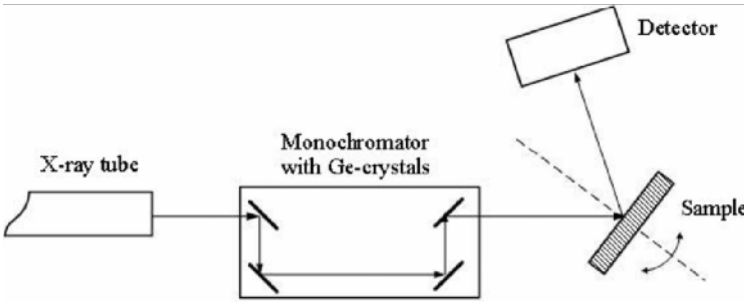

Figure 4.11. Illustration of high-resolution X-ray diffraction system (after [16])

caused by cracking and local elastic expansion or contraction of the crystal lattice [15]. In these cases, the crystal structure is no longer perfect (*d* is changed) and the diffraction peaks are broadened and shifted, as shown in Figure 4.10(b). Thus, by examining the changes of the X-ray diffraction pattern, the residual stress can be characterized.

For the applications of conventional X-ray diffraction, the main restriction is the low penetration depth of X-rays into the workpiece material. Because the strain can only be measured within the irradiated surface layer, with low penetration depth of X-rays, only the stress close to the surface can be detected quantitatively. Tonshoff *et al.* [16] used a high-resolution X-ray diffractometer (shown in Figure 4.11) to detect the damaged layer of machined silicon wafers.

This diffractometer consists of a four-crystal monochromator that produces a highly parallel and monochromatic incident beam so that a high resolution of X-ray diffraction can be achieved.

4.2.2 Electron Diffraction

Electron diffraction is similar to a regular microscope. The major difference is that, instead of a light beam, an electron bean is utilized in order to be able to visualize small objects (of the order of nanometers). This electron beam is directed

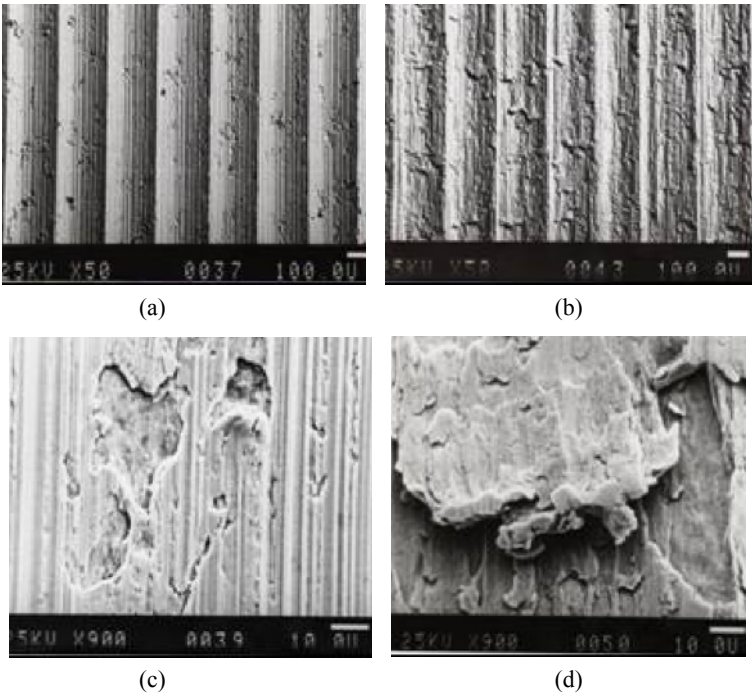

Figure 4.12. A Influence of cutting speed in turned surfaces: (a) cutting speed of 283 m/min under 50×, (b) cutting speed of 71 m/min under 50×, (c) cutting speed of 283 m/min under 900×, (d) cutting speed of 71 m/min under 900× [17]

and focused to the tested surface. In scanning electron microscopy (SEM), when the electron beam is incident on the surface, the electron will be refracted by the surface, therefore, the surface of the material will be detected; transmission electron microscopy (TEM) is the reflection of the electrons that passes through the specimen, therefore the crystal structure of the specimen can be detected. Compared with the traditional microscopes, the SEM has many advantages, including a larger depth of field and much higher resolution [18].

Under SEM, it is possible to observe the influence of cutting speed on the surface finish of turned surfaces in steel AISI 12L13, which is shown in Figure 4.12. The turning tool used is cemented carbide P10; feed rate employed is 0.25 mm/rev; depth of cut is 0.5 mm.

4.2.3 Cross-sectional Microscopy

For the cross-sectional microscopy method, the tested samples must be appropriately prepared, before observation under an optical microscope. Normally, the sample preparation consists of four general steps [1]: cleaving, sanding, polishing and etching. (1) Cleaving is done perpendicularly to the machined surface. (2) The

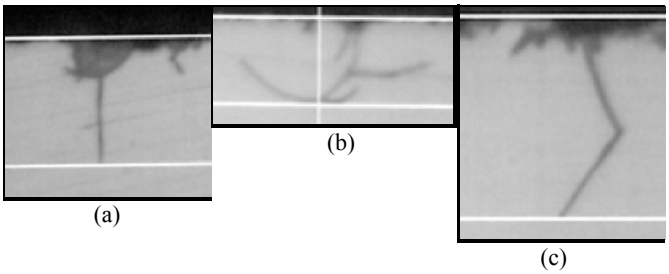

Figure 4.13. Crack configurations and depth in ground silicon wafers: (a) depth of 15.9 μm, (b) depth of 8.2 μm, (c) depth of 19.9 μm

surface of the cleaved sample is wet-sanded to remove enough material from the cross-section of interest to ensure that any damage incurred during cleaving is removed. (3) The test surface is refined by polishing. The polished surface should also be maintained flat and perpendicular to the machined surface. (4) The test surface is placed into "Yang" solution [19] (H_2O: HF49%: Cr_2O_3 = 500 ml: 500 ml: 75 g) for 5 s at room temperature, which will make the microstructure more discernible for microscopy observation. The sample preparation process is very critical to obtain the true signal.

Cross-sectional microscopy can also be used to assess the subsurface damage, providing information about the subsurface damage depth and subsurface damage distribution. But the sample preparation process is tedious. If not properly done, the sample preparation process itself will generate damage.

Using cross-sectional microscopy technology, the subsurface cracks in silicon wafers machined by various mechanical processes have been studied and the results of subsurface cracks, including crack configurations and crack depth are shown in Figure 4.13.

4.3 Elementary Analysis Technologies

4.3.1 X-ray Fluorescence

X-ray fluorescence, also known as (XRF) is the reaction from the electrons to the X-rays. The X-rays excite the electrons and they "jump" from the inner shell to an outer one. When the electron jumps, it leaves a vacancy and that vacancy is immediately filled by another electron. The "reaction" of the electron jumping from one shell to another is called fluorescence. Figure 4.14 shows graphically the definition of XRF [20, 21].

A typical result obtained from XRF analysis is shown in Figure 4.15. The elements that show higher peaks are the ones that have a major concentration in the material. In this example, the predominating elements are lead and aluminum. Other elements that also have been detected are chromium, iron, and titanium, but their concentration is not significant [20, 21].

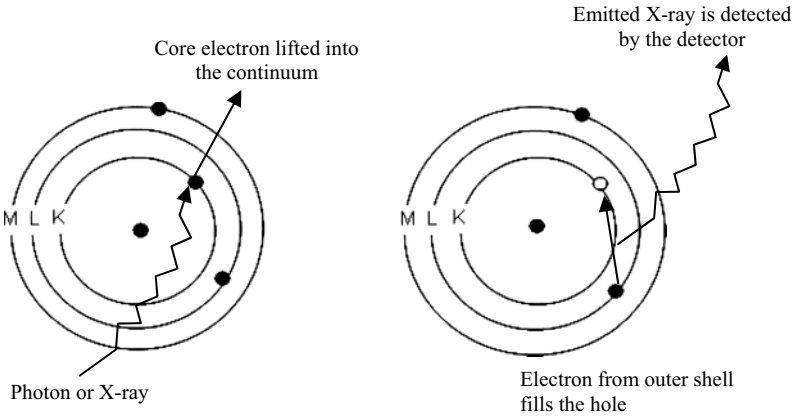

Figure 4.14. Illustration of XRF (after [21])

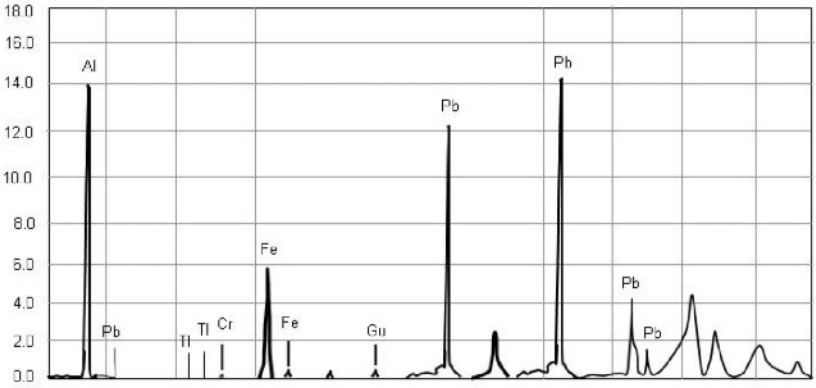

Figure 4.15. Results of XRF analysis (after [21])

4.3.2 Others

Energy-dispersive X-ray spectroscopy (EDS, EDX or EDXRF) is another analytical technique used for the elemental analysis of a sample. Sometimes EDX is used in conjunction with SEM.

The fundamental principle of EDX characterization capability is that each element has a unique atomic structure, therefore allowing X-rays characteristic of an element's atomic structure to be identified uniquely from each other. The X-ray characteristic is the energy absorption that will produce electron movements between orbital on the atom, therefore emitting X-rays. This emitting X-ray together with the amount of energy submitted will determine the element that is being scanned [22].

Auger electron spectroscopy (AES) can also be used to determine the chemical composition of the tested surface, and it can be applied to all solid materials, including polymers and glasses. Underlying the spectroscopic technique is the Auger

effect, which is based on the analysis of energetic electrons emitted from an excited atom after a series of internal relaxations.

In general, AES is able to analyze the furthest two through ten atomic layers of the surface. However, if the interested region is below the surface, ion etching can be used to remove the topmost atomic layers. For the detailed information about ion etching, please refer to [23].

AES and X-ray photoelectron spectroscopy (XPS, presented in Section 4.4.1) give similar information, but the Auger spot size is much smaller than the XPS one, therefore, having the capability of identifying very fine features on the surface.

4.4 Chemical Composition Analysis Technology

X-ray photoelectron spectroscopy (XPS) is also known as electron spectroscopy for chemical analysis (ESCA). It is a surface analysis technique where a sampling volume that extends from the surface to a depth of approximately 50–70 Å can be analyzed. It is used to determine quantitatively elemental states in the material, and provide chemical composition of the detected elements within the material. Composition depth profiling can be achieved by using an ion beam to sputter etch the sample between analysis cycles.

The working principle of XPS is shown in Figure 4.16. When the tested sample is irradiated by the monochromatic X-rays, the photoelectrons whose energies are characteristic of the elements within the sampling volume will be emitted. Therefore, by detecting small shifts in the atomic binding energies of the photoelectrons, the chemical states of the elements can be determined. The fundamental principle is that the core electronic levels of the binding energies are uniquely different for each specific element in the material, so elemental analysis can be obtained from the spectra. All elements except hydrogen and helium are detectable from XPS. The intensity of the peaks on the spectra is related to the concentration of the element within the tested region. Also, small shifts in element binding energies (commonly referred as the chemical shifts) provide information about the chemical state of the element, which are due to the modification of the electronic levels caused by changes [24–26]. Figure 4.17 shows the XPS spectra results on polyethylene terephthalate [27].

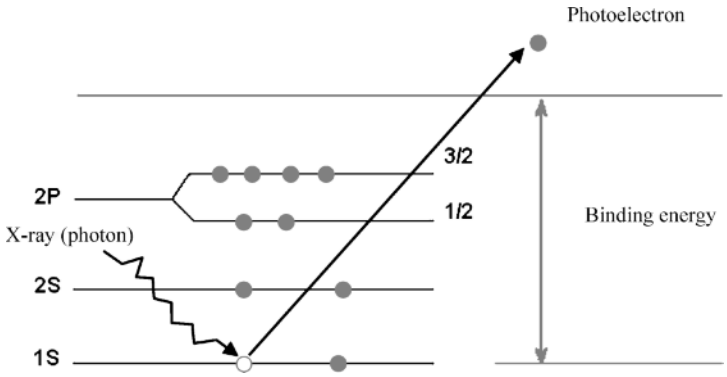

Figure 4.16. Basic principle of XPS (after [24])

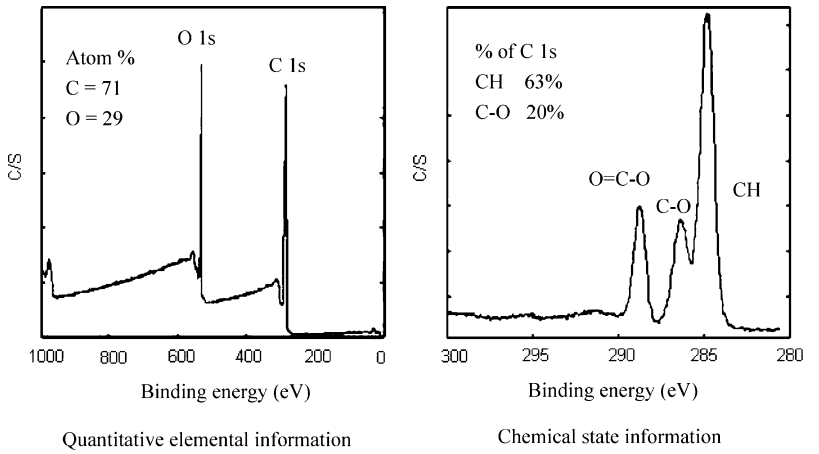

Figure 4.17. XPS results of polyethylene terephthalate (after [27])

4.5 Microcrystalline Structure and Dislocation Density Characterization Technology

Transmission electron microscopy (TEM) is a microscopy technique used to characterize the microstructure of materials with very high spatial resolution. Information about the morphology, crystal structure and defects, crystal phases and composition can be obtained from TEM.

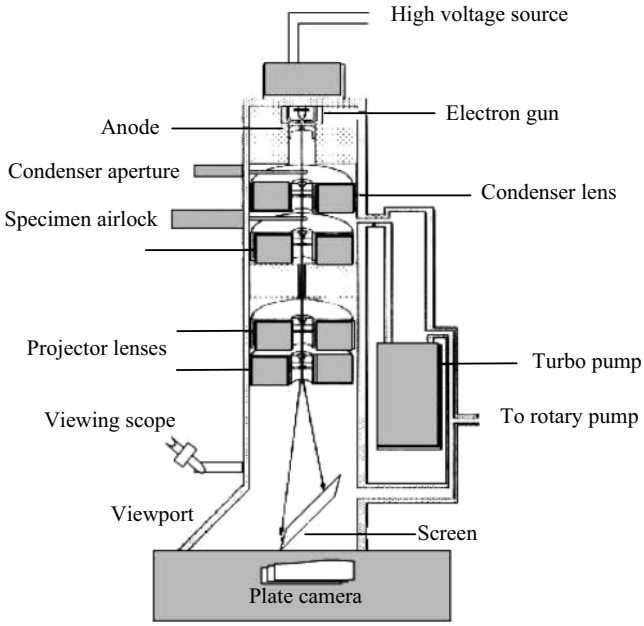

Figure 4.18. Illustration of TEM (after [28])

In TEM, a beam of electrons is transmitted through a very thin specimen, interacting with the specimen when they pass through the specimen. Then the electrons are focused with electromagnetic lenses and the image is observed on a fluorescent screen, or recorded on film or digital camera. Compared with the light used in the optical microscope, the electrons are accelerated at several hundred kV, giving wavelengths much smaller than that of light: 200 kV electrons have a wavelength of 0.025 Å. However, the resolution of TEM is limited by the aberrations inherent in electromagnetic lenses, to about a few angstroms.

References

[1] Stephenson D.A., Agapiou J.S., (1996) Metal Cutting Theory and Practice, Marcel Dekker, New York
[2] Davies H., (1954) The Reflection of Electromagnetic Waves from a Rough Surface, Proc. Inst. Elec. Eng., Vol. 101, pp. 209
[3] Vorburger T.V., Teague E.C., (1981) Optical Techniques for On-Line Measurement of Surface Topography, Precision Engineering, Vol. 3, No. 2, pp. 61–83
[4] Stover J.C., (1990) Optical Scattering Measurement and Analysis, McGraw-Hill, New York
[5] Nicodemus F.E., Richmond J.C., Hsia J.J., Ginsberg I.W., Limperis T., (1977) Geometric Considerations and Nomenclature for Reflectance, NBS Monograph 160, U.S. Dept. of Commerce, Washington, DC
[6] Persson U., (1992) Real Time Measurement of Surface Roughness on Ground Surfaces Using Speckle-contrast Technique, Optics and Lasers in Engineering, Vol. 17, No. 2, pp. 61–67
[7] Asakura T., (1978) Surface Roughness Measurement, Speckle Metrology, ed. Erf R.K., Academic Press, New York
[8] Fujii H., Asakura T., (1974) Effect of Surface Roughness on the Statistical Distribution of image Speckle Intensity, Optics Communications, Vol. 11, No. 1, pp. 35–38
[9] Bai C., (1992) Scanning Tunneling Microscopy and its Application, Springer Verlag, Berlin
[10] Guntherodt H.J., Wiesendanger R., (1991) Scanning Tunneling Microscopy I-III, Springer Verlag, Berlin
[11] Stroscio J.A, Kaiser W.J., (1993) Scanning Tunneling Microscopy, Academic Press
[12] Online: Atomic Force Microscope, http://www.nanoscience.com/education/AFM.html
[13] Hecht E., (2002) Optics, 4th edn., Addison Wesley , New York
[14] Online: Limits of Resolution: X-ray Diffraction, http://physics.bu.edu/py106/notes
[15] Bismayer U., Brinksmeier E., Guttler B., Seibt H., Menz C., (1994) Measurement of Subsurface Damage in Silicon Wafers, Precision Engineering, vol. 16, pp. 139–143
[16] Tonshoff H.K., Schmieden W.V., Inadaki I., Konig W., Spur G., (1990) Abrasive Machining of Silicon, Annals of the CIRP, vol. 39 no. 2, pp. 621–630
[17] Davim J.P. (1991) Influência das condições de corte na microgeometria das superfícies obtidas por torneamento, MSc thesis, University of Porto, Porto (in portuguese)
[18] Online: The Microscopy Facility, http://bioweb.usu.edu/microscopy/
[19] Yang K H., (1984) An Etch for Delineation of Defects in Silicon, Journal Electromechanical Society, Solid State Science and Technology, Vol. 131, No. 5, pp. 1140–1145
[20] Lachance G.R., Claisse F, (1995) Quantitative X-ray Fluorescence Analysis: Theory and Application, Wiley, Chichester

[21] Online: Wikipedia: X-ray Fluorescence, http://en.wikipedia.org/wiki/X-ray_fluorescence
[22] Online: Surface Science Techniques, http://www.uksaf.org/tech/edx.html
[23] Online: Wikipedia: Auger Electron Spectroscopy, http://en.wikipedia.org/wiki/Auger_electron_spectroscopy
[24] Barr T.L., (1994) Modern ESCA: The Principles and Practice of X-Ray Photoelectron Spectroscopy, CRC Press, Boca Raton
[25] Carlson, T.A., (1978) X-ray Photoelectron Spectroscopy, Plenum, New York
[26] Pais A., (1983) Subtle is the Lord: The Life and Science of Albert Einstein, Oxford University Press, New York
[27] Online: http://www.eaglabs.com/techniques/analytical_techniques/xps_esca.php
[28] Flegler S.L., Heckman J.W., Klomparens K.L., (1993) Scanning and Transmission Electron Microscopy: An Introduction, W.H. Freeman, New York

5

Surface Integrity of Machined Surfaces

Wit Grzesik[1], Bogdan Kruszynski[2], Adam Ruszaj[3]

[1] Faculty of Mechanical Engineering, Department of Manufacturing Engineering and Production Automation, Opole University of Technology,
P.O. Box 321, 45-271 Opole, Poland,
E-mail: w.grzesik@po.opole.pl

[2] Faculty of Mechanical Engineering, Department of Machine Tools and Manufacturing Engineering, Technical University of Lodz,
Stefanowskiego 1/15, 90-924 Lodz, Poland,
E-mail: kruszyn@p.lodz.pl

[3] Faculty of Mechanical Engineering, Institute of Manufacturing Engineering and Production Automation, Cracow University of Technology,
Al. Jana Pawla II, 31-864 Cracow, Poland,
E-mail: ruszaj@m6.mech.pk.edu.pl

This chapter presents the basic knowledge on surface integrity produced in traditional and non-traditional machining processes. An extended overview of fundamental characteristics of surface finishes and surface integrity including surface roughness/surface topography, specific metallurgical and microstructure alterations and process-induced residual stresses is carried out. Surface roughness was determined by many important 3D roughness parameters and representative scanned surface topographies were included. They allow recognizing the structural features, i.e., determined and random components of the machined surfaces. Moreover, some practical formulae for prediction of the theoretical surface roughness in typical cutting operations (turning and milling) and grinding operations are provided. On the other hand, possible surface alterations resulting from abusive machining operations are demonstrated. Finally, the state-of-the-art of machining technology is addressed to many finishing cutting, abrasive and non-traditional (EDM, ECM, LAM, USM, etc.) operations to show how the manufacturing processes can be effectively utilized and optimized in practice.

5.1 Introduction

5.1.1 Machining Surface Technology

A manufacturing/machining process produces a surface characterized by the shape (topography), metallurgy and mechanical properties. These surface aspects clearly indicate that a machined surface is very complex and consists of a system of interrelated features that influence the surface functional performance. In order to consider the various generating mechanisms within a machining process, it is proposed to divide them simplistically into three unit event mechanisms: chemical, mechanical, and thermal, or more appropriately to five types: chemical, mechanical, mechanothermal, thermomechanical and thermal [1], as shown in Figure 5.1. It should be borne in mind that these fundamental phenomena will always be present to a greater or lesser degree, but with various energy partitions, in all machining processes. Over the range of energy inputs to the generated surface specified in Figure 5.1, the total energy balance suggests a sevenfold increase in the energy entering the surface.

Obviously, a high-energy input increases the likelihood of metallurgical damage and therefore results in a poor surface integrity. In particular, the mechanically affected layer consists of things like deposits, laps, folds and plastic deformation. The heat-affected layer consists of things like phase transformations, cracking and

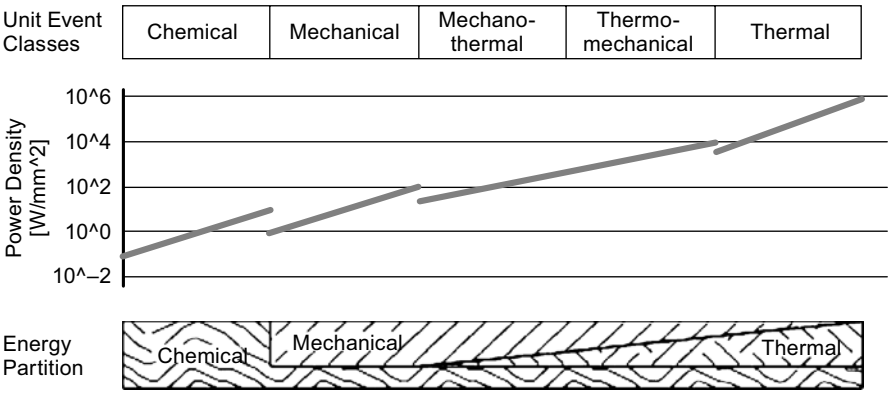

Typical Process	CHM	AJM	Turning	Grinding	EDM
Tool	–	abrasive	cutting tool	grinding wheel	shaped tool
Machine	bath	enclosure	lathe, mill	grinding M/c	EDM bath
Operating Conditions	etch rate, velocity, potential	speed, distance	feed, speed	speed, DOC	feed, potential

Figure 5.1. Generating mechanisms in typical machining processes [1]

re-tempering, and chemically affected layers are generated by the surface chemical changes. Moreover, the stress-affected layers are developed by the residual stresses resulting from a combination of the mechanical and thermal influences.

In conjunction with the magnitude of the power density, five main processes: electrochemical machining (ECM), abrasive jet machining (AJM), turning (T), grinding (G) and electrodischarge machining (EDM) can be distinguished at positions appropriate to the balance of the inherent generating mechanisms.

Additionally, in order to consider the influence of machining conditions, such as speed, feed, depth of cut, tool state and lubrication/cooling, etc., on the surface integrity the appropriate machining processes can be termed abusive, conventional and gentle, as proposed in Figure 5.2. In general, abusive machining results in low or poor surface integrity by generating more heat and high strains and strain rates. In contrast, gentle machining conditions mean that little heat is generated and a surface with little or ideally no strained layers is produced.

Taking into account different types of energy transferred to the surface and subsurface layer, the basic factors influencing surface integrity are temperatures generated during processing, residual stresses, metallurgical (phase) transformations, and surface plastic deformation, tearing and cracking. These and other surface integrity-related problems will be discussed in terms of traditional processes (performed with tools with geometrically defined cutting edges), grinding (performed with abrasive tools with geometrically undefined cutting edges) and non-traditional processes. The three groups of machining processes will successively be overviewed in Section 5.2.

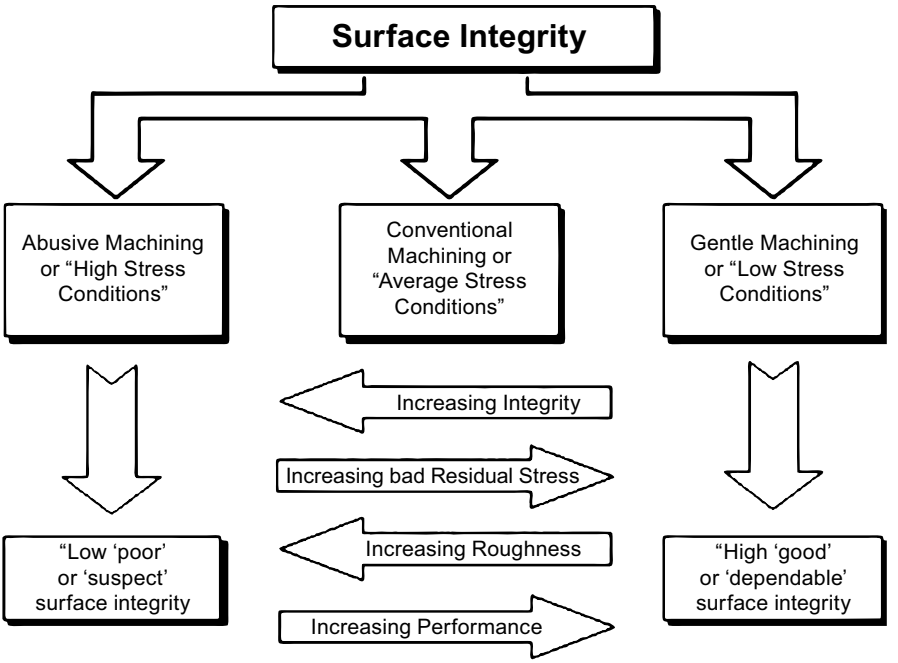

Figure 5.2. Influence of machining conditions on surface integrity [1]

5.1.2 Factors Influencing Surface Integrity

5.1.2.1 Traditional Machining

Each type of cutting tool will leave unique marks on the machined surface. The direction of the dominating surface pattern, lay, will be influenced by the machining method. The practical results of the surface texture will be affected by a number of different factors in the processes related to the cutting tool (stability, overhang, cutting geometry, tool wear), the machinery (stability, machining environment, coolant application, machine conditions, power and rigidity) and the workpiece (material structure and quality, design, clamping, previous machining process). In particular, the resulting dynamic and static stability of the total process system is of vital consequence to the quality of surface texture achieved.

As mentioned in Section 5.1.1 the machining conditions used mean that the surface integrity is produced in general (normal) and two extremes, i.e., gentle or abusive process, as shown in Figure 5.3. General refers to machining conditions that are normally achieved by utilizing the manufacturer's recommendations and are expected in a conventional workshop. Gentle machining will occur when using the new tool with sharp cutting edges, which have a very small radius, typically below 10–20 μm. As a result, the surface integrity will be high due to marginal disturbance to the surface from the tertiary shear zone. As the tool wear progresses, the radius of the cutting edge increases and a flat land appears from the clearance face. This causes that rubbing will increase between the tool and the workpiece, and the abusive conditions result in low surface integrity. In addition, much heat is generated and a heat-affected layer produced has predominantly a negative influence on the surface functional performance.

Figure 5.4 illustrates typical ranges of the roughness average (R_a) values achievable in many traditional machining operations under "normal" conditions, as well as non-traditional processes. Higher or lower values of R_a may be obtained under various machining conditions, i.e., rough, medium or finish operations. As can be seen in this diagram, a very smooth surface with the lowest R_a parameter of 0.01–0.02 μm

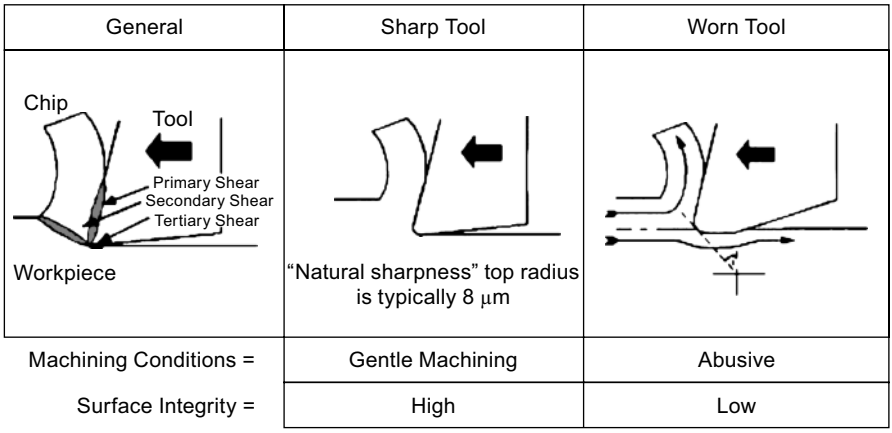

Figure 5.3. Three types of machining conditions vs. surface integrity [1]

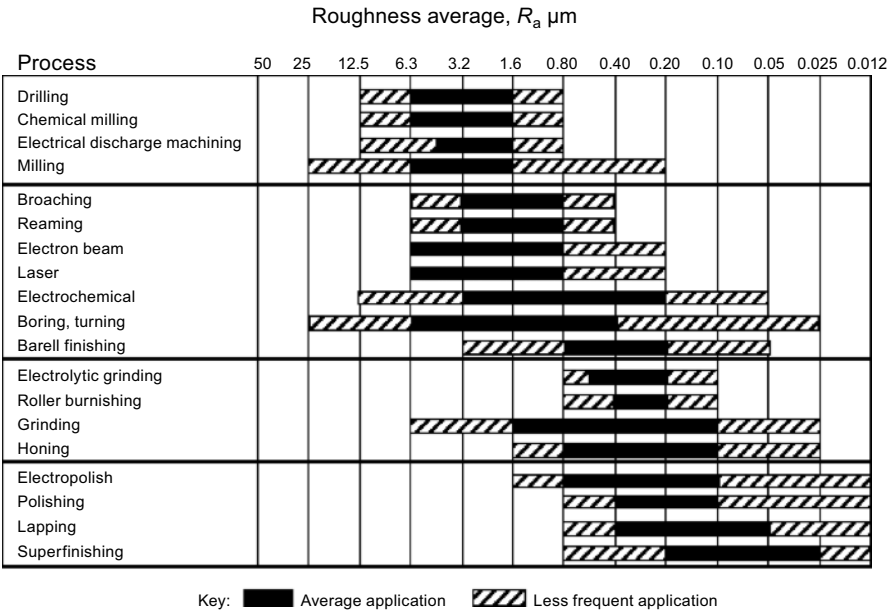

Figure 5.4. Typical ranges of surface finish from common machining processes

can be produced in superfinishing, which is one of the finishing abrasive processes utilized in precision manufacturing branches. In contrast, the hole surfaces by drilling have the R_a parameter between 1.6 and 6.3 μm. These effects are comparable to those achievable in both ECM and EDM processes. In many cases, two or more steps are necessary to get a good finish. For example, rough and finish turning followed by rough and finish grinding operations are obvious to obtain a 0.5 μm R_a on steel shafts.

5.1.2.2 Grinding

Generally, grinding belongs to those manufacturing processes that usually constitute the final technological operation and for this reason the attention paid to the creation of surface layer is fully understandable. The evidences of how much attention has been focused on this field are the numerous research studies and publications devoted to this problem.

There are a great number of parameters influencing the surface layer in grinding, i.e., grinding wheel characteristics and topography, work material characteristics, kinematics, environment (grinding fluids), etc. Due to these, any prediction of the surface layer properties in grinding is extremely difficult, especially under theoretical consideration. This is because numerous investigations have been carried out to find the relations between particular process parameters and surface roughness experimentally. When considering grinding wheel characteristics one should take into consideration: the type of abrasive material (mainly conventional or superabrasives) grain size, structure (or concentration in the case of superabrasives), grade (hardness) and bonding material. All of these properties may strongly influence surface layer properties: geometrical, physical and/or chemical.

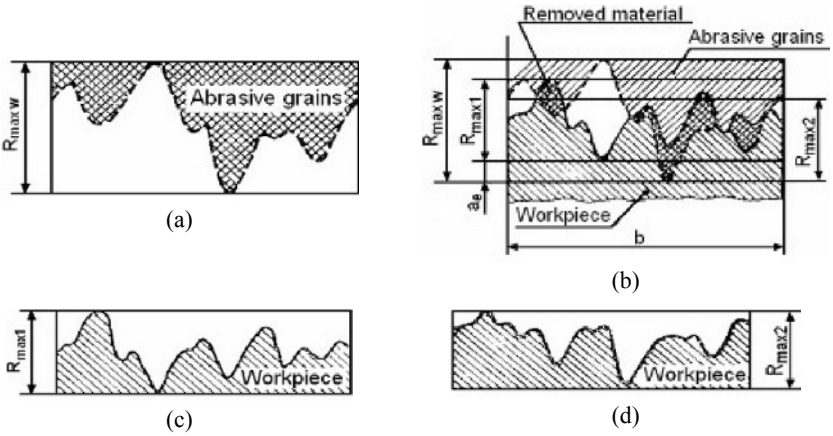

Figure 5.5. Roughness generation for random distribution of abrasive grains in grinding wheel. R_{max1} − maximum height of initial surface profile, R_{maxw} − maximum height of active surface profile, R_{max2} − maximum height of resultant surface profile. (a) active topography of grinding wheel; (b) initial workpiece profile; (c) projection of both profiles, and (d) resultant workpiece profile

A scheme of roughness generation for random distribution of abrasive grains in the grinding wheel is shown in Figure 5.5. In this case the resultant surface roughness depends on the active topography of the wheel surface (in separate steps) and infeed value a_e. Grinding wheel cutting properties and, as a result, grinding effects may be influenced by a dressing process (mainly dressing depth and dressing feed) which may change the topography of active surface of grinding wheel.

The work material characteristics, mainly thermal and mechanical properties, may strongly influence surface layer generation. For example, thermal properties influence energy partition in grinding, which change grinding temperatures as well as temperature gradients and rates. This, in turn, influences surface generation.

The third important group of factors influencing the process of surface layer creation consists of kinematical parameters of grinding: wheel speed and feed motions (e.g., work speed and depth of cut) that influence creation of surface microgeometry. These parameters also generate fields of temperatures and fields of stresses in the work material during grinding that, in turn, create such properties of the surface layer like microhardness, residual stress, structure changes or even burns and microcracks.

The fourth group of factors that influence creation of the surface layer in grinding is of environmental character. Grinding, generally, is a highly energy-consuming process that needs application of cutting fluids to lubricate the cutting zone and remove some heat generated to lower grinding temperatures, which usually have a detrimental effect on surface layer properties. The kind of grinding fluid, its properties and strategy of fluid supply are of essential importance. Also in dry grinding environmental effects (e.g., oxidation) may strongly affect surface integrity.

5.1.2.3 Non-traditional Machining

In non-traditional machining processes material is removed as a result of very complicated physical, electrochemical and mechanical phenomena.

In EDM (electrodischarge machining) process the material is removed during controlled electrical discharges into the interelectrode gap. They include such phenomena as: material melting, evaporating and sometimes mechanical disruption resulting from high internal stresses created due to very high temperature gradients. It is worth noting that the mean plasma temperature in the discharge channel is in the range of 6000–12000 K. As a result, the surface layer after EDM has a very complex structure with properties somewhat different from those inside the workpiece. Properties of the surface layer created in EDM process depend mainly on the energy and power of electrical discharge, which can be changed by varying the amplitude of pulse voltage and pulse current, time of pulse and time of the interval between successive pulses. The properties of the dielectric, its hydrodynamic parameters and properties of the machine and electrode-tool also have a significant part in creation of the surface layer properties.

In LBM (laser beam machining) the material is, similarly as in EDM, removed as a result of thermal processes. The laser beam is emitted by a laser focused on the very small surface of the machined material, which causes the power density of the laser beam to be very high (10^8–10^{14} W/cm^2). The laser beam is partly reflected and partly absorbed by the machined surface. The absorbed energy is exchanged into heat and the resulting temperature in the machined area can be at least the same as in EDM process. Moreover, the surface layer after LBM has a very complex structure with properties different from those of the bulk material. Properties of the surface layer generated in LBM process depend mainly on the power of the laser beam and power density on the machined surface. The properties of the machined material and the type of atmosphere in the machining area also significantly affect the surface layer properties.

In ECM (electrochemical machining) process, the material is removed as a result of the electrochemical dissolution process, which is carried out in an electrolyte. During this process, atoms on the machined surface become ions, which migrate in the electrical field generated between anode (machined material) and cathode (electrode-tool) into the interelectrode gap. Then, the material is removed atom by atom at a temperature lower than 100 K. Because of these facts, in the ECM process the machined surface properties are created as a result of electrochemical phenomena, whose course depends mainly on interelectrode voltage, current density, properties of both machined material and applied electrolyte. It is worth noting that in the ECM process the additional internal stresses in the surface layer are not created, however, under some conditions the oxides and hydroxides can form on the machined surface and change surface layer properties. In order to obtain the uniform machined surface integrity special attention should be paid to electrolyte hydrodynamic conditions.

In USM (ultrasonic machining) process, the tool vibrates with an ultrasonic frequency and the abrasive grains are transported (usually using a special liquid) between vibrating tool and machined material. When the power and the amplitude of the vibrating tool have proper values, the tool hits the abrasive grains and some amount of material is removed due to plastic deformation, cracking, chipping and

cavitation phenomena. Taking the cavitation phenomena into account, the surface-layer properties depend mainly on the amplitude, frequency and power of the ultrasonic vibrations, the sort and dimensions of abrasive grains, concentration of abrasive grains in the liquid and mechanical properties (hardness, plasticity, brittleness) of the tool and machined material.

5.2 Surface Texture in Typical Machining Operations

5.2.1 Turning and Boring Operations

Turning basically generates cylindrical parts with a single-point tool being, in most cases, stationary with the rotating workpiece. As a result, the surface texture contains parallel lays (precisely helical texture). The average wavelength ($R\lambda_q$) across the lay is almost identical to the feed rate, whereas the value with the lay is much smaller and distorted by vibrations, tearing and built-up depostions. According to Sandvik Coromant, turning operations are performed with the following parameters: finish (f = 0.1–0.3 mm/rev, a_p = 0.5–2.0 mm), medium (f = 0.2–0.5 mm/rev, a_p = 1.5–5.0 mm) and rough (f = 0.5–1.5 mm/rev, a_p = 5–15 mm). The generated surface finish and dimension tolerance are affected by a combination of nose radius size, feed rate, machining stability, workpiece, tool clamping and machining conditions. The theoretical maximum profile height R_{tmax} or the theoretical average roughness R_{ag} in external and internal turning with a single-point cutting tool is largely determined by the well-known relationship between the feed rate (f) and nose radius (r_ε).

$$R_{t\max} = \frac{0.125 f^2}{r_\varepsilon} \text{ or } R_{ag} = \frac{0.321 f^2}{r_\varepsilon}, \text{ [mm]} \tag{5.1}$$

Equation 5.1 clearly indicates that the minimum height of irregularities on the machined surface can be achieved by minimizing feed rate and maximizing tool nose radius. In precision operations with small feed rates, the cutting-edge preparation and its radius are key factors in obtaining smooth machined surfaces. In order to improve production performance, the wiper indexable inserts have provided turning with higher feed rate. Principally, they are designed in the form of a carefully composed combination of radii with some insert geometry modification (Figure 5.6). In consequence, such modified cutting tool inserts provide smaller profile height due to a smoothing out effect on the turned surface.

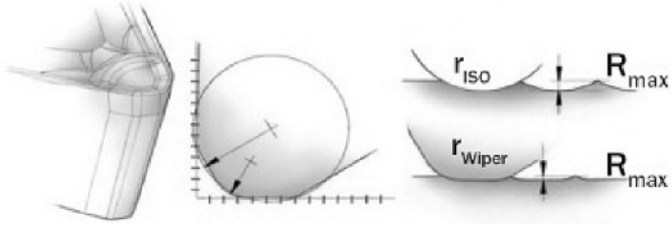

Figure 5.6. Wiper geometry and corresponding surface finish [2]

For instance, using the largest permissible 1.2 mm nose radius at a feed rate of 0.15 mm/rev might generate a surface finish of 1 μm R_a on a low alloy steel component. It should be noted that wiper inserts allow to double feed rate in comparison to standard rounded inserts when keeping the same value of R_a parameter.

Figures 5.7(a) and (b) present some representative surface topographies obtained in finish/precision turning operations of C35 carbon steel and aluminum alloy respectively. Appropriate surface structures were periodic anisotropic (determination coefficient $s_{Kd} = 0.58$) and mixed periodic anisotropic with lower value of $s_{Kd} = 0.43$ and thereby with higher random component.

The internal turning (*boring*) operations are performed with stationary tools, as opposed to boring operations with rotating tools, like in machining centers. A general rule is to minimize tool overhang and to select the largest possible boring bar diameter in order to obtain the best possible stability and thereby accuracy. Moreover, the radial deflection of the boring bar and vibration tendency can be minimized while a nose radius is somewhat less than the cutting depth.

The boring bar deflection is dependent on the bar material, hence solid carbide bars and, recently, tuned boring bars (silent tools) with integrated damping elements are used to improve the dynamic behavior of these tools. As a result, machining of holes with a ratio of the hole length to its diameter (L/D) up to 14 can be performed with good surface finish, as indicated in Figure 5.8.

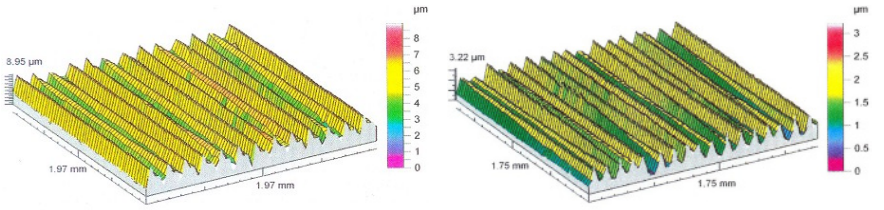

(a) (b)

Figure 5.7. 3D images of surfaces after finish turning of C35 carbon steel with P20 carbide tools at $v_c = 3.2$ m/s and $f = 0.15$ mm/rev (a), and aluminum alloy AK12 with KD100 diamond tools at $v_c = 6.6$ m/s and $f = 0.1$ mm/rev (b). Roughness parameters: (a) $S_a = 1.23$ μm, $S_t = 8.95$ μm, $S_{sk} = -0.0418$, $S_{ku} = 2.38$; (b) $S_a = 0.563$ μm, $S_t = 3.22$ μm, $S_{skv} = 0.262$, $S_{ku} = 2.01$

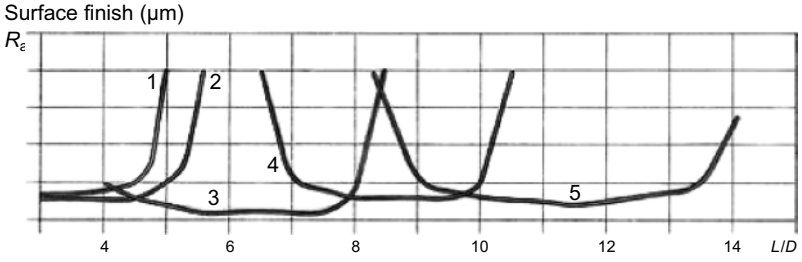

Figure 5.8. Surface finish vs. L/D factor in boring operations. 1-solid steel bar, 2-carbide bar, 3-short, damped bar, 4-long, damped bar, 5-extra long, damped bar. Source: Sandvik Coromant [2]

5.2.2 Drilling and Reaming Operations

Hole making is among the most important operations in manufacturing and one of the most common is drilling. *Drilling* is associated with subsequent machining operations such as trepanning, counterboring, reaming and boring. Common to all these processes is a main rotating movement combined with a linear feed. Drilling can be performed with classical twist drills, brazed and solid cemented carbide twist drills, drills with through-collant holes and indexable insert drills of various insert clamping systems.

With modern tools, the hole quality is good and subsequent operations for improving accuracy and surface texture are often unncessary. The achievable hole tolerances are almost halved to +0.25 mm (IT 7) and with moderate feed possible surface finish is 0.5 μm R_a. Typically, hole tolerances for brazed and solid cemented carbide twist drills can be within IT8 and finishes within 1 μm R_a depending on drill length, tool holding and machining parameters.

Figure 5.9 presents an exemplary surface topography of a cylindrical hole surface and a set of appropriate 3D roughness parameters. For this case the surface structure is mixed anisotropic with determination coefficient of S_{Kd}=0.16.

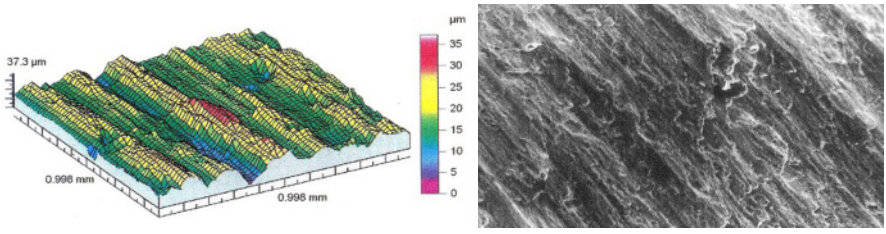

(a) (b)

Figure 5.9. Scanned topography (a) and optical image at magnification 200× (b) of surfaces after drilling of C45 carbon steel with high-speed steel twist drill at v_c = 0.6 m/s and f = 0.15 mm/rev. Roughness parameters: (a) S_a = 3.59 μm, S_t = 37.3 μm, S_{sk} = –0.1, S_{ku} = 3.2

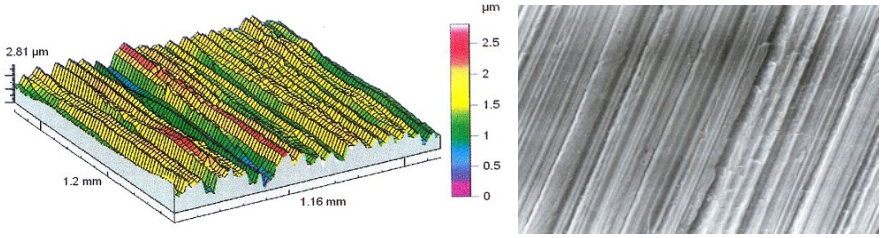

(a) (b)

Figure 5.10. Scanned topography (a) and optical image at a magnification of 200× (b) of surfaces after finish reaming of C45 carbon steel with a Ti(C,N) coated high-speed steel reamer at v_c = 0.8 m/s and f = 1.4 mm/rev. Roughness parameters: S_a = 0.356 μm, S_t = 2.81 μm, S_{sk} = –0.191, S_{ku} = 2.57

Accuracy of the hole (achievable tolerances after reaming are within IT6-10) and quality of finish produced by *reaming* depend primarily upon the condition of the starting hole, rigidity of the machine and fixture, correct speed and feed, and a suitable and properly applied cutting fluid. To obtain smooth hole finishes (R_a parameter below 0.63 μm) reamers must operate without chatter or process instabilities. In comparison to the effect of drilling from Figure 5.9, Figure 5.10(a) presents the surface topography of the hole surface made by reaming and appropriate 3D roughness parameters. For this case the surface structure is random anisotropic with isotropic component of 6.12%.

5.2.3 Milling Operations

The surface finish in milling is, in comparison to turning and boring, affected by a number of additional factors resulting from differences in tooling construction and process kinematics. The formation of rouhgness in *face* and *peripheral* (slab) milling operations using multitoothed cutters is shown schematically in Figure 5.11.

The surface roughness or waviness in *face milling* operations is determined by insert nose geometry, feed per tooth (insert), spindle and cutter runout, and stability of the workpiece and fixturing interact. When a radiused insert is used, the theoretical average roughness R_a (CLA) can be calculated as

$$R_{at} = \frac{r - \sqrt{r^2 - \left(\frac{f_t}{2}\right)^2}}{2}, \tag{5.2}$$

where: r is nose radius and f_t is feed per tooth (insert).

It should be noted that Equation 5.2 is exact for a single-toothed cutter called *fly mill* without spindle runout. In finish milling, fine finishes are often produced using cutters with corner chamfered inserts or wiper inserts. When using corner chamfer inserts, the chamfer should be parallel to the machined surface and the feed per

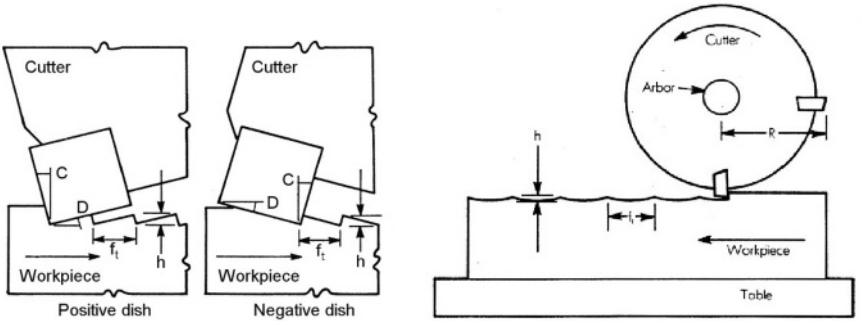

Figure 5.11. Schemes to calculate theoretical roughness in face (a) and peripheral (b) milling operations

tooth should be less than the chamfer length. In practice, the insert land may not always be parallel to the direction of the feed and both negative and positive dishes are used, as depicted in Figure 5.11. In such a case, an estimate of peak-to-valley (P–V) roughness height is based on the following formula:

$$R_{zt} = \frac{f_t}{\tan C + \cot D}, \tag{5.3}$$

where: f_t is feed per tooth (insert), D is the face clearance angle (dish), C is the lead angle if dish is positive or trailing angle if dish is negative.

In most face milling applications, the spindle is tilted slightly in the direction of feed to provide relief or dish behind the cut. Spindle tilt produces a concave machined surface and results in a flatness error. The depth of the concavity d_f can be calculated from the Kirchner–Schulz formula [3]:

$$d_f = \tan\Theta\left[\frac{D_e}{2} - \left(\frac{D_e^2}{4} - \frac{e^2}{4}\right)^{\frac{1}{2}}\right], \tag{5.4}$$

where: D_e is the effective diameter of the cutter, e is the width of the workpiece and Θ is the spindle tilt angle.

The P–V roughness height generated by up and down peripheral milling can be obtained by means of the following formula:

$$R_{zt} = \frac{f_t^2}{8\times\left(R \pm \frac{f_t \times N}{\pi}\right)}, \tag{5.5}$$

where: R is cutter radius, N is number of teeth in cutter and f_t is feed per tooth (insert). Sign (+) is valid for up milling and (–) for down milling.

Figures 5.12 and 5.13 present exemplary surface topographies of milled surfaces after finish peripheral and face milling operations respectively, along with sets of appropriate 3D roughness parameters.

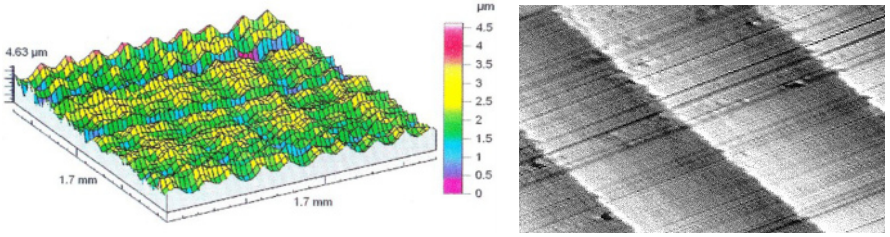

(a) (b)

Figure 5.12. Scanned topography (a) and optical image at a magnification of 160× (b) of surfaces after finish peripheral milling of aluminum-silicon alloy (0.5% Si) with a CrN coated carbide cutter at $v_c = 4.1$ m/s and $f = 7.2$ m/min. Roughness parameters: $S_a = 0.51$ µm, $S_t = 4.63$ µm, $S_{sk} = -0.12$, $S_{ku} = 3.23$, surface structure-periodic anisotropic

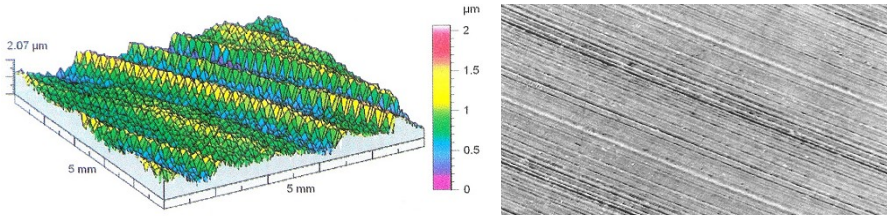

(a) (b)

Figure 5.13. Scanned topography (a) and optical image at a magnification of 250× (b) of surfaces after finish face milling of low alloy steel with a TiN coated P10 carbide end-mill of 14 mm in diameter at $v_c = 4.6$ m/s and $f = 0.96$ mm/rev. Roughness parameters: $S_a = 0.232$ µm, $S_t = 2.07$ µm, $S_{sk} = 0.19$, $S_{ku} = 2.75$, surface structure-mixed anisotropic

5.2.4 Hard Machining Operations

Figure 5.14 presents some characteristic surface profiles and corresponding 3D topographies for hard turning (HT) with CBN (Figure 5.14(a)) and mixed ceramic (Figure 5.14(b)) tools at the same cutting parameters (v_c=100 m/min, f=0.1 mm/rev and a_p=0.2 mm). It can be noted that the relevant surface profiles contain more sharp (CBN HT) or blunt (MC HT) peaks with characteristic lateral smaller flashes (circled in upper surface profiles) resulting from a side-flow effect.

3D surface roughness parameters for the surface turned with CBN tools with a tool nose of 0.8 mm and feed of 0.1 mm/rev are: S_a=0.34 µm, S_z=2.93 µm, S_{ku}=3.28 and S_{sk}=1.68. On the other hand, the corresponding roughness parameters obtained after turning of a 60 HRC alloy steel with mixed ceramic tools are: S_a=0.53 µm, S_t=3.47 µm, S_{ku}=2.27 and S_{sk}=1.43.

Characteristic surface profiles generated by conventional and wiper ceramic tools are magnified in Figure 5.15. It was observed that due to the smoothing effect

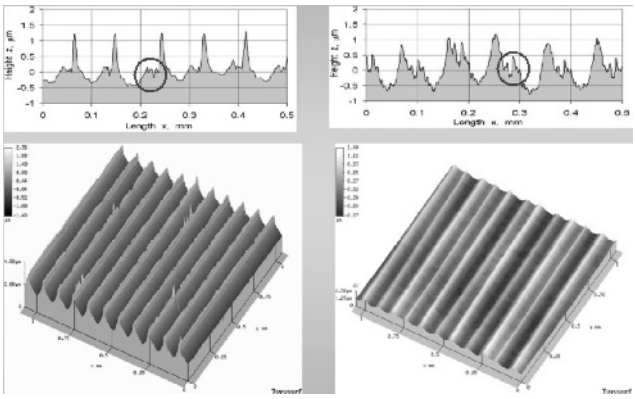

(a) (b)

Figure 5.14. Typical surface profiles and corresponding 3D visualizations produced in CBN HT (a) and MC HT (b) hard turning operations [4]

(a) (b)

Figure 5.15. Characteristic shapes of the profiles generated in turning with conventional (a) and wiper (b) ceramic tools for constant cutting speed of 100 m/min and feed rate of 0.1 mm/rev. Vertical magnification –7000×. Horizontal magnification –200× [5]

wiper tools produce blunt irregularities with the RMS profile slope ranging from $R\Delta q = 1.5°$ to 5.5° as in Figure 5.15b. On the other hand, more sharp profiles with $R\Delta q$ values of 5–10° were recorded for standard tools (Figure 5.15(a)). As can be expected, distinct differences in surface profile shapes will result in corresponding bearing area values and further in the contact capabilities of surfaces.

5.2.5 Broaching and Burnishing Operations

Broaching is usually employed to machine fast in a single stroke some form of external or internal surfaces on a part. Typical internal broaching operations are the sizing of circular and noncircular holes and cutting of serrations, slots, straight or helical internal splines, gun rifling, and keyway cutting. Good finish and accuracy are obtainable over the life of a broach because roughing and finishing are done by separate teeth. Hence, it competes favorably with other processes, such as boring, milling, shaping, and reaming to produce similar shapes. As can be seen in Figure 5.4 broached surfaces with 0.4 μm R_a roughness and IT6(5) dimension tolerance are achievable. Typical broaching operations are used to produce a surface finish of 3.2–0.8 μm R_a, which corresponds to IT 9(8) ISO tolerance. Surface profile contains randomly distributed irregularities and texture lays are parallel to the linear travel of a broach.

Roller burnishing is a surface finishing operations in which hard, smooth rollers or balls are pressed against the work surface to generate the finished surface

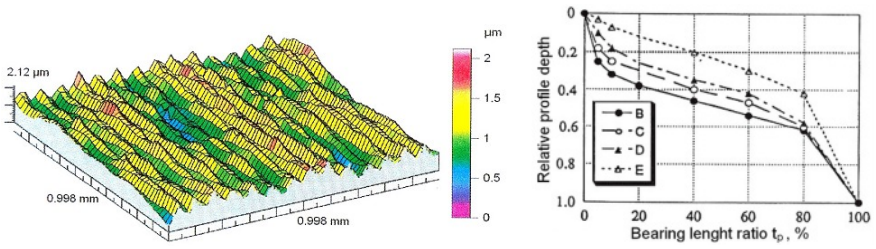

(a) (b)

Figure 5.16. Scanned topography after diamond burnishing of 45C steel with $v_b = 0.8$ m/s and $f = 0.07$ mm/rev (a) and the bearing curves of surfaces with $R_a = 0.1$ μm processed by: (B) grinding, (C) polishing, (D) superfinishing and (E) burnishing (b). Roughness parameters: $S_a = 0.245$ μm, $S_t = 2.12$ μm, $S_{sk} = 0.14$, $S_{ku} = 2.63$, surface structure: mixed-periodic anisotropic

through plastic deformation. Burnishing is used to improve surface finish, control tolerance, increase surface hardness, and induce compressive residual stresses in order to improve fatigue life. Turned, bored and milled surfaces with roughnesses between 2 and 5 μm are suitable for burnishing because they have uniform asperities. When the initial surface roughness is $R_a = 1.5–2.0$ μm, it is reduced down to 0.05–0.3(0.5) μm (Figure 5.16(b)) by single or multipass operations and the bearing length ratio t_p30 can approach 30–50%, as shown in Figure 5.16(b). Part dimensional accuracies can often be controlled within ±5 μm with proper part preparation.

5.2.6 Grinding Operations

Grinding is often used to produce parts with fine surface finishes and tight tolerances. As can be seen in Figure 5.4 ground surfaces with 0.1 μm R_a roughness and IT6(5) dimension tolerance are achievable. Typical grinding operations are used to produce surface finish of 1.6–0.1 μm R_a that corresponds to IT (8-5) ISO tolerance. The surface profile contains randomly distributed irregularities and texture lays depend on the grinding method used (they are parallel in cylindrical grinding, radial in face grinding, concentric in cup grinding). Figures 5.17 and 5.18 present exemplary surface topographies and optical images of ground surfaces under defined operation conditions, along with sets of appropriate 3D roughness parameters and characteristic surface features.

When the wheel is dressed frequently so the wheel wear is not a significant variable, the ground surface finish depends primarily on the grinding conditions, wheel type and wheel dressing method. In particular, smoother surface finishes are usually obtained with fine-grained wheels; as the wheel grit size increases, the effective spacing of cutting edges decreases, so the roughness peaks are more closely spaced and thus shorter. Also, a smoother finish is usually obtained if the wheel hardness increases. Finally, it should be noted that the ground surface finish deteriorates markedly if chatter occurs.

A number of equations for the geometric roughness in grinding have been proposed [6]. For example, the theoretical R_a value in cylindrical plunge grinding can be estimated by the equation

$$R_{at} = R_1 \left[\frac{v_w a}{v_s} \right]^x , \tag{5.6}$$

where: v_w is the workpiece velocity, v_s is the wheel velocity, a is the depth of cut during the spark-out phase, and R_1 is empirical coefficient and exponent x=0.15–0.6.

On the other hand, this roughness parameter in cylindrical grinding can be calculated as follows:

$$R_{at} = K_3 \left(\frac{2\rho v_{fd}}{\mathrm{HRC}} \right)^{0.5} \left(\frac{a_d}{v_{fd}} \right)^{0.3} \frac{F_n'^{\frac{1}{3}}}{D_{eq}^{\frac{1}{6}} V_{bm}^{0.13}} , \tag{5.7}$$

where: K_3 is a constant that considers wheel characteristic, $2\rho(d_g)$ is the grain diameter, v_{fd} is feed during wheel dressing, a_d is the depth of cut during the spark-

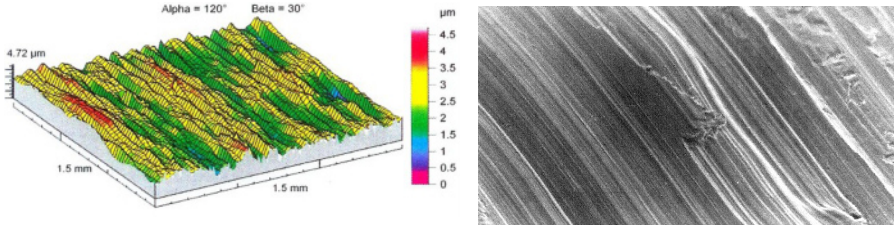

(a) (b)

Figure 5.17. Scanned topography (a) and optical image at a magnification of 300× (b) of surfaces after cylindrical-plunge grinding of 42HRC low alloy steel with a 38 A 60 K 5 V BE 43 grinding wheel at $v_c = 31$ m/s, $v_w = 0.52$ m/s and infeed $f_r = 0.006$ mm/rev. Roughness parameters: $S_a = 0.478$ μm, $S_t = 4.72$ μm, $S_{sk} = -0.322$, $S_{ku} = 3.3$, surface structure-random anisotropic, isotropic content – 13.8%

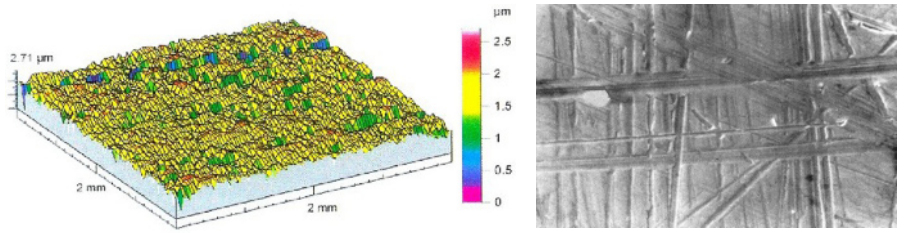

(a) (b)

Figure 5.18. Scanned topography (a) and optical image at a magnification of 200× (b) of surfaces after surface grinding on a vertical-spindle grinder of 65HRC low alloy steel with a 38 A 60 K 5 V BE 43 grinding wheel at $v_c = 31$ m/s, $v_w = 0.48$ m/s and axial feed $f_a = 0.008$ mm/rev. Roughness parameters: $S_a = 0.2$ μm, $S_t = 2.71$ μm, $S_{sk} = -1.58$, $S_{ku} = 7.15$, surface structure-random anisotropic, isotropic content –6.19%.

out phase, D_{eq} is the equivalent wheel diameter, V_{bm} is the percentage volume of bond material in the wheel, F_n' is specific normal load.

The finish in straight surface grinding is found empirically to depend only on the speed ratio v_w/v_s, and the roughness increases with this ratio. In creep feed grinding, the empirical roughness is generally proportional to the product $(v_w/v_s)\bullet a^{1/2}$.

5.2.7 Non-traditional Machining Operations

The EDM process produces the spark-machined surfaces having a matte appearance similar to a shot-blasted surface. It consists of very small spherical craters as a result of the metal being removed by individual sparks, as shown in Figure 5.19. The finish is therefore non-directional and very suitable for holding a lubricant. Surface finishes of 0.25 μm R_a and better have been obtained, typically 0.8–3.2 μm

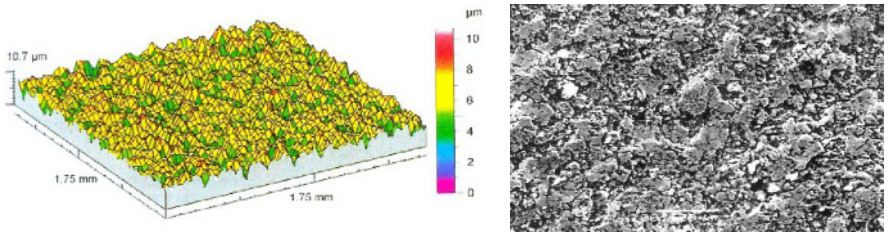

(a) (b)

Figure 5.19. Scanned topography (a) and optical image at a magnification of 200× (b) of surfaces after WEDM of tungsten carbide with current $I = 8$ A, voltage $V = 80$ V, impulse time $t_{imp} = 0.6$ µs, interval time $t_{int} = 4.3$ µs. Roughness parameters: $S_a = 1.03$ µm, $S_t = 10.7$ µm, $S_{sk} = -0.465$, $S_{ku} = 3.47$, surface structure-random anisotropic, isotropic content −56.6%.

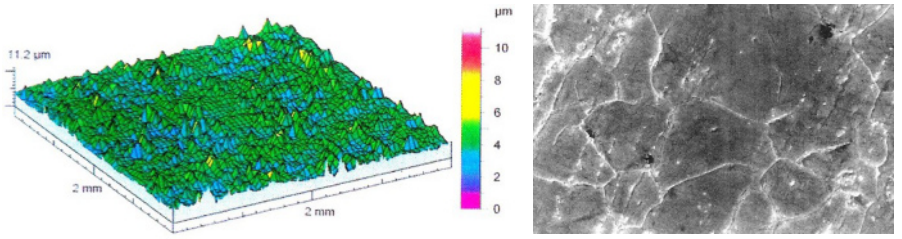

(a) (b)

Figure 5.20. Scanned topography (a) and optical image at magnification 150× (b) of surfaces after ECM of special alloy U-500 with current I=1500 A, voltage V=12 V, NaCl electrolyte. Roughness parameters: $S_a = 0.662$ µm, $S_t = 11.2$ µm, $S_{sk} = -1.61$, $S_{kuv} = 6.65$, surface structure-random anisotropic, isotropic content −37.2%.

in finishing and 6.3−12.5 µm in roughing EDM operations. Irregularities have small radii of peaks, about 2−10 µm, and they are inclined at relatively large angles ($R\Delta q$ is between 10−30°). These profile characteristics cause the bearing ratio of the EDM profile to be extremely low. The random surface texture is created by individual electric sparks and is termed as point (P) [7, 8].

After ECM, the initial surface texture disappears fully during the electrochemical dissolution and its influence on the final state of the surface can be neglected. The height of irregularities depends mainly on the current density, and decreases when this parameter increases. The surface texture is undetermined and the surface produced is matte or semi-matte. The obtainable value of R_a is between 0.32 to 1.25 µm. Very soft peaks, in comparison to milled and ground surfaces, with radii of 90−220 µm, are produced within the surface profile. Typically, they are characterized by the $R\Delta q$ parameter between 2°30' and 8°. The bearing curve is similar to that for ground surfaces.

Figure 5.20 presents exemplary surface topography and optical image of ECM surfaces under defined operation conditions, along with sets of appropriate 3D roughness parameters and characteristic surface features.

5.3 Strain Hardening and Microstructural Effects in Machining

5.3.1 Physical Background

In metal cutting, the chip formation area consisting of three characteristic zones I–III can be schematically presented as in Figure 5.3(a). The extensive primary deformation (PDZ) zone is distinguished within this area by a number of slip lines including the entry boundary on which plastic deformation begins and the exit boundary on which chip material is entirely work hardened. A material particle during deformation is more intensively deformed between the shear band and the upper boundary. Then, the material adjacent to the tool chip interface is subsequently deformed in some depth due to intensive interfacial friction. The relevant region is called the secondary deformation (SDZ). Additionally, the tertiary deformation zone (TDZ) localized below the cutting edge in depth corresponding to the thickness of subsurface layer is separated.

In general, the shear yield strength in cutting exceeds the shear yield strength of a bulk material by a factor of 2–4, depending on the intensity of plastic deformation in the primary deformation zone (PDZ). As shown in Figure 5.21, the cutting edge radius (in general, cutting-edge preparation) and the rake angle are predominant factors controlling the distribution of elastic stresses in the subsurface layer. As shown in Figure 5.21(b), the compressive zone expands visibly when cutting with rounded cutting edge (higher ratio of the cutting edge radius r_n to undeformed chip thickness h) and larger negative rake angles. As a consequence, in such cases the work-hardening effect will probably be more intensive due to the plowing effect.

Figure 5.21 demonstrates that the machined surface is formed by fracture under shearing stress. With ductile metals and alloys, both sides of a shear fracture are plastically strained, so that some degree of plastic strain is an obvious feature of machined surfaces. The amount of strain and the depth below the machined surface to which it extends can vary greatly, depending on the material being cut, the tool geometry, and the cutting conditions, including the presence or absence of a lubricant.

In grinding, the high cutting speeds result in temperatures at the grain tip that

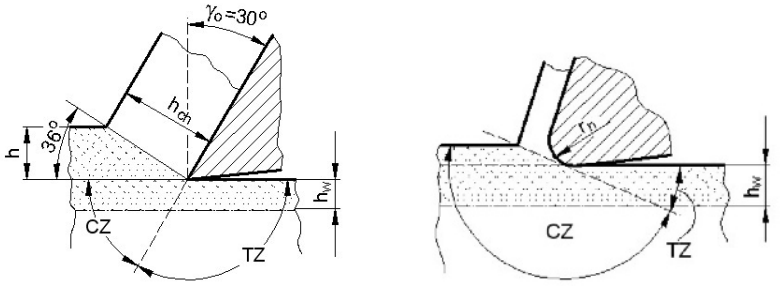

Figure 5.21. Distribution of stresses in the subsurface layer for sharp (a) and rounded (b) cutting edge [4, 9]. CZ compressive zone, TZ tensile zone.

may be as high as 1700°C. Moreover, 60 to 90% of the total energy consumed in grinding flows instantaneously into the workpiece, causing rapid local increases in temperature. As a result, various forms of thermal damage such as dimensional errors, material structural changes, burning and surface cracking and high tensile residual stresses can occur in grinding [10]. These effects can also occur, but not so intensively, in machining operations with tools with geometrically defined geometries, especially in dry, hard and HSM processes of difficult-to-machine materials (hardened steels, austenitic stainless steels, titanium-based alloys, nickel- and cobalt-based superalloys).

5.3.2 Built-up-edge Phenomenon

Under some machining conditions, usually at cutting speeds ranging from 30 to 60 m/min, the severe friction between the chip and the tool causes that the chip material welds itself to the tool face and forms a pile of material, which is referred to as a *built-up-edge* (BUE). Imaginarily, built-up formation is similar to what happens when you walk through mud. Due to extreme work hardening, the hardness of the BUE when machining steels is about 600–650 HV or more. Often the built-up-edge continues to grow and then breaks up when it becomes unstable and the broken pieces are carried away by the underside of the chip and randomly deposited on the new workpiece surface. Figure 5.22 shows these mechanisms and the rough workpiece surface with characteristic leaps. One cycle including formation, growing and breaking up takes about 0.01–0.02 μs, which means that 10–500 leaps of 2–30 μm in height can be formed on the machined surface.

The built-up formation is commonly observed when form turning, broaching, reaming and threading using uncoated high-speed steel tools at relatively low cutting speeds. The BUE is one of the principal factors adversely affecting surface finish. The gradual growth and rapid decay of the size of the BUE causes a sawtoothed surface, which is characteristic of the BUE component of surface roughness. In addition, the cutting tip becomes larger and the desirable diameter of the workpiece changes when a built-up-edge is present. It should be noted that apart from BUE sharp debris occurs on the part of the machined surface where cutting tool loses contact with the workpiece.

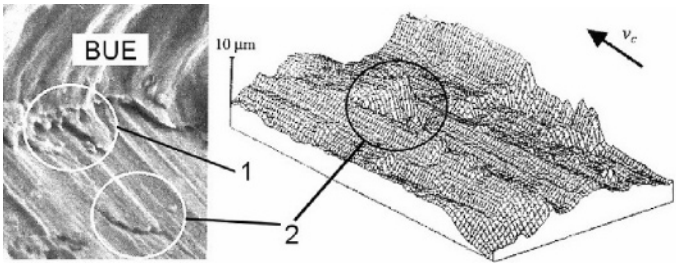

Figure 5.22. SEM image of built-up-edge formation and its transfer on the machined surface. 1 – place where BUE breaks down, 2 – leap on the machine surface.

5.3.3 Microstructural Effects (White Layer Formation)

5.3.3.1 Traditional Machining

White layer formation is a specific problem in drilling and hard machining, since these processes produce the highest surface temperature within the part. In drilling, white layer formation results from the heating produced by both the cutting action of the point and the rubbing of the corner. Although the drill removes much of the heat-affected layer as it penetrates the workpiece (Figure 5.23), some sections near the hole entry and at significant depths may remain after the operation.

During hard machining, the austenite temperature of the workpiece material in the contact zone is reached during extremely short time of approximately 0.1 ms and structural changes must be expected. A metallurgically unetchable structure, called a "white layer", followed by a dark etching layer result from microstructural changes observed in hard machining, as for example on AISI 52100 steel surfaces of 60 HRC hardness (Figure 5.24).

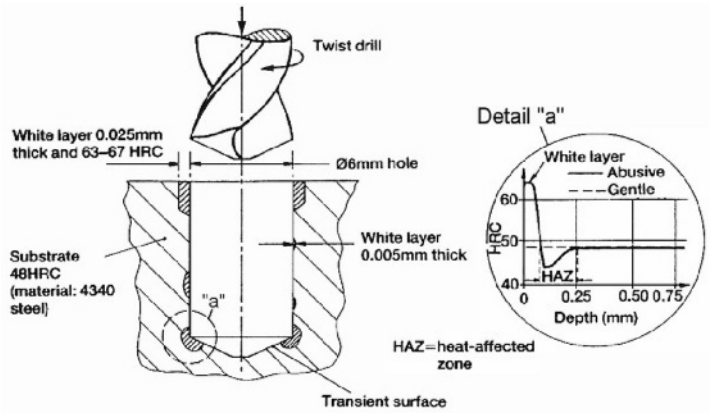

Figure 5.23. White layer formation when drilling steel [3]

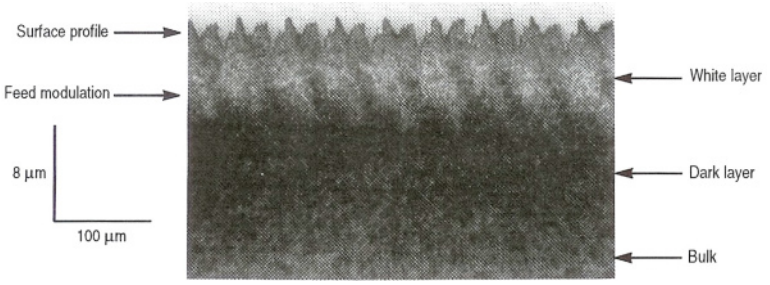

Figure 5.24. Optical micrograph of microstructural changes in a hard turned surface of 52100 steel [4]

White layers consist of over 60% austenite, which is a non-etching white component in contrast to the dark martensite scoring. Due to this fact, it is suggested [11] that the term "white layer" is misleading and it is proposed to distinguish two groups of this structure's appearance in micrographs. When applying special etching chemicals or increased etching time, white layers of the first group remain white. On the other hand, chemicals affect white layers of the second group and a fine-grained martensitic structure becomes visible. Both types of white layer are distinguished by high brittleness and susceptibility to cracking and therefore they are classified as a defect of the machined components.

5.3.3.2 Grinding

As was discussed above a white layer is formed in the machining surface in many machining processes. However, grinding seems to be more sensitive to form a white layer at a surface due to the high temperatures, rapid heating and quenching, which result in phase transformations. The second reason is the relatively high heat flow into the workpiece that is caused by the poor heat conductivity of the conventional grinding aluminum oxide wheels and the intensive rubbing and plowing effects produced by the negative rake angles of the individual abrasive grains. On the other hand, the white layer formed in a grinding process is a newly developed machining method called grinding hardening, which is applied in many manufacturing industries. However, in such a case the basic principle of the grind-hardening process is to use the grinding heat effectively. It was documented that the properties of white and dark layers by hard turning and grinding are fundamentally different in four aspects: surface structure characteristics, microhardness, microstructures and chemical composition.

The white layer after grinding (similar to a hard-turned surface) usually is followed by a dark layer, with the bulk material underneath. However, the thickness of a turned white layer is usually below 12 μm in abusive turning conditions, while a ground white layer could extend as deep as 100 μm [12]. Moreover, the turned white and dark layers have much more retained austenite (approximately 10–12%) than those of the ground ones (approximately 3%). This results from the fact that the transformation rate of austenite to martensite is more rapid in grinding than in hard turning. For example, for a hardened AISI 52100 bearing steel, the thickness ratio of dark layer to white layer is 2.5:1 for the turned surface and 5.3:1 for the ground surface, which is likely a result of differences in strain hardening and heat generation in theses two machining processes.

The microstructure of the turned dark layer (Figure 5.25(a)) includes the ferrite matrix etched, and the cementite particles, which exhibit their original globular shape and distribution. In contrast, the ground dark layer was etched more severely, hence is softer than the turned one, which is clearly seen from the tempered martensite matrix structure (Figure 5.25(b)). Moreover, the cementite particles protrude from the etched material in the ground dark layer. It can be concluded that thermal processes dominate white layer formation during grinding.

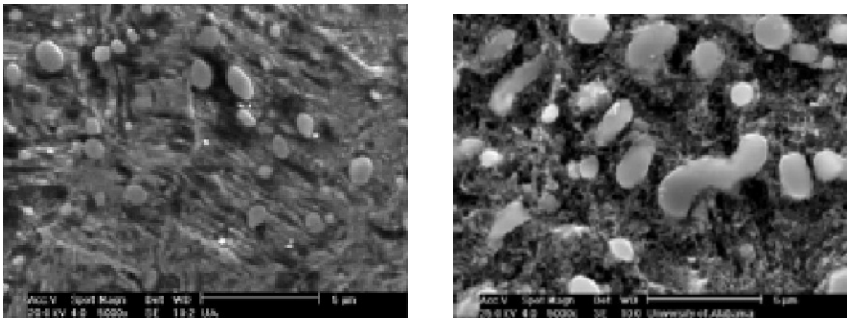

(a) (b)

Figure 5.25. Microstructures of turned (a) and ground (b) dark layer [12]

5.3.3.3 Non-traditional Machining

The subsurface produced by the EDM consists of the metallurgically and chemically affected zones. There are essentially three layers: a melted and re-deposited layer, a heat-affected layer and the bulk material. The outer layer consists of a re-solidified layer that has a re-cast structure. This layer and the outermost regions of the transformed layer often consist of the white layer. The re-cast layer tends to be very hard and brittle with hardness greater than 65 HRC. Beneath the white layer lies an intermediate layer where the heat generated is insufficient to cause melting or a white layer but high enough to induce microstructural transformations. Furthermore, cracks can extend beyond the white layer. An indication of the magnitudes of these layers is shown in Figure 5.26. The depths of the melted layer and the transformed layer are approximately the same and twice the white layer depth. The depth of all layers increases with pulse duration.

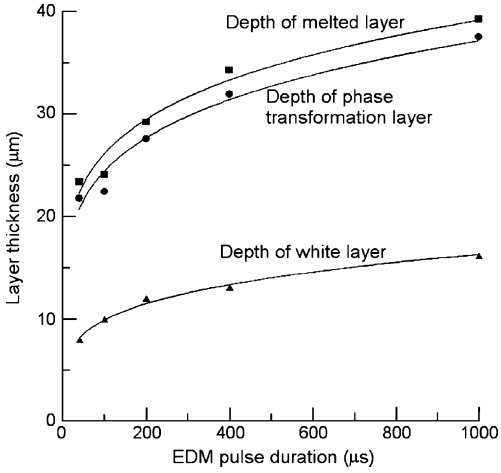

Figure 5.26. Depth of the melted, transformed and white layers on the EDM surface [13]

In addition to the metallurgical changes, there will be chemical changes due to reactions with the dielectric and due to tool deposition. Tool material has been shown to preferentially deposit on the work surface along the crater. Typically, for various types of steel workpieces, the average copper concentration is 10% with diffusion up to 20 μm, which is lesser than the total heat-affected zone. The carbon content of the surface layer also increases, mainly due to reactions with the cracked dielectric. Other processes with dominant thermal effects are laser beam machining, electron beam machining, ion beam machining and plasma beam machining.

In ECM, the material is removed by dissolution during electrolysis without contact between the tool and the workpiece, and there are no sparks, arcs or high temperatures generated. As a result, there are normally no thermal effects or metallurgical changes on ECM surfaces. Unfortunately, when the surface is subjected to chemical attack, grain boundaries are selectively attacked. This phenomenon is termed intergranular attack (IGA). Despite intergranular attack also severe selective etching and pitting can occur under abusive operating conditions.

5.3.4 Distribution of Micro/Nanohardness

5.3.4.1 Traditional Machining

Conventional machining operations produce a variety of alterations of subsurface layer including plastic deformation resulting in the compressed layer of metal. Among the factors influencing the hardening of the surface layer, the depth of cut, undeformed chip thickness (the cutting edge radius) and rake angle are the most important. Examples of the dependence of microhardness on the depth of cut and cutting edge radius in the turning of carbon steel are shown in Figure 5.27. As is evident from Figure 5.27(a), a change of the depth of cut from 0.1 to 1.2 mm at a distance of 20 μm from the surface increases hardness by 17%. It should be noted that an increase of the depth of cut causes the hardness increment to be much intensive than the depth of the hardened layer. As a result, in finishing turning operations the depth of cut must be reduced accordingly. The influence of the cutting edge radius of 5–150 μm on the strain-hardening effect is illustrated in Figure 5.27(b). In this case, hardness at the point localized at 20 μm below the surface increases by 25%.

Moreover, detail "a" in Figure 5.23 shows the microhardness traverse in the subsurface layer produced by abusive drilling of AISI 4340 steel that has been quenched and tempered to 52 HRC. In particular, the white layer of 61 HRC hardness exists to a depth of about 0.03 mm due to re-hardening of the primary martensite. At that point, the hardness drops off rapidly to the value of 43 HRC. The hardness then increases to the base hardness value of 48 HRC at the depth of about 0.25 mm below the surface.

Corresponding microhardness distribution (using a Knoop indenter and 100 g load) in the surface layer from Figure 5.24, is shown in Figure 5.28. It should be noted that the hardness is similar in the white layer of a few micrometers in thickness, whereas the dark layer with an overtempered martensite is substantially softened. The total machining-thermally affected zone is about 20 μm in thickness,

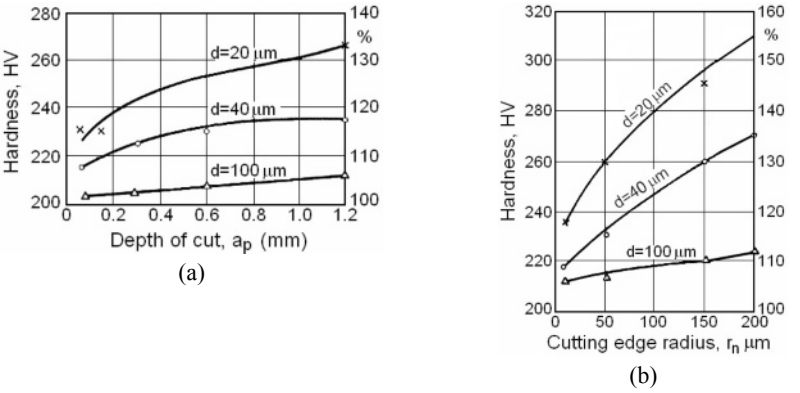

Figure 5.27. Dependence of microhardness of the subsurface layer on depth of cut (a) and cutting edge radius (b) [9]

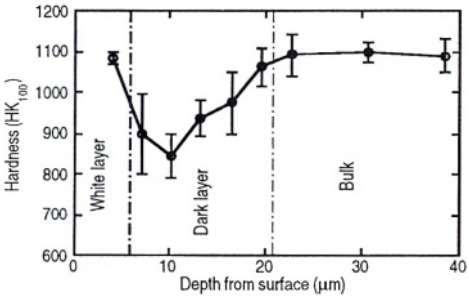

Figure 5.28. Microhardness distribution in a hard turned surface of 52100 steel [4]

which is about one tenth of the depth of cut ($a_p = 200$ μm). Typically, the depth of the white layer increases rapidly with tool wear and cutting speed but for the bearing steel tested a saturation is observed at $v_c = 3$ m/s.

5.3.4.2 Grinding

When certain materials are ground, a phase transformation can be observed in the surface layers. The best example of this is grinding of a hardenable steel, for instance an AISI 4340 steel that has been quenched and tempered to 52 HRC. The surface is heated to a temperature over 840°C and subsequently hardened, and a layer of untempered martensite of 61HRC is produced. The untempered martensite is not only hard but also very brittle. Below the untempered martensite layer, an overtempered martensite layer usually exists that is softer than the base material.

In this zone, the microhardness traverse from the surface to the bulk material indicates a characteristic leap (fault) similar to that shown in Figure 5.23 for a drilled surfaces. As a result, the white layer of over 60HRC in hardness exists at a depth of about 0.03 mm. At this point, the hardness drops rapidly to a value of 43 HRC. The hardness then increases to the base hardness value of 52 HRC at a depth of about 0.25 mm below the surface.

Figure 5.29 shows the measured microhardness profiles below the ground surface produced on an AISI 52100 bearing steel. This microhardness profile, Figure 5.29, indicates that the white layer is much harder than the dark layer and bulk material. It can also be seen that the microhardness of the ground white layer is about 40% higher than that of the turned one. Hardness variation is observed due to the randomly distributed hard cementite particles [14].

Figure 5.30 shows the influence of the workpiece surface speed v_w and the material removal rate on the depth of heat-affected zone (HAZ) when grinding a 100Cr6 V bearing steel with a white ceramic (aluminum oxide) wheel at a wheel surface speed of 45 m/s. As can be seen from Figure 5.30 the depth of the HAZ decreases with decreasing the wheel speed and particularly on decreasing the machining removal rate from 8 to 2 mm^3/mm s.

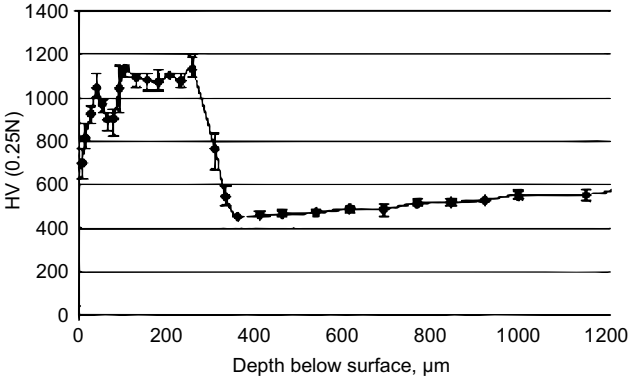

Figure 5.29. Microhardness profile of the ground surface [14]

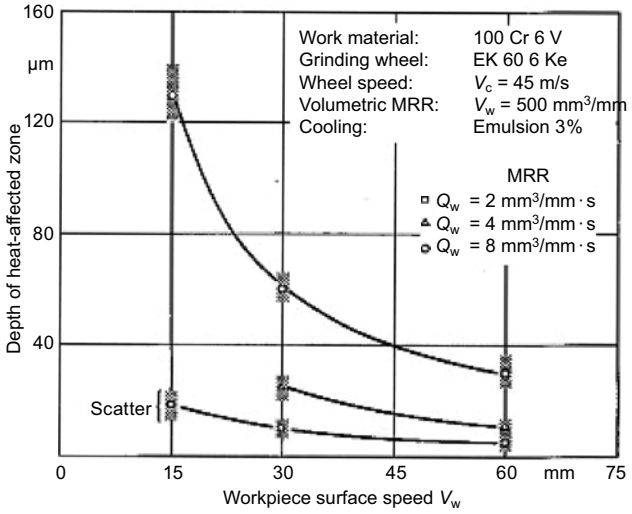

Figure 5.30. Influence of work surface speed and machining removal rate on the depth of heat-affected zone [15]

5.3.4.3 Non-traditional Machining

As with other electrical discharge methods, EDM produces a recast layer of 0.002–0.13 mm depth. Metal removal rate, choice of electrode, equipment, and efficiency in flushing the dielectric fluid through the working area all affect the thickness of this zone. As shown in Section 3.3.3, depending upon workpiece composition and the influence of previously mentioned factors, the heat-affected zone may show evidence of metallurgical change. As a result, evidence of selective material removal, annealing, re-hardening and re-casting may be found. In some cases, the re-cast layer may be detrimental to workpieces, which are subject to high stress in service.

5.4 Residual Stresses in Machining

5.4.1 Physical Background

Residual stresses in the surface layer may be caused by the following phenomena:

- plastic deformation due to mechanical influences;
- plastic deformation due to thermal gradient;
- phase transformation.

The total resulting residual stress depends on the balance between these three factors.

Residual stresses due to plastic deformation caused by mechanical influences appear in the MAZ. If the cohesion of the material is not destroyed, the compressive residual stress remains in the layer elongated by plastic deformation, while in deeper layers the low tensile stresses appear due to stress equilibrium.

When a temperature gradient of sufficient magnitude is created in the work material, plastic deformation occurs as described previously. Because of the relative "shrinkage" of the surface sublayer in this process tensile residual stresses are created in the upper part of the surface layer. Such stresses are characteristic of abusive cutting and grinding

Residual stress due to phase transformations occurs when the transformations are associated with changes in volume, for example when ferrite (austenite)/ martensite transformations in steel occur. Tensile residual stresses occur with decreases in volume and compressive residual stresses occur with increases. In the surrounding layers residual stresses of opposite sign are created.

In many cases all of the phenomena described above are involved and the resultant residual-stress profile with depth below the surface is a consequence of their effects. It is worth pointing out that in areas where MAZ and HAZ zones are present it is extremely difficult to predict residual-stress distribution because of a number of possible influences and interrelationships.

5.4.2 Models of the Generation of Residual Stresses

Residual stress-generating mechanisms can be simplistically represented by three separate models [4]:

1. Thermal phase transformation called thermal or hot model (Figure 5.31(a)) in which the residual stress is caused by a volume change. If the change in phase causes a decrease in volume, the surface layer is under tension and a tensile residual stress is induced. On the other hand, an increase in volume results in the compressive residual stress. The model is adequate for the conventional heat treatment of steel.
2. Thermal/plastic deformation called mixed model (Figure 5.31(b)) in which heat causes expansion of the surface layer and this expansion is relieved by plastic flow, which is restricted to the surface layer. When cooling, the surface layer contracts, resulting in a tensile residual stress.
3. With predominant mechanical plastic deformation, called mechanical or cold model (Figure 5.31(c)), for which the residual stress is compressive because the surface layer is compacted by mechanical action. This model applies to burnishing in which significant tangential compressive stresses with a maximum value at a certain depth below the surface are generated.

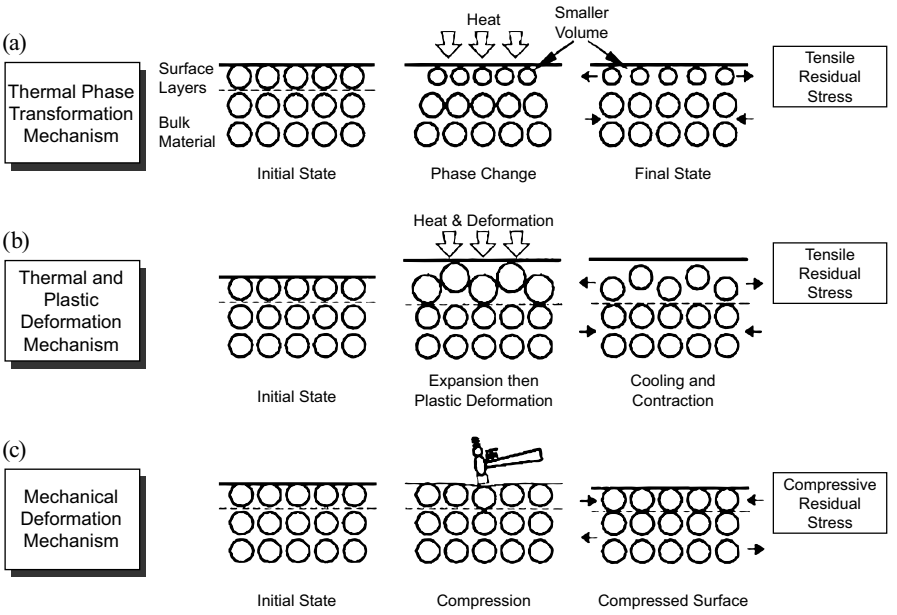

Figure 5.31. Three residual-stress models [4]

5.4.3 Distribution of Residual Stresses into Subsurface Layer

5.4.3.1 Traditional Machining

Typical residual stress patterns produced in different cutting and abrasive processes on steel specimens are shown in Figure 5.32. Figure 5.32 shows the influence of the cutting speed on the residual stress component σ_x parallel to the cutting direction when planning AISI 304 stainless steel under orthogonal machining condition. High tensile stresses of about 700 MPa that decrease visibly in the depth direction are present at the surface.

At 400 to 600 μm depth the region with compressive residual stresses is reached. In addition, at lower cutting speed the tensile stresses penetrate deeper into the workpiece. A typical residual-stress pattern produced by carbide face milling for a sharp tool and for cutters with varying degrees of cutter wear (0.2 and 0.4 mm) is shown in Figure 5.32(b).

The sharp cutter has a stress of zero at the surface and it becomes compressive below the surface. In contrast, for the worn cutters, tensile stress is evidently induced at the surface and it changes into compressive stress at greater depths. During hard machining white layers and residual stress formation are influenced considerably by the sharpness of the cutting tool. With sharp tools the surface microstructure remains much the same as the bulk material and the surface residual stresses tend to be compressive as indicated by curve #1 in Figure 5.32(c).

As the tool flank increases, friction increases and the thermal load on the surface layer grows. This leads to the development of white layers and a greater tendency to induce tensile residual stresses in the surface layer of the hard machined part as depicted by curve #2 in Figure 5.32(c).

In addition, Figure 5.32(d) shows residual stress patterns for low-stress (1), conventional (2) and high-stress (3) grinding conditions (the latter is observed in dry grinding with a relatively hard wheel). In particular, for low-stress grinding, soft and open wheels are used at lower cutting speeds than for conventional grinding, typically 18 m/s rather than 30 m/s [10].

The changes of the distribution of residual tangential stress in the sublayer with cutting time are shown in Figure 5.33(a). It should be noted that the tensile stresses occur near the machined surface and their values increase progressively with tool wear as depicted in Figure 5.33(b). In addition, corresponding displacement of the point of the maximum compressive stresses of about −800 MPa deeper beneath the surface is observed. The effect of the influence of tool flank wear was confirmed for Al_2O_3-TiC ceramic tools and the differences in the shapes of stress distribution curves for these two cutting tool materials are marginal.

The combination of martensite and extremely fine-grained austenite structure constituents can cause different residual stresses in the white layer. In particular, the residual stresses of the dominating austenite material components are clearly shifted towards compressive stresses. Oppositely, the martensite tensile residual stresses result from lower specific volume and consequently higher density of austenite. Compressive residual stresses induced by hard turning were found to improve rolling contact fatigue (RCF). Hard turned surfaces may have more than 100% longer fatigue life than ground ones with an equivalent surface finish of 0.07 μm but this positive effect can be significantly reduced by the presence of a white layer.

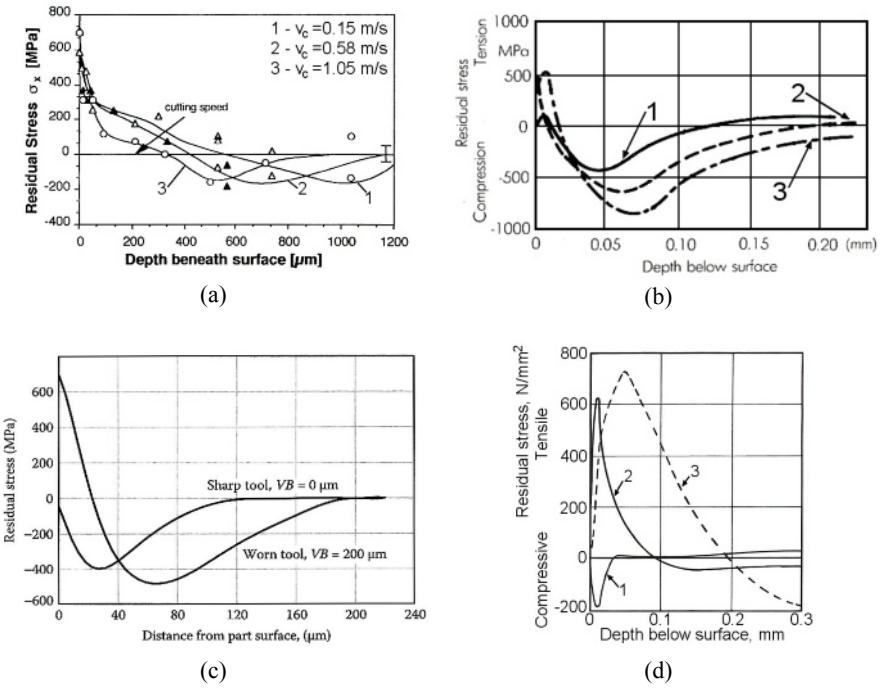

Figure 5.32. Residual-stress profiles produced in different machining processes: (a) after planning of AISI 304 steel (a_p = 0.08 mm, γ_0 = 0°), (b) after face milling of AISI 4340 steel (R_c52), (v_c = 55 m/min, f_t =0.13 mm/tooth, a_p =1 mm) [4, 10]. 1-sharp tool, 2 and 3–0.20 and 0.40 mm wear land, (c) after turning of hardened steel with sharp and worn tools, and (d) induced in the workpiece by various grinding conditions.

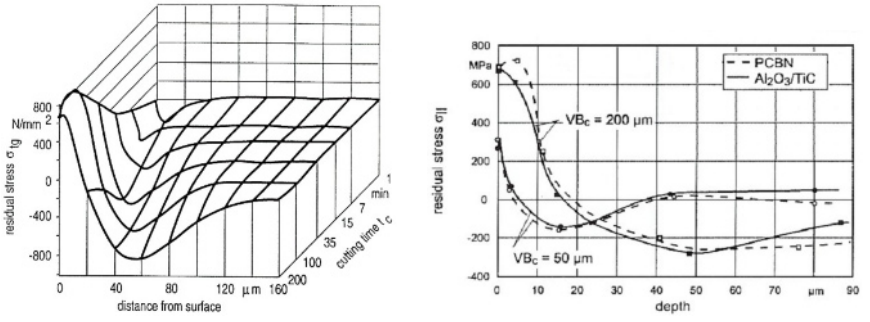

Figure 5.33. Modification of residual-stress profile in the surface layer within tool life period; work material: 16MnCr6 case-hardened steel of 62 HRC, tool material: CBN (a) and comparison of residual stress distribution when turning with PCBN and Al_2O_3-TiC ceramic tools (b) [4]

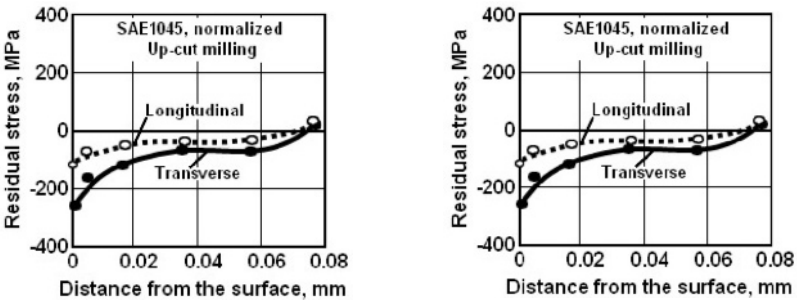

Figure 5.34. Residual stress distribution in longitudinal and transverse directions after up-cut milling (a) and down-cut milling (b) [16]

In milling, similarly to grinding, a particular tool is not continuously in action. Nevertheless, in down-cut, up-cut and face-milling operations the residual stresses are due to the three basic factors: plastic deformation, temperature and martensite forming.

Chip formation (i.e., metal separation) tends to give tensile stresses, while smearing (i.e., plastic deformation) of the surface tends to give compressive ones. The temperature effect is favored in down-cut milling and face milling with an inclined cutting axis and smearing effect in up-cut milling and face milling with perpendicular axis. The depth of the stress-affected layer is usually thicker than in grinding.

Typical examples of residual stress shapes are shown in Figure 5.34 for down-cut milling (a) and up-cut milling of recrystallized 0.45%C steel, respectively.

5.4.3.2 Grinding

The residual stresses are generated in a ground surface due to the combined action of mechanical and thermal effects. The thermal effect is probably the more important of the two effects. During the grinding operation, the temperature rapidly increases in a thin surface layer of the workpiece, while the bulk inner remain cool. As the plastically deformed surface layer cools, its thermal contraction is aided by the part's interior, generating tensile residual stresses at the surface. The higher the grinding power, the more dominant the tensile residual stress contribution σ_{thermal}. For the highest power, martensitic hardening may occur, shifting the residual stress in the compressive direction [16].

In conventional grinding with aluminum oxide grinding wheels high tensile residual stresses are observed on, or close to the surface, whereas the application of superabrasives (CBN or diamond) usually generates compressive or low tensile residual stresses (Figure 5.35). Also, deeper residual stress deposition is observed for aluminum oxide grinding wheels caused by deeper temperature penetration.

It can be seen from Figure 5.36 that even for the increasing specific material removal rates (higher grinding depth and/or higher workspeed) the residual stresses in CBN grinding remain compressive. On the contrary, in aluminum oxide grinding the residual stress, which is slightly compressive for low material removal rates, sharply increases towards high tensile values with the increase of material removal rates.

Manufacturing components typically result from a succession of operations but in most cases it is the last operation that governs the residual-stress profile imparted to the component prior to its use. Exceptions occur when the final machining operation has a penetration depth smaller than the previous ones and in such cases the superimposition of residual stress must be considered as in Figure 5.37.

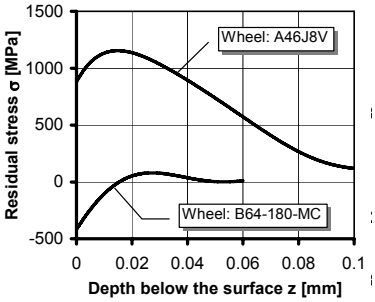

Figure 5.35. The influence of abrasive material on residual stress [17]. Surface grinding, work material: 100Cr6, 62 HRC, v_s=30 m/s, v_w = 0.4 m/s; a_e=7.5 μm

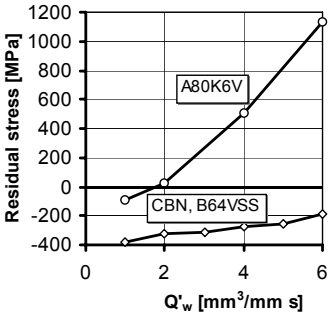

Figure 5.36. Influence of abrasive material and specific material removal rate on residual stress in grinding [18]. Internal grinding, work material: 100Cr6, 62 HRC, v_s = 40 m/s; v_{fr} = 1 m/s, fluid: emulsion 4%

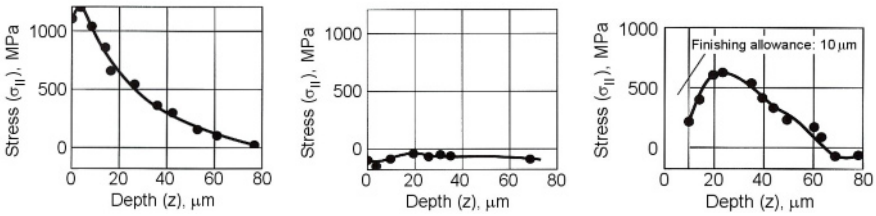

Figure 5.37. Residual-stress profiles in internal grinding cycles: roughing with material removal rate (MRR) of 6 mm^3/mm (a), finishing with MRR = 1 mm^3/mm (b), roughing and finishing (c). Workpiece: 62 HRC 100Cr6 bearing steel, 40 mm in diameter. Corundum grinding wheel: A80K6 V, 30 mm diameter, 8 mm width, 40 m/s cutting speed. Dressing: D 427 diamond cup wheel, 0.7 speed ratio, 40 overlap, 2 μm infeed. Cooling: 4% emulsion [19]

5.4.3.3 Non-traditional Machining

It is generally accepted that ECM produces "stress-free" surface layers, i.e., the residual stress is effectively zero. This is due to the fact that metal removal in ECM is performed by electrochemical action rather than mechanical forces or thermal pulses (by melting or vaporization of the metal as in EDM). The heat that is generated in the working zone as a result of the high current flow through the electrode and the electrolyte is removed by the electrolyte. Moreover, the ECM process is not affected by the workpiece hardness and there is no burning or thermal damage like in ECM processes.

5.4.4 Special Finishing Treatments Improving Stress Patterns

In conventional grinding-based technology, superior surface quality and the fatigue strength of gears, bearing rings, crankshafts, camshafts, etc., are usually ensured by microfinishing, superfinishing or honing. When using hard turning, special abrasive finishing processes such as CBN grinding and belt grinding are proposed for machining synchronizing cones/planes on gearwheels. It was proven [5] that additional belt grinding allows generating higher compressive tangential residual stresses localized closer to the machined surface, and removing partly or completely the white layer. As a result, fatigue life after belt grinding, in particular with oscillating movement of the belt, increases between 30% and 50%. In particular, residual stress variations after grinding and hard turning are distributed in such away that the highest values of compressive residual stresses are localized at approximately 5–20 μm below the machined surface. On the other hand, after belt grinding (Figure 5.38) the highest compressive stress of –500 MPa exists distinctly closer to the workpiece surface.

The residual stress profiles for the four finished surfaces in the case of carburized medium carbon steel (58–62 HRC) are shown in Figure 5.39(a). Figure 5.39(b) plots the surface residual stresses and the area between the compressive portion of the residual stress profile till 100 μm depth and the depth axis. It is clear from Figure 5.39(a) that the highest surface compressive stresses of –800 MPa are produced

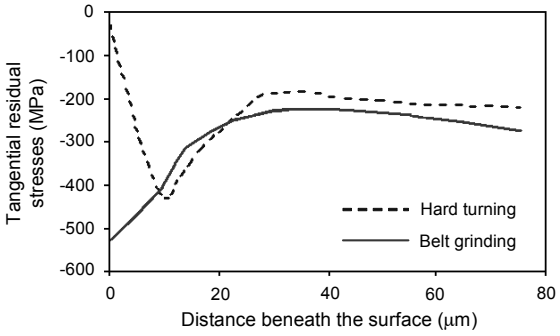

Figure 5.38. Comparison of residual stress distributions after hard CBN turning and belt grinding case-hardening 27MnCr5 steel [20]

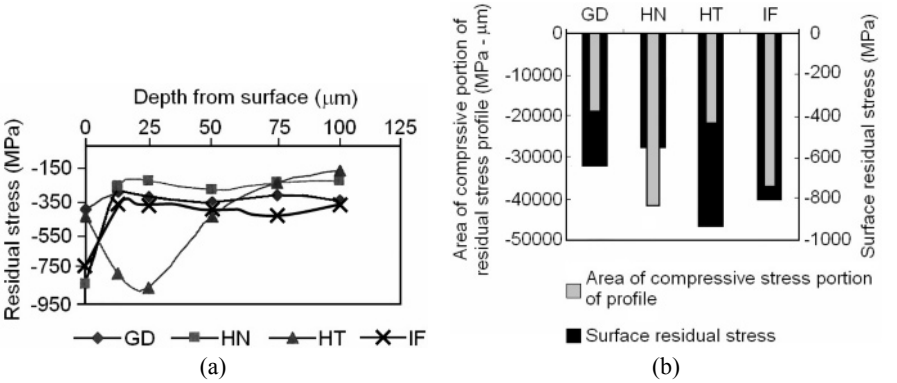

Figure 5.39. Residual-stress profiles (a) and areas of compressive portion of residual stress (b) for different finishing method [21] GD – grinding, HN – honing, HT – hard turning, IF – isotropic finishing.

by honing, whereas the same stresses but below the surface (at 25 μm depth) are generated by hard turning.

Furthermore, Figure 5.39(b) shows that IF bearing has both a large area of compressive stress and a high compressive surface stress. This operation produces the best surface finish. Although, the surface compressive stress of HT bearing is less than the HN bearing, its area of compressive stress is much larger, which explains its higher relative bearing life. The GD surface has the lowest surface stress, a fairly small area and the worst finish.

5.5 Inspection of Surface Integrity

5.5.1 Possible Defects of Machined Surfaces

5.5.1.1 Traditional Machining

Possible surface alterations that occur in conventional metal-removal processes include, depending on the workpiece material grade, the following alterations: plastic deformation and built-up-edge, laps and tears and crevice-like defects, burrs, microcracks, and untempered and overtempered martensite [22]. The depth of the mechanically affected (plastically deformed) zone is reasonably constant across the surface in stable machining processes. Usually, the fragmented layer with severe fragmented grains is adjacent to the surface. The total depth of deformation (the depth of the combined fragmented and deformed layers) increases with increasing tool wear, cutting speed, chip-tool contact length and depth of cut (in turning). As explained in Section 3.2 the built-up edge is created between the tool and the chip at lower cutting speeds. On the other hand, at high cutting speeds, discontinuities such as side flow are present.

Some of the BUE remains on the workpiece as shown in Figure 5.40. A BUE deposit is a form of lap and as such is an addition to a surface. Often a crack is formed below the BUE on the workpiece surface (see Figure 5.40(b)). This crack

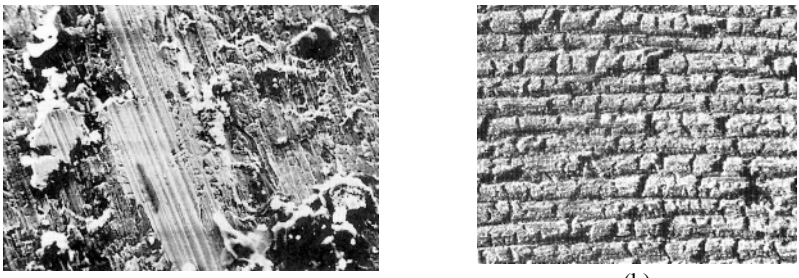

(a) (b)

Figure 5.40. Surface produced on steel by cutting, as observed with a SEM (a) and surface finish on AISI 1018 steel in face milling showing small particles of BUE and cracks (b) [23]

or crevice-like defect can be highly detrimental to the fatigue strength of the material. Tears (removals from the surface) occur because, in some instances, the adhesion between the tool and the surface is so high as to tear away some parts of the surface. As a result, a depression in the surface (called the tear-out) occurs, causing the surface topography to be disturbed.

Microcracks and macrocracks are often produced during traditional machining processes. Cracking can occur in the region of the built-up edge, in the vicinity of untempered martensite. Moreover, burrs produced at the edge of machined surfaces by any machining processes in which there are plastic deformations, are considered to be the initiation sites for cracks and therefore produce a poor SI.

5.5.1.2 Grinding

Typical alterations observed for grinding operations include plastic deformation and plastically deformed debris, burrs, microcracks, and untempered and overtempered martensite [22]. In an abrasive-type operation such as grinding, plastically deformed debris is created by the abrasive grit during its plowing action into the workpiece. Such debris contributes substantially to the surface roughness. In grinding, plastic deformation can occur in conjunction with thermal effects and producing cracks and burrs. It is generally accepted that burrs cause cracking and produce a poor surface integrity.

Cracking tends to be more pronounced when more brittle materials are ground. Microcracking is particularly prevalent during conventional or abusive grinding of cast nickel alloys and cobalt-based alloys. When the temperatures at the workpiece surface exceed the threshold values, surface oxidation and burning occur. The principal factors that influence the threshold temperature, above which significant thermal damage occurs, are wheel speed, work speed, force intensity and wheel sharpness. In general, higher work speeds and sharp wheels allow surfaces to be produced without significant thermal damage occurring.

Examples of microcracks that appear in ground surfaces are shown in Figures 5.41 and 5.42. Figure 5.42 indicates that cracks have some definite relationship to the grinding marks (surface lay). For example, in flat surfaces they are always found to be primarily perpendicular to the grinding marks. Typical depths of such cracks are several tenths of a millimeter.

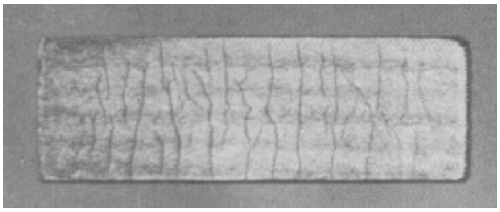

Figure 5.41. Microcracks net on ground flat surface [24]

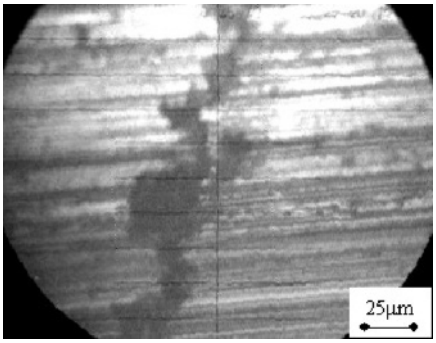

Figure 5.42. Microcrack produced in grinding. Magnification 400× [25]

5.5.1.3 Non-traditional Machining

Non-traditional machining operations produce, similarly to conventional machining operations, a variety of surface alterations. Typical alterations observed for electrical discharge machining (EDM) operations include microcracks, heat-affected zone (HAZ) or re-cast layer, re-spattered metal or vapor-deposited metal, and untempered or overtempered martensite. During thermal machining process such as EDM, particles of metal are vaporized and are then re-deposited on the machined surface. The re-cast metal is usually porous and cracked. The cracks can extend from the re-deposited metal into the workpiece surface layer. The layer of re-deposited material is usually thin (after finishing operations maximum depth of this effect is about 0.013 mm) but it has been found, regardless of thickness, that this coating is highly detrimental to the fatigue life of the finished part [22]. It should be noted that in extreme thermal processes like EDM, LBM and EBM, the surface cracks have a depth that corresponds approximately to white layer (WL) or untempered martensite (UTM) layer [1].

Major advantages of the ECM process include stress-free and burr-free machining; no burr or thermal damage to workpiece surface under normal operating conditions, and low tool wear (since there is no tool–workpiece contact). As a result, undesirable surface defects that can occur with mechanical machining or grinding operations are avoided. As discussed previously, intergranular attack (IGA) is a form of cracking produced by ECM. Such cracks can be very long and sharp. Selective etching or pitting resulting from non-uniform dissolution has been greatly minimized or avoided by the development of better electrolytes and operating con-

ditions. In general, the ECM process has a neutral effect on mechanical properties of a subsurface layer.

5.5.2 Part Distortion due to Improper Process Performance

Whenever a surface is machined by a metal removal process, there is a tendency for distortion to occur. This distortion is produced either by the removal of prior residual stresses from the workpiece or by the introduction of new residual stresses into the workpiece. Basically, the distortion of the workpiece is a function of the bulk residual stress induced by the machining process. It is also a function of the dimension of the workpiece and the Young's modulus. One conventional method of measuring distortion in machining is to determine the change in deflection in a 3.5" gage length, which can subsequently be plotted against various machining parameters.

The relative distortion, which occurs during gentle and abusive grinding and milling operations performed on the four materials (18% maraging steel, AISI 4340 alloy steel, low alloy steel and titanium alloy) is schematically shown as a diagram in Figure 5.43. It is evident from this bar diagram that the gentle surface grinding operations produce very little distortion on any of the materials tested. In contrast, the same operations under abusive grinding conditions produce a very high tensile distortion on AISI 4340 steel, tool steel and titanium alloy specimens. By contrast, the abusive face milling operations cause the distortion is also high but it performs in the compressive direction. Moreover, rough electrical discharge processes produce distortion similar to that characteristic for the abusive surface grinding. On the other hand, electrochemical processes, either finish or rough, cause practically no distortion on any of the materials selected.

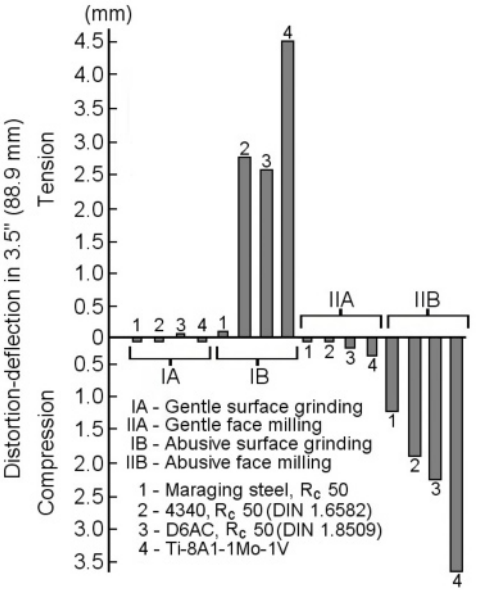

Figure 5.43. Specimen distortion produced by conventional machining methods [22]

References

[1] Griffits BJ (2001) Manufacturing Surface Technology. Penton Press, London
[2] Sandvik Coromant (2008) Handbook of Metal Cutting. Elanders, Sweden
[3] Stephenson DA, Agapiou JS (1997) Metal Cutting Theory and Practice, Marcel Dekker, New York
[4] Grzesik W (2008) Advanced Machining Processes of Metallic Materials, Elsevier, Amsterdam
[5] Grzesik W, Rech J, Wanat T (2007) Surface finish on hardened bearing steel parts produced by superhard and abrasive tools. Int J Mach Tools Manuf 47: 255–262
[6] Malkin S (1989) Grinding Technology: Theory and Applications of Machining with Abrasives. Ellis Horwood, Chichester
[7] Oczoś KE, Liubimov V (2003) Geometrical structure of the surface (in Polish). Atlas of Surfaces, Publishing House of Rzeszów Technical University, Rzeszów
[8] Nowicki B (1991) Geometrical Structure. Surface Roughness and Waviness (in Polish), WNT, Warsaw
[9] Kaczmarek J (1976) Principles of Machining by Cutting, Abrasion and Erosion, Peter Peregrinus Limited, Stevenage
[10] Boothroyd G, Knight W A (1989) Fundamentals of Machining and Machine Tools, Marcel Dekker, NewYork
[11] Klocke F, Kratz H (2005) Advanced tool edge geometry for high precision hard turning, Annals of the CIRP, 54/1, 47–50.
[12] Guo YB, Janowski GM (2004) Microstructural characterization of white layers by hard turning and grinding. Trans. NAMRI/SME 32: 367–374.
[13] Rajurhar KP, Pandit SM (1984) Quantitative expression of some aspects of surface integrity of EDM components. Trans ASME J Eng Ind 106:171–177
[14] Guo YB, Sahni J (2004) A comparative study of the white layer by hard turning, Int J Mach Tools Manuf 44: 135–145
[15] König W, Klocke F (1996) Fertigungsverfahren. Band 2. Schleifen, Honen, Läppen. VDI-Verlag, Düsseldorf
[16] Totten GE, Howes MAH, Inoue T (2002) Handbook of Residual Stress and Deformation of Steel, ASM International, Material Park (OH)
[17] Malkin S (1985) Current trends in CBN grinding technology, Annals of the CIRP 34/2: 557–563
[18] Brinksmeier E (1985) X-ray stress measurements-a tool for the study and layout of machining processes. Annals of the CIRP 34/1: 485–490
[19] Cottel CM, Sprague JA, Smidt FA (1999) ASME Handbook. Surface Engineering. Vol. 5. ASM International, Material Park (OH)
[20] Rech J, Moisan A (2003) Belt grinding: a way to optimize the surface integrity of cut surfaces. In: Proceedings of the 3rd International Conference on Machining and Measurements of Sculptured Surfaces (MMSS), Cracow, pp. 125–132.
[21] Hashimoto F, Melkote SN, Singh R, Kalil R (2007) Effect of finishing methods on surface characteristics and performance of precision components in rolling/sliding contact. Proc. 10th CIRP International Workshop on Modeling of Machining Operations. Reggio Calabria, Italy pp. 21–26
[22] Drozda NN (ed.), (1983) Tool and manufacturing engineers handbook, Vol. 1, Machining, Society of Manufacturing Engineers, Dearborn
[23] Kalpakjan S (1989) Manufacturing Engineering and Technology, Addison-Wesley, Reading
[24] Kruszyński B (1990) Basics of the surface layer. The Technical University Press. A Series of Mechanics, vol. 79, Łódź
[25] Kruszyński B (2001) Surface Integrity in Grinding. The Technical University Press. A Series of Monographs, Łódź

6

Surface Integrity of Micro- and Nanomachined Surfaces

M.J. Jackson

Center for Advanced Manufacturing, Purdue University, 401 North Grant Street, West Lafayette, Indiana, IN 47907, USA,
E-mail: jacksomj@purdue.edu

Micro- and nanomachining processes are being developed that minimize the damage created due to the removal of materials at low and high material removal rates. In order to characterize the level of damage induced, the integrity of the workpiece surface requires to be measured. This chapter provides a state-of-the-art review of micro- and nanomachining and the measurement of surface integrity of micro- and nanomachined surfaces.

6.1 Micromachining

There is a substantial increase in the specific energy required with a decrease in chip size during machining. It is believed this is due to the fact that all metals contain defects such as grain boundaries, missing and impurity atoms, etc., and when the size of the material removed decreases the probability of encountering a stress-reducing defect decreases. Since the shear stress and strain in metal cutting is unusually high, discontinuous microcracks usually form on the primary shear plane. If the material is very brittle, or the compressive stress on the shear plane is relatively low, microcracks will grow into larger cracks giving rise to discontinuous chip formation. When discontinuous microcracks form on the shear plane they will weld and reform as strain proceeds, thus joining the transport of dislocations in accounting for the total slip of the shear plane. In the presence of a contaminant, such as carbon tetrachloride vapor at a low cutting speed, the re-welding of microcracks will decrease, resulting in a decrease in the cutting force required for chip formation. A number of special experiments that support the transport of microcracks across the shear plane, and the important role compressive stress plays on

the shear plane are explained. An alternative explanation for the size effect in cutting is based on the belief that shear stresses increase with increasing strain rate. When an attempt is made to apply this to metal cutting, it is assumed in the analysis that the von Mises criterion applies to the shear plane. This is inconsistent with the experimental findings by Merchant. Until this difficulty is resolved with the experimental verification of the strain-rate approach, it should be assumed that the strain-rate effect may be responsible for some portion of the size effect in metal cutting. The size effect dominates the integrity of the machined surface, and as such, it is critical to be able to measure the effects of it in order to know the number of defects contained within the freshly machined surface. This chapter focuses on the effects of machining on surface integrity and its measurement.

6.2 Machining Effects at the Microscale

It has been known for a long time that a size effect exists in metal cutting, where the specific energy increases with decrease in deformation size. Backer *et al*. [1] performed a series of experiments in which the shear energy per unit volume deformed (u_S) was determined as a function of specimen size for a ductile metal (SAE 1112 steel). The deformation processes involved were as follows, listed from top to bottom with increasing size of specimen deformed:

- surface grinding;
- micromilling;
- turning; and
- tensile test.

The surface grinding experiments were performed under relatively mild conditions involving plunge-type experiments in which an 8-inch (20.3 cm) diameter wheel was directed radially downward against a square specimen of length and width 0.5 in (1.27 cm). The width of the wheel was sufficient to grind the entire surface of the work at different downfeed rates (t). The vertical and horizontal forces were measured by a dynamometer supporting the workpiece. This enabled the specific energy (u_S) and the shear stress on the shear plane (τ) to be obtained for different values of undeformed chip thickness (t). The points corresponding to a constant specific energy below a value of down feed of about 28 μinch (0.7 μm) are on a horizontal line due to a constant theoretical strength of the material being reached when the value of, t, goes below approximately 28 μinch (0.7 μm). The reasoning in support of this conclusion is presented in Backer *et al*. [1].

In the micromilling experiments, a carefully balanced 6-inch (152 cm) carbide-tipped milling cutter was used with all but one of the teeth relieved so that it operated as a fly milling cutter. Horizontal and vertical forces were measured for a number of depths of cut (t) when machining the same sized surface as in grinding. The shear stress on the shear plane (τ) was estimated by a rather detailed method presented in Backer *et al*. [1]. Turning experiments were performed on a 2.25-inch (5.72 cm) diameter SAE 1112 steel bar premachined in the form of a thin-walled tube having a wall thickness of 0.2 inch (5 mm). A zero degree rake angle carbide

tool was operated in a steady-state two-dimensional orthogonal cutting mode as it machined the end of the tube. Values of shear stress on the shear plane (τ) versus undeformed chip thickness were determined for experiments at a constant cutting speed and different values of axial infeed rate and for variable cutting speeds and a constant axial infeed rate [1]. A true stress–strain tensile test was performed on a 0.505-inch (1.28 cm) diameter by 2-inch (5.08 cm) gage length specimen of SAE 1112 steel. The mean shear stress at fracture was 22,000 psi (151.7 MPa). This value is not shown in Figure 6.1 since it falls too far to the right. Taniguchi discussed the size effect in cutting and forming [2]. Shaw [3] discusses the origin of the size effect in metal cutting, which is believed to be primarily due to short-range inhomogeneities present in all engineering metals. When the back of a metal cutting chip is examined at very high magnification by means of an electron microscope individual slip lines are evident. In deformation studies, Heidenreich and Shockley [4] found that slip does not occur on all atomic planes but only on certain discrete planes. In experiments on deformed aluminum single crystals the minimum spacing of adjacent slip planes was found to be approximately 50 atomic spaces, while the mean slip distance along the active slip planes was found to be about 500 atomic spaces. These experiments further support the observation that metals are not homogeneous and suggest that the planes along which slip occurs are associated with inhomogeneities in the metal. Strain is not uniformly distributed in many cases. For example, the size effect in a tensile test is usually observed only for specimens less than 0.1 inch (2.5 mm) in diameter. On the other hand, a size effect in a torsion test occurs for considerably larger samples due to the greater stress gradient present in a torsion test than in a tensile test. This effect and several other related ones are discussed in detail by Shaw [3].

6.2.1 Shear-angle Prediction

There have been many notable attempts to derive an equation for the shear angle (ϕ) shown in Figure 6.1 for steady-state orthogonal cutting. Ernst and Merchant [5] presented the first quantitative analysis. Figure 6.2 shows forces acting on a chip at

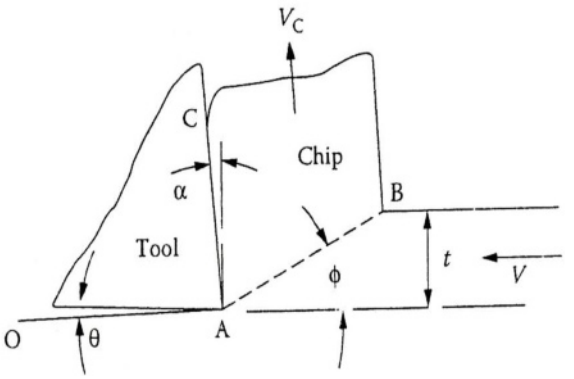

Figure 6.1. Nomenclature for two-dimensional steady-state orthogonal cutting process

the tool point where: R = the resultant force on the tool face, R' = the resultant force in the shear plane, N_C and F_C are the components of R normal to and parallel to the tool face, N_S and F_S are the components of R' normal to and parallel to the cutting direction, F_Q and F_P are the components of R normal to and parallel to the cutting direction, and $\beta = \tan^{-1} F_C/N_C$ (is called the friction angle).

Assuming the shear stress on the shear plane (τ) to be uniformly distributed it is evident that:

$$\tau = \frac{F_S}{A_S} = \frac{R'\cos(\phi + \beta - \alpha)\sin\phi}{A}, \tag{6.1}$$

where A_S and A are the areas of the shear plane and that corresponding to the width of cut (b), times the depth of cut (t). Ernst and Merchant [5] reasoned that τ should be an angle such that τ would be a maximum and a relationship for ϕ was obtained by differentiating Equation 6.1 with respect to ϕ and equating the resulting expression to zero produces,

$$\phi = 45 - \frac{\beta}{2} + \frac{\alpha}{2}. \tag{6.2}$$

However, it is to be noted that in differentiating, both R' and β were considered independent of ϕ.

Merchant [6] presented a different derivation that also led to Equation 6.2. This time an expression for the total power consumed in the cutting process was first written as,

$$P = F_P V = (\tau A V)\frac{\cos(\beta - \alpha)}{\sin\phi\cos(\phi + \beta - \alpha)}. \tag{6.3}$$

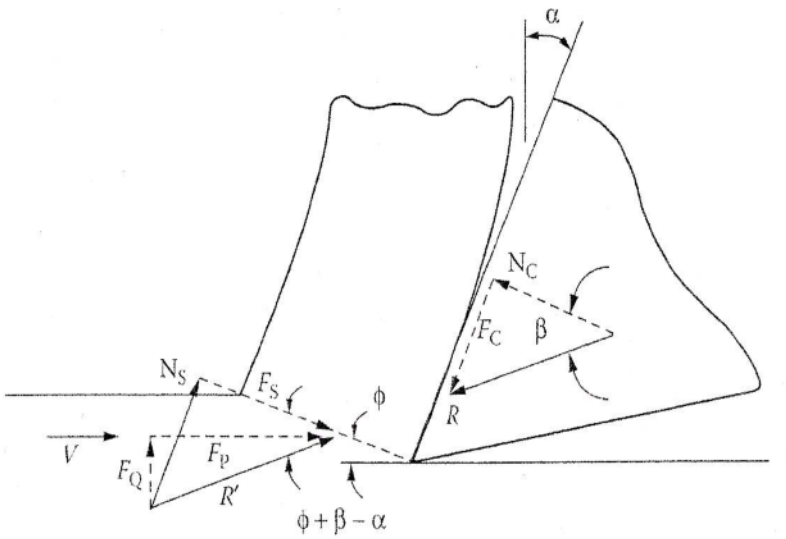

Figure 6.2. Cutting forces at the tool tip for the cutting operation shown in Figure 6.1

It was then reasoned that ϕ would be such that the total power would be a minimum. An expression identical to Equation 6.2 was obtained when P was differentiated with respect to ϕ, this time considering τ and β to be independent of ϕ. Piispanen [7] had done this previously in a graphical way. However, he immediately carried his line of reasoning one step further and assumed that the shear stress τ would be influenced directly by normal stress on the shear plane as follows,

$$\tau = \tau_0 + K_\sigma , \tag{6.4}$$

where K is a material constant. Piispanen then incorporated this into his graphical solution for the shear angle. Upon finding Equation 6.2 to be in poor agreement with experimental data Merchant also independently assumed that the relationship given in Equation 6.4, and proceeded to work this into his second analysis as follows. From Figure 6.2 it may be seen that,

$$\sigma = \tau \tan(\phi + \beta - \alpha), \tag{6.5}$$

or, from Equation 6.4

$$\tau_0 = \tau + K\tau \tan(\phi + \beta - \alpha). \tag{6.6}$$

Hence,

$$\tau = \frac{\tau_0}{1 - K \tan(\varphi + \beta - \alpha)}. \tag{6.7}$$

When this is substituted into Equation 6.3 we have,

$$P = \frac{\tau_0 A V \cos(\beta - \alpha)}{[1 - K \tan(\phi + \beta - \alpha)]\sin\phi \cos(\phi + \beta - \alpha)}. \tag{6.8}$$

Now, when P is differentiated with respect to ϕ and equated to zero (with τ_0 and p considered independent of ϕ we obtain,

$$\phi = \frac{\cot^{-1}(K)}{2} - \frac{\beta}{2} + \frac{\alpha}{2} = \frac{C - \beta + \alpha}{2}. \tag{6.9}$$

Merchant called the quantity, $\cot^{-1} K$, the machining "constant" C. The quantity C is seen to be the angle the assumed line relating τ and ϕ makes with the τ-axis [6, 7, 9]. Merchant [8] has determined the values of C given in Table 6.1 for materials of different chemistry and structure being turned under finishing conditions with different tool materials. From this table it is evident that C is not a constant. Merchant's empirical machining "constant" C that gives rise to Equation 6.9 with values of ϕ is in reasonably good agreement with experimentally measured values.

While it is well established that the rupture stress of both brittle and ductile materials is increased significantly by the presence of compressive stress (known as the Mohr effect), it is generally believed that a similar relationship for flow stress does not hold. However, an explanation for this paradox with considerable supporting experimental data is presented below. The fact that this discussion is limited to steady-state chip formation rules out the possibility of periodic gross cracks being

Table 6.1. Values of C in Equation 6.9 for a variety of work and tool materials in finish turning without a cutting fluid

Work material	Tool material	C (degrees)
SAE 1035 Steel	HSS*	70
SAE 1035 Steel	Carbide	73
SAE 1035 Steel	Diamond	86
AISI 1022 (leaded)	HSS*	77
AISI 1022 (leaded)	Carbide	75
AISI 1113 (sulfurized)	HSS*	76
AISI 1113 (sulfurized)	Carbide	75
AISI 1019 (plain)	HSS*	75
AISI 1019 (plain)	Carbide	79
Aluminum	HSS*	83
Aluminum	Carbide	84
Aluminum	Diamond	90
Copper	HSS*	49
Copper	Carbide	47
Copper	Diamond	64
Brass	Diamond	74

* HSS = High-speed steel

involved. However, the role of microcracks is a possibility consistent with steady-state chip formation and the influence of compressive stress on the flow stress in shear. A discussion of the role microcracks can play in steady-state chip formation is presented in the next section. Hydrostatic stress plays no role in the plastic flow of metals if they have no porosity. Yielding then occurs when the von Mises criterion reaches a critical value. In general, if a small amount of compressibility is involved yielding will occur when the von Mises criterion reaches a certain value. However, based on the results of Table 6.1 the role of compressive stress on shear stress on the shear plane in steady-state metal cutting is substantial. The fact there is no outward sign of voids or porosity in steady-state chip formation of a ductile metal during cutting and yet there is a substantial influence of normal stress on shear stress on the shear plane represents an interesting paradox. It is interesting to note that Piispanen [7] had assumed that shear stress on the shear plane would increase with normal stress and had incorporated this into his graphical treatment. References [9–39] describe, in detail, the nature of chip formation as a function of crack generation during machining. It should be noted that cracks are propagated into the bulk of the material as chips form on the surface. Hence, cracks are ever present in the surface of the material that contributes to a reduction in the fatigue strength of the material. Figure 6.3 shows the cracks present on a freshly cleaved surface of single-crystal lithium fluoride. Therefore, the measurement of surface integrity becomes critical at the microscale in order to monitor the depth to which those cracks have penetrated into the bulk of the material and rendered its properties damaged beyond function.

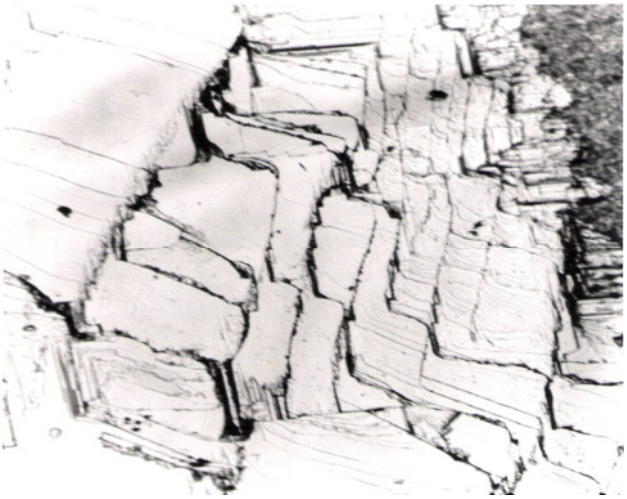

Figure 6.3. Unpolished surface of the LiF single crystal showing cleavage steps

6.2.2 Pulsed Waterdrop Micromachining

Micromachining of semiconductor materials is of critical importance to electronic industries that rely on the removal of material from single crystals. Traditional methods use grinding and polishing techniques to remove material with variable material removal rates. However, these techniques impart high machining stresses in the substrate that tend to produce microcracks that are not desirable, especially when one considers that subsequent deposition of metals and non-metals can be comprised owing to the creation of cracks in and on the surface. However, pulsed erosion of single crystals can be performed that minimize the size of those cracks by carefully selecting the removal of substrate material directly from the surface as opposed to the bulk of the substrate using a specially designed pulsed water drop impact machine tool. Pulsed water drop machining uses a tetrahedral machine tool that specifically absorbs dynamic and regenerative vibrations that prevent microcracks from expanding during the micromachining operation. The process minimizes the level of stresses induced in the surface of the semiconductor material.

Single-crystal materials were initially impacted with methanol, water, oil, and mercury drops then etched to reveal dislocation activity on the surface of the crystals. However, Jolliffe did not impact single-crystal MgO beyond its damage threshold. Jolliffe noted that dislocation movement due to repeated impact by liquids is caused by the extension of dislocation loops to form slip bands on $\{110\}_{45}°$ planes. The nature of impact damage in single-crystal magnesium oxide due to liquid impact was in the form of slip bands in <100> directions until the material reached its damage threshold. When the limit was reached, {110}-type cracks appeared in <100> directions that were formed by the interaction of $\{110\}_{45}°$ slip planes. In addition to the characteristic slip-band pattern for single- and multiple impacts on (001) magne-

sium oxide, there is a fracture annulus surrounding the impact zone. The cracks within the fracture annulus have the following characteristics:

(I) Microcracks at the release radius are very short in length.
(II) Microcracks exist in an annulus whose boundary is square in shape with a slight tendency to be elliptical. The diagonals associated with this annulus are the [010] and [100] directions.
(III) Owing to symmetry in four directions around the [001] impact axis, the damage is the same in eight octants.
(IV) Microcracks intersect the surface tangent to the impact release radius within the <100> radial directions.
(V) Microcracks located near to <110> radial directions are of two varieties. Those that intersect on the (001) impact face, and those that are apparent distortions in the radial direction of type (II) fractures. Intersections of these cracks from two quadrants form W-shaped cracks.

The characteristic microcracks have been identified in single-impact water-drop experiments. Cracks found immediately at the release radius are short in depth (less than 5 μm) and are thought to be cracks created by grinding and polishing that are excited by the passing Rayleigh wave. The onset of visible cracking at the release radius was used as a measure of the damage threshold of the material at a known impact velocity. This tends to give a conservative estimate of the absolute damage threshold of the material. At the point where damage occurs is the point at which material is removed. This process has been adapted to remove material at the microscale and uses the precise location of impacting liquid droplets with minimal fracture tendency.

An experimental investigation concerning the machining of single-crystal materials using pulsed droplet impact was conducted using a specially designed pulsed drop machining center using a tetrahedral framework structure. This apparatus has been discussed elsewhere and functions in much the same way as a multiple-impact jet apparatus, the only difference being in the way that the vibrations are absorbed by the structure once impacts take place. Lithium fluoride is used as the model material. The experimental procedure involves using this apparatus to remove small amounts of material using drops of liquid approximately 1–1.5 mm in diameter. The machining center uses a two-stage pressure reservoir to accelerate a nylon piston into a titanium shaft positioned at the rear of a liquid-filled nozzle. Owing to the high solubility of water in lithium fluoride, hexadecane ($C_{16}H_{34}$) was used as the impacting fluid. The rapid insertion of the shaft into the nozzle forces a high-velocity jet of liquid from the orifice onto the sample that is located on a computer-controlled *x*-*y* stage. The computer monitors the velocity of the jet of liquid as it emerges from the orifice.

Single crystals of lithium fluoride in the form of undoped high-purity single crystals were initially unpolished. Figure 6.3 shows the unpolished stepped surface showing terraces of cleavage steps. Crystran prepared the specimens for impact experiments by cleaving and polishing the crystals. The crystals were cleaved to size on {100} planes and mechanically polished on one side to remove cleavage steps. Chemical polishing was performed to remove mechanically induced polishing dislocations from the surface of the crystal. This was achieved by immersing the crystals in a bath of hydrochloric acid (HCl) at 50°C followed by immersion in

ammonium chloride (NH_4Cl) to remove etch pits. A light mechanical polish using 0.25 μm diamond paste followed immersion in order to obtain a clean surface. The surfaces were then orientated to within two degrees of a {100} plane. The impact face was denoted the (001) plane. The properties of single-crystal lithium fluoride are shown in Table 6.2. Figure 6.4 shows the surface of the initially etched surface of the lithium fluoride single crystal. The erosion resistance of a material is characterized by determining its absolute damage threshold velocity (ADTV), or the point at which material is removed from the surface. This is the velocity below which, for a given liquid drop size, the sample will never experience any damage regardless of the number of impacts to which it is exposed, but will experience dislocation motion. Owing to the high accuracy of the impact velocity and positioning, this parameter can be simply obtained from a single-crystal sample. The sample (typically a twenty-five millimeters' diameter disc) has up to fifteen sites selected on its surface, each one allocated an impact velocity. Each site was initially impacted once at that velocity and inspected for damage using an optical microscope at one hundred times magnification. The lowest velocity at which damage is observed after a single impact was recorded as damage threshold velocity (D.T.V.) at one impact, i.e. the single-impact threshold velocity, and the sample returned to the multiple impact jet apparatus so that each site can be impacted again.

Impact damage was detected by inspecting the surface of impact using an optical microscope. After the crystal was impacted it was etched to reveal dislocation movement and the formation of surface cracks. The samples were thoroughly washed in a solution of water and non-ionic surfactant prior to etching the (001) surface. Once the sample was dried, hydrogen peroxide (H_2O_2) was used to reveal etch pits and regions of crack formation. Each sample was etched for ten minutes at room temperature. The purpose of this exercise was to determine the impact conditions where material removed is activated by the formation of microcracks on the surface

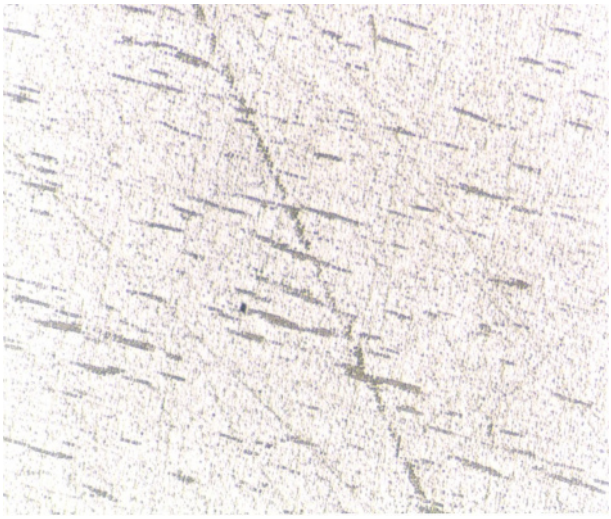

Figure 6.4. Initially etched surface of the (001) plane of single-crystal lithium fluoride showing polishing dislocations

Table 6.2. Properties of single-crystal lithium fluoride

Young's modulus, $E_{<100>}$, (MPa)	64.8
Poisson's ratio, $\nu_{<100>}$	0.27
Density, ρ, (kg m^{-3})	2600
Fracture toughness, $K_{IC<100>}$, (MPa $m^{1/2}$)	0.2
Slip system	$\{110\}<1\bar{1}0>$
Cleavage plane	{100}
Water solubility, (mg/100 g water)	270
Knoop hardness (kg mm–2) (001)<100> (001)<110> (1$\bar{1}$0)<00$\bar{1}$> (1$\bar{1}$0)<11$\bar{1}$> (110)<110>	 87–96 93–103 87–98 97–120 93–116

of the material. The damage pattern observed after liquid impact on single-crystal lithium fluoride was typically a series of discrete circumferential cracks around an undamaged central zone. The cracks observed immediately outside the release radius are type-III cracks that were used to detect the onset of the damage threshold. The pressure pulses produced by liquid impact are intense because of the compressible behavior of the liquid in the first stages of impact. Damage observed in single-crystal lithium fluoride was in the form of slip-band development in <100> directions until the material reached its damage threshold limit, or machining limit. At the damage threshold limit a number of fractures and types of fracture are evident. In addition to type-III cracks at the release radius, type-IV cracks are observed in <100> directions. Figure 6.5 shows type-IV cracks to the right of the photograph. The cracks shown are variable in length; the largest emanating from the center of impact that, unusually, has a subsidiary crack running in the <110> direction. Referring to type-III cracks, substantial surface and near-surface tensile stresses developed ahead of the shear wave in polycrystalline zinc sulfide just before the Rayleigh surface wave begins to develop. However, there was no evidence in the case of single-crystal lithium fluoride of subsurface tensile cracking associated with bulk waves. Type-III cracks at the periphery of the impact zone did not have subsidiary cracks attached to them at trajectories associated with bulk waves. Although when one looks at a cross-section of type-IV cracks some distance away from the center of impact, there was evidence of subsurface tensile cracks that were presumably caused by the interaction of $\{110\}_{45}°$ slip planes.

Figure 6.5 also shows the existence of type-V cracks. These cracks are apparent distortions of type-II cracks in the radial <110> directions. Figure 6.6 shows the intersections of these cracks from two quadrants. They are typically W-shaped cracks and are associated with liquid impact on single-crystal materials, particularly magnesium oxide. The increase in the number of W-shaped cracks occurred beyond the damage threshold limit of the material and was largely associated with the appearance of cracks in the <100> radial directions within the impact zone.

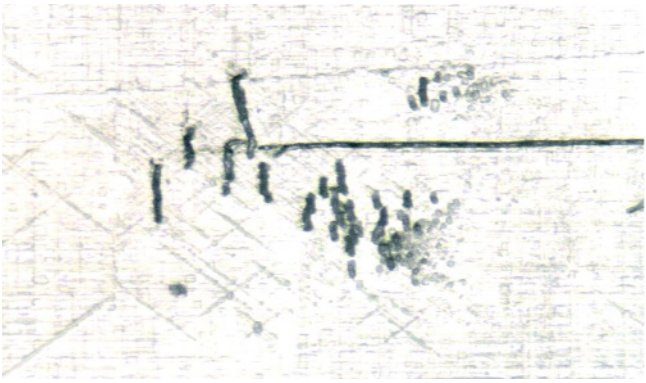

Figure 6.5. Dislocation-etched (001) impact face of single-crystal lithium fluoride. Hexadecane was used to impact the surface at 200 m s^{-1} through a 0.8 mm diameter nozzle. The Figure shows type-IV cracks in <100> radial directions, type-V cracks to the left of type-IV cracks, and a central impact crack some distance away from the center of impact

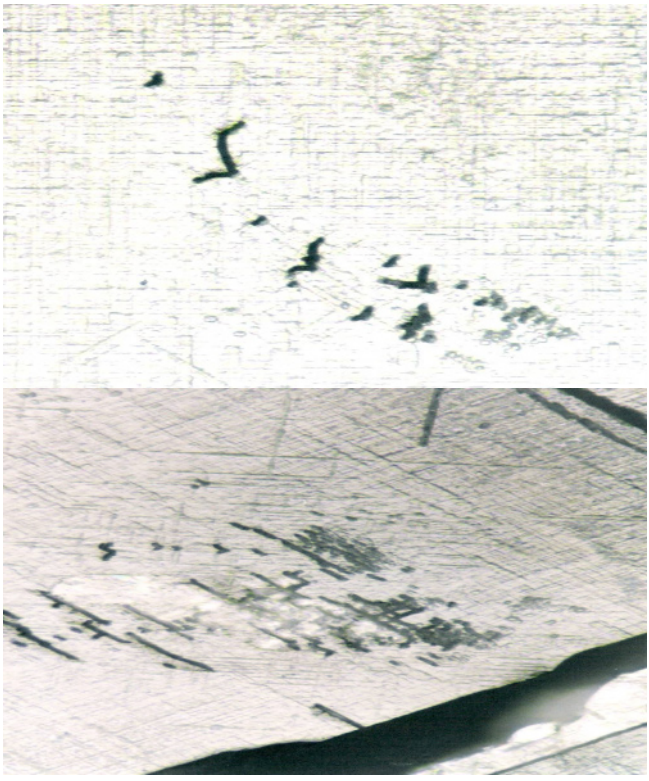

Figure 6.6. Dislocation-etched (001) impact face of single-crystal lithium fluoride. Hexadecane was used to impact the surface at 200 m s^{-1} through a 0.8 mm diameter nozzle. The Figure shows cracks that are apparent distortions in the radial direction of type-II cracks. Intersections of these cracks from two quadrants form W-shaped cracks as shown

In some materials, repeated impact produces local failure on, or near the impact axis. In this case, the damage was located beneath the surface at a depth of about half the radius of the contact region *R*. This is where Hertz theory for elastic contact would predict the maximum shear stress. However, for loading that is dominated by a stress wave this is unlikely to be the full explanation. Experiments show that subsurface axial cracks in PMMA form when the release waves from the contact periphery interact giving net tension. Interestingly, the release waves will also travel in the liquid giving cavitation when they cross. A third mechanism for damage at or near the central axis with polycrystalline materials is by the action of compressive or shear loading that generates tensile failure at grain boundaries between grains depending on their orientation and anisotropy. Once a pit develops, hydraulic loading by trapped liquid can develop damage. Central damage is likely to be less important than circumferential cracking in the rain erosion situation since it depends on multiple impacts on the same site.

Central impact damage in single-crystal lithium fluoride initially occurs as slip bands move causing a "rippling" effect to be seen in the centrally loaded impact zone. As slip-band development continues after repeated impact, cracks begin to appear above the damage threshold limit, i.e., after type-III and -IV cracks have been established. Slip development leads to cracks predominantly in the [010] direction. As the severity of the impacts increases, cracking occurs in all principal <100> directions. These cracks are thought to be due to the interaction of $\{110\}_{45}°$ slip planes. The most likely explanation for central impact damage in single-crystal lithium fluoride is that hydrostatic compressive loading during impact enables subsurface slip bands to interact, i.e., shear interactions of slip planes. The slip planes, which have a greater tendency to slip, will do so, thus causing a "rippling" effect on the surface of the impact site. As the severity of impact continues, {110}-type cracks form due to the interaction of $\{110\}_{45}°$ slip planes. It should be noted that they did not observe cracks within the central impact region of single-crystal magnesium oxide. However, they did notice that slip-plane interactions did occur within the central impact region but without crack formation. The damage threshold curve for single-crystal lithium fluoride subjected to multiple liquid impact is shown in Figure 6.7. The single-impact

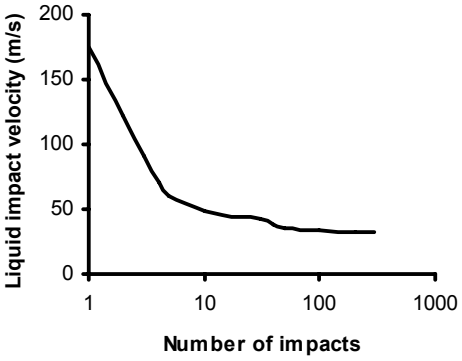

Figure 6.7. Experimental damage threshold curve for single-crystal lithium fluoride. The single-shot threshold velocity from a 0.8 mm diameter nozzle is 175 m s^{-1}, whilst the machining threshold velocity after three hundred impacts was 32 m s^{-1}.

threshold velocity from a 0.8 mm diameter nozzle was found to be 175 m s^{-1}, whilst the absolute machining threshold, i.e., DTV after 300 impacts, or the machining threshold was 32 m s^{-1}. This technique is adapted to machine materials at the microscale and a series of experiments is currently underway to determine the conditions under which machining is performed for a wide variety of engineering materials.

6.3 Nanomachining

Nanomachining can be classified into four categories:

- Deterministic mechanical nanometric machining. This method utilizes fixed and controlled tools, which can specify the profiles of three-dimensional components by a well-defined tool surface and path. The method can remove materials in amounts as small as tens of nanometers. It includes typically diamond turning, micromilling and nano/microgrinding, etc.;
- Loose abrasive nanometric machining. This method uses loose abrasive grits to removal a small amount of materials. It consists of polishing, lapping and honing, etc.
- Non-mechanical nanometric machining. It comprises focused ion beam machining, micro-EDM, and excimer laser machining.
- Lithographic method. It employs masks to specify the shape of the product. Two-dimensional shapes are the main outcome; severe limitations occur when three-dimensional products are attempted. It mainly includes X-ray lithography, LIGA, electron beam lithography.

Mechanical nanometric machining has more advantages than other methods since it is capable of machining complex 3D components in a controllable way. The machining of complex surface geometry is just one of the future trends in nanometric machining, which is driven by the integration of multiple functions in one product. For instance, the method can be used to machine micromolds and dies with complex geometric features and high dimensional and form accuracy, and even nanometric surface features. The method is indispensable to manufacturing complex microscale and miniature structures, components and products in a variety of engineering materials. This section of the chapter focuses on nanometric cutting theory, methods and its implementation and application perspectives [40–44].

Single-point diamond turning and ultraprecision grinding are two major nanometric machining approaches. They are both capable of producing extremely fine cuts. Single-point diamond turning has been widely used to machine non-ferrous metals such as aluminum and copper. An undeformed chip thickness about 1 nm is observed in diamond turning of electroplated copper [45]. Diamond grinding is an important process for the machining of brittle materials such as glasses and ceramics to achieve nanometer levels of tolerances and surface finish. A repeatable optical quality surface roughness (surface finish < 10 nm R_a) has been obtained in nanogrinding of hard steel by Stephenson *et al*. [46] using a 76 μm grit cBN wheel on the ultraprecision grinding machine tool. Recently, diamond fly cutting and diamond milling have been developed for machining non-rotational, non-symmetric geome-

try, which has enlarged the product spectrum of nanometric machining [47]. In addition, the utilization of ultrafine grain hard metal tools and diamond-coated microtools represents a promising alternative for microcutting of even hardened steel [48–52]. Nanomachining is critical in areas such as silicon wafer manufacture in order to minimize or eliminate the effects of subsurface damage and cracking.

6.3.1 Cutting Force and Energy

In nanomanufacturing, the cutting force and cutting energy are important issues. They are important physical parameters for understanding cutting phenomena as they clearly reflect the chip-removal process. From the aspect of atomic structures cutting forces are the superposition of the interactions forces between workpiece atoms and cutting tool atoms. Specific energy is an intensive quantity that characterizes the cutting resistance offered by a material [53]. Ikawa *et al*., and Luo *et al*. [52–55] have acquired the cutting forces and cutting energy by molecular dynamics simulations. Ikawa et alia [52] have carried out experiments to measure the cutting forces in nanometric machining. Figure 6.4 shows the simulation and experimental results in nanometric cutting. Figure 6.4(a) illustrates the linear relation exists between the cutting forces per width and depth of uncut in both simulations and experiments. The cutting forces per width increase with the increment of the depth of cut.

The difference in the cutting force between the simulations and the experiments is caused by the different cutting edge radii applied in the simulations. In nanometric machining the cutting edge radius plays an important role since the depth of cut is similar in scale. Under the same depth of cut higher cutting forces are needed for a tool with a large cutting edge radius compared with a tool with a small cutting edge radius. The low cutting force per width is obviously the result of fine cutting conditions, which will decrease the vibration of the cutting system and thus improve the machining stability and will also result in better surface roughness.

A linear relationship between the specific energy and the depth of cut can also be observed in Figure 6.8(b). The Figure shows that the specific energy increases with a decreasing of depth of cut, because the effective rake angle is different under different depths of cut. In small depths of cut the effective rake angle will increase with the decreasing of depth of cut. Large rake angle results in the increasing of specific energy. This phenomenon is often called the “size effect”, which can be clearly explained by material data listed in Table 6.3. According to Table 6.3, in nanometric machining only point defects exist in the machining zone in a crystal, so it will need more energy to initiate the atomic crack or atomic dislocation. The decreasing depth of cut will decrease the chance for the cutting tool to meet point defects and result in the increasing of the specific cutting energy.

If the machining unit is reduced to 1 nm, the workpiece material structure at the machining zone may approach atomic perfection, so more energy will be required to break the atomic bonds. On the other hand, when the machining unit is higher than 0.1 μm, the machining points will fall into the distribution distances of some defects such as dislocations, cracks, and grain boundaries. The pre-existing defects will ease the deformation of workpiece material and result in a comparatively low specific cutting energy.

Table 6.3. Material properties under different machining units [56]

	1 nm–0.1 μm	**0.1–10 μm**	**10 μm–1 mm**
Defects/Impurities	Point defect	Dislocation/crack	Crack/grain boundary
Chip-removal unit	Atomic cluster	Subcrystal	Multicrystals
Brittle fracture limit	10^4–10^3 J/m^3 Atomiccrack	10^3–10^2 J/m^3 Microcrack	10^2–10^1 J/m^3 Brittle crack
Shear failure limit	10^4–10^3 J/m^3 Atomic dislocation	10^3–10^2 J/m^3 Dislocation slip	10^2–10^1 J/m^3 Shear deformation

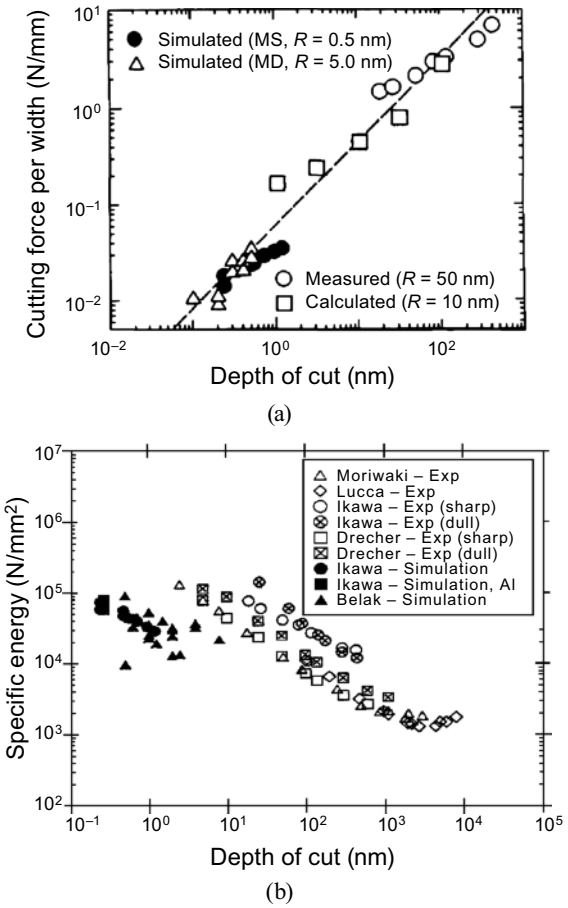

Figure 6.8. Comparison of results between simulations and experiments: (a) cutting force per width against depth of cut, (b) specific energy against depth of cut [52]

Nanometric cutting is also characterized by the high ratio of the normal to the tangential component in the cutting force [53–56], as the depth of cut is very small in nanometric cutting, and the workpiece is mainly processed by the cutting edge. The compressive interactions will thus become dominant in the deformation of workpiece material, which will therefore result in the increase of friction force at the toolchip interface and the relative high cutting ratio. Usually, the cutting force in nanometric machining is very difficult to measure due to its small amplitude compared with the noise (mechanical or electronic) [52]. A piezoelectric dynamometer or load cell is used to measure the cutting forces because of their high sensitivity and natural frequency [57].

6.3.2 Cutting Temperatures

In molecular dynamics simulation, the cutting temperature can be calculated under the assumption that cutting energy totally transfers into cutting heat and results in the rise of cutting temperature and kinetic energy of system. The lattice vibration is the major form of thermal motion of atoms. Each atom has three degrees of freedom. According to the theorem of equipartition of energy, the average kinetic energy of the system can be expressed as:

$$\bar{E_k} = \frac{3}{2} N k_{\mathrm{B}} T = \sum_i \frac{1}{2} m(V_i^2) , \tag{6.10}$$

where $\bar{E_k}$ is average kinetic energy in the equilibrium state, k_{B} is Boltzmann's constant. T is temperature, m_i and V_i are the mass and velocity of an atom respectively, and N is the number of atoms. The cutting temperature can be deduced as:

$$T = \frac{2E_k}{3Nk_{\mathrm{B}}} . \tag{6.11}$$

Figure 6.9 shows the variation of cutting temperature on the cutting tool in a molecular-dynamics simulation of nanometric cutting of single-crystal aluminum. The highest temperature is observed at the cutting edge, although the temperature at the flank face is also higher than that at the rake face. The temperature distribution suggests that a major heat source exists in the interface between the cutting edge and workpiece and the heat is conducted from there to the rest of the cutting zone in workpiece and cutting tool. The reason is that because most cutting actions take place at the cutting edge of the tool, the dislocation deformations of workpiece materials will transfer potential energy into the kinetic energy and result in a rise in temperature. The comparative high temperature at the tool flank face is obviously caused by the friction between tool flank face and workpiece. The released energy due to the elastic recovery of the machined surface also contributes to the increment of temperature at the tool flank face. Although there is also friction between the tool rake face and the chip, the heat will be taken away from the tool rake face by the removal of the chip. Therefore, the temperature at the tool rake face is lower than that at the tool cutting edge and tool flank face. The temperature value shows that the cutting temperature in diamond machining is quite low in comparison with

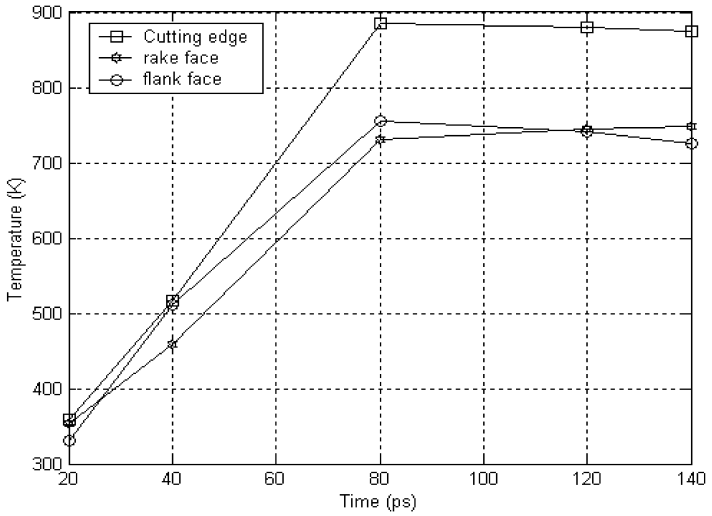

Figure 6.9. Cutting temperature distribution of cutting tool in nanometric cutting (cutting speed = 20 m/s, depth of cut = 1.5 nm, cutting edge radius = 1.57 nm) [58]

that in conventional cutting, due to low cutting energy as well as the high thermal conductivity of diamond and the workpiece material. The cutting temperature is considered to govern the wear of a diamond tool in a molecular-dynamics simulation study by Cheng *et al*. [58]. More in-depth experimental and theoretical studies are needed to find out the quantitative relationship between cutting temperature and tool wear although there is considerable evidence of chemical damage on diamond in which temperature plays a significant role [52].

6.3.3 Chip Formation

Chip formation and surface generation can be simulated by molecular-dynamics simulation. Figure 6.10 shows an MD simulation of a nanometric cutting process on single-crystal aluminum. From Figure 6.10(a) it is seen that after the initial plow of the cutting edge the workpiece atoms are compressed in the cutting zone near to the rake face and the cutting edge. The disturbed crystal lattices of the workpiece and even the initiation of dislocations can be observed in Figure 6.10(b). Figure 6.10(c) shows the dislocations have piled up to form a chip. The chip is removed with the unit of an atomic cluster as shown in Figure 6.10(d). Lattice-disturbed workpiece material is observed on the machined surface.

Based on the visualization of the nanometric machining process, the mechanism of chip formation and surface generation in nanometric cutting can be explained. Owing to the plowing of the cutting edge, the attractive force between the workpiece atoms and the diamond tool atoms becomes repulsive. Because the cohesion energy of diamond atoms is much larger than that of Al atoms, the lattice of the workpiece is compressed. When the strain energy stored in the compressed lattice exceeds a specific level, the atoms begin to re-arrange so as to release the strain

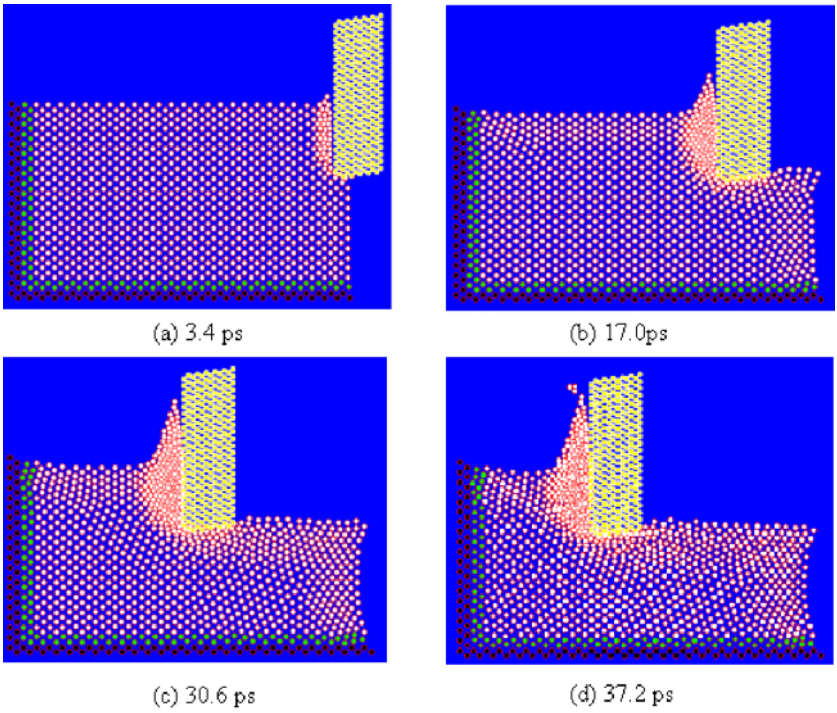

Figure 6.10. MD simulations of the nanometric machining process (Cutting speed = 20 m/s, depth of cut = 1.4 nm, cutting edge radius = 0.35 nm) [58]

energy. When the energy is not sufficient to perform the re-arrangement, some dislocation activity is generated. Repulsive forces between compressed atoms in the upper layer and the atoms in the lower layer are increasing, so the upper atoms move along the cutting edge, and at the same time the repulsive forces from the tool atoms cause the resistance for the upward chip flow to press the atoms under the cutting line. With the movement of the cutting edge, some dislocations move upward and disappear from the free surface as they approach the surface.

This phenomenon corresponds to the process of the chip formation. As a result of the successive generation and disappearance of dislocations, the chip seems to be removed steadily. After the passing of the tool, the pressure at the flank face is released. The layers of atoms move upwards and result in elastic recovery, so the machined surface is generated. The conclusion can therefore be drawn that the chip removal and machined surface generation are in nature the dislocation slip movement inside the workpiece material crystal grains. In conventional cutting the dislocations are initiated from the existing defects between the crystal grains, which will ease the movement of dislocation and result in smaller specific cutting forces compared with that in nanometric cutting. The height of the atoms on the surface layer of the machined surface create the surface roughness. For this, 2D MD simulation R_a can be used to assess the machined surface roughness. The surface integrity parameters can also be calculated based on the simulation results. For example, the residual stress of the machined surface can be estimated by aver-

aging the forces acting on the atoms in a unit area on the upper layer of the machined surface. Molecular-dynamics (MD) simulation has been proved to be a useful tool for the theoretical study of nanometric machining [59]. At present, the MD simulation studies on nanometric machining are limited by the computing memory size and speed of the computer. It is therefore difficult to enlarge the dimension of the current MD model on a personal computer. In fact, the machined surface topography is produced as a result of the copy of the tool profile on a workpiece surface that has a specific motion relative to the tool. The degree of the surface roughness is governed by both the controllability of machine tool motions (or relative motion between tool and workpiece) and the transfer characteristics (or the fidelity) of tool profile to workpiece [52]. A multiscale analysis model, which can fully model the machine tool and cutting tool motion, environmental effects and the tool–workpiece interactions, is much needed to predict and control the nanometric machining process in a determinative manner in order to eliminate subsurface damage.

6.4 Surface Integrity

Many machining processes will induce surface/subsurface damage into the material. Subsurface damage means that there is some damaged layer below the surface, like subsurface cracks, dislocations, residual stress, etc. In order to avoid failures in machined surfaces, the subsurface damaged layer must be eliminated. Therefore, it is necessary to detect the subsurface damage depth caused by the machining process. There are many techniques applicable to characterize subsurface damage in nano- and micromachining. However, X-ray methods are the most commonly applied to measuring the damage sustained to micro- and nanomachined surfaces.

6.4.1 X-ray Diffraction

X-ray diffraction is a widely used method to determine residual stresses from lattice deformation of a crystal. A crystal lattice is a regular three-dimensional distribution (cubic, rhombic, etc.) of atoms in space. When X-rays are incident at a particular angle, they are reflected specularly (mirror-like) from the different planes of crystal atoms. However, for a particular set of planes, the reflected waves interfere with each other. A reflected X-ray signal is only observed if Bragg's condition is satisfied for constructive interference.

Figure 6.11 illustrates how the principle of X-ray diffraction operates. Figure 6.11(a) shows X-rays incident upon a simple crystal structure. Bragg's condition is satisfied for both ray A and ray B. Figure 6.11(b) shows the diffraction geometry. The extra distance travelled by ray B must be an exact multiple of the wavelength of the radiation. This means that the peaks of both waves are aligned with each other. Bragg's condition can be described by Bragg's Law: $2d\sin\theta = m\lambda$, where d is the distance between planes, θ is the angle between the plane and the incident (and reflected) X-rays, m is an integer called the order of diffraction and λ is the wavelength.

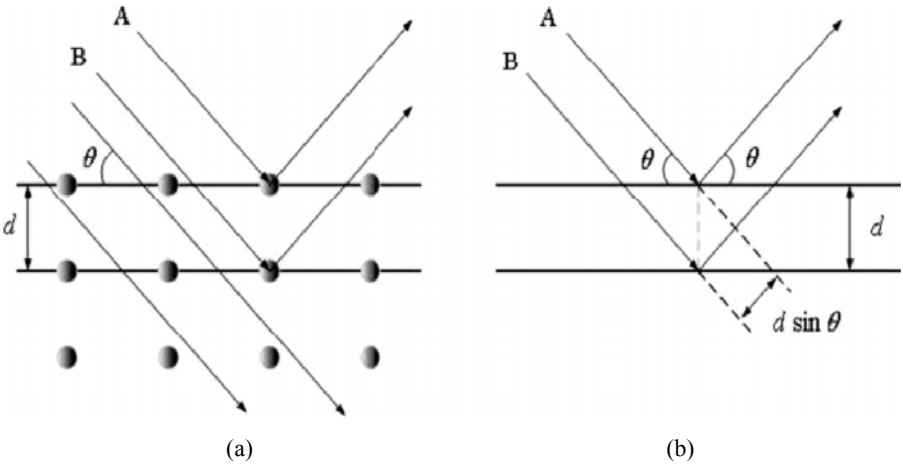

(a) (b)

Figure 6.11. Illustration of X-ray diffraction: (a) X-rays A and B incident upon a crystal, and (b) diffraction geometry

Figure 6.12(a) shows a standard X-ray diffraction pattern with aligned sharp peaks for a perfect crystal structure. During machining processes, residual stress may result from non-uniform and permanent three-dimensional changes in the material. These changes usually occur as plastic deformation and may also be caused by cracking and local elastic expansion, or contraction of the crystal lattice. In these cases, the crystal structure is no longer perfect (d is changed) and the diffraction peaks are broadened and shifted, as shown in Figure 6.12(b). Thus, by examining the changes of the X-ray diffraction pattern, the residual stress can be characterized and the related defects can possibly be identified.

For the applications of conventional X-ray diffraction, the main restriction is the low penetration depth of X-ray into the workpiece material. Because the strain can only be measured within the irradiated surface layer, with low penetration depth of X-ray, only the stress close to the surface can be detected quantitatively. High-resolution diffractometers consist of a four-crystal monochromator that produces a highly parallel and monochromatic incident beam so that a high resolution of X-ray diffraction can be achieved. X-ray diffraction techniques can measure sur-

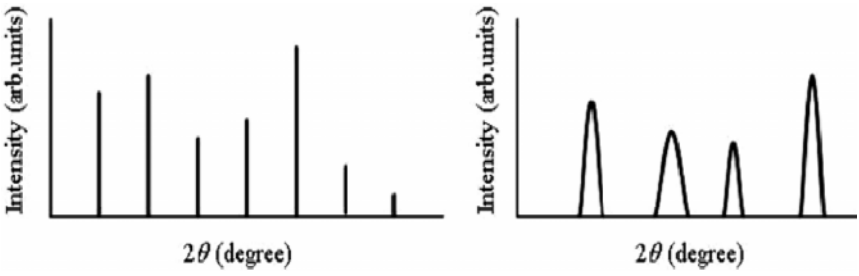

(a) (b)

Figure 6.12. Illustration of X-ray diffraction patterns: (a) for a perfect crystal, and (b) for an imperfect crystal

face defects at short distances into the workpiece. For surface measurement of integrity, microscopic techniques such as scanning tunneling and atomic force are proving to be highly valuable.

6.4.2 Scanning Tunneling and Atomic Force Microscopy

Microscopic techniques include the use of scanning tunneling and atomic force microscopes for measuring surface defects. Scanning tunneling microscopy is a process that relies on a very sharp tip connected to a cantilever beam to touch a surface composed of atoms that is electrically conductive. It is a process that is conducted in an ultrahigh vacuum where a sharp metal tip is brought into extremely close contact (less than 1 nm) with a conducting surface (Figure 6.13). A bias voltage is applied to the tip and the sample junction where electrons tunnel quantum-mechanically across the gap. A feedback current is monitored to provide feedback and is usually in the range between 10 pA and 10 nA. The applied voltage is such that the energy barrier is lowered so that electrons can tunnel through the air gap. The tip is chemically polished or ground, and is made of materials such as tungsten, iridium, or platinum-iridium.

There are two modes of operation: (I) *Topography mode* where the tip scans in the *x*-*y* plane where the tunneling current is kept constant and secondly; (II) *Constant height mode* where the tip is scanned in the *x*-*y* plane at constant depth and the tunneling current is modulated.

Figures 6.14 and 6.15 show images of quantum "corrals" on the surfaces of copper (111) and silver (111) that demonstrate the observations of ripples of electronic density distribution for surface electrons afforded by the scanning tunneling microscope technique. These observations are for conductive surfaces only. Non-

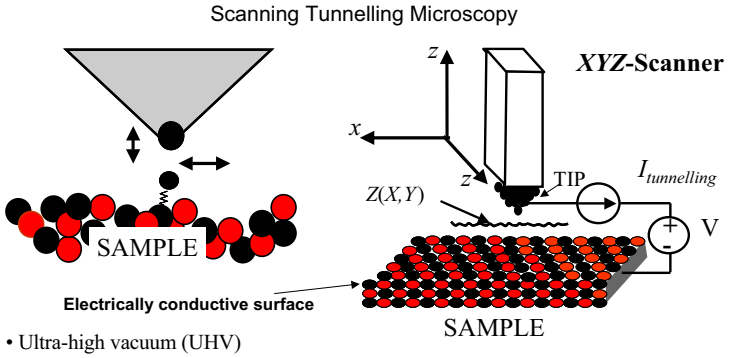

Figure 6.13. Basic principle of operation of the scanning tunneling microscope [60]

conductive surfaces can still be imaged but require a technique known as atomic force microscopy. Atomic force microscopy is a powerful technique that can be used to measure surface integrity at the nanoscale.

The atomic force microscope (AFM) is used in ambient conditions and in ultra-high vacuum, and a sharp tip connected to a cantilever beam is brought into contact with the surface of the sample (Figure 6.16). The surface is scanned, causing the beam to deflect that is monitored by a scanning laser beam. The tip is micro-machined from materials such as silicon (Figures 6.17 and 6.18), tungsten, diamond, iron, cobalt, samarium, iridium, or cobalt-samarium permanent magnets.

Confinement of Electrons to Quantum Corrals on a Metal Surface

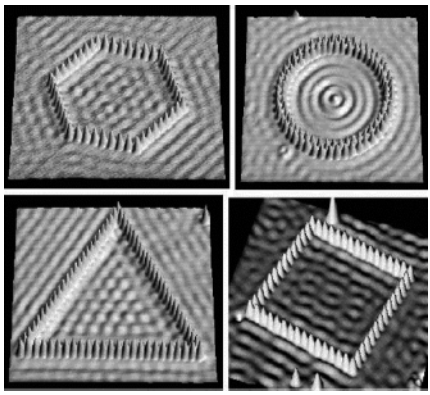

Images of variously-shaped quantum "corrals" formed by using low temperature STM to position Fe atoms on a Cu(111) substrate. The observed ripples represent the electronic density distribution for surface electrons, where quantum states are observed inside the corrals.

M.F. Crommie, C.P. Lutz, D.M. Eigler, *Science 262, 218–220 (1993).*
www.almaden.ibm.com/vis/stm/library.html

Figure 6.14. Images of quantum "corrals" formed by positioning atoms on a (111) copper substrate [61]

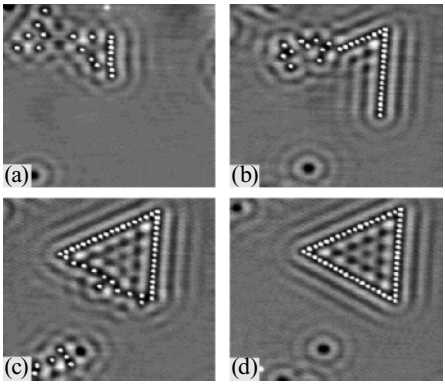

Sequence of low-temperature STM images (49 nm × 49 nm) showing the construction of a triangular "corral" composed of Ag atoms on a Ag(111) substrate.

K.-F. Braun, K.-H. Rieder, Phys. Rev. Lett. 88, 096801 (2002).

Figure 6.15. Sequence of low-temperature images showing the construction of a triangular "corral" of silver atoms on a (111) surface of silver [62]

The cantilever beam and tip are controlled by certain physical laws and as such possess a spring constant, k, and a resonant frequency, f_0. The tip and cantilever experience a displacement force that is dominated by surface tension in ambient conditions (AFM mode), and chemical, van der Waals, and electrostatic forces in vacuum (STM mode). In summary, the modes of operation of the AFM are static and dynamic. In static AFM, the force between tip and surface is variable and is non-linear compared to the surface–tip distance. Figure 6.19 shows the basic principle of operation in the static mode. The Figure shows the contact mode, non-contact mode, and the intermittent dynamic modes and explains the differences between them.

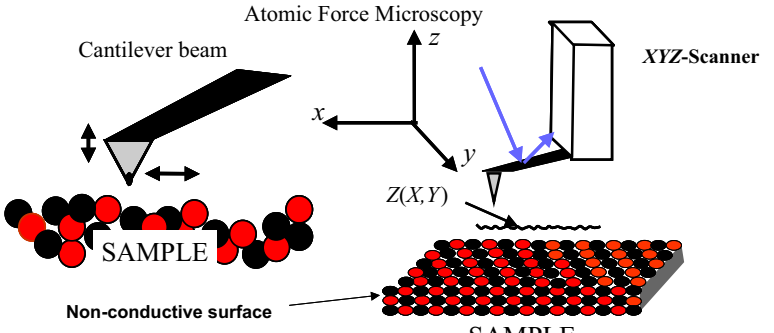

- Ambient conditions
- A sharp tip at end of cantilever beam is brought into contact with sample surface
- Surface is scanned by cantilever beam, like phonograph stylus
- Beam's low spring constant allows small forces (~10^{-9} N) to be resolved
- Beam's deflection is monitored via laser beam reflection
- Feedback mechanism if force between tip and sample

Franz J. Giessibl, "Advances in atomic force microscopy,"
[Online]: xxx.lanl.gov, arXiv:cond-mat/0305119 v1 6 May 2003.

Figure 6.16. Principle of atomic force microscopy on a non-conductive surface [63]

Silicon Cantilever with Integrated Tip

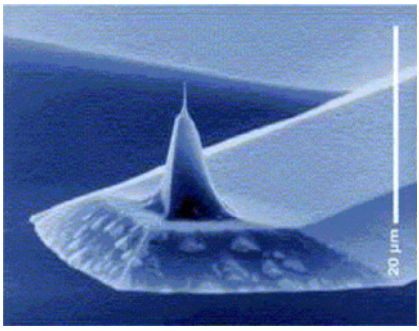

Scanning electron micrograph of a micromachined silicon cantilever with an integrated tip pointing in the [001] crystal direction.

Nanosensors, 2002, POINTPROBE sensors, Nanosensors AG, NANOSENSORS GmbH und Co.KG, Koogstraat 4, 25870 Norderfriedrichskoog, Germany.

Figure 6.17. Silicon cantilever beam with integrated tip. Courtesy of Nanosensors

Advances in the use of atomic force microscopy are reviewed by Giessibl [60] who presents an overview of the development of the technique and how it can be used for imaging the integrity of surface features.

The contact mode shows provides images of atomically resolved surfaces such as the potassium bromide surface (001) shown in Figure 6.20. Here, the small and large protrusions are attributed to K^+ and Br^- ions. The tip exerts a large normal and

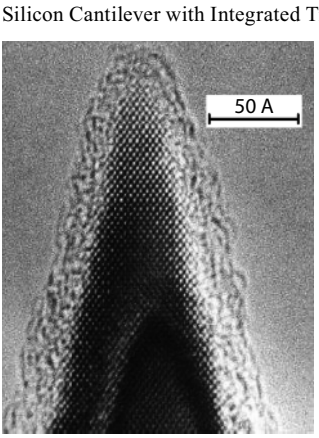

Figure 6.18. Transmission electron micrograph of an AFM tip [64]

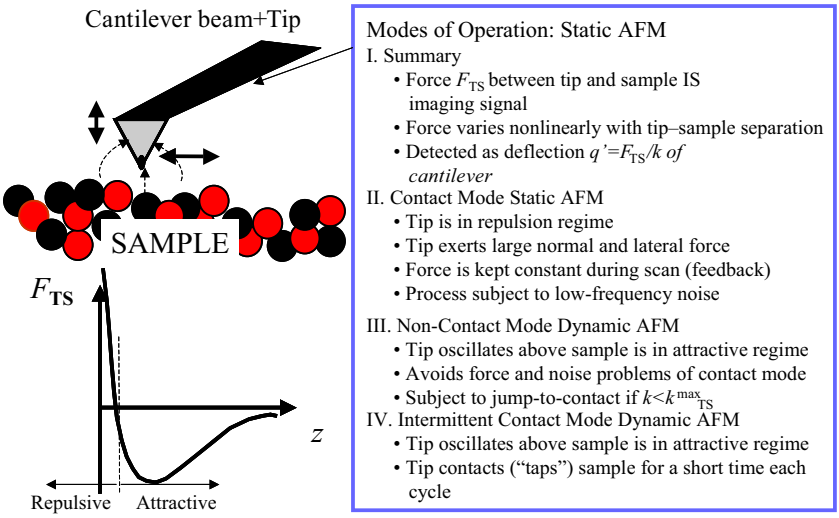

Figure 6.19. Modes of operation of the atomic force microscope [60]

lateral force in the repulsive regime when the tip is scanning the surface of the potassium bromide layer.

Figure 6.22 shows the image generated by the non-contact dynamic AFM imaging regime. The tip oscillates above the sample in the attractive force range, which tends to avoid the noise and force deflections associated with the repulsive range. The image shows distinctive variations in height that can be used to manipulate features at the nanoscale in three dimensions. This technique can be used to manipulate nanotubes and other forms of carbon to construct nanoproducts. There are two modes of operation for the dynamic AFM. These modes are AM-AFM where excitation of the cantilever tip is done at a fixed amplitude and frequency, and FM-AFM where excitation is performed at fixed amplitude and a varying frequency.

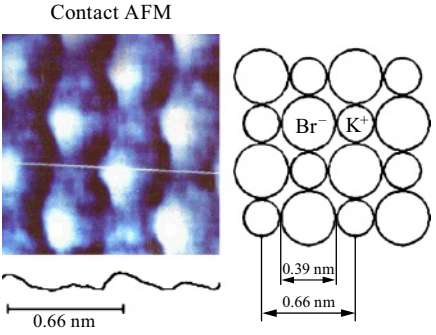

Atomically resolved image of KBr(001) in contact AFM mode. The small and large protrusions are attributed to K^+ and Br^- ions, respectively.

Giessibl, F. J. and G. Binnig, 1992b, "True atomic resolution on KBr with a low-temperature atomic force microscope in ultrahigh vacuum", Ultramicroscopy 42-44, 281–286.

Figure 6.20. Atomic resolution of KBr surface using an AFM in ultrahigh vacuum [65]

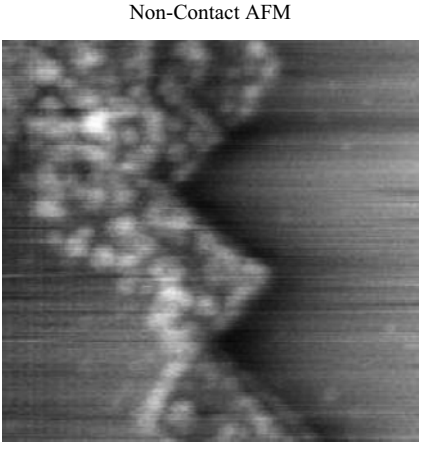

Non-contact AFM image of a cleavage face of KCl (001) with mono-and double steps of a height of 3.1 and 6.2 Å, respectively. Image size 120 nm × 120 nm.

Giessibl, F. J. and B. M. Trafas, 1994, "Piezoresistive cantilevers utilized for scanning tunneling and scanning force microscope in ultrahigh vacuum", Rev. Sci. Instrum. 65, 1923–1929.

Figure 6.21. Non-contact AFM image of a cleavage face of potassium chloride showing distinctive variations in height [65]

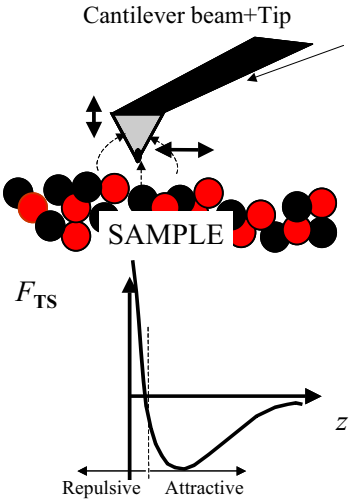

Modes of Operation: Dynamic AFM - *Two Modes*

1. **AM-AFM**: Excitation at fixed amplitude & frequency→changes in vibration amplitude & phase as tip approaches sample are detected as signal in time $\tau_{AM} = 2Q/f_0$ (*slow*)
   -Provides near-atomic resolution.

2. **FM-AFM**: Excitation at fixed amplitude & *varying* frequency→ changes in frequency as tip approaches sample are detected as signal in time $\tau_{FM} = 1/f_0$.(*fast*)
   -Provides atomic resolution.

Franz J. Giessibl, "Advances in atomic force microscopy,"
[Online]: xxx.lanl.gov, arXiv:cond-mat/0305119 v1 6 May 2003.

Figure 6.22. Modes of operation of the dynamic AFM [60]

AM-AFM provides near-atomic resolution, whereas FM-AFM provides absolute atomic resolution.

A commercial instrument that can be used for measurement of surface integrity using the AFM principle is one provided by the Veeco Metrology Group. This piece of equipment can be used to measure nanoscale features such as single-electron transistors with a little modification.

6.4.3 Surface Spectroscopy

In surface spectroscopy processes such as micro-Raman spectroscopy, laser light is focused on the surface through a microscope (a confocal microscope where a spatial pinhole is used to eliminate the out-of-focus light thus increasing the contrast is typically used), resulting in a spot size of about 1 μm (spot sizes as small as 0.3 μm can be obtained if an oil immersion objective is used). Generally, the spatial resolution of micro-Raman can be 1 μm. The scattered light of the sample is collected, through the same microscope focused on the entrance slit of a spectrometer (detection device). The sample can be mounted on a computer-controlled X–Y stage, which allows the sample to be scanned in small steps (typically 0.1 μm) in a given direction. The total collection volume depends on the light-scattering properties of the material being analyzed. Furthermore, the light penetration depth changes with wavelength. Therefore, it is possible to probe different depths of the sample by varying the wavelength. Figure 6.23 shows the operating principle of a Raman spectrometer that is used to measure surface features that change the stress state on the surface of micro- and nanomachined surfaces.

With laser scattering, a laser beam directly illuminates the sample and the amount and distribution of back-scattered light can be monitored. The basic principle of light-scattering technology is that different microstructures in a sample may cause a change in the scattering characteristic of the reflected light. Figure 6.24 illustrates a laser scattering system. A laser beam passes through a pinhole and illuminates a small area of the sample. Light is reflected from the illuminated spot on the sample to the objective where it is directed by a beamsplitter toward the confocal pinhole aperture. The pinhole positioned in front of the detector gives the system its confocal property by rejecting light originating from neighboring focal planes. Light rays from an unfocused plane are blocked from reaching the detector. However, all light rays originating from the focal plane pass through the pinhole aperture and are collected by the detector. The ability to closely discriminate between the light rays originating at the focal plane and those originating from the unfocused planes enables a laser scattering system to be a powerful tool in generating depth-precise images. The depth of the skin can be measured using laser scattering techniques.

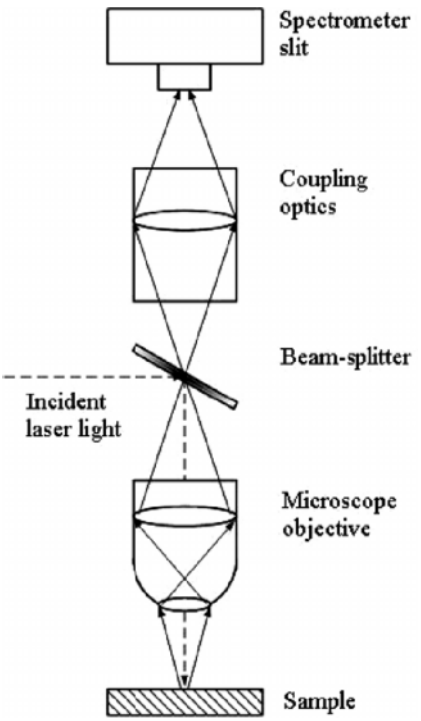

Figure 6.23. Illustration of micro-Raman spectroscopy

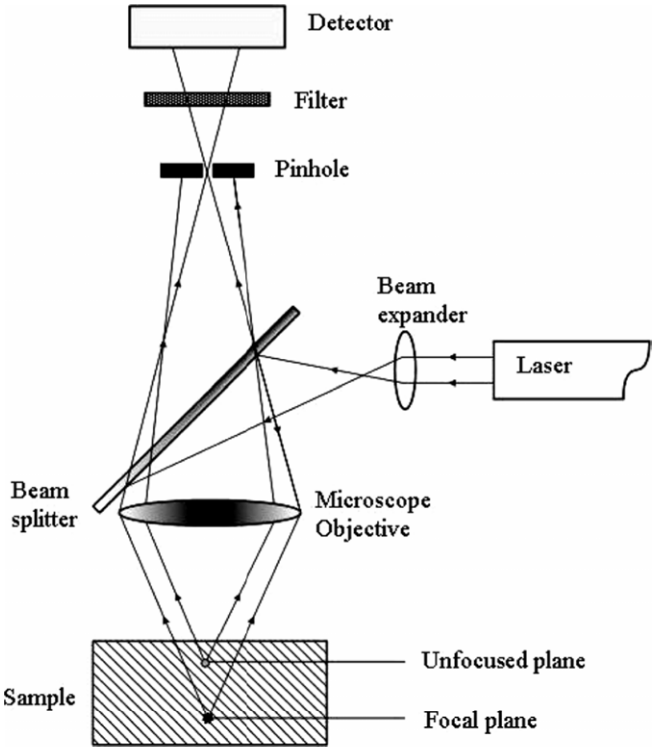

Figure 6.24. Schematic diagram of a laser scattering system

6.5 Conclusions

In order to characterize the level of damage induced in micro- and nanomachining processes, the integrity of the workpiece surface requires to be measured. This chapter has provided an outline of the problems created by machining, has provided a state-of-the-art review of micro- and nanomachining processes, and the measurement of surface integrity of micro- and nanomachined surfaces. Although not exhaustive, the chapter has shown how X-ray diffraction and microscopic techniques are used to measure surface characteristics of micro- and nanomachined surfaces.

References

[1] Backer WR, Marshall ER, and Shaw MC, 1952, The size effect in metal cutting, Trans. ASME, **74**, 61–72.
[2] Taniguchi N, 1994, Current trends in precision machining, Precision Engineering, **16**, 5–24.
[3] Shaw MC, 1952, Mechanics of three-dimensional cutting operations, J. Franklin Inst., **254**, 2, 109.

[4] Heidenreich RO, Shockley W, 1948, Structure of Metals, Report on Strength of Solids, Phys. Soc. of London, 57, London, UK.
[5] Ernst HJ, Merchant ME, 1941, Chip formation, friction, and finish of metals, Trans. Am. Soc. for Metals, **29**, 299–378.
[6] Merchant ME, 1945, Mechanics of the metal cutting process I: Orthogonal cutting and a type 2 chip, J. Appl. Phys., **16**, 267–275.
[7] Piispanen V, 1937, Theory and formation of metal chips, Teknillinen Aikakaushehti (Finland), **27**, 315–331.
[8] Merchant ME, 1950, Machining Theory and Practice, Am Soc. for Metals, 5–44.
[9] Merchant ME, 1945, Mechanics of the metal cutting process II: Orthogonal cutting, J. Appl. Phys., **16**, 318–324.
[10] Barrett CS, 1943, Structure of Metals, McGraw Hill Co., New York, USA
[11] Bridgman PW, 1952, Studies in Large Plastic Flow and Fracture, McGraw Hill Co., New York, USA.
[12] Langford G, Cohen M, 1969, Fracture and flow in solids, Trans. ASM, **62**, 623–632.
[13] Piispanen V, 1948, Formation of metal chips, J. Appl. Phys., **19**, 876–881.
[14] Blazynski TZ, Cole J M, 1960, Fracture in plastic metals, Proc. Instn. of Mech. Engrs., **1**, 74, 757–763.
[15] Shaw MC, 1950, A quantized theory of strain hardening as applied to the cutting of metals, J. AppI. Phys., **21**, 599–606.
[16] Walker TJ, 1967, PhD Dissertation, Carnegie-Mellon University, Pennsylbania, USA.
[17] Walker TJ, Shaw M C, 1969, Failure of metals in machining, Advances in Machine Tool Design and Research, Pergamon Press, 241–252. Oxford, UK.
[18] Usui E, Gujral A, Shaw MC 1960, Wear of materials in machining, Int. J. Mach Tools and Res., **1**, 187–197.
[19] Vyas A, Shaw MC, 1999, Machining effects in metals, Trans. ASME-J. Mech. Sci., **21**, 1, 63–72.
[20] Eugene F, 1952, Analysis of fracture in machined metals, Annals of CIRP, **52**, 11, 13–17.
[21] Shaw MC, 1980, A note on the failure of metals during machining, Int. Jour. Mech. Sc., **22**, 673–686.
[22] Kwon KB, Cho DW, Lee SJ, Chu CN, 1999, Failure and fracture during machining, Annals of CIRP, **47**/1, 43–46.
[23] Eyring H, Ree T, and Harai N, 1958, Metal machining and surface effects, Proc. Nat. Acad. Sci., **44**, 683–687.
[24] Eyring H, Ree T, 1961, Significant structure of flow in solids, Proc. Nat. Acad. Sci., **47**, 526–537.
[25] Eyring H, Jhon MS, 1969, Significant Theory of Liquids, J. Wiley and Sons, New York, USA.
[26] Kececioglu D, 1958, Force components, chip geometry, and cutting energy in orthogonal and oblique machining of 1015 steel, Trans. ASME, **80**, 149–168.
[27] Kececioglu D, 1958, Shear zone temperature in metal cutting and its effects on shear flow stress, Trans. ASME, **80**, 541–546.
[28] Kececioglu D, 1960, Shear zone size, compressive stress, and shear strain in metal cutting and their effects on mean flow stress, Trans. ASME-J. Eng for Industry, **82**, 79–86.
[29] Anderson TL, 1991, Fracture Mechanics, CRC Press, Florida, USA.
[30] Zhang B, Bagchi A, 1994, Finite element analysis of chip formation and comparison with machining experiments, Trans. ASME- J. of Eng for Industry, **116**, 289.
[31] Argon AS, I. J, Safoglu R, 1975, Structure of solids, Metallurgical Transactions, **6A**, 825–835.
[32] Komanduri R, Brown RH, 1967, Machining of metallic materials, Metals and Materials, **95**, 308–315.

[33] Drucker DC, 1949, Analysis of structure in machined surfaces, J. Appl. Phys., **20**, 1–8.
[34] Fleck NA, Muller GM, Ashby MF, Hutchinson JM, 1994, Dislocation motion in bcc metals, Acta Metallurgica et Materialia, **41**, 10, 2855–2867.
[35] Stelmashenko NA, Walls MG, Brown LM, Milman YV, 1993, Structure of metal structures and materials, Acta. Metallurgica et Materialia, **40**, 10, 2855–2862.
[36] Ma Q, Clarke DR, 1995, The structure of machined surfaces, J. Materials Research, **46**, 3, 477–483.
[37] Nix WD, Gao H, 1998, Dislocation motion of flowing metals, J. Mech. and Physics of Solids, **1**, 4, 853.
[38] Gao H, Huang Y, Nix WD, Hutchinson JW, 1999, Structure of metals, J. of Mechanics and Physics of Solids, 47, 1239.
[39] Dinesh D, Swaminathan S, Chandrasekar S, and Farris TN, 2001, Dislocation theories applied to machining, Proc ASME-IMECE, 1–8, New York, USA.
[40] Committee on Technology National Science and Technology Council, "National Nanotechnology initiative: Leading to the next industrial revolution", Washington D.C. 2000, Washington D.C., USA.
[41] Snowdon K, McNeil C, Lakey J., Nanotechnology for MEMS components. mstNews 2001; **3**, 9–10.
[42] EI-Fatatry A, Correial A., Nanotechnology in Microsystems: potential influence for transmission systems and related applications., mstNews 2003; **3**: 25–26.
[43] Werner M, Köhler T, Grünwald W., Nanotechnology for applications in microsystems. mstNews 2001; **3**: 4–7.
[44] El-Hofy H, Khairy A, Masuzawa T, McGeough J., Introduction. In: McGeough J eds. Micromachining of Engineering Materials. New York: Marcel Dekker, 2002. USA.
[45] Donaldson R, Syn C, Taylor J, Ikawa N, Shimada S., Minimum thickness of cut in diamond turning of electroplated copper. UCRL-97606 1987.
[46] Stephenson DJ, Veselovac D, Manley S, Corbett J., Ultra-precision grinding of hard steels. Precision Engineering 2001; **15**: 336–345.
[47] Rübenach O., Micro technology – applications and trends. Euspen online trainingleclecture.http://www.euspen.org/training/lectures/course2free2view/02MicroTechApps/demolecture.asp (accessed July 2007).
[48] Diamond milling processes for the generation of complex optical mold inserts. http://www.lfm.uni-bremen.de/html/res/res001/res108.html (accessed July 2007).
[49] Weck M., Ultraprecision machining of microcomponents. Machine Tools 2000; 113–122.
[50] Schütze A, Lutz-Günter J, Nano sensors and micro integration. mstNews 2003; **3**: 43–45.
[51] Ayman EI-Fatatry, Correial A, Nanotechnology in Microsystems: potential influence for transmission systems and related applications. mstNews 2003; **3**: 25.
[52] Ikawa N, Donaldson R, Komanduri R, König W, Mckeown PA, Moriwaki T, Stowers I., Ultraprecision metal cutting – the past, the present and the future. Annals of the CIRP 1991; **40**(2): 587–594.
[53] Shaw MC, Principles of Abrasive Processing, New York: Oxford University Press, 1996, New York, USA.
[54] Komanduri R, Chandrasekaran, Raff L, Effects of tool geometry in nanometric cutting: a molecular dynamics simulation approach. Wear 1998; **219**: 84–97.
[55] Luo X, Cheng K, Guo X, Holt R, An investigation on the mechanics of nanometric cutting and the development of its test-bed. International Journal of Production Research 2003; **41** (7): 1449–1465.
[56] Taniguchi N, Nanotechnology, New York: Oxford University Press, 1996.
[57] Dow T, Miller E, Garrard K., Tool force and deflection compensation for small milling tools. Precision Engineering 2004; **28** (1): 31–45.
[58] Cheng K, Luo X, Ward R, Holt R, Modelling and simulation of the tool wear in nanometric cutting. Wear 2003; **255**: 1427–1432.

[59] Shimada S, Molecular dynamics simulation of the atomic processes in microcutting. In McGeough J, eds., 'Micromachining of Engineering Materials', New York: Marcel Dekker, 2002: 63–84.
[60] FJ Giessibl, Advances in Atomic Force Microscopy, Accessed on line at: xxx.lanl.gov/arXiv:cond-mat/0305119. Accessed December 2004.
[61] Crommie MF, Lutz CP, Eigler DM, Atomic force microscopy, Science, 262, 218–220, 1993.
[62] Braun KF, Reider KH, AFM resolution and feature size effects, Phys. Rev. Lett, 88, 096801, 2002.
[63] Marcus R, Ravi T, Gmitter K, Chin K, Liu D, Orvis W., Ciarlo D, Hunt C, Trujillo J, Formation of Silicon Tips with 1 nm Radius, Appl. Phys. Lett., 56, Number 3, 236–238, 1990.
[64] Giessibl FJ and Binnig G, True Atomic Resolution on KBr with a Low Temperature Atomic Force Microscope in Ultra High Vacuum, Ultramicroscopy, 42–44, 281–286, 1992.
[65] Giessibl FJ and Trafas BM, Piezoresistive Cantilevers Utilized for Scanning Tunneling and Scanning Force Microscopes in Ultra High Vacuum, Rev. Sci. Instrum., 65, 1923–1929, 1994.

Index